# Micro cavity plasma arrays –
# Their general discharge performance, electric field strengths and potential for plasma catalysis

DISSERTATION

zur
Erlangung des Grades
„Doktor der Naturwissenschaften"

an der Fakultät für Physik und Astronomie
der Ruhr-Universität Bochum

von
Sebastian Dzikowski

aus
Hattingen

Bochum 2024

**1. Gutachter:** Prof. Dr. Achim von Keudell
**2. Gutachter:** Prof. Dr. Judith Golda

Datum der Disputation: _____

RUHR-UNIVERSITY BOCHUM

DOCTORAL THESIS

---

# Micro cavity plasma arrays - Their general discharge performance, electric field strengths and potential for plasma catalysis

---

*Author:*
Sebastian DZIKOWSKI

*Supervisor:*
Prof. Dr. Achim VON KEUDELL

*A thesis submitted in fulfillment of the requirements
for the degree of Doctor of Natural Sciences*

*in the*

Experimental Physics II
Faculty of Physics and Astronomy

October 25, 2024

# Declaration of Authorship

I, Sebastian DZIKOWSKI, declare that this thesis titled, "Micro cavity plasma arrays - Their general discharge performance, electric field strengths and potential for plasma catalysis" and the work presented in it are my own. I confirm that:

- This work was done wholly or mainly while in candidature for a research degree at this University.

- Where any part of this thesis has previously been submitted for a degree or any other qualification at this University or any other institution, this has been clearly stated.

- Where I have consulted the published work of others, this is always clearly attributed.

- Where I have quoted from the work of others, the source is always given. With the exception of such quotations, this thesis is entirely my own work.

- I have acknowledged all main sources of help

- Where the thesis is based on work done by myself jointly with others, I have made clear exactly what was done by others and what I have contributed myself.

Signed:

_____

Date:

_____

*"Provide the best performance you can. And when you have done, challenge yourself. Flap your wings and tear out trees. "*

Jonas Vingegaard

# *Abstract*

This thesis is dealing with the physics of a plasma discharge created in a metal-grid array, which is a modular-structured alternative to silicon-based devices developed originally by G. Eden. It consists of a magnet working as an electrically grounded electrode, a 40 µm thick dielectric foil and a high voltage energised and 50 µm thick nickel-grid on the top. This grid contains between hundreds and thousands laser-drilled cavities in the 100 µm range placed uniformly in regular pattern. By applying a bipolar voltage excitation, several physical phenomena occur. On the level of the cavity array, an ionisation wave propagates along the cavity surface. However, the dominant process is not fully understood and still under investigation. The metal-grid array can give more insight into the exact physical processes of this ionisation wave. Since it exhibits clear differences to silicon-based devices, it enables the analysis to which extent surface properties and cavity shape affect the global discharge performance. On a single cavity level, the bipolar excitation is responsible for an asymmetric discharge formation in the cavities. Therefore, these metal-grid arrays show promising performance for surface treatment and plasma-surface interaction because these asymmetric discharges lead to a local displacement of the discharge within the cavities. In simulations on almost identical devices, it was found that a strong electric field is the dominant force for the motion of charged particles. Although this parameter is therefore of high importance, any experimental data are barely available for these kind of discharges. Laser- and many emission-based techniques are not applicable due to complex geometric structures or missing optical access. However, the metal-grid array allows optical access for emission spectroscopy. Hence, the Stark effect of an allowed and forbidden helium line within the discharge can be analysed. Their line separation is proportional to the electric field and is measured spatially-integrated and time-resolved depending on the operation parameters and cavity dimension. Finally, this device allows to exchange all components due to the magnetic character of the nickel-grid. The dielectric can be coated with a catalyst before it is integrated into the device. This allows to analyse plasma-assisted catalysis in microscopic discharge dimensions.

# Contents

# List of Abbreviations

| | |
|---|---|
| **AC** | **A**lternating **C**urrent |
| **AES** | **A**uger **E**lectron **S**pectroscopy |
| **APTD** | **A**tmospheric **P**ressure **G**low **D**ischarge |
| **APTD** | **A**tmospheric **P**ressure **T**ownsend-like **D**ischarge |
| **CCD** | **C**harge **C**oupled **D**evice |
| **CFC** | **C**hloro **F**luoro **C**arbons |
| **CRC** | **C**ollaborative **R**esearch **C**entre |
| **DC** | **D**irect **C**urrent |
| **DBD** | **D**ielectric **B**arrier **D**ischarge |
| **DPP** | **D**ecreasing **P**otential **P**hase |
| **EEDF** | **E**lectron **E**nergy **D**istribution **F**unction |
| **E-FISH** | **E**lectric **F**ield **I**nduced **S**econd **H**armonic |
| **FF** | **F**ield **F**ree |
| **FWHM** | **F**ull **W**idth of **H**alf **M**aximum |
| **GRC** | **G**ordon **R**esearch **C**onference |
| **HIPMS** | **HI**gh **P**ower **M**agnetron **S**puttering |
| **HCFC** | **H**ydro **C**hloro **F**luoro **C**arbons |
| **HV** | **H**igh **V**oltage |
| **ICCD** | **I**tensified **C**harge **C**oupled **D**evice |
| **IPC** | **I**n **P**lasma **C**atalysis |
| **IPP** | **I**ncreasing **P**otential **P**hase |
| **LSM** | **L**aser **S**canning **M**icroscope |
| **MCP** | **M**ulti **C**hannel **P**late |
| **MCPA** | **M**icro **C**avity **P**lasma **A**rray |
| **MFC** | **M**ass **F**low **C**ontroller |
| **MGA** | **M**etal **G**rid **A**rray |
| **MHCD** | **M**icro **H**ollow **C**athode **D**ischarge |

| | |
|---|---|
| **NHP** | **N**egative **H**alf **P**hase |
| **NIR** | **N**ear **I**nfra **R**ed |
| **NUV** | **N**ear **U**ltra **V**iolette |
| **OES** | **O**ptical **E**mission **S**ectroscopy |
| **PEEK** | **P**oly **E**ther **E**ther **K**etone |
| **PGS** | **P**lane **G**rating **S**pectrometer |
| **PHP** | **P**ositive **H**alf **P**hase |
| **PMT** | **P**hoto **M**ultiplier **T**ube |
| **PPC** | **P**ost **P**lasma **C**atalysis |
| **PRI** | **P**hase **R**esolved **I**mages |
| **PROES** | **P**hase **R**esolved **O**ptical **E**mission **S**pectroscopy |
| **QMS** | **Q**uadropol **M**ass **S**pectrometer |
| **SBA** | **S**ilicon **B**ased **A**rray |
| **SDBD** | **S**urface **D**ielectric **B**arrier **D**ischarge |
| **TDLAS** | **T**unable **D**iode **L**aser **A**bsorption **S**pectroscopy |
| **TTL** | **T**ransistor **T**ransistor **L**ogic |
| **USB** | **U**niverse **S**erial **B**us |
| **VDBD** | **V**olume **D**ielectric **B**arrier **D**ischarge |
| **VOC** | **V**olatile **O**rganic **C**ompounds |
| **XPS** | **X**ray **P**hoto-electron **S**pectroscopy |

# Physical Constants

| | |
|---|---|
| Speed of Light | $c_0 = 2.997\,924\,58 \times 10^8\,\mathrm{m\,s^{-1}}$ |
| Elementary charge | $e = 1.602\,176\,634 \times 10^{-19}\,\mathrm{C}$ |
| Planck constant | $h = 6.626\,070\,15 \times 10^{-34}\,\mathrm{J\,Hz^{-1}}$ |
| Vacuum electric permittivity | $\epsilon_0 = 8.854\,187\,818\,8 \times 10^{-12}\,\mathrm{F\,m^{-1}}$ |
| Vacuum magnetic permeability | $\mu_0 = 1.256\,637\,061\,27 \times 10^{-6}\,\mathrm{N\,A^{-2}}$ |
| Electron mass | $m_e = 9.109\,383\,713\,9 \times 10^{-31}\,\mathrm{kg}$ |
| Boltzmann constant | $k_B = 1.380\,649 \times 10^{-23}\,\mathrm{J\,K^{-1}}$ |
| Bohr radius | $a_0 = 5.291\,772\,105\,44 \times 10^{-11}\,\mathrm{m}$ |
| Avogardo constant | $N_A = 6.022\,140\,76 \times 10^{23}\,\mathrm{mol^{-1}}$ |
| Atomic mass constant | $m_u = 1.660\,539\,068\,92 \times 10^{-27}\,\mathrm{kg}$ |

# Chapter 1

# Introduction

During the welcome ceremony of the Gordon Research Conference (GRC), taking place at the Bryant University in Smithfield (RI, United States) in 2018, Professor A. B Murphy made an interesting point while he was talking about plasmas. He stated for himself that plasmas are only existing for the majority of people in our daily life by looking into the sun and observing lightnings during thunderstorms. But if all people knew how much plasma technology has been used in the manufacturing of their electrical devices on which they are watching permanently, they would probably not only use the sun or lightning for the plasma terminology.

Indeed, in the last decades, the spectrum of industrial applications, especially based on low-temperature plasmas has continuously gained in importance [1–3]. These are used to a significant part for the manufacturing of semiconductor chips, flat panel displays and solar panels [3]. Furthermore, low-temperature plasmas are also attracting growing attention for medical applications as wound healing [4] or sterilisation [5, 6].

Typically, plasmas are subdivided in several categories depending on e.g. their dimensions or the pressure at which these sources usually operate. Microplasma sources as a category are comprising a zoo of several designs and pave the way for further promising applications and processes at atmospheric pressure [3, 7]. This requires no complex pump- and vacuum-systems.

A rather simple device is already realised by two enclosed plane-parallel oriented electrodes forming a plasma jet. A very established representative of this design is the so-called COST reference jet serving as a source of reactive species, especially for medicine and biological uses [8–11]. However, the effective discharge volume does not justice the term "microplasmas" due to its dimensions with gap sizes of up to 1 mm and a channel length of few centimetres.

Instead, this terminology is much more valid for plasmas ignited in micro-cavities (micro-pores) which are incorporated either in the electrode- or dielectric-material and exhibit typical geometric dimensions of 100 µm in length, width, and height. Additionally, it is also possible to place up to 2000 cavities per square centimetre next to each other in an uniform pattern leading to the concept of microplasma-arrays

developed originally by the group of G. Eden [12, 13]. They took advantage of the
fact that silicon being the fundamental part of this device can be processed with
high accuracy by using wet-etching procedures and many more micro-structuring
techniques. Figure 1.1 shows a sketch of the cross-section of a single cavity of three
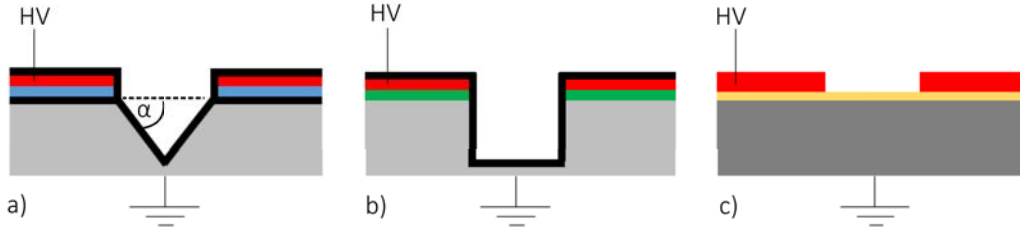different structures which are described in following.



FIGURE 1.1: Cross-section of various MCPA configurations. Silicon-
based devices are illustrated with pyramidal inverted cavities in a)
and cylindrical shaped cavities in b). The MGA is shown in c). The
colors represent following materials: Silicon $\mapsto$ grey, $Si_3N_4 \mapsto$ black,
polyimide $\mapsto$ blue, nickel $\mapsto$ red, $SiO_2 \mapsto$ brown, CoSm (magnet) $\mapsto$
dark grey and $ZrO_2 \mapsto$ yellow. Schematic is not to scale.

Based on this, they are able to produce inverted pyramidal cavities with different
sizes on a silicon wafer which acts as the electrically grounded electrode as shown in
figure 1.1a). In a second and third step, this silicon-wafer is covered with both, a
dielectric and a nickel layer. The latter serves as a high-voltage electrode to which
voltages up to $500\,\text{V}$ are applied. This structure having a thickness less than $1\,\text{mm}$
is equivalent to the basic setup of a dielectric barrier discharge (DBD). Depending
on the respective field of applications, other structures can be implemented into the
wafer e.g. micro-channels.

The group of R. Dussart went a step further and implemented not only cylindrically
shaped cavities as shown in figure 1.1b), but also four different sized trench-structures
on a single wafer by using among other procedures plasma-etching processes [14].
This kind of electrode configuration allowed to investigate the influence of the cavity
dimension on the discharge performance under identical conditions.

Simply through their nature and manufacturing process, such devices provide advan-
tages in many perspectives [12, 13]: (i) The discharge itself is precisely limited in space
through the cavity confinement being a great feature for understanding the discharge
dynamic. (ii) The discharge can occur either as a volume discharge like a micro hollow
cathode discharge (MHCD) or as a surface DBD depending on the polarity of the
applied excitation. (iii) The combination of this cavity arrangement and its either
partial or entire experimental simultaneous observation allows a kind of comparability
without investigating several single-cavity devices. All cavities are almost identical
shaped in their geometric dimensions, energised simultaneously and exposed to the
identical ambient influence as temperature, pressure and impurities. (iv) As a fourth
point, a single cavity might be interesting for experimental- and model-based research

but is not relevant for industrial usage. However, through incorporating more and more cavities in a single array and multiplying more of these arrays in further stages, also industrial applications such as large surface treatments, UV- and, light-sources, and water-cleaning units are realisable [7, 12, 13, 15].

Two basic findings have been made for these plasmas with respect to the discharge performance. The first refers to the phase-dependent discharge formation inside the cavities [14, 16, 17] : Typically, microplasma arrays are operated as DBDs with a bipolar sinusoidal voltage waveform excitation in the kHz-range. This leads to a concentration of the discharge close to the cavity edge when the nickel-electrode is applied with a positive voltage. In contrast to this, a negative voltage leads to a cavity-centred discharge formation. This asymmetric discharge performance was associated to the movement of electrons accelerated along the cavity height and cavity radius.

The second observation describes the interaction between all cavities. Phase-resolved images (PRI) showed that not all cavities ignite simultaneously but rather by an ionisation wave propagating with velocities up to $10\,\mathrm{km\,s^{-1}}$ along the cavity surface [14, 16, 18]. Several wave-runs can occur during each half-phase. Each one corresponds to a single discharge pulse in the voltage-current characteristic and hence exhibits a great analogy to the typical behaviour of DBDs as calculated in [19, 20]. In a simulation, the wave-phenomena itself was related to the production of secondary electrons due to ions or photo-ionisation in surrounding cavities [21, 22]. Although one half-period has been investigated more in depth, the exact processes within both half-periods are not fully understood.

## 1.1 Motivation and key questions

One of the greatest global challenges is the man-made climate change. Its effects are already being evident today on many levels e.g. species extinction and climate refugees due to the increasing global temperature. These are all consequences of greenhouse gas emissions like carbon dioxide and methane but also chlorofluorocarbons (CFCs), volatile organic compounds (VOC) and hydrochlorofluorocarbons (HCFCs) and many more. Low-temperature plasma sources in general can help with some of the environmental aspects in addition to their promising technical and medical applications [23, 24].

Up to now, DBDs are already used for industrial exhaust gas purification to remove CO [25], $NO_x$ [26], $SO_2$ [27] or volatile organic compounds (VOCs) [28]. Especially microplasmas are found to be useful to convert such exhaust gases due to their low-temperature nature and chemical reactivity [29]. Based on the temperature aspect, induced reactions are not thermodynamically limited since only electrons reach temperatures up to $8\,\mathrm{eV}$ while heavy particles like ions and neutrals almost stay at room temperature $(300\,\mathrm{K})$. However, it has to be stated that such plasma-chemical

processes fight with low energy efficiencies and a bad selectivity [30, 31]. The latter can lead e.g. to the formation of unwanted co-products [32–34].

A very promising way to tackle these challenges for chemical conversion in gas or air treatment is based on the combination of such non-thermal plasma sources with a catalyst. This combination is named plasma-catalysis, plasma-assisted catalysis or plasma-enhanced catalysis in the literature and allows both concepts to bring their respective strengths into play to create a synergistic effect, higher conversion efficiencies and a general improved performance than catalyst and plasma would achieve separately [31, 35].

In principal, plasma-enhanced catalysis can be performed in two different ways that depend on the relative position of plasma and catalyst to each other [24]: (i) In-plasma-catalysis (IPC) describes the configuration where the discharge and the catalyst are not spatially separated and can therefore interact with each other. In this case, the strongest interaction between both takes place. (ii) Post-plasma-catalysis (PPC) describes a setup where the catalyst is placed downstream of the discharge region.

Due to its reactivity, the plasma can avoid catalyst deactivation or poisoning [30]. Moreover, it is a source of long- and short-lived species that are able to reach the catalytic surface and contribute to chemical conversion [31, 32].

However, it needs to be emphasized that not only the plasma has an influence on the introduced catalyst, but also the catalyst on the plasma. Exemplary, the catalyst can be responsible for the formation of surface discharges. The surface morphology itself allows the discharge to take place in micrometer large pores where the electric field is clearly increased. This was studied in detail by a simulation made by Zhang et al. [36]. They investigated a simple plane-parallel DBD where one of both dielectrics contains a pore on the micrometer scale shown in figure 1.2a). A key result was that the electric field is increased by a factor of eight inside the pore compared to the discharge volume above. This results in higher electron- and ion-densities, electron- and ion-temperatures and volume ionisation coefficient that can enhance the plasma-catalysis process. In contrary, the discharge volume above remains unaffected from the higher electric field inside the pore and can be hence neglected for further considerations in the first order. Figure 1.2b) shows exemplary the electric field profile along the whole discharge volume. Additionally, this simulation showed that this effect of increased electric field strengths inside the pore can be increased further by increasing the applied voltage and by decreasing the pore diameter [36].
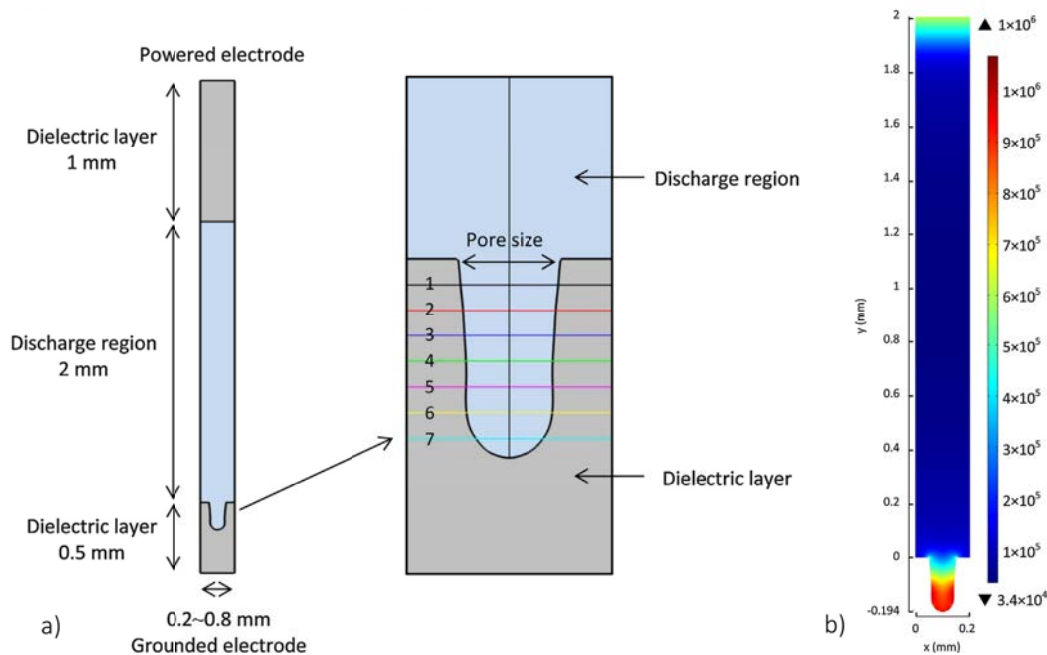
FIGURE 1.2: a) Sketch of DBD with integrated pore in the bottom dielectric. b) Electric field distribution along the complete discharge volume [36].

Thus, it becomes clear that the electric field has a huge impact on a micro-discharge for plasma-enhanced catalysis but it is also a fundamental plasma parameter for understanding DBDs in general [37, 38]. If the macroscopic electric field can be controlled in space and time, fluxes and energies of charged particles on surfaces become adjustable [19, 38] which leads to an optimisation of laboratory plasmas and their applications and modelling approaches.

Although the informative value of this parameter is of cardinal significance, experimental data are rather rare and forces one to resort to modelling and simulation [39–41]. This can be explained by the complex setup and small dimension of such microplasma devices whereby many diagnostics are often not applicable. Electrical probes are too large compared to the micrometer dimension so that they cannot be inserted in the discharge volume or would affect the discharge too much [42]. Also laser-based methods as Electric Field Induced Second Harmonic (E-FISH) [43] can be categorically excluded for many plasma sources since the optical path is often blocked [44]. With respect to the configuration made by Zhang [36], there is no chance to bring the laser beam into the pore.

Optical emission spectroscopy (OES) offers the possibility to collect the emission from the discharge zone in many cases. The most known method is based on the relative line intensity ratio of nitrogen such as the 'second positive system' ($N_2$(C-B, 0-0)) and 'first negative system' ($N_2^+$(B-X, 0-0)) [9, 37]. However, it must be taken into account that depending on the used operation gas, a certain amount of nitrogen has

to be added. This is necessary to detect a sufficient signal of the nitrogen system without changing the discharge performance too much. Also, this method is based on the knowledge of further plasma parameter like the electron energy distribution function (EEDF) that is mostly unknown and has to be assumed. The analysis of the emission via OES requires clear optical access to the discharge. For the pore-discharge, however, a view into the pore from above is due to the second electrode not possible. The same applies to bed packed reactors where the catalytic material prevents a view into the discharge volume [35, 45, 46].

The microplasma arrays, however, provide optimal optical access from different sides to make electric field measurements possible. By considering the pore dimensions and setup used in the simulation of Zhang, a great analogy to the microplasma arrays can be identified. Therefore, microplasma arrays are also attractive plasma devices for plasma-enhanced catalysis. A direct advantage is an unobstructed view into the different scaled cavities (pores) for observing the plasma-catalyst interaction, discharge performance and plasma parameters inside. Furthermore, the asymmetric discharge characteristic of the arrays allows a switching between IPC and PPC and therefore an individual investigation under equal operation conditions.

The unobstructed view into the cavities of the microplasma array allows to observe the so-called Stark effect. In high electric field regimes, the degeneracy of helium energy levels is resolved leading to the shifting and splitting of allowed and forbidden spectral lines by some tenth of nanometers. The resulting displacement between these lines can be converted into electric field strengths using a proportional correlation calculated theoretically by Foster in 1924 [47]. This ab-initio optical diagnostic tool has been already applied successfully on numerous other types of discharges such as plasma jets [48, 49], DBDs [50, 51] and glow-discharges [38, 52] by using the allowed $492.19 \, \text{nm}$ ($^1\text{D} \mapsto {}^1\text{P}^\text{o}$) and forbidden $492.06 \, \text{nm}$ ($^1\text{F}^\text{o} \mapsto {}^1\text{P}^\text{o}$) helium lines. Compared to other OES-based techniques, the required setup is rather simple and the correlation between line displacements and electric field is only based on quantum mechanical calculations. Therefore, no further plasma parameters are needed in the first order to examine electric field strengths. On the other side, plasma parameters such as temperatures and densities can have an impact for line broadening and densities of excited energy levels.

While the basic concept of arrays seems suitable for electric field measurements via OES, the choice of silicon-based arrays (SBA) is rather problematic. The manufacturing process is already very complex and includes up to 20 steps [53]. Therefore, an integration of a catalyst without its destruction during manufacturing is rather difficult. Furthermore, these devices do not leave the manufacturing process free of defects and are observed to be very vulnerable to destruction during plasma operation. The dielectric layer becomes damaged due to a strong ion bombardment resulting in an electrical breakthrough and destruction [54, 55]. In general, these devices have historically shown a short life span under laboratory conditions where parameters such

as power, pressure and admixtures are constantly varied over a wide range, making time-consuming measurements almost impossible.

A modular- and flexible layer-structured metal-grid array (MGA) was developed to tackle these challenges. This MGA is composed of a magnet working as an electrically grounded electrode, a dielectric foil and a nickel-foil acting as powered electrode on the top with laser-drilled cavities as sketched in figure 1.1c). It must be mentioned that no positive feature as cavity accuracy or sizing suffers up by using laser-drill technology in comparison to the SBA. Moreover, it is possible to produce a nickel-grid with four different sized cavity-structures placed next to each other in a line and operated in a gas flow supplied channel-like housing. This allows the adjustment of ideal operating conditions along the channel (from sub-array to sub-array) like e.g. the EEDF which is necessary for an effective gas treatment. Due to the magnetic character of the nickel foil, this is pulled towards the magnet and a hard stable device is realised. An additional advantage is that the dielectric foil can be covered with a catalytic material before it is integrated into the assembly. However, it must be mentioned that the cavity shape as well as the surface material composition is not identical compared to silicon-based devices by G. Eden and might cause differences in the global discharge performance e.g. internal electric field distribution or secondary electron emission coefficients.

In summary, the MGA offers the possibility of closing many gaps: (i) It gives the chance to investigate whether cavity shape as well as the material composition have an impact on the discharge performance in microplasma arrays in general. (ii) It allows an optical access from above for investigating electric field strengths in cavity-like structures. (iii) It gives the possibility to investigate the plasma-catalyst interaction in micro-structured dimensions. With respect to all this, the following key-questions are addressed and were investigated in the frame of project A6 of the collaborative research centre (CRC)1316 "Transient atmospheric plasmas - from plasmas to liquids to solids" and in cooperation with GREMI in Orlèans, France:

> *KQ* 1.1*: Do the cavity shape and the non-dielectrically covered nickel-electrode have an influence on global discharge properties such as pulsing, asymmetric discharge characteristic and ionisation wave propagation?*

> *KQ* 1.2*: Can further insights be gained into the wave mechanism with respect to already assumed processes such as photo-ionisation?*

> *KQ* 2.1*: How strong is the electric field and by which parameters is it influenced?*

> *KQ* 2.2*: Can a distinction in electric field strength be notified between both half-phases? If so, how can these electric field strengths be connected to the asymmetric discharge characteristic?*

*KQ* 3.1*: Does the catalyst implemented in the MGA have an effect on the global discharge characteristics, gas conversion and selectivity?*

## 1.2   Thesis outline

This thesis is divided in the following chapters:

**Chapter** 2 gives an overview of the fundamentals of DBDs with a subsequent closer look on microplasma-arrays. With respect to the latter, important experimental and simulated findings are illustrated. In addition, the required physics regarding OES in general and Stark Effect in particular are introduced here. Finally, a brief detour is given to plasma-enhanced catalysis.

**Chapter** 3 starts with a detailed description of the developed MGA which is afterwards accompanied by its electrical and gas supply. Also, all diagnostic setups are listed and explained

**Chapter** 4 deals with the question whether surface properties and cavity shape have an influence on the discharge performance of microplasma-arrays with focus on asymmetric discharge characteristic, pulsing and ionisation-wave propagation. Altogether, the aim is to determine to what extent MGA and SBA are comparable.

**Chapter** 5 is presenting the findings of electric field analysis. Spatially integrated and time-resolved measurements are demonstrated as a function of many parameters e.g. cavity dimension and voltage amplitude. A basic model is set up to bridge the gap between the measured electric fields and the asymmetric discharge characteristic.

**Chapter** 6 concentrates on the catalytic operation of the MGA and includes the impact of the catalyst on the discharge within the cavities but also their ability for gas conversion. Also, surface investigations of the dielectric after plasma-operation are illustrated.

**Chapter** 7 summarises the results obtained in frame of this thesis.

**Chapter** 8 gives brief outlook for future investigations which are necessary to answer further open questions.

# Chapter 2

# Fundamentals

## 2.1 Atmospheric pressure dielectric barrier discharges

Dielectric barrier discharges (DBD) have been examined by W. Siemens in 1857 for the first time for ozone production [56]. Up to today, a great range of further industrial applications such as surface treatment and modifications (e.g. increase in surface energy) [57] and ultraviolet excimer and fluorescent lamps have been developed [58, 59]. More applications can be found in detail in [60].

This type of discharge is characterised by the presence of at least one dielectric layer in the gap volume between both electrodes. Figure 2.1 shows possible dielectric layer arrangements for a simple plane-to-plane electrode configuration.

Due to the presence of one or more dielectric barriers, a current transport between both electrodes can only be realised through a discharge. A direct current (DC) would lead to a single discharge pulse. After this pulse, the applied electric field is completely shielded within the gap and the potential polarity has to be changed as a consequence. That is why an alternating current (AC) is applied for a continuous operation. This leads to a limited current in general and also to a protection of the electrode surfaces.
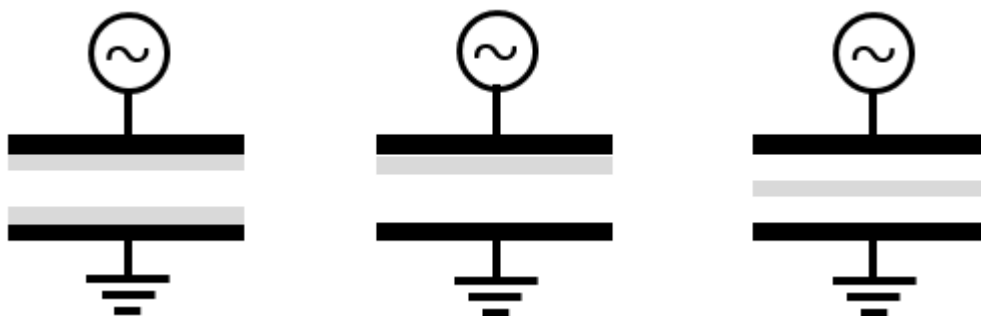


FIGURE 2.1: Sketch of various DBD configurations. The electrodes (black) are applied with AC voltage and covered or separated from each other with a dielectric (grey).

As dielectric layer various materials are applicable. Typically, glass, quartz and ceramics are used but thin enamel and polymer layers can also be applied. The choice

of the material and its properties such as thickness and dielectric constant have a direct influence on the so-called displacement current. This is a part of the electrical current that is only given by the temporal deviation of the applied voltage excitation. The additional discharge current has no contribution in it.

Since DBDs are operated at or close to atmospheric pressure, the gap distance between both electrodes is in a range of millimetres up to several centimetres. Therefore, applied voltages between a few hundreds volts and kilovolts are required to ignite a discharge inside the gap. Typical frequencies cover a range from few Hz and some MHz.

### 2.1.1   Filamentary mode

In most atmospheric pressure operated DBDs short-lived current filaments are observed [61]. These so-called microdischarges take place when the breakdown originates from electron avalanches accelerating inside the discharge gap. Due to many collisions at atmospheric pressure, high charged particle densities can be built-up at the avalanche front. If the operation conditions such as pressure and gap size are suitable, ion densities of about $10^8 \, \mathrm{cm}^{-3}$ can be produced after the formation of one electronic avalanche [62]. In this case, this production can occur without participation of secondary electrons generated either on surfaces or by Penning ionisation with metastable species.

Electrons and ions differ in their respective drift velocities resulting in a charge carrier separation. This can lead to the creation of a space charge field that superposes the applied electric field and accelerates electrons further between cathode and positive space charge. In this region, an avalanche propagation is promoted by collisional ionisation resulting in a formation of a bright and thin plasma channel which is also denoted as a streamer. It is assumed for the positive streamer mechanism that photo-ionisation by ultraviolet radiation originated from the plasma channel proceeds ionisation before and supports the streamer propagation. Typically, a streamer has a propagation velocity of about $10 \, \mathrm{km \, s}^{-1}$ and its radius is in a range between a few hundred micrometers and some millimetres [61]. However, the latter depends on the gas density and ionisation properties of the gas [60].

When the streamer has bridged the discharge gap and has reached the dielectric surface, a microdischarge is developed. Due to its high conductivity, electric charges are deposited there and a surface discharge with a clearly larger diameter than the filament is formed. The progressively accumulating surface charges counteract the applied electric field until the microdischarge is extinguished and residuals finally remain. Typical life-times of such filaments in DBDs are below $100 \, \mathrm{ns}$ [62]. These residuals weakened the local electric field and define therefore the filament location more dominantly during increasing voltage excitation. When the voltage polarity is reversed and the applied frequency is high enough to allow these residuals to survive

for reducing the local ignition voltage, prior positions are preferred as starting point for new streamers with reversed polarity.

Finally, the applied excitation plays a significant role for the formation of filament patterns. Higher voltages and lower frequencies lead to a more statistical appearance. In case of higher frequencies, filament formation is also dominated by residuals such as excited and charged species in the discharge gap [62].

As described before, the breakdown follows the streamer procedure but a single plasma filament can be characterised as a transient glow discharge consisting of a distinct cathode fall and a positive column [63]. So, typical electron densities of $10^{14}\,\mathrm{cm}^{-3}$ to $10^{15}\,\mathrm{cm}^{-3}$ and current densities of $100\,\mathrm{A\,cm}^{-2}$ to $1000\,\mathrm{A\,cm}^{-2}$ can be achieved [60]. Therefore, these filamentary discharges can show a homogeneous emission intensity under specific operation conditions. It has to be considered that this emission is caused by the overlapping radiation of all individual streamers.

In summary, all streamers let the discharge also looks like a homogeneous discharge appearance although the responsible process is based on the single streamer mechanism. As a consequence, it is nevertheless named as filamentary mode in this thesis to distinguish between the so-called second stable "homogeneous mode". In contrast to the filamentary mode, the streamer mechanism does not play a role in this homogeneous mode as explained in the following.

### 2.1.2 Homogeneous mode

The appearance of the homogeneous discharge mode is characterised by a Townsend-based breakdown [62, 64] which requires two properties: (i) a rather slow gas bulk ionisation and (ii) ionisation at low E/N regime. Therefore, a streamer cannot be formed since produced ions are able to reach the cathode in a spatial charge-free field. A second aspect is that secondary electrons can be released through ion impacts that can afterwards contribute to a maintenance of the discharge. During breakdown, the discharge homogeneity is given by the ratio of the ionisation in the gas bulk ($\alpha$-coefficient) to the secondary electron emission at the cathode ($\gamma$-coefficient) determined by the ratio of mean free path $\lambda_m$ of electrons to the discharge gap size $d$. Since the mean free path is inversely proportional to pressure $p$, Townsend breakdown is most probable for small $pd$ products. Thus, this product represents a criterion whether a Townsend or a streamer breakdown takes place. Typically, streamer breakdown is mostly defined by $pd$ values higher than $200\,\mathrm{Torr\,cm}$ while Townsend breakdown occurs at a clearly lower regime of about $30\,\mathrm{Torr\,cm}$ [62].

With respect to definitions made by Massines et al. [62], Radu et al. [64] and Bartnikas et al. [65], two different homogeneous DBDs regimes are existing: (i) Atmospheric pressure Townsend-like discharges (APTD) and (ii) atmospheric pressure glow discharges (APGD). Due to an applied waveform excitation, both modes are characterised by a strong periodically occurring current and emission signals and an

influence of expired half-phase on the following one. Each electrode changes its status between "electrically grounded" and "high voltage" from half-phase to half-phase.

### 2.1.2.1  Atmospheric pressure Townsend-like discharge

In the first instance an APTD is characterised by a low ionisation rate. Hence, the formation of a quasi-neutral plasma bulk (positive column) is not possible, resulting in an approximately undisturbed electric field within the discharge gap which is equivalent to the applied electric field in vacuum. By monitoring the voltage-current characteristic (UI) of an individual discharge pulse, a respective increasing discharge current and gap voltage are observable and no Townsend-plateau (voltage threshold) is formed.

A simulated and measured UI-characteristic can be discussed as illustrated in figure 2.2 to better understand the discharge dynamic in this mode. Naudé at al. obtained simulated results by using an equivalent circuit of a DBD. They have worked on a parallel plane electrode configuration where both electrodes are covered with a dielectric and applied frequencies of few kHz and peak-to-peak voltages in the range of 10 kV [66]. The discharge gap is 1 mm and only nitrogen is used as working gas. The authors have divided the discharge dynamic into the following three phases taking place from half-phase to half-phase with reverse polarities:

I) In this phase, the discharge is off and the detected current consists mainly of the displacement current ($I_{Cgas}$, dark grey and full line in figure 2.2b). An insignificant small discharge current ($I_{discharge}$, grey and dotted line in figure 2.2b) is generated by secondary electrons produced by metastable impacts on the cathode (not shown here). The phase shift between applied voltage ($V_{PS}$, black line in figure 2.2a) and gap voltage ($V_{gas}$, black line in figure 2.2a) is caused by residual ions and electrons of the previous half-phase of a reverse applied polarity. These charge carriers are adsorbed on the dielectrics and its electrical potential leads to a superposition with the applied voltage. At the same time, the voltage across dielectrics ($V_{sd}$, grey line in figure 2.2a) has to decrease and the necessary ignition voltage is therefore not reached within the gap.

II) The gap voltage reaches the required ignition voltage and a discharge current begins to increase strongly up to a value of about 6 mA for a duration of 12 μs. While the gap voltage is increasing, ions absorb more and more kinetic energy and boost the secondary electron production at the cathode. This leads to an exponentially increasing discharge current with the rising gap voltage and electron accumulation at the anode. Since the voltage across the dielectric decreases, the electron surface density on the dielectric of the cathode drops and less secondary electrons are available [67]. As a result, the discharge current begins to saturate and reaches its maximum value when the voltage across the dielectrics disappears.

III) During this Townsend discharge, the gap voltage stays almost constant and an increase of the applied voltage only influences the voltage across the dielectrics. This is caused by the better conductivity of the plasma within the gap and accumulating charge carriers adsorbed at the dielectric surface. At the end, the discharge current slowly decreases since it is mainly given by the temporal derivative of the applied voltage [66] and leads finally to discharge extinction.
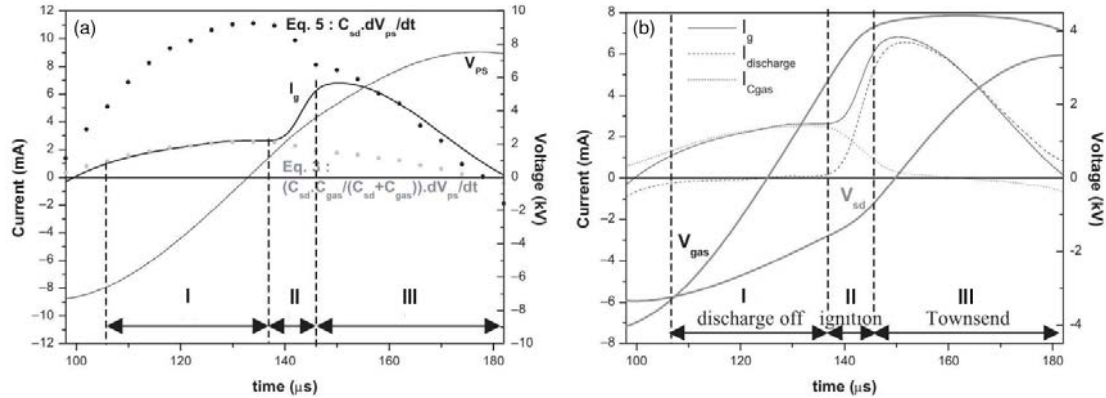


FIGURE 2.2: Voltage and current characteristic of a) measurements and b) simulations by Naude et. al. [66] made in an atmospheric pressure Townsend discharge in nitrogen. The discharge is operated in a plan-parallel electrode configuration having a discharge gap of 1 mm. The bipolar sinusoidal excitation is characterised by a peak-to-peak voltage of 15 kV and a frequency of 6 kHz. Both electrodes are covered with a dielectric. Illustrated profiles comprise the discharge current $I_{discharge}$ (grey and dotted line), displacement current $I_{Cgas}$ (bright grey and dashed line in b)), sum of both and measured current $I_g$ (black line in a) and b)), applied voltage $V_{PS}$ (black line), gap voltage $V_{gas}$ (black line) and voltage across the dielectrics $V_{sd}$ (grey line in b)).

### 2.1.2.2 Pulsating Townsend mode

As shown in figure 2.2 only one broad discharge current peak occurs. But this APTD mode can also take place in the so-called pulsating Townsend mode where multiple current peaks at each half-phase are observable [20]. This is depicted in figure 2.3. The first ignition proceeds as explained in the three phases before. However, as the current becomes smaller, a second breakdown with smaller amplitude can occur if the voltage is increased further. This procedure repeats until the maximum voltage of the applied excitation is reached.

Based on simulations, this pulsating Townsend mode can be attributed to dielectric properties in combination with the gap size between electrodes. A significant factor seems to be the desorption of previously adsorbed electrons on the cathode which serve as primary electrons for an avalanche breakdown for a subsequent current pulse after the initial one [20]. During this, a huge ion density is built-up close to the cathode while it is assumed that the electron density distribution is formed immediately. This leads to a modification of the internal electric field and to absence of quasi-neutrality. Additionally, rather slow ions can produce secondary electrons by
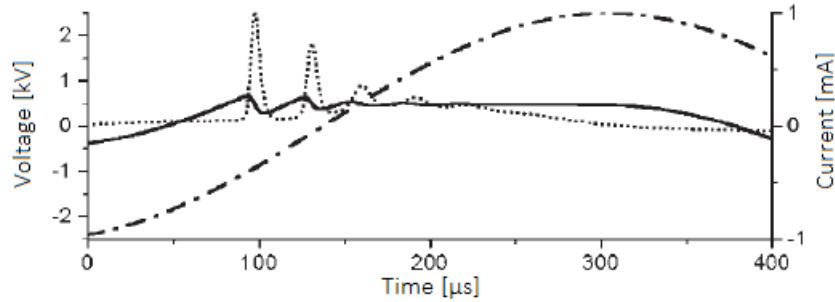
FIGURE 2.3: Voltage and current characteristic of a pulsating Townsend discharge simulated by Golubovskii et al. of a dielectric barrier discharge [20]. This characteristic shows the applied voltage (dashed dotted line), the current (dotted line) and the gap voltage between electrodes (solid line).

hitting the anode. The time between the production of ions close to the cathode and subsequent formation of secondary electrons at the anode is responsible for the pulsed appearance of discharge current peaks.

Whether pulsing takes place and how strong it is depends on two processes: (i) If the electron desorption proceeds more effectively compared to the APTD, a stronger damping of the pulsed structure occurs. In case that the electron desorption predominates the ion-induced secondary electron emission, no pulses develop [68]. (ii) An additional factor is the spatial ion density formation within the discharge volume. It can change the electric field distribution and influence the electron multiplication coefficient, consequently. This results in a wave-formed electric field and particle density distribution in space and time as seen in simulations [68].

### 2.1.2.3 Atmospheric pressure glow discharge

While APGD and APTD are based on the Townsend-breakdown mechanism, they differ significantly afterwards in their UI-characteristic. In case of the APGD, current and voltage rise and the Townsend-plateau are exceeded. After ignition, the discharge turns into a glow discharge, resulting in the formation of a cathode fall, a negative glow, a Faraday dark space and a positive column [69]. The increasing conductivity of the plasma and charge carrier deposition on dielectric surfaces lead to a rapid collapse of the gap voltage while the voltage across the dielectrics rise simultaneously. As a result, the plasma can no longer be maintained and extinguishes finally. This is also different to the APTD where deposited charge carriers on dielectrics do not exceed a critical threshold. Thus, a decreasing voltage across the dielectrics does not lead to a drop of gap voltage. This fast dynamic is also noticeable in typical pulse durations of about 1 µs with almost identical operation parameters which are 10 times shorter than in APTD. Figure 2.4 shows a typical measured voltage-current characteristic of an atmospheric pressure glow discharge.

When the current pulse is finished, both dielectric surfaces are uniformly covered with
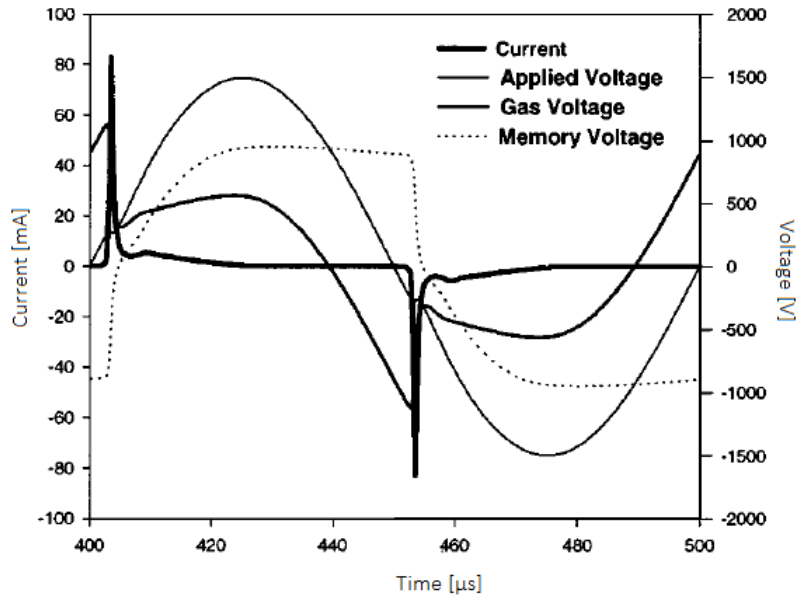
FIGURE 2.4: Voltage and current characteristic of an atmospheric pressure glow discharge measured by Massines et al. of a dielectric barrier discharge [69]. This characteristic shows the applied voltage (dashed dotted line), the current (dotted line) and the gap voltage between electrodes (solid line).

charged particles, resulting in a constant ignition voltage for all subsequent half-phases of equal polarity. A further increasing of the applied voltage is not sufficient to re-ignite the discharge and the next discharge occurs only after zero-crossing of the applied voltage.

### 2.1.2.4 Pseudo-glow discharge

Under similar conditions, another form of homogeneous discharge at atmospheric pressure can be built up consisting of a sequence of short discharge and emission pulses at both half-periods during excitation. This leads to the definition "pseudo-glow discharge" since each discharge pulse of the sequence is based on the continuous APGD mechanism [65]. An alternative definition is called the pulsating glow-discharge. Figure 2.5 shows a typical voltage current characteristic of a pseudo-glow discharge measured by Radu et al. in a dielectric barrier discharge [64].

For ignition of each individual discharge pulse, the required ignition voltage has to be reached across the gap by increasing the applied voltage as it is the case for the single pulse within APGD. However, this mechanism also leads to extinction due to produced surface charges deposited on dielectric surfaces. The applied voltage has to be increased further to overcome the extinction and to ignite a next pulse. This procedure continuous until the voltage amplitude of the applied excitation is reached. It has been observed that the number and width of an individual pulse of the pulse series depend on the excitation frequency as well as on the applied excitation form
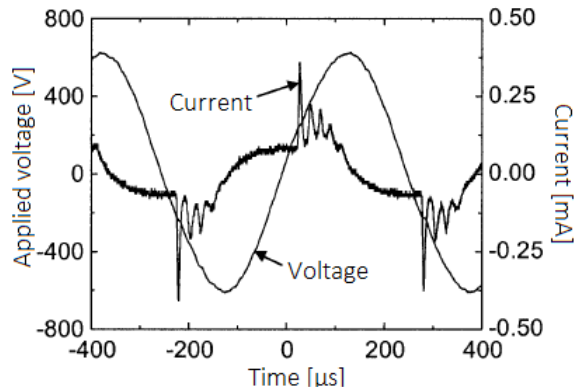
FIGURE 2.5:  Voltage and current characteristic of a pseudo-glow
discharge measured by Radu et al. on a dielectric barrier discharge
[64].

(triangular, sinus,...) [70, 71]. As an example, increasing applied voltages lead to more
pulses per sequence [64].

One point that cannot be ignored is the significant influence of the first expired
discharge pulses on the following within the same polarity and half-phase. In the
case of APGD, there is always only one pulse per half-period. In the time between
these pulses, concentrations of metastables and excited species built up in the single
discharge and decay almost completely and play therefore no role in the ignition
phase. In contrast, in the pseudo-glow discharge during the same half-period, the
ionisation rate coefficient of successive discharge pulses has a large dependency on
pulses before. Thus, the required voltage enhancement for ignition of subsequent
discharge pulses is clearly lower in comparison to already expired pulses. This is
reached by higher metastable and excited particle species that increase the ionisation
rate trough Penning ionisation of available impurities. Due to this, explicit lower E/N
values for breakdown are needed than in the case where no metastables or excited
particles are available.

If the applied voltage is high enough and a high number of discharge pulses occur, the
formation of a quasi continuous glow-discharge and its superposition on the pseudo-
glow discharge pulses can be registered [64]. In this case, the generation of a glow
discharge is a direct result of higher ionisation rates within the plasma bulk caused by
the temporal convergence of all occurring pulses.

A special role is played to impurities and the used gas [64]. It has been observed that
small amounts of about 0.1 % vol. of nitrogen, argon and hydrogen are responsible
for a higher number of discharge pulses per sequence. These impurities allow the
gas molecules to be ionised effectively through Penning ionisation with metastable
species resulting first in a higher ionisation rate coefficient and second in lower ignition
voltages. In case that the concentration of impurities is too high, a transition to a
spark discharge takes place. From this point, quenching of metastable species through

impurities surpasses Penning ionisation and Townsend breakdown cannot be induced, consequently.

### 2.1.2.5 Memory effect

All named atmospheric pressure discharge modes exhibit a strong periodicity in form of current and emission due to the periodically applied excitation. Each discharge shows a similar characteristic as a DC discharge but it is influenced through discharges of previous half-periods. This leads to the so-called "memory effect".

This effect is of great importance and visible in the very first applied excitation cycles where the first initial discharge is ignited in the respective half-period. At the beginning, these discharges have a rather filamentary mode changing with further half-periods to a Townsend-breakdown dominated behaviour [62]. In comparison to pulse duration of the respective discharge, the transient behaviour is based on clearly longer time scales caused through temperature effects and stored potential energy by excited and ionised particles on dielectric surfaces and in gap volume between both electrodes [62].

While a lot of mechanisms are responsible for the memory effect, they are based nevertheless on the same principle: produced species of previous half-periods are still available for following cycles and can therefore influence discharges. As mentioned, the Townsend-breakdown depends on the ratio of a secondary electron emission and ionisation within the plasma bulk. The former is strongly influenced by the memory effect.

After each discharge, electrons are deposited on the anode. At the entry of the next half-phase, this electrode becomes the cathode and a huge amount of weak bound (1-2 eV) electrons are available [68]. This leads to a strong contribution of secondary electron emission and a modification of the internal electric field. This release of electrons can be caused by metastables if their flux on the dielectric surface is high enough [62]. This kind of species possess enough energy for that and for the production of secondary electrons through Penning ionisation. However, their influence in noble gases is rather negligible due to their lifetimes of about 200 ns at atmospheric pressure [72] .

Further, ions can also survive from half-period to half-period to contribute to secondary electron emission and manipulate the electric field.

### 2.1.2.6 Distinction between APTD and APGD

In order to be able to assign experimental observations to respective modes, criteria for interpretation are of great importance. Massines at al. have created a table containing typical plasma parameters and properties and its magnitudes as illustrated in table 2.1 for APTD and APGD [62]. However, it must be mentioned that these values and

facts are only an orientation and do not represent exact definitions. All illustrated values are observed for simple plane parallel electrode configurations and can thus differ for more complex geometries. In these sources, inhomogeneous electric field distributions can cause a kind of distortion of this parameters. Furthermore, amounts of admixtures and impurities can also shift these thresholds.

|  | APTD | APGD |
|---|---|---|
| Maximum electron density [$cm^{-3}$] | $10^7$-$10^8$ | $10^{10}$-$10^{11}$ |
| Maximum ion density [$cm^{-3}$] | $10^{10}$ | $10^{11}$ |
| Neutral plasma formation | no | yes, positive column |
| Metastable density [$cm^{-3}$] | $10^{13}$ | $10^{11}$ |
| Current density [$mAcm^{-2}$] | 0.1-10 | 10-100 |
| Gas voltage variation at current maximum | constant (Townsend plateau) | decrease (cathode fall formation) |
| Process gas | $N_2$, air, $N_2O$ | Penning mixtures in He, Ar, Ne |
| Discharge gap size | $< 2\,mm$ | $> 2\,mm$ |
| Driving frequency | $< 10\,kHz$ | $> 1\,kHz$ |
| Power density for excitation at $10\,kHz$ | $\sim Wcm^{-3}$ | $\sim 0.1\,Wcm^{-3}$ |
| Approach to resolve filaments | current, optical | PMT, ICCD |

TABLE 2.1: Typical orders of magnitude of different plasma parameters in APTD and APGD [62].

## 2.2 Microplasma arrays

In most DBD applications, simulations, and experiments, electrodes are covered with the same dielectric arranged in a simple planar-parallel configuration. In between both electrodes, the discharge is operated in the volume which is called volume DBD (VDBD). By pushing both electrodes together and decreasing the width of one electrode, no volume for the VDBD is available and a so-called surface DBD (SDBD) ignites along the dielectric close to the smaller electrode.

To enclose this SDBD more and more along the dielectric, a further electrode segment can be placed on the dielectric layer. In case that the distance between both electrode segments is in the micrometer range, a kind of cavity is created. By putting more and more electrode segments on the dielectric, a high number of cavities is created leading finally the so-called micro cavity plasma arrays (MCPA). Such devices are basically characterized by a large number of small cavities in micrometer scale incorporated uniformly in an arrangement in electrode and dielectric material.

Such devices can differ in their geometric structure and in the way how they are formed in the electrode or dielectric material. Figure 2.6 shows a sketch of the cross-section of three different cavity configurations. Areas of the same color correspond to the

same material. Figure 2.6a) represents the cross-section of a silicon-based cavity with inverted pyramidal cavities, b) silicon-based cavity with a cylindrical shaped cavity and c) of a metal-grid array (MGA). These cavity structures and their formation to the respective array are described in detail in the following subsections.
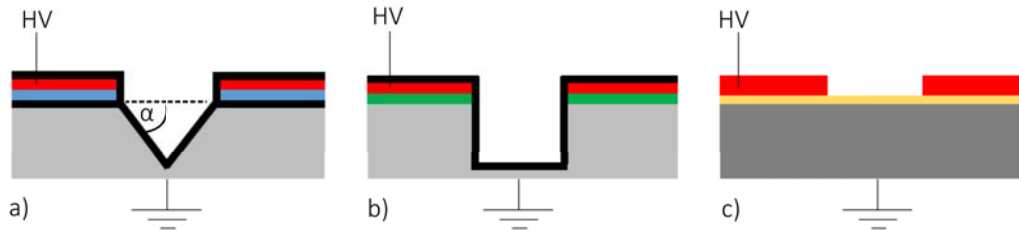


FIGURE 2.6: Cross-section of various MCPA configurations. Silicon-based devices are illustrated with pyramidal inverted cavities in a) and cylindrical shaped cavities in b). The MGA is shown in c). The colors represent following materials: Silicon $\mapsto$ grey, $Si_3N_4 \mapsto$ black, polyimide $\mapsto$ blue, nickel $\mapsto$ red, $SiO_2 \mapsto$ brown, CoSm (magnet) $\mapsto$ dark grey and $ZrO_2 \mapsto$ yellow. Schematic is not to scale.

## 2.2.1 Setup and structure of silicon-based arrays

### 2.2.1.1 Pyramidal inverted cavities

The most known array device was developed by the group of G. Eden and contains inverted pyramidal cavities with a squared base. Its cross-section is shown in figure 2.6a). Such forms are realised by micro-structure techniques under clean room conditions allowing one to incorporate a large number of functions in micrometer- and nanometer-scale in a controllable way. A detailed description of this device can be found in [7, 12, 13]. Cavities or trenches are incorporated through wet etching with potassium hydroxide (KOH) in a p-doped and $300\,\mu m$ thick silicon wafer (grey) that serves as the grounded electrode. Since various planes of the crystal lattice in silicon react differently to the etching, the pyramidal structure is formed with an angle of $54.7°$ between cavity side wall and cavity opening ($\alpha$ in figure 2.6a)). Under this angle and a base length of $50\,\mu m$, a cavity depth of $35\,\mu m$ is achieved.

As a first coating, the complete structure is covered with a $0.1\,\mu m$ thick layer of silicon nitride ($Si_3N_4$, black) by using plasma-supported chemical vapour deposition. Afterwards, a polyimide (blue) follows on the $Si_3N_4$-surface. This is applied by Spin-coating and can be processed further by dry etching. The task of this approximately $8\,\mu m$ thick polyimide layer is to ensure a clear separation to the nickel layer (red) that is deposited up next through physical vapour deposition. This nickel layer has a thickness between $0.12\,\mu m$ and $0.2\,\mu m$ and works as a high-voltage applied electrode. However, the polyimide as well as the nickel layer are not deposited on the cavity wall inside. These layers are defined through photolithography on a chromium-mask and formed respectively by using wet- or reactive ion-etching processes. Basically, the layer deposition processes set up a sandwich-like structure as a simple DBD configuration

(electrode-dielectric-electrode). Finally, the whole structure including the cavity wall inside is covered again with $Si_3N_4$ as protection against the ambient.

### 2.2.1.2   Cylindrical cavities

A prominent alternative is developed by the group of R. Dussart. Although both devices are based on a silicon-wafer, they show differences in their structure and their manufacturing process as described in detail (20 steps under clean room conditions) in [53]. Here, cylindrical cavities are processed in a $500\,\mu m$ silicon-wafer having a resistivity between $2\,\Omega\,cm$ and $5\,\Omega\,cm$. Its cross-section is shown in figure 2.6b).

Silicon dioxide ($SiO_2$, brown) with a thickness of $6\,\mu m$ is applied as a first dielectric layer. After this, a $10\,\mu m$ thick titanium layer and a $100\,nm$ thick copper layer are deposited on $SiO_2$ by use of metal deposition (sputtering) for a better bonding in the following. The cavity structure is again defined through photolithography by using a photoresist. Afterwards, the $1\,\mu m$ nickel electrode is created by stepwise electrochemical precipitation. The subsequent etching process of the cavity structure is built up gradually and consists of (i) wet etching for removing the copper and titan layer and (ii) plasma-enhanced etching for cleaning $SiO_2$. (iii) At the end, $2\,\mu m$ deep cavities are incorporated in the silicon-wafer by using a passivation phase and anisotropic etching.

Finally, the topside is covered with $Si_3N_4$ that acts as dielectric cover of electrodes and is applied by plasma-supported chemical vapor deposition. As a result, a cavity arrangement e.g. $50 \times 50$ cavities with a diameter of $150\,\mu m$ and a depth of about $10\,\mu m$ are formed. A titanium layer with a thickness of $10\,nm$ is added to the back so that a $200\,nm$ contact layer applied on it adheres better.

In the frame of this method to produce silicon-based arrays (SBA), it was also possible to develop a single wafer with four different sized structures. Instead cavities, closed trenches were processed that allowed to investigate the influence of the dimension on the discharge under equal operation conditions. Otherwise, each single sized structure would have to be investigated individually [14].

### 2.2.1.3   Operation challenges

Although both silicon-based configurations have a final dielectric protective layer, lifetimes of only some minutes to few hours are achieved [12, 53] making reproducible and time-consuming investigations on ionisation wave propagation and asymmetric discharges difficult to observe. The reasons for instabilities occurring during operation and subsequent destruction are diverse: (i) Silicon-based arrays have a low thermal capacity due to their small size. In case of an increased electric field at some areas e.g. sharp edges within the cavity, thermal overstressing occurs. This leads to a damage of the dielectric layer and hence to an electrical short circuit. (ii) As described above, a lot of manufacturing processes are necessary to built such silicon-based

devices. Therefore, it is difficult to ensure that all array-devices are produced under same clean conditions. Especially, not quite clean surfaces lead to a poor bonding between adjacent layers and an inhomogeneous setup resulting into a detachment from each other [53]. Therefore, such devices are already error-prone before first operation. Under certain circumstances, these cannot be ignited at all. (iii) The complete nickel electrode becomes dielectrically covered in the manufacturing process so that no contacting is possible. Thus, a small area of protective dielectric has to be removed. The subsequent contacting must assure a low resistance for a operation of all cavities. (iv) Due to strong electric fields along the boundary edge between cavity wall and basis, strong ion bombardment occurs. This high energetic ions are responsible for a removal of the dielectric layer. In the UI characteristic, an Ohmic behaviour is detectable instead of a capacitive one which results finally in a thermal overstressing and destruction [54]. An additional effect is observable on silicon-based microhollow cathode devices where the silicon-wafer is not dielectrically coated. It could be found that blister-like structures arise on the silicon-surface formed through helium implantation during plasma operation. With time, the pressure inside increases and the blisters explode resulting in a destruction of the homogeneous silicon surface. This leads to an increasing electric field on the sharp edges and hence to an appearance of micro-arcs [55]. The same effect can also take place in silicon-based arrays if the dielectric coating is not deposited ideally.

## 2.2.2 Setup and structure of metal-grid arrays

To tackle all known manufacturing and operation problems of silicon-based devices, a metal grid array (MGA) has been developed in frame of this thesis. Its concept is already published in [73]. The corresponding cross-section is illustrated in 2.6c) and its complete setup is explained in detail in section 3.1.1. Instead of the silicon wafer, a simple magnet (CoSm, dark grey) serving as the grounded electrode is used and completely covered with a laser-cut ceramic foil ($ZrO_2$, yellow). On top, a nickel foil with laser-drill cavities is pulled due to its magnetic character to the magnet. Compared to silicon-based devices where all layers are hold together by adhesion, this MGA is mechanical fixed. A further difference is that the nickel electrode is not dielectrically covered leading to losses of charged particles. The influence of these distinctions on the discharge behaviour compared to SBA is investigated in chapter 4.

## 2.2.3 Physical phenomena

### 2.2.3.1 Asymmetric discharge characteristic

Almost all explained atmospheric pressure DBD modes were investigated on simple and plan-parallel electrode configurations where both electrodes are covered with the same dielectric material. However, a deviation from one of these two properties leads to an asymmetric discharge. In case of silicon-based arrays where both electrodes and corresponding dielectrics form a cavity, a strong deviation between half-phases occurs.

This can be observed in inverted pyramidal [16] as well as cylindrical shaped cavities [17]. Furthermore, this effect occurs in silicon-based trenches [14].

It has been observed by ICCD-camera investigations in head-on observation (optical axis is parallel to surface normal of array) that the occurring emission structure within a cavity during a discharge pulse changes between both half-phases. During the positive half-period (PHP, $U_{app} > 0$) an increased emission takes place close to the cavity edge, resulting in a ring-shaped emission structure. In contrast, a more cavity center concentrated emission structure appears in the negative half-period (NHP, $U_{app} < 0$). This phenomenon is shown in figure 2.7 where the applied triangular voltage excitation (black), the corresponding photomultiplier signal (red) and a phase-resolved image of the discharge within a single cavity of a silicon-based array is illustrated. This content is taken from [16]. The applied voltage amplitude is set to 400 V at a frequency of 50 kHz. The cavities have a base length of 50 µm and are operated in argon at a pressure of about 500 mbar.
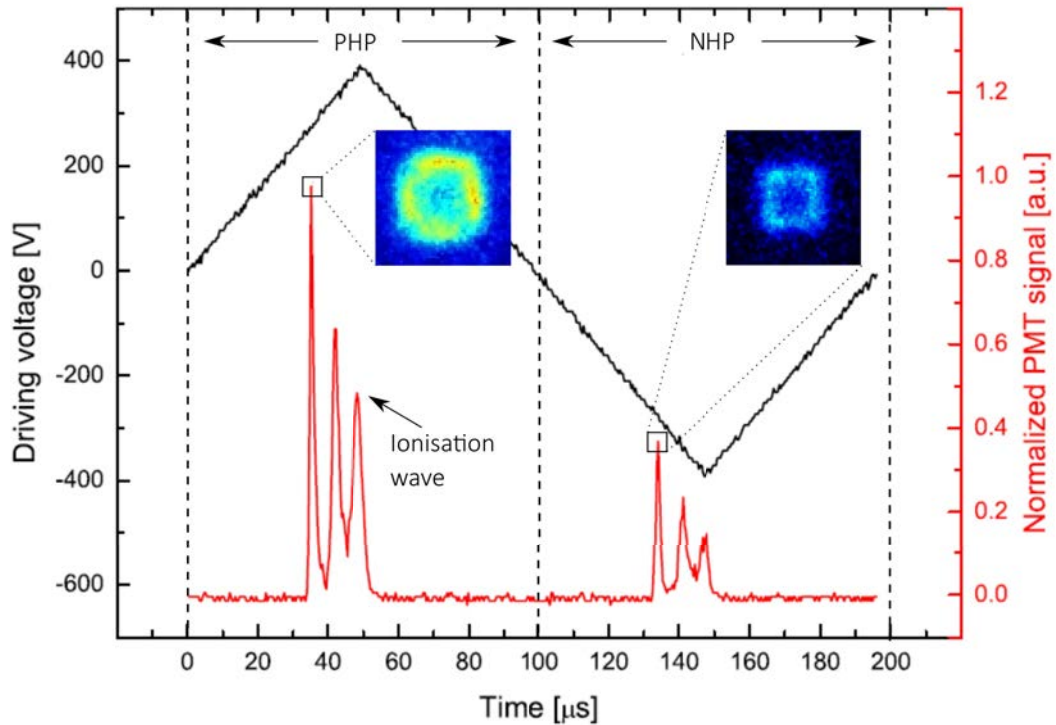


FIGURE 2.7: Illustration of the the asymmetric discharge phenomena recorded on a silicon-based array [16]. The voltage amplitude is set to 400 V at a frequency of 50 kHz. The cavities have a base length of 50 µm and are operated in argon at a pressure of about 500 mbar.

In a first simple attempt to understand this asymmetry, the electron movement within the cavity was considered as illustrated through dashed black arrows in figure 2.8. When the nickel electrode is positively charged, electrons are accelerated due to the applied electric field distribution out of the cavity in direction to the dielectrically covered nickel electrode (PHP, see figure 2.8a)). After exceeding a threshold energy for ionisation along their trajectory, further electrons are produced and a Townsend

avalanche is created. Since electrons have a high mobility, clouds (red areas) consisting of ions and excited particles remain behind. As soon as the applied voltage on nickel electrode becomes negative, this process runs in the other direction shown in figure 2.8b). In this negative half period, electrons move to the centre of the cavity bottom resulting in an ion and excited species cloud inside.
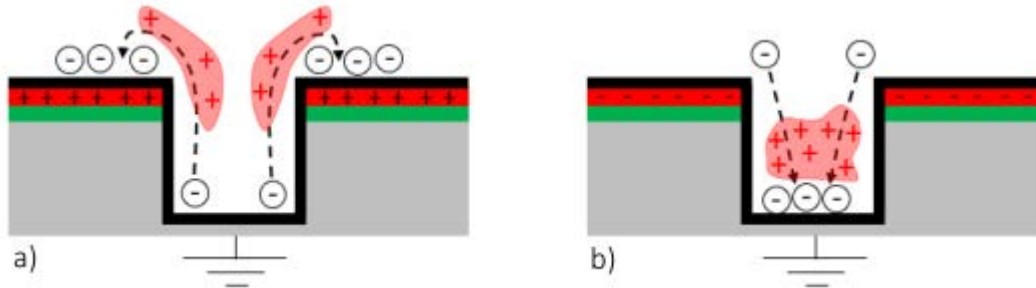


FIGURE 2.8: Simple picture of the asymmetric discharge characteristic as described in [16, 17]. A distinction is made between a) PHP and b) NHP.

### 2.2.3.2 Wave propagation

The asymmetric discharge characteristic deals with the phase-depending dynamic within a single cavity. However, an array consists of hundreds to thousands of cavities which do not ignite simultaneously. Instead, the ignition (ionisation) takes place from cavity to cavity in a form of an ionisation wave propagating across the cavity surface (array). Each ionisation overrun corresponds to a single detected discharge pulse as illustrated in figure 2.7. This was observed by the use of phase-resolved imaging on SBA containing pyramidal [16, 18] and cylindrical formed cavities [14]. The propagation velocity was measured to about $10\,\mathrm{km\,s^{-1}}$ in both half-phases.

Investigations regarding the processes which are responsible for wave propagation are only limited available. Wollny et al. published a modelling approach based on the generation of secondary electrons through photons and ions. In a first attempt, the wave propagation was only based on ion induced secondary electrons when the silicon-wafer is applied with a positive DC voltage of $500\,\mathrm{V}$ [21]. The implementation of both mechanisms has only been studied in a row of three adjacent cavities for a time range of $50\,\mathrm{ns}$ after ignition when a negative voltage is applied on the nickel electrode [22]. The involving processes are sketched in figure 2.9 and summarised in the following:

 (i) As an initial condition, a plasma density of $5 \times 10^{10}\,\mathrm{cm^{-3}}$ is set at the left vertex of the left cavity opening. In contrast to measurements, this simulation does not consider a time-dependent applied excitation. The discharge ignition (t= 0) is started by an abrupt DC voltage application on the nickel electrodes of $-500\,\mathrm{V}$.

 (ii) As described before, a negative charged nickel electrode yields an electron movement and avalanche in direction to cavity bottom. Thus, the electron

density rises and ions as well as excited species are generated. Due to de-excitations photons are produced radiating to adjacent cavities around.

(iii) In the meantime, ions drift opposite to electrons out of the cavities and strike on the dielectric surface characterised in this model by a secondary electron emission coefficient of about 0.15 on all surfaces. These induced secondary electrons also run into the cavity and an electron density of $10^{15}\,\mathrm{cm^{-3}}$ is reached after t= 25 ns shielding the applied electric field. Finally, the discharge passes from a Townsend to a glow- discharge regime.

(iv) An amount of produced secondary electrons drift further across the dielectric surface on the top of the array in direction to the adjacent cavity where these serve as initial electrons for ignition. Because of the negative applied potential again, an electron avalanche is built-up in direction to the cavity bottom and the discharge ignites, consequently.

(v) Secondary electrons in adjacent cavities can also be generated by photo-ionisation. As described in (ii), photons are already produced in the very first ignited cavity and radiate in all directions. In this model secondary electron emission caused by photons on dielectric surface is quantified with a coefficient of 0.05. Interesting is that this kind of secondary electron production leads to an electron density larger than $10^{10}\,\mathrm{cm^{-3}}$ at t= 30 ns after ignition of the first cavity. This results in wave velocity of about $5\,\mathrm{km\,s^{-1}}$ that is in great accordance to measured values at almost equal conditions. Omitting this photo-electron process only yields velocities of about $1\,\mathrm{km\,s^{-1}}$.
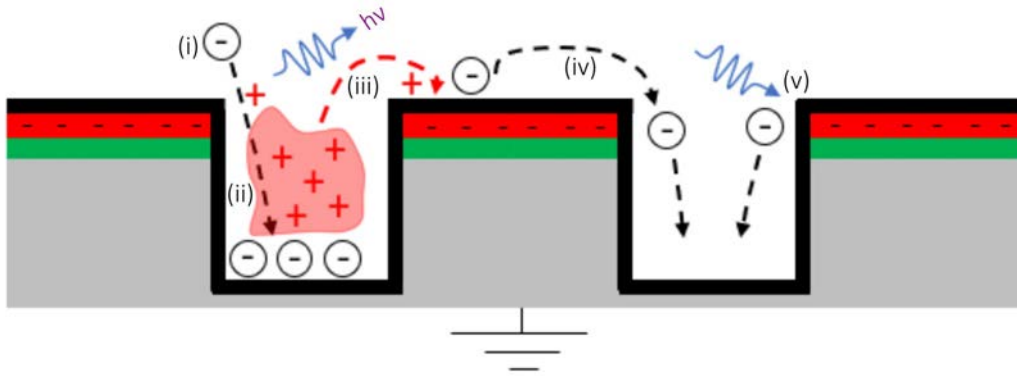


FIGURE 2.9: Schematic sketch of wave propagation mechanism along cavity surface as investigated in [21, 22].

**Summary**

In summary, micro cavity plasma arrays (MCPA) can be divided in two main categories: (i) the silicon-based arrays (SBA) with either inverted pyramidal- or cylindrical cavities and (ii) the metal-grid array (MGA). The latter is still being developed today at the chair of Experimental Physics II at Ruhr-University in Bochum and is the basis of this doctoral thesis.

## 2.3 Optical emission spectroscopy

Not all kind of typical plasma diagnostic tools can be used to investigate micro cavity plasma arrays. For example, electrical probes are not suitable since they would influence the discharge volume within $100\,\mu m$ cavities too much. Active spectroscopic methods can only be applied for observing the discharge above the cavity volume due to free optical access. But to study the discharge taking place inside the cavities, another kind of spectroscopy must be used.

Optical emission spectroscopy (OES) is a powerful diagnostic technique for those in-cavity observations. Based on radiating atoms, molecules and their ions, this diagnostic technique enables a view into a variety of plasma processes and its parameters [74]. In contrast to laser-based diagnostics where these named species become excited by laser-radiation, OES is a passive diagnostic: The discharge emission is provided without additional effort so that an optical setup is less complex. Additionally, OES is a non-invasive diagnostic. This means that the discharge is not influenced as in cases of probes and active spectroscopic methods. On the other hand, the subsequent processing of measured data is complex. Often, models and known plasma parameters such as the electron temperature are needed to get to other parameters.

In general, emission occurs when a bound electron in an atom or molecule changes its energy level from an upper $\Psi_u(n_u, l_u, m_u)$ to a lower state $\Psi_l(n_l, l_l, m_l)$. To describe these levels within atoms, quantum numbers are used. The principal quantum number $n$ defines the shell to which the state of the electron belongs. This quantum number is a natural number. The second quantum number is defined as the angular momentum quantum number $l$ describing the magnitude of the angular momentum of an electron on its orbit. The relation to $n$ is given by

$$l = 0, 1, 2, ..., n-1 \tag{2.1}$$

A further quantum number standing for projection of the angular momentum in a specific direction is the so-called magnetic quantum number $m$. Its possible values depends on $l$ with

$$-l \le m \le l \tag{2.2}$$

For allowed optical transitions between upper and lower states, the following so-called selection rules must apply as follows

$$\Delta l = l_u - l_l = \pm 1, \tag{2.3}$$

$$\Delta m = m_u - m_l = 0, \pm 1. \tag{2.4}$$
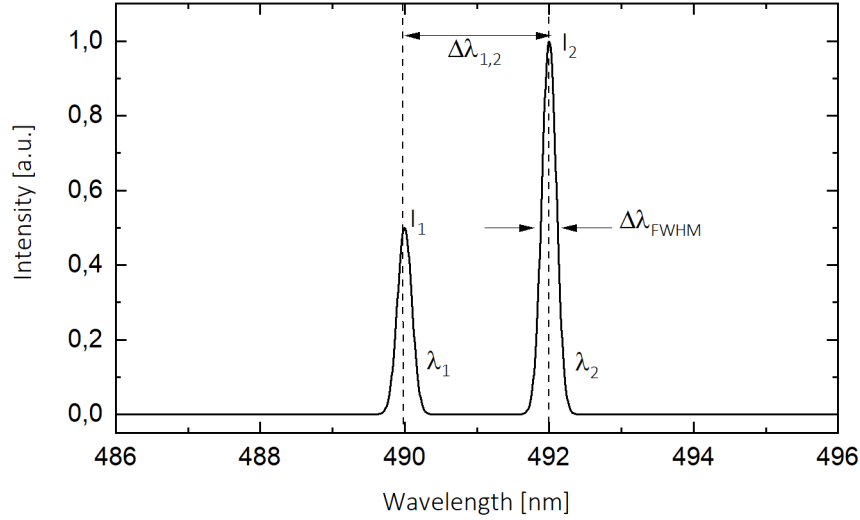
FIGURE 2.10: Properties of a line radiation using the example of the
492 nm and 490 nm line [74].

Figure 2.10 shows a sketched spectrum with typical line characteristics providing
informations about plasma parameters. The particle composition of discharges can be
identified only by the detected wavelength positions $\lambda_1, \lambda_2, ...\lambda_i$ since each species is
related to its own individual spectrum. The emissivity $\epsilon_{u,l}$ of a single optical line that
is proportional to the intensity $I$ is given by

$$\epsilon_{u,l} = n_u A_{u,l} \frac{hc}{4\pi\lambda_{u,l}} \tag{2.5}$$

and depends on the wavelength position $\lambda_{u,l}$ and density of excited species $n_u$. The
rate with which excited particles de-excite in lower states is given by the Einstein
coefficient $A_{ul}$. The speed of light and and the Planck constant are given by $c$ and $h$,
respectively.

### 2.3.1   Excitation process

Optical transitions can only occur when particles are transferred in an excited state.
This can happen through radiative or three-body recombination of ions and de-
excitation by ionisation but the most essential process is excitation by electron impact.
Typically, processes are described by their rate coefficients. For electron impact
excitation the corresponding rate coefficient $X_{exc}$ is quantified by

$$X_{exc}(T_e) = \int\limits_{E_{thr}}^{\infty} \sigma(E)\sqrt{\frac{2}{m_e}}\sqrt{E}f(E)dE \tag{2.6}$$
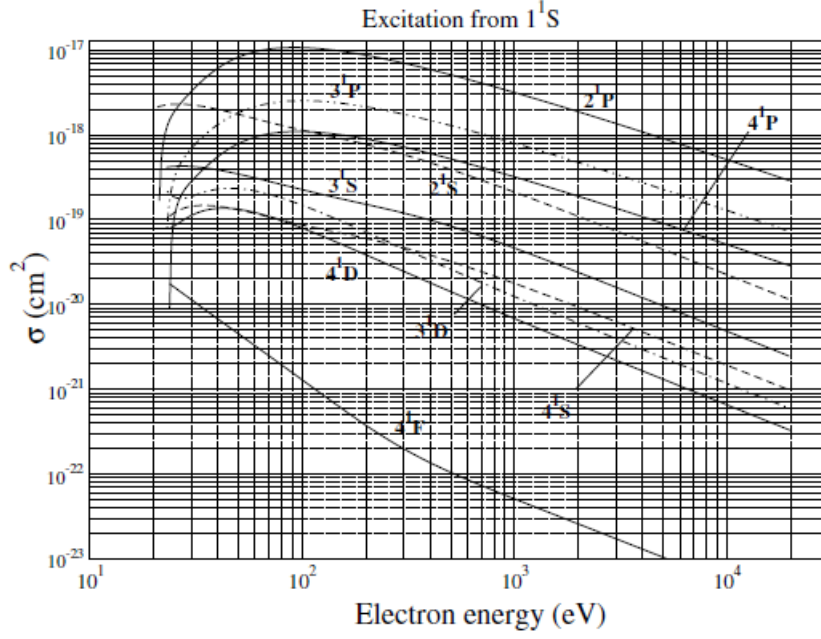
FIGURE 2.11: Recommended electron impact excitations for transitions between atomic terms of He I with $n_u \leq 4$ [75].

As can be seen, this coefficient is a function of the cross-section $\sigma(E)$ having a dependency on electron energy $E$ and electron mass $m_e$. The threshold energy $E_{thr}$ takes into account that only electrons above the respective excitation energy contribute to excitation. A further parameter is the normalised electron energy distribution function $f(E)$ often assumed by a Maxwell distribution function with a corresponding electron temperature $T_e$. However, it must be mentioned that this assumption is not generally valid for low temperature plasmas.

In this thesis helium transitions play an important role. Figure 2.11 shows the cross-section for He I excitation from the ground state to various excited levels depending on electron energy $E$. Ralchenko et al. [75] obtained these by analytic fit functions and collision-strengths $\Omega(X)$ with $X = E/E_{thr}$ described by

$$\sigma(E, \Delta E) = \pi a_0^2 \frac{R_y}{g_u E} \Omega \left( \frac{E}{E_{thr}} \right) \tag{2.7}$$

and

$$\Omega(X) = \left( A_1 + \left( \frac{A_2}{X} \right) + \left( \frac{A_3}{X^2} \right) + \left( \frac{A_4}{X^3} \right) \right) \left( \frac{X^2}{X^2 + A_5} \right). \tag{2.8}$$

They depend on the Rydberg energy $R_y$, the Bohr radius $a_0$, the statistical weight of the upper level $g_u$ and corresponding fit parameter $A_i$ listed in the appendix in A.1.

### 2.3.2   Broadening mechanisms

In addition to line intensities and wavelength positions, the full width at half maximum (FWHM) $\Delta\lambda_{FWHM}$ of a spectral line gives also insight into processes and parameters of a discharge as for example the electron density.

In an ideal case, a spectral line is an infinitely narrow line described mathematically as a delta function. However, broadening mechanisms occur in reality and they must be carefully taken into account for the analysis of OES spectra. For example these mechanism decide, if two very close spectral lines, their splitting and their shift can be resolved.

Moreover, typical physically parameters, as temperatures or particle densities can be determined with information of the respective broadening mechanism [74]. In the following, all major variants with their corresponding FWHM are explained and estimated with focus on the helium line emitting 492.19 nm under typical operation conditions within a MCPA.

**Natural width**

The most basic mechanism is caused by the Heisenberg's uncertainty principle. This results in a natural broadening $\Delta\lambda_{Natural}$ calculated with equation

$$\Delta\lambda_{Natural} = \frac{\lambda_0}{2\pi c\tau} \tag{2.9}$$

and depends on the wavelength of emitted light $\lambda_0$ and lifetime of the upper state $\tau$. The lifetime of the 492.19 nm helium line is about 50 ns [76] resulting in a FWHM of about $3 \times 10^{-6}$ nm. This can be neglected in comparison to further broadening mechanisms.

**Doppler broadening**

Doppler broadening takes place when emitting particles are in motion and follow a velocity distribution (Maxwell distribution). Various velocities of moving emitters lead to different Doppler shifts. As a consequence their cumulative effect is responsible for a Doppler broadened line. Its FWHM is calculated with

$$\Delta\lambda_{Doppler} = \sqrt{\frac{8ln(2)k_B T}{mc^2}} \cdot \lambda_0 \tag{2.10}$$

where the gas temperature $T$ is about 300 K and the helium atom mass $m$ is four atomic units. The Boltzmann constant is described by $k_B$. The FWHM is estimated to be $3.342 \times 10^{-3}$ nm.

**Pressure broadening**

In this thesis, the discharge is operated at or close to atmospheric pressure. A higher pressure leads to more inelastic collisions between particles and emitter. This results in a pressure broadening. The corresponding FWHM is calculated with

$$\Delta\lambda_{Pressure} = -\frac{\lambda_0^2 \sigma_{AB}}{\pi c} \cdot \sqrt{\frac{2}{\mu \pi k_B T}} \cdot p \tag{2.11}$$

and depends on operation pressure $p$, the reduce mass $\mu$ and the collision cross-section $\sigma_{AB}$. With a pressure of about $10^5\,\text{Pa}$, a collisional cross-section between two helium atoms of $2.4 \times 10^{-19}\,\text{m}^2$ and a reduced mass of two atomic units, the FWHM can be estimated to be $1.211 \times 10^{-3}\,\text{nm}$ .

**Resonance broadening**

Resonance broadening describes interaction between particles in the ground state and an excited state. The corresponding FWHM is given by

$$\Delta\lambda_{Resonance} = 1.63 \cdot 10^{-15} \cdot \sqrt{\frac{g_i}{g_k}} \lambda_0^2 \lambda_R f_R n_g \tag{2.12}$$

and depends on statistical weights $g_i = 3$, $g_k = 5$ of upper and lower state and atomic absorption oscillator strength $f_R = 0.273$ of the resonance transition wavelength $\lambda_R = 58.4\,\text{nm}$ [77]. The particle density $n_g$ can be taken from the ideal gas law in dependency on operation pressure and gas temperature $T$. The corresponding FWHM is calculated to be $9.811 \times 10^{-2}\,\text{nm}$.

**Van der Waals broadening**

Van der Waals Broadening is caused by the weak interaction between neutral molecules or atoms. This interaction takes place if the species are close enough whereby their energy levels get changed marginally. Relation 2.13 shows the equation to calculate the FWHM caused by the Van der Waals broadening. In addition to variables already listed, this FWHM also depends on reduced mass $\mu$, the Bohr radius $a_0$ and the atomic polarizability $\bar{a}$. The difference in squared coordinates between the upper and lower state is given by $\overline{R}^2$ where each component can be calculated with relation 2.14. These relations depend on the angular momentum quantum number $l_j$ that is for upper level $l_u = 3$ and for lower one $l_l = 2$. Moreover, the relation 2.14 also depends on the squared effective quantum number $n_j^{*2}$ calculated as described in relation 2.15. The ionisation energy of hydrogen is given by $E_H = 13.6\,\text{eV}$, for helium $E_{He} = 25.59\,\text{eV}$. For the upper state, the energy is $E_u = 23.74\,\text{eV}$ and for the lower one $E_l = 21.22\,\text{eV}$. This allows to calculate $\overline{R}^2$ to be $471.843$ and finally to determine a contribution to the FWHM of $7.994 \times 10^{-3}\,\text{nm}$.

$$\Delta\lambda_{VdW} = 8.18 \cdot 10^{-10}\lambda_0^2(\overline{a}\overline{R}^2 a_0^2)^{2/5}\left(\frac{T}{\mu}\right)^{3/10} n_g \tag{2.13}$$

$$\overline{R}_j^2 = \frac{n_j^{*2}}{2}\cdot(5n_j^{*2} + 1 - 3l_j(l_j + 1)) \tag{2.14}$$

$$n_j^{*2} = \frac{E_H}{E_{He} - Ej} \tag{2.15}$$

**Stark broadening**

The last broadening mechanism deals with collisions between emitter and charged particles such as ions and electrons. The so-called Stark broadening is calculated with

$$\Delta\lambda_{Stark} = \frac{6Z_A\lambda_0^2\hbar}{\pi c Z_B m}\cdot(n_i^2 - n_k^2)\cdot n_A^{2/3} \tag{2.16}$$

and depends on the charge of colliding particle (here electron) $Z_A = 1$ and emitting particle (here helium) $Z_B = 2$. The quantum number of the upper level is given by $n_i = 4$ and for the lower level by $n_k = 2$. The density of the perturbing particles is described by $n_A$. It can be estimated for DBDs by using the ideal gas law with $T_e = 10\,000\,\text{K}$ to be $7.34 \times 10^{23}\,\text{m}^{-3}$. A value of $1.3 \times 10^{-8}\,\text{nm}$ can be determined as contribution to the FWHM.

Table 2.2 shows a summary of all estimated FWHM and its corresponding line profile. In conclusion, the Resonance Broadening has the largest influence while the Stark Broadening has the smallest impact. Generally, a spectral line can be described in the limiting case mathematically either by a Lorentz or by a Gaussian function. The latter assumes that the underlying temperature-based mechanism is described through a Maxwell distribution. The choice between both depends on the dominant broadening mechanism and its respective profile.

| Kind of broadening | FWHM (nm) | Profile |
|---|---|---|
| Doppler | $3.342 \times 10^{-3}$ | Gaussian |
| Natural | $2.558 \times 10^{-6}$ | Lorentzian |
| Pressure | $1.211 \times 10^{-3}$ | Lorentzian |
| Resonance | $9.811 \times 10^{-2}$ | Lorentzian |
| Van der Waals | $7.994 \times 10^{-3}$ | Lorentzian |
| Stark | $1.318 \times 10^{-8}$ | Lorentzian |

TABLE 2.2: Summary of calculated FWHM and corresponding line profiles.

### 2.3.3 Line splitting and Stark Effect

As already mentioned, FWHM and intensities of optical lines can give insight into plasma processes and its parameters. A further information can be gained from optical emission spectra by investigating the spacing $\Delta\lambda_{1,2}$ between two spectral lines as shown in figure 2.10.

The probably most known method to investigate a parameter based on shifting and splitting of optical lines is the so-called Zeemann effect describing that optical transitions get shifted and split in strong magnetic field strengths. Analogous to this, the Stark effect describes the same effect only with respect to strong electric fields as assumed in MCPA.

In both cases, the principle is the same: strong magnetic or electric field strengths cause a lifting of the degeneracy of atomic energy levels. The interaction between energy levels and static electric fields is of high importance to be able to determine which electric field strength is responsible for shifting and splitting of spectral lines.

Here, an overview of this interaction and its corresponding calculations and assumptions are given. The original calculations were done by Foster by using a perturbation method [47]. An updated revision was done by Marlous Hofmans and Ana Sobata. This is described in [48] and in the appendix A.2.

The time-independent Schrödinger equation according to 2.17 has to be solved to get to know how energetic levels shift and split and which optical transitions consequently appear through an interaction with an electric field. In this case, $\psi$ is the wave function, $\hat{H}$ the Hamiltonian and $E$ the energy.

$$\hat{H}\psi = E\psi \tag{2.17}$$

In case of hydrogen, the Hamiltonian $\hat{H}_H$ is given by

$$\hat{H}_H = -\frac{\hbar^2}{2m}\nabla^2 - \frac{e^2}{4\pi\epsilon_0}\frac{1}{r} \tag{2.18}$$

can be solved exactly by using spherical coordinates.

In this thesis the electric field is investigated with helium. Thus, the situation is more complex due to the additional second electron in the shell. The corresponding Hamiltonian $\hat{H}_{He}$ has the following form

$$\hat{H}_{He} = -\frac{\hbar^2}{2m}\left(\nabla_1^2 + \nabla_2^2\right) - \frac{e^2}{4\pi\epsilon_0}\left(\frac{1}{r_1} + \frac{1}{r_2} - \frac{1}{r_{12}}\right) \tag{2.19}$$

and cannot be solved exactly. In comparison to hydrogen, this Hamiltionian consists of terms for the first and second electron and additionally of a Coloumb interaction term between them (indexed by 1,2 and 12).

However, the helium atom can be approximated through a hydrogen-like potential. The validation of this approximation is estimated with the Coloumb force described by

$$F_e = \frac{e^2}{4\pi\epsilon_0} \frac{1}{r_{12}^2}. \tag{2.20}$$

The distance between both electrons $r_{12}$ can be expressed by the electron orbital radius $a_n$ described with

$$a_n = \frac{a_0 n^2}{Z}. \tag{2.21}$$

This depends on the principal quantum number $n$, Bohr radius $a_0$ and atomic number $Z$ (for helium Z= 2). In case of both electrons in the ground state (n= 1), the distance can be calculated to be

$$r_{12} = 2a_1 = a_0. \tag{2.22}$$

For the excited case where one electron is still in the ground state and the second one is in the fourth shell (n= 4), the resulting electron distance is calculated to be

$$r_{12} = a_4 - a_1 = \frac{15a_0}{2}. \tag{2.23}$$

In comparison to the situation of both electrons in their ground state, the distance is longer by a factor of 15/2. Comparing the associated Coloumb force as described in equation 2.20, this is smaller by a factor of $(15/2)^2$. As a result, wave functions of both electrons do not overlap with each other.

A further reason that the interaction between both electrons can be neglected is connected to the exchange integral $J_{ex}$. This gives an estimation of the frequency with which two electrons exchange their quantum states. This is described and calculated in detail in [48]. If a time of $\pi/2\mathrm{J}_{ex}$ is passed, both electrons have exchanged their quantum states. After $\pi/\mathrm{J}_{ex}$ they are back in their original orbit. Typical helium transitions show an exchange period of seconds. Generally, residence times in atmospheric plasmas are in the range of nanoseconds to microseconds and are clearly smaller than the exchange period. Hence, wave functions of electrons have no overlap with each other and the interaction term in the helium Hamiltonian 2.19 has no significant influence. The helium atom can then be described as a hydrogen

atom with an extra electron (charge) yielding to a perturbation calculation. The perturbation term has the form

$$\hat{H}^{1'} = eF_e z \tag{2.24}$$

and depends on the interacting electric field directed along the positive z-axis.

## Transitions

An interacting electric field provides not only a displacement and splitting of optically allowed lines, but also of optically forbidden ones which normally show almost no radiation in absence of an electric field. These include electric quadrupole transitions that do not follow selection rules as described in 2.3 and 2.4.

Foster obtained successfully the linear Stark effect by using quantum mechanical perturbation theory for allowed and forbidden (electrical quadrupole) helium transitions whose final level can be divided into the 2S- and 2P-level. Both show a rather negligible Stark displacement in an electric field range lower than $100\,\text{kV}\,\text{cm}^{-1}$ that is of interest for plasma experiments [38]. Although many transitions are available, not all are suitable candidates for electric field determination. Especially, the final levels influence the practicability of electric field measurements.

Transitions ending on 2S-level are characterised generally through weak forbidden lines that become only noticeable compared to allowed ones at field strengths around $90\,\text{kV}\,\text{cm}^{-1}$. Thus, they have no practical use for electric field investigations. A prominent example of this is the allowed $396.47\,\text{nm}$ ($1s2s\,^1\text{S} \rightarrow 1s4p\,^1\text{P}^\text{o}, \Delta l = 1$) and the forbidden $397.20\,\text{nm}$ ($1s2s\,^1\text{S} \rightarrow 1s4d\,^1\text{D}, \Delta l = 2$) line.

Better suitable candidates are lines whose transitions end at the 2P-level. These include for example the allowed $438.79\,\text{nm}$ ($1s2p\,^1\text{P}^\text{o} \rightarrow 1s5d\,^1\text{D}^\text{o}, \Delta l = 1$) and forbidden $438.32\,\text{nm}$ ($1s2p\,^1\text{P}^\text{o} \rightarrow 1s5p\,^1\text{P}^\text{o}, \Delta l = 2$) transition. Those show a great sensitivity to electric field strengths compared to transitions ending on the 2S-level, even for values lower than $10\,\text{kV}\,\text{cm}^{-1}$ and especially, more intensive forbidden lines.

Since all examined lines by Foster are characterised by a low intensity anyway, the most intensive allowed $492.19\,\text{nm}$ ($1s2p\,^2\text{P}^\text{o} \rightarrow 1s4d\,^1\text{D}^\text{o}, \Delta l = 1$) and its forbidden counterpart at $492.06\,\text{nm}$ ($1s2p\,^2\text{P}^\text{o} \rightarrow 1s4f\,^1\text{F}^\text{o}, \Delta l = 2$) are chosen for electric field investigations in this thesis.

## Magnetic quantum number

Due to the interaction with high electric fields, allowed as well as forbidden lines become split and several shifted sub-transitions occur. In this case, all allowed sub-transitions shift to larger wavelengths while forbidden ones move to the opposite direction. Their

displacements depend on the change of the magnetic quantum number described by the selection rule in equation 2.4.

Figure 2.12 shows all possible allowed and forbidden sub-transitions in dependency on upper $m_u$ and lower magnetic quantum number $m_l$. Instead of the origin allowed 492.19 nm transition 9 optical lines occur in presence of an electric field. The same amount can be registered in place of the forbidden 492.06 nm transition.

But the total number can be reduced under certain aspects. (i) As explained before, 2P-levels show a low sensitivity to electric fields so that the lower magnetic quantum number $m_l$ can be neglected and observed changes are therefore mostly dominated by the upper quantum number $m_u$. This is for optical determination of electric field strengths of great importance because all sub-transitions characterised by the same upper quantum number can be combined to a single, overlapping line. (ii) Since the degeneracy is not lifted with respect to $m$, the sign can also be neglected (marked in grey in figure 2.12) and finally five allowed and forbidden sub-transitions remain, respectively.

## Polarisation

A further distinction of remaining sub-transitions is made by their polarisation state and therefore their relation to the electric field orientation. This depends on the change of magnetic quantum number as follows

$$\Delta m = \begin{cases} 0 & \pi\text{-polarised}, \\ \pm 1 & \sigma\text{-polarised}. \end{cases} \qquad (2.25)$$

In case that the magnetic quantum number does not change during transition ($\Delta$m=0) as shown in equation 2.25, the emission is linearly polarised in electric field direction and defined as $\pi$-polarised. In contrast, the emission is polarised orthogonally to the occurring electric field if the magnetic quantum number is changed by plus or minus 1 ($\Delta$m = $\pm$1). This so-called $\sigma$-polarised light is denoted as circular polarised. The algebraic sign describes the rotational direction which is clockwise if $\Delta$m = 1, otherwise counter-clockwise.

In previous works where the Stark effect was measured for e.g. a plasma jet [48, 49] or DBDs [50, 51], a polariser was always used to suppress $\sigma$-transitions. Therefore, the $[2-1]^\sigma$ transition does not become visible leading to a less complex spectrum.

A final overview of all occurring sub-transitions and their polarisation state is given in table 2.3 in form of $[m_u - m_l]^{\pi,\sigma}$.
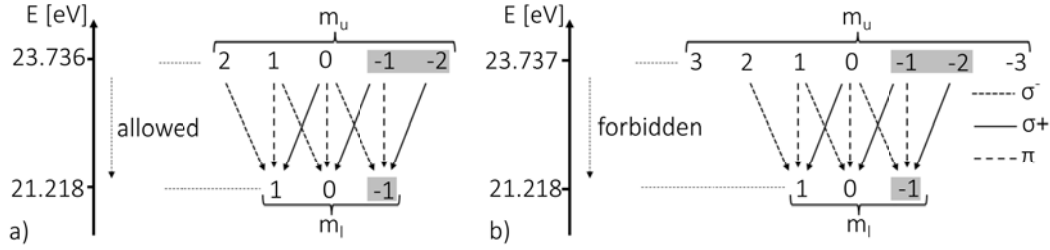
FIGURE 2.12: Sketch of all possible transitions between the [1s4d]- and [1s2p]-level depending on the magnetic quantum number and selection rules. The negative values can be neglected due to the degeneracy (grey marked). The lines are valid for the allowed and forbidden transitions.

| Upper level | $m_u$ | Transition |
|:---:|:---:|:---:|
| 4D | 2 | $[2-1]^\sigma$ |
| 4D | 1 | $[1-1]^\pi, [1-0]^\sigma$ |
| 4D | 0 | $[0-0]^\pi, [0-1]^\sigma$ |
| 4F | 2 | $[2-1]^\sigma$ |
| 4F | 1 | $[1-1]^\pi, [1-0]^\sigma$ |
| 4F | 0 | $[0-0]^\pi, [0-1]^\sigma$ |

TABLE 2.3: Summary of all possible allowed and forbidden transitions depending on the upper magnetic quantum number. The corresponding intensities were calculated theoretically by Foster in [47].

## Wavelength displacement

To involve all transitions as listed in table 2.3 in a practical use, the knowledge of their wavelength displacement depending on electric field strengths is required. Figure 2.13 shows this correlation for electric field strengths up to $100\,\mathrm{kV\,cm^{-1}}$ calculated theoretically by Foster [47]. In this context, all displacements are referred to the unaffected $492.19\,\mathrm{nm}$.

Figure 2.13 displays the Stark-effect. The trends show a nice symmetry to the linear Stark-effect of hydrogen. If no electric field is applied, the degeneracy is not lifted and all allowed transitions show the unaffected $492.19\,\mathrm{nm}$ optical line. At the same time, all forbidden transitions would be described by a wavelength of $492.06\,\mathrm{nm}$ but they do not radiate due to their forbidden character. An increasing electric field leads to a shifting and splitting of these transitions and also to a radiation of forbidden transitions. It is noticeable, that allowed transitions shift to longer wavelengths while forbidden transitions go to shorter wavelengths.

Moreover, the displacements of all transitions can be approximated by three simple trends. The first trend describes all five forbidden transitions (dashed line). Up to a value of about $70\,\mathrm{kV\,cm^{-1}}$, the shifts of individual transitions lie on top of each other. Only the [2-1] transition shows a significantly larger displacement with respect to the remaining forbidden transitions in range between $80\,\mathrm{kV\,cm^{-1}}$ and $100\,\mathrm{kV\,cm^{-1}}$.
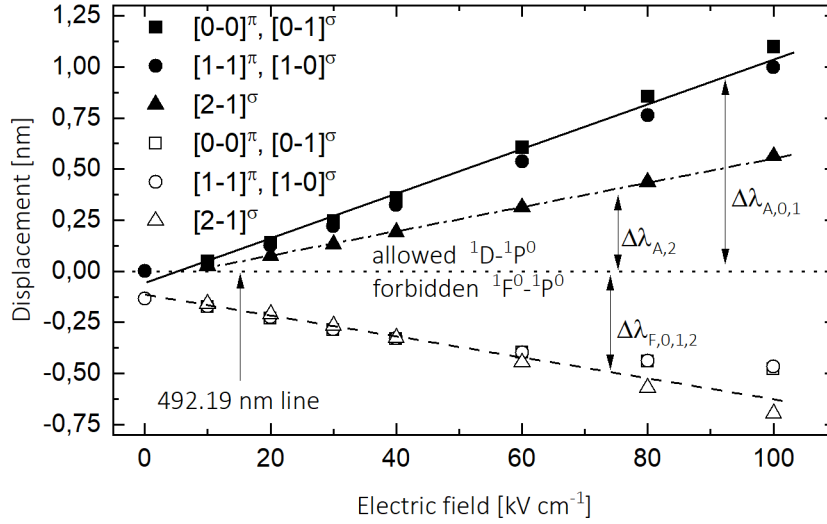
FIGURE 2.13: Theoretical calculated displacements by Foster [47]

The second trend includes all transitions characterised by $m_u = 0, 1$ (full line). Since the difference between both is hardly resolvable, the average of both was always taken in previous works. Its displacement (average) to the first trend is indicated as $\Delta\lambda_{21} = \lambda_{A,0,1} - \lambda_{F,0,1,2}$. The indices stand for involved allowed (A) or forbidden (F) transitions with upper magnetic states.

The third approximated trend stands for the allowed [2-1] transition (pointed dashed line). Its displacement with respect to the first one is given by $\Delta\lambda_{31} = \lambda_{A,2} - \lambda_{F,0,1,2}$.

## Allowed-forbidden method

The correlation between wavelength displacements and electric field is defined by the named three trends. To measure the electric field strengths, one possibility is just to identify the absolute wavelength position of one of the allowed approximated trends. The resulting displacement to the unaffected 492.19 nm line can be then converted into electric filed strengths. However, the informative value of the forbidden trends gets lost. To include these, the so-called "allowed-forbidden" method is executed where the displacement between a forbidden and an allowed trend is taken into account.

This offers two advantages: (i) The measurement is easier to perform. Taking figure 2.12 again into account, it is noticeable that the displacement of an individual trend is already in a range of a tenth of a nanometer. Thus, an investigation between a forbidden and allowed trend shows a larger displacement which allows them to be better separated from each other. (ii) The electric field is determined by the information of allowed and forbidden transitions. Thus, measured electric fields contain automatically an average value.

| i | $a_i$ | $b_i$ |
|---|-------|-------|
| 0 | $-0.093\,\text{nm}$ | $-21.176\,\text{kV}\,\text{cm}^{-1}$ |
| 1 | $-0.543\,\text{nm}\,\text{nm}^{-1}$ | $-164.512\,\text{kV}\,\text{cm}^{-1}\,\text{nm}^{-1}$ |
| 2 | $0.982\,\text{nm}\,\text{nm}^{-2}$ | $70.452\,\text{kV}\,\text{cm}^{-1}\,\text{nm}^{-2}$ |
| 3 | $0.982\,\text{nm}\,\text{nm}^{-2}$ | $70.452\,\text{kV}\,\text{cm}^{-1}\,\text{nm}^{-2}$ |

TABLE 2.4: Coefficients for equations 2.26 and 2.27.

Based on the calculation of Foster, there is a clear correlation between the shift of an individual transition and the occurring electric field. This must also mean that there is a fixed correlation between the displacements of allowed and forbidden transitions and the occurring electric field. In order to avoid that these displacements lead to different electric field strengths due to e.g. measurement uncertainties, $\Delta\lambda_{31}$ must be a function of $\Delta\lambda_{21}$ described by

$$\Delta\lambda_{31} = a_3 \cdot \Delta\lambda_{21}^3 + a_2 \cdot \Delta\lambda_{21}^2 + a_1 \cdot \Delta\lambda_{21} + a_0. \tag{2.26}$$

The corresponding electric field can then be calculated by taking $\Delta\lambda_{31}$ or $\Delta\lambda_{21}$ into account. In this thesis the electric field is determined through $\Delta\lambda_{21}$ by using equation

$$E(\Delta\lambda_{21}) = b_3 \cdot \Delta\lambda_{21}^3 + b_2 \cdot \Delta\lambda_{21}^2 + b_1 \cdot \Delta\lambda_{21} + b_0. \tag{2.27}$$

The coefficients for equation 2.26 and 2.27 can be taken from table 2.4.

**Relative intensities**

In addition to wavelength displacements, the electric field can also be obtained by analysing the intensities of all transitions listed in table 2.3. This approach was also successfully exploited from Obradovic and Kuraica in [78] by investigating a modified Grimm glow discharge.

The relative intensities were also theoretically determined by Foster. Figure 2.14 shows the sum of the calculated relative intensities for the three trends depending on the electric field. In comparison to the wavelength displacement based method, this kind of determination is more challenging due to two facts: (i) For example, in a range between $30\,\text{kV}\,\text{cm}^{-1}$ and $70\,\text{kV}\,\text{cm}^{-1}$ the relative intensities show just a weak sensitivity which is not practicable. (ii) The intensities depend additionally on how all sub-levels are occupied by the discharge while wavelength displacements just depend on the electric field in the discharge. According to equation 2.5 the emissivity depends on the density of these excited states. Thus, this kind of determination is not considered in this thesis.
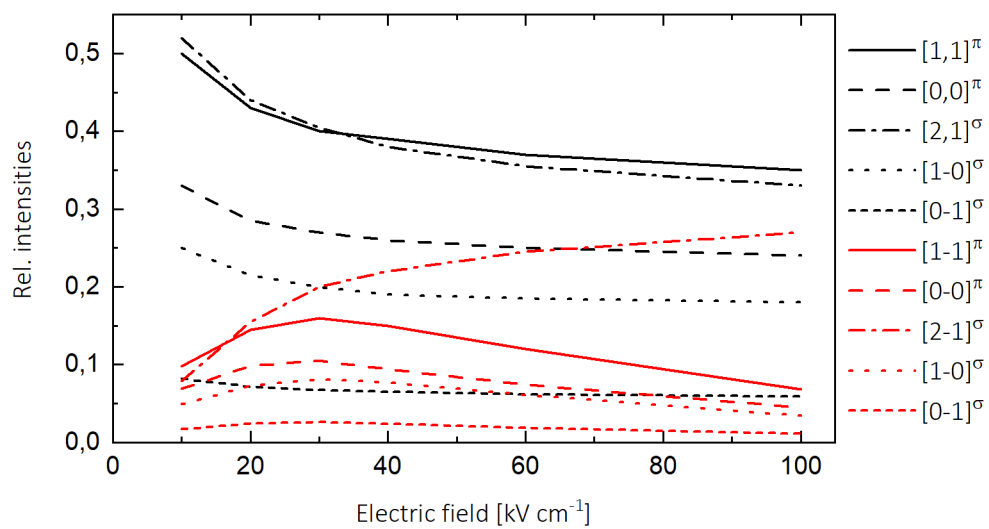
Figure 2.14:  Sum of the relative intensities for all three trends
calculated by Foster [79]

# Chapter 3

# Experimental setup

## 3.1 Micro cavity plasma array

As already described in section 2.2, the setup and production of an SBA is complex and error-prone providing a limited lifetime under laboratory conditions. In comparison, the MGA is constructed in a simpler way which is not based on micro-structure technique and can be divided principally into three main parts: (i) A magnet working as an electrical grounded electrode, (ii) a dielectric foil and (iii) a high voltage (HV) driven metal-foil containing hundreds to thousands of holes. All these components are put together to a layer structure described in detail in the following and is already published as a concept in [73].

### 3.1.1 Single cavity-structured metal-grid array

Figure 3.1a) shows schematically the cross-section of these three components forming a single cavity-structured MGA. Its operation in helium shortly after ignition is shown in figure 3.1b). The cylindrical shaped samarium cobalt (SmCo) magnet having a diameter of 22 mm and a height of 5 mm is glued succinctly and concentric in a squared polyether ether ketone (PEEK) carrier. This carrier has a base length of 30 mm and the same height as the magnet.

The whole carrier and magnet surface is covered with a 40 µm thick ceramic foil made of zirconium dioxide ($ZrO_2$, relative permittivity $\epsilon_r \approx 27$) to avoid parasitic discharges around. This ceramic foil serves as a dielectric barrier between the grounded magnet and the HV supplied metal-foil on top.

This 50 µm thick metal-foil made of nickel has a laser cut squared shape with a base length of 30 mm and contains uniformly laser drilled circular holes covering a square of $10 \times 10$ mm in the centre. In this frame holes, with a diameter $d$ are arranged in lines and columns separated from each other by a distance $a$. This is shown in the zoom of the sketch in figure 3.2. In this thesis the diameters are varied between 200, 150, 100, and 50 µm at a constant edge-to-edge distance of 200 µm resulting in $26 \times 26$, $28 \times 28$, $31 \times 31$, and $35 \times 35$ holes, respectively. In the following, this nickel-foil with
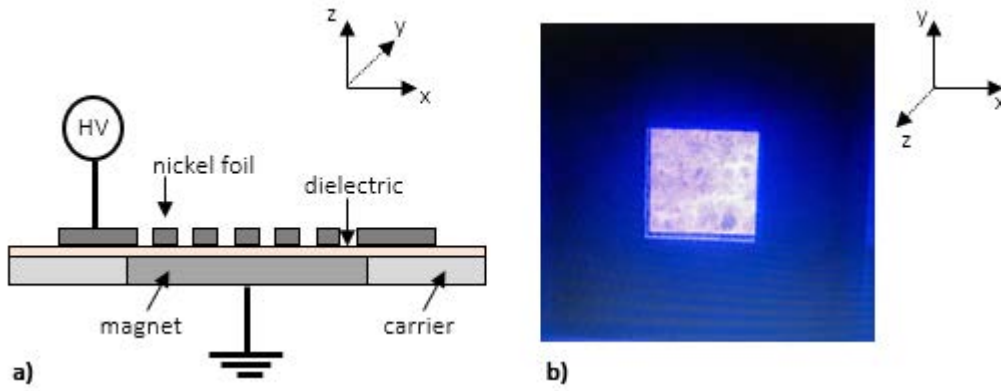
FIGURE 3.1: Concept of a MGA in a) and a photography of this device
in operation in helium shortly after ignition in b).

its incorporated holes is named "nickel-grid" or "metal-grid" to distinguish it from a
foil without holes used to form a micro-channel on an enlarged carrier [80].

Due to the magnetic character of this nickel-grid, it is pulled to the magnet and
the incorporated holes form with the dielectric at bottom the so-called cavities.
Additionally, the whole three-layer structure gains more stability and is secured
against shifting along dielectric surface since the magnetic force holds all layers
together. Nevertheless, it remains possible to disassemble this configuration into
its individual parts again for post-operation investigations that is a further feature
compared to silicon-based devices.

### 3.1.2   Influence of magnetic field

#### 3.1.2.1   Discharge within micro-cavities

The electrical grounded electrode is realised by a magnet and it is known that its
magnet fields can influence discharges in a strong way [81]. Therefore, it is important
to know whether the resulting magnet field influences the discharge in MGA.

The magnetic field strength $B$ on the magnet surface was measured to be about $0.2\,\mathrm{T}$
with a Gauss-meter (LakeShore - Model 421) and a corresponding probe (MMT-6J04-
VH). A discharge is typically described as magnetized when the gyration radius $r_g$ of
particles is larger then their mean free path $\lambda_m$ under respective conditions [81]. This
is described by

$$r_g = \frac{mv}{eB} > \lambda_m = \frac{k_B T_{Gas}}{p\sigma_{e/I}} \tag{3.1}$$

With the assumption that the gas temperature $T_{Gas}$ is about $330\,\mathrm{K}$ [82], the electrons
have a mean energy of about $2\,\mathrm{eV}$ and the total momentum transfer cross-section
between helium and an electron or a helium ion is about $\sigma_e = 7 \times 10^{-20}\,\mathrm{m^2}$ [83]

and $\sigma_I = 1 \times 10^{-18} \, \text{m}^2$ [84]. A necessary magnetic field strength of about $22 \, \text{T}$ for electrons and $230 \, \text{T}$ for ions at a pressure $p$ of $0.2 \times 10^5 \, \text{Pa}$ is obtained. For an operation at atmospheric pressure a five times higher magnetic field is required.

Due to that, magnetic field strengths must be significantly higher than the used magnet in MGA can provide. All in all, the discharge in micro cavities is not influenced by this magnet.

### 3.1.2.2 Zeeman patterns

Magnetic fields are not only able to influence the behaviour of the discharge as described above, but also the discharge's radiation can be affected. This leads to the so-called Zeeman effect, which is also responsible for the splitting of optical lines like the Stark-effect. With respect to the electric field measurements, it could lead to interpretation problems since it is difficult to assign the displacement and the splitting to the respective effect.

However, the Zeeman pattern might be neglected in case of the MGA. In high power magnetron sputtering discharges (HIPMS) where higher field strengths up to $180 \, \text{mT}$ occur, this effect was estimated to be still negligible [85]. By assuming that the Landé-g factors of the used helium transitions are in the range of 2 as typical for all other lines, the magnetic field is too low to evoke a resolvable Zeeman pattern in MGA.

### 3.1.3 Nickel-grid with multiple cavity-structures

All components can be exchanged after each measurement due to the magnetic holding to investigate an influence of various cavity dimensions or dielectric properties on the discharge. However, this procedure on single arrays does not allow to compare directly a cavity dimension dependency since accurate equal operation conditions cannot be reached again. This affects e.g. the material composition of all individual components. Different thickness of the dielectric can provide varying field strengths due to the simple estimation by E= U/d. In this formula $E$ is the electric field, $U$ the applied voltage to electrodes and $d$ the effective distance between them. In addition to the material composition, the exact gas composition for operation can not be ensured from measurement to measurement with different single arrays.

To tackle these problems, a concept is reused that was already applied in an experiment for SBA. There, different sized trench structures were engraved on a single silicon wafer in a $2 \times 2$ pattern in place of cavities [14]. Based on this concept and the goal to take control over the EEDF from cavity structure to cavity structure for gas reformation in a channel-like construction, an enlarged nickel-grid was developed containing a cavity property variation in a row ($1 \times 4$ pattern). This is depicted in figure 3.2a) where the area covered by holes (cavities) is represented by dashed lines.

Here, each cavity-structure, named in the following "sub-array", is separated from the adjacent one with a distance of 1 mm ($\delta s$ in figure 3.2a)). The thickness, material composition and the possible hole arrangement are equal to the values described for the single cavity-structured arrays in 3.1.1. Only the surface dimension changes to $88 \times 27$ mm.

Along these four sub-arrays, either the cavity diameter $d$ or the edge-to-edge distance $a$ can be varied. In this thesis two different options are used: (i) 200 µm, 150 µm, 100 µm and 50 µm cavities with a constant edge-to-edge distance of 200 µm and (ii) 200 µm cavities with an edge-to-edge distance of 200 µm, 150 µm, 100 µm and 50 µm. In the first option, it results in 25 ,28, 33 and 40 cavities per line and column, respectively. In the second option, it results in 25 ,28, 33 and 41 cavities per line and column, respectively.

Figure 3.2b) shows the first option in operation in helium, taken shortly after ignition. The cavity diameter decreases from left to right.

Finally, it has to be noted that all sub-arrays are operated under equal electrical conditions such as the applied voltage, frequency and waveform excitation since all sub-arrays are incorporated in the same nickel-foil. So, the only independent change in discharge is achieved in their cavity diameter or edge-to-edge distance.

### 3.1.4   Flow-operated metal-grid array

This nickel-grid has to be placed in an appropriate channel-like housing equipped with further components like magnet and dielectric to guarantee that the gas flow streams from sub-array to sub-array along the multiple nickel-grid. Based on this, the following adaptations are implemented in comparison to the single MGA:

- The PEEK carrier is enlarged to $88 \times 27 \times 10$ mm (length, width, depth) and has holes for electrical contact and gas flow supply. Additionally, a magnet with the size of $88 \times 27 \times 5$ mm is also glued succinctly and concentric in this carrier.

- The surface of the ceramic foil is enlarged to $88 \times 27$ mm and is therefore congruent to the nickel-grid. Additionally, this dielectric foil consists of holes for magnetic pins serving as electrical contact to the nickel-grid.

- The nickel-grid with four different sub-arrays as described in 3.1.3 and shown in figure 3.2a) is then put on the dielectric foil.

An aluminium mounting is connected to the carrier at bottom to enable a gas supply via Swagelok-adapters and mounting possibilities to xyz-stages. Finally, the upper side of this carrier is sealed with a 2 mm thick glass (BK7) or quartz cover that enables the following:

- A gas-flow channel is realised with a gap distance of about 2 mm between nickel-grid and glass surface inside and a cross-section of about $31.5 \, \text{mm}^2$. This allows
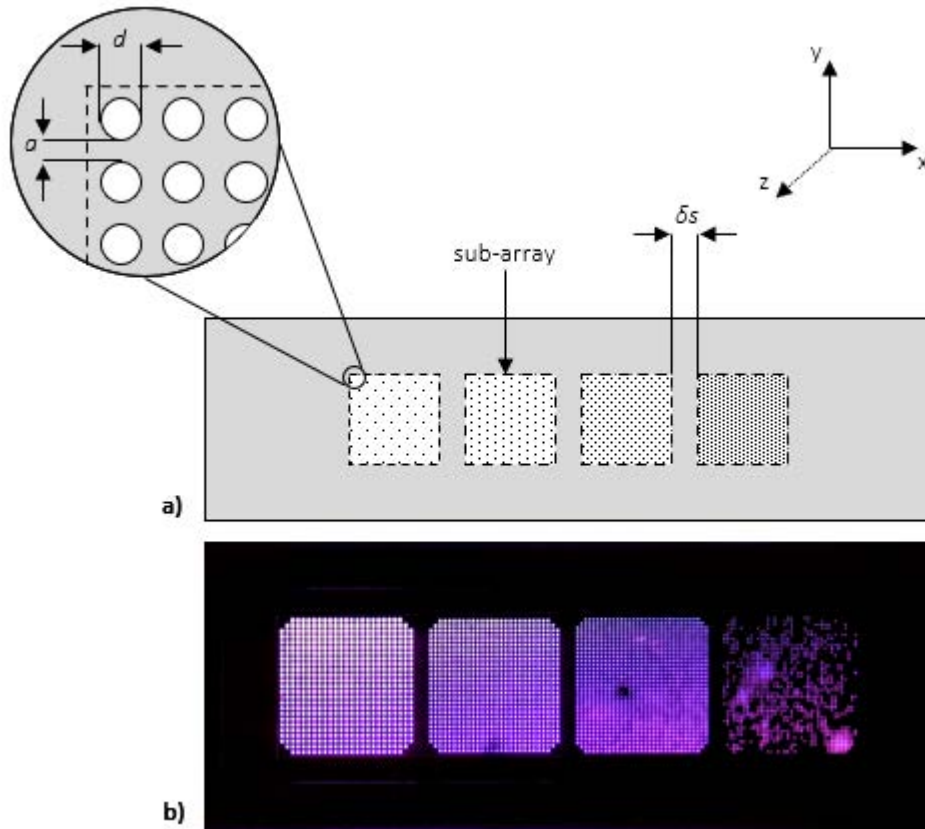
FIGURE 3.2: Multiple cavity-structured metal-grid as a a) schematic sketch and b) as photography during operation in helium taken shortly after ignition. The cavity diameter decreases from left to right (200 µm, 150 µm, 100 µm and 50 µm).

that the gas can flow very close along the cavities and dielectric surface to be treated from sub-array to sub-array in gas-flow direction.

- Optical access for diagnostics is available from the top and from the side for wavelengths between near ultra-violet (NUV, 100 nm) and near infrared (NIR, 950 nm). The insight from the sides allows an investigation along the nickel-grid surface or more specifically along the whole channel or along an individual sub-array. On the other side, the view from above gives an insight into the cavities. Since all connections and supplies are installed at the bottom of the carrier, all optical accesses are unhindered.

Finally, it has to be noted that this flow-operated MGA can also be used in a defined gas atmosphere within a chamber which is explained in the next section.

## 3.2 Gas supply and vacuum chamber

As described above, depending on the setup of the MGA, it can be operated either with a gas flow or in a closed and defined gas atmosphere. To ensure both, a gas
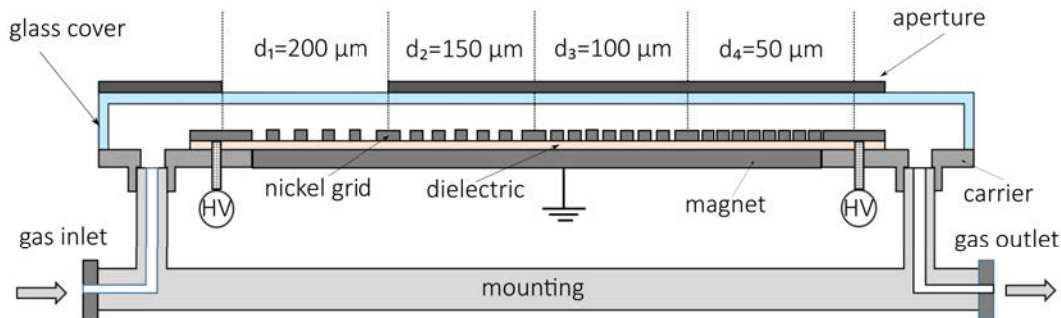
FIGURE 3.3: Sketch of the multiple cavity-structured MGA.

supply and a vacuum chamber are required which is depicted as an overview in figure 3.4.

A mass flow controller (MFC) is integrated by stainless steel pipes with a diameter of 6 mm between a gas bottle and the Swagelok gas access of the multiple cavity-structured MGA to obtain a controllable and defined gas flow. In this thesis all measurements are performed with helium as carrier gas having a purity of 99.999 %. The gas flow is set at the maximum adjustable flow of the MFC at 2 slm (standard litre per minute). Thus, a heating of the magnet inserted in the MGA is limited up to 70 °C due to the constant cooling by the gas flow. This value is based on experimental observations. A temperature higher than 80 °C would lead to a demagnetisation of the magnet and therefore to a destruction of the MGA. A thermocouple is mounted on the underside of the magnet and connected to a thermometer (Voltcraft K204) to measure the magnet temperature as shown in figure 3.4.

Admixtures such as nitrogen can be added up to 20 sccm (standard cubic centimetre per minute) to the helium flow. The gas flow can be rerouted around the MFC through a bypass that can be closed by valves for flushing the whole system.

This kind of setup enables to compare several simultaneously gas-flow operated MGAs that differ in their material composition or cavity structures. A second MCPA that is e.g. equipped with a catalyst on the dielectric previously can be connected in series after the first device. Due to that, both devices work with an identical gas composition. This system can be isolated from the remaining gas system and from the ambient atmosphere by further valves to avoid impurities.

While these gas flow operated MGAs are separated from the gas system, a valve to a cylindrical, $50 \times 30$ cm (height×diameter) dimensional stainless steel vacuum chamber can be opened. This allows to investigate the single-cavity as well as the multiple cavity-structured MGA in a controlled atmosphere depending on pressure. Three pressure gauges are installed at the chamber to monitor the pressure: (i) a capacitive-based probe (Vacuubrand DVR 5) for a pressure range between 1000 and 10 mbar for controlled gas inlet, (ii) a Pirani probe (Edwards APG-MP-16ST) for a
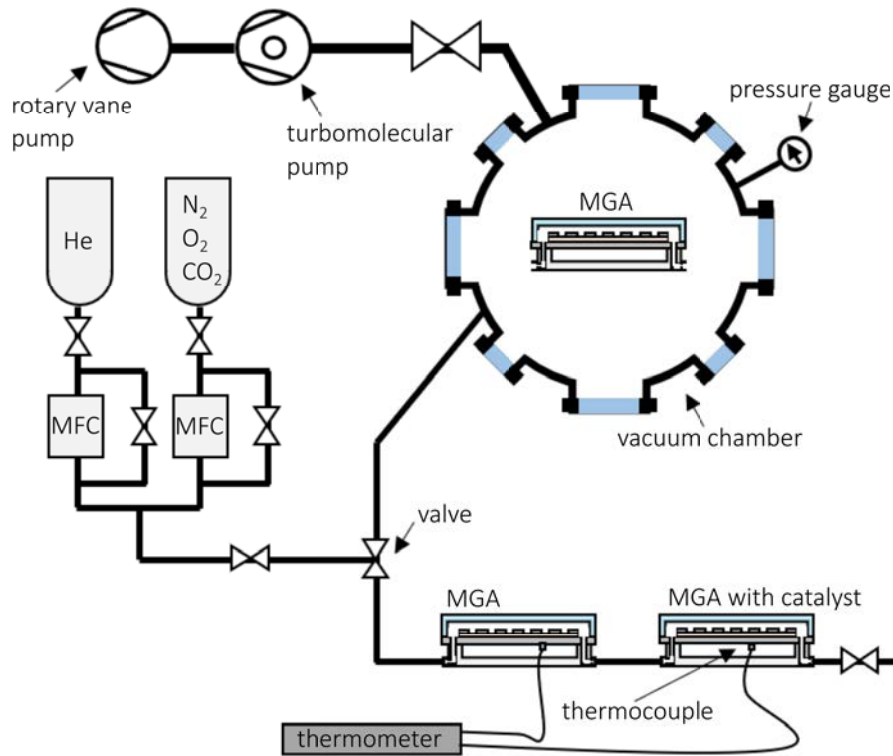
FIGURE 3.4: Sketch of gas supply and vacuum system.

pressure range between 10 and $10^{-4}$ mbar and (iii) a magnetron-based probe (Edwards AIM-SNW25) between $10^{-4}$ and $10^{-7}$ mbar for pumping.

Before initial operation of the MGA, a pump combination consisting of a turbomolecular pump (Pfeiffer TMU 520PC) and a rotary vane pump (Pfeiffer MD4TC) evacuates the vacuum chamber to a pressure of about $3 \times 10^{-6}$ mbar. After reaching this pressure, a valve (VAT series 10.8) separates the whole pump system from the vacuum chamber that can than be filled with the working gas. In this thesis, measurements were performed in helium in a pressure range between 300 and 1000 mbar.

### 3.2.1   Interaction between sub-arrays

A successive treatment of the gas should occur to realise an effective gas reformation and destruction of VOCs along the gas channel where the four sub-arrays are placed in series. This treatment includes processes e.g. excitation or ionisation from cavity structure to cavity structure in gas flow direction.

But to understand fundamental plasma properties in a single cavity structure, these processes are not favourable, because the discharge of the respective cavity structure is influenced through species generated in the discharge of the cavity structure before.

In this thesis, the global discharge performance inside an individual cavity structure is investigated by using helium as working gas that allows a more defined performance than an operation with admixtures or air. Furthermore, helium is also necessary for measuring electric field strengths by using Stark shift and splitting as mentioned before.

The transit time between two cavity structures and lifetimes of involved species are of high importance to get an estimation if this interaction from sub-array to sub-array occurs. The passing time $T$ can be calculated with

$$T = \frac{A \cdot \delta s}{F} \tag{3.2}$$

where $A$ is the effective cross-section within the channel, $F$ the gas flow and $\delta s$ the distance between two cavity structures (see figure 3.2). With the gas flow of 2 slm, a cross-section of about $31.5\,\text{mm}^2$ and a distance of 1 mm, a transit time of 945 µs is estimated.

Since the lifetime of excited helium species is in the nanosecond range, these cannot interact with the adjacent cavity structure. Also helium metastables might not play a role. In a previous experiment, their lifetime was determined to be about 10 µs by using tunable diode laser absorption spectroscopy (TDLAS) on a self-pulsing jet at atmospheric pressure [86]. This is by a factor of 100 lower compared to the transit time.

The same applies for reactive species such as O and OH whose lifetimes are also in the range of few hundred microseconds [87, 88]. However, an interaction between cavity structures with respect to gas treatment would be desirable since one could adjust the properties of the species step-by-step. To make this possible, the gas flow can be increased, the cross section can be reduced and the distance between the structures can be decreased to reduce the transit time.

### 3.2.2   Gas flow simulation

Taking figure 3.2b) into account again, it is observable that not in all cavities a discharge is ignited. Especially, the 50 µm cavities show operation problems leading to a low intensity and therefore to a bad signal-to-noise ratio.

A first possible reason for the non-operating cavities might be that during assembling of used components (dielectric, nickel-grid) to the layer structure, dust gets in between. Due to that, these layers are separated from each other locally and ignition cannot occur. The second reason is based on the gas stream above the cavity structure that does not arrive the dielectric at bottom in the 50 µm cavities. This fact was already noticed in a COMSOL simulation done in a frame of a master-thesis [89] and illustrated in figure 3.5. Due to that, cavities are not cleaned with fresh helium and impurities

such as nitrogen and oxygen are therefore still available in a too high concentration in the cavity volume after assembling. In such a gas composition, quenching is the dominant factor and a discharge cannot be established. In larger cavities it is well observable that flushing with fresh helium has a positive effect. After a flushing time of about 20 min, the dominant emission of nitrogen (422 nm) almost completely disappeared. Due to that, more and more cavities ignite, the discharge is more stable and the dominant emission is coming from helium (706 nm).
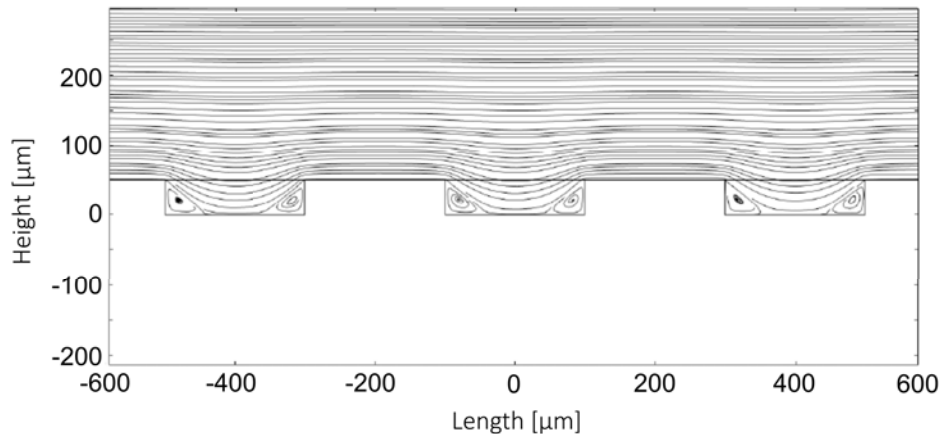


FIGURE 3.5: Simulated streamlines of the gas flow along three cavities having a diameter of 200 µm in the gas flow operated reactor. This simulation was done with COMSOL. The helium gas flow is set to be 2 slm.

## 3.3 Electrical supply

Figure 3.6 illustrates the electrical supply for the single and multiple cavity-structured MGA. A function generator (Tektronix AFG 3021B) provides a bipolar, triangular waveform signal with a voltage amplitude up to 4 V and a frequency between 5 kHz and 25 kHz. To operate both reactors this signal is transported via BNC-cables to two amplifiers (FM Electronic DCU 600-40 HF) which amplify the voltage up to 800 V. The amplifiers are limited by a current of either 200 mA or 100 mA.

An inductive coupled current probe (I-probe, Tektronix P6021) and capacitative-resistive coupled voltage probe (U-probe, Tektronix P6015A, duty factor of 1000) are installed and connected to an oscilloscope (Lecroy 8404M-MS, bandwidth of 4 GHz) to measure and monitor current and applied voltage time-resolved. These probes also allow to estimate the coupled power into the MGA devices that is in the range of about 1 mW. The electrical connection as well as the electrical probes can be changed at any time between both flow-operated MGAs and the device operated in the vacuum chamber.
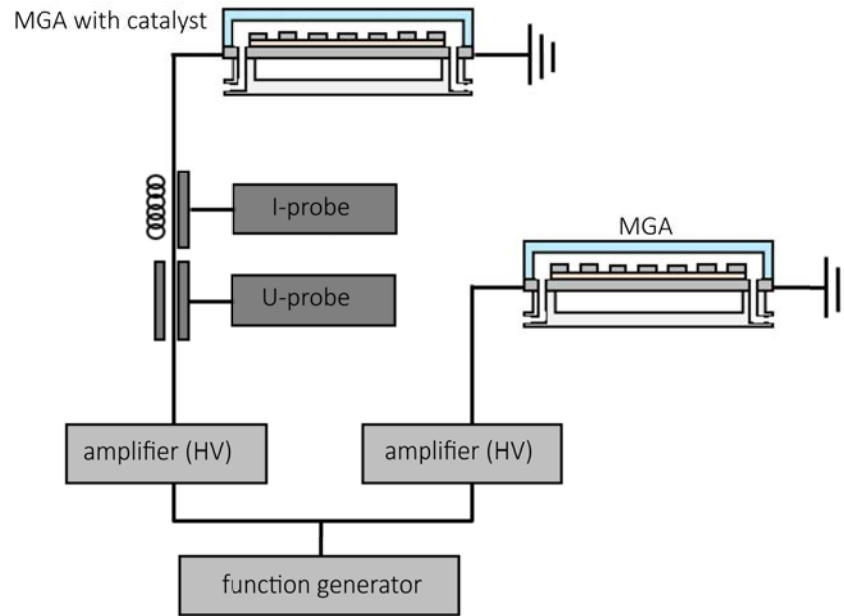
FIGURE 3.6: Overview of the electrical supply and diagnostic of MGA.

## 3.4 Optical diagnostics for flow-operated MGA

Since the flow-operated MGA is sealed with a glass cover on top, an optical access for optical diagnostics is realised. The optical investigation of the discharge, is, however, challenging due to the following reasons. It is difficult to investigate the macroscopic physics along the four different sub-arrays in the channel taking place on the millisecond time scale and the microscopic physics within a single cavity up to the nanosecond time scale with only one optical system. It must be considered that also wavelength resolved information with a resolution up to one tenth of a nanometer are required. This is why four different emission-based techniques are executed in this thesis as explained in the following. An overview of the complete optical setup is shown in figure 3.7.

**Highly-resolved spectroscopy for measuring Stark displacements**

Highly wavelength-resolved and phase-resolved optical emission spectroscopy (PROES) is the main diagnostic in this thesis. This is executed through a combination of a two meter long plane grating spectrometer (PGS, Carl Zeiss Jena Plangitterspektrograph 2) and an attached intensified charge-couple device (ICCD) camera (Andor iStar DH320T-25U-A3) at the exit of the PGS. This combination allows to resolve the displacements of a few tenths of a nanometre only of all Stark shifted and split helium sub-transitions.

A combination of a collimator and light fibre with a diameter of 150 µm is installed on an electrically driven stage (Zaber Technologies LSM100A-SV1), captures the emission of the respective cavity-structure and transfers the emission to the entrance slit of the
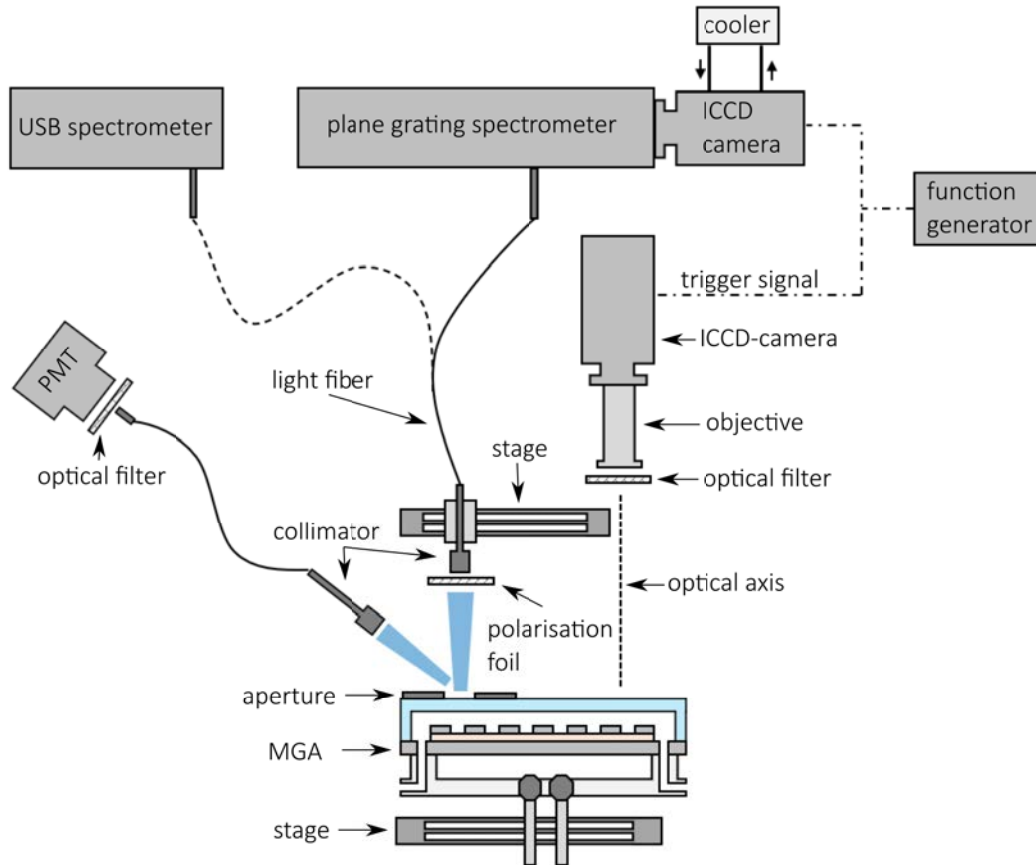
FIGURE 3.7: Sketch of the optical diagnostic system applied on the flow-operated MGA.

PGS. An aperture can also be positioned along the glass cover to avoid scattered light from adjacent cavity-structures. The distance between collimator and glass cover of the flow-operated MGA is about 5 mm where a polariser can be placed in between if electric field strengths measurements are executed.

Figure 3.8 illustrates the setup and the light path inside the PGS. At first, the light is coupled in the entrance slit of the PGS having a width of 25 µm. This value is based on experimental observations and shows the best resolution at the most sufficient intensity. Afterwards, a mirror reflects the light to a concave mirror characterised by a focal length of 2 m. From there, the light is reflected on a rotating adjustable diffraction grating having a lattice constant $G$ of 1302 grating grooves per millimetre where the incoming light is deflected. This light radiates again at the concave mirror and then to the exit of the PGS where the ICCD-camera is installed. In the first spectral order, a wavelength range of about 8 nm is imaged on 1024 detector pixels of the ICCD-camera yielding to a spectral resolution of about 8 pm per pixel. Through rotation of the diffraction grid, the respective wavelength range is adjustable.

The following equations are needed to calculate from the pixel scale $Px$ to the wavelength scale $\lambda$
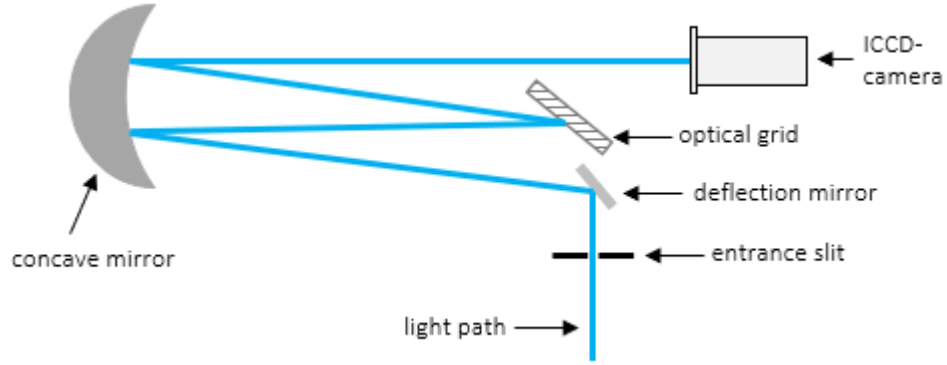
FIGURE 3.8: Setup and light path within PGS

$$\lambda_0(\alpha) = 2\frac{sin(\alpha)}{nG} \tag{3.3}$$

$$\lambda(\alpha, Px) = \lambda_0 \pm cos(\alpha)\frac{2w(Px - s)}{mGl} \tag{3.4}$$

where $\alpha$ is the deviation angle, $\lambda_0$ the central wavelength position, $n$ the spectral order and $m$ the amount of horizontal detector pixels. The displacement of the central camera position is described by $s$ and is set to be five pixels. The optical path length is given through $l$ and is $4150\,\text{mm}$.

The CCD chip detects wavelengths between $400\,\text{nm}$ and $800\,\text{nm}$ and consists of $1024 \times 256$ detector pixels where each pixel has a size $w$ of $25\,\mu\text{m} \times 25\,\mu\text{m}$. At the end, the entrance slit is imaged on the CCD chip through a nearly 1:1 ratio.

A non-negligible property of the PGS is its "Ebert mount" configuration. This causes the entrance slit image to be tilted depending on the selected wavelength on the detector pixels. To compensate this, the entrance slit can be tilted until the image is perfectly vertically aligned. Afterwards, the intensity in each column of the CCD chip is accumulated over the vertical image via "full vertical binning".

A microchannel plate (MCP) coupled to the CCD chip has the task to work as a fast gated intensifier synchronised to the excitation cycle of the MGA in the kHz-range. Typically, the CCD chip integrates over few seconds but the integration time depends on the emission intensity of the respective transitions. In case of electric field measurements taking the peak of the $492.19\,\text{nm}$ helium line into account, the integration time is about $20\,\text{min}$.

An important point of a spectrometer is the instrumental profile describing the broadening of a narrow optical line only by its path through the spectrometer. To measure this, a narrow $632.8\,\text{nm}$ HeNe-laser radiation is coupled into PGS and then detected with the ICCD-camera. Figure 3.9 shows this detected and normalised optical
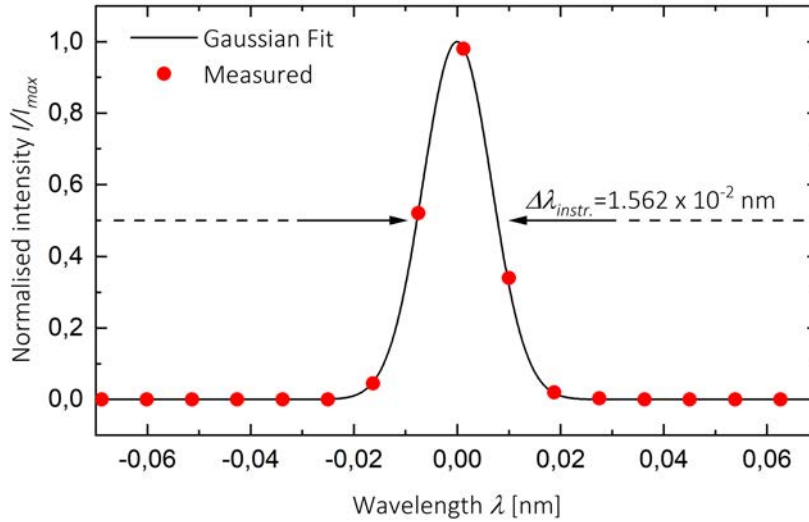
FIGURE 3.9: Detected (red point) and fitted (black line) 632.8 nm HeNe-laser radiation. This spectrum is normalised on the maximum intensity and centralised on the central wavelength for a better overview.

line (red points) that can be fitted with a Gaussian profile (black line) having FWHM of about 0.02 nm.

The principle of PROES is exploited in this thesis to get time-resolved recordings for investigating kinetic processes within the discharge [90]. Since the time window in which the emission of the respective optical line has to be captured decreases with higher temporal resolution, this technique suffers from low intensities.

However, this principle exploits that most of plasma sources are typically operated with a periodic excitation. Due to that, the used optical system can accumulate the weak intensity from period to period. But on the other side, this presumes a long-time stable plasma source.

Two parameters are of importance for this PROES technique: (i) The gate time in which the multi-channel plate within the ICCD camera opens specifying the time-resolution as shown in figure 3.10. In order to open the multi-channel plate, it is triggered by a TTL-signal (blue curve in figure 3.10) made by the same function generator as for the electrical excitation of the MGA (red curve in figure 3.10). As a result, the TTL-signal is in phase with the triangular voltage waveform excitation and takes also place periodically.

PROES allows time-resolutions up to few nanoseconds. The exact time-resolution depends on the operating conditions and the used emitted optical line. In this thesis, the shortest gate time is set to 200 ns which allows sufficiently high resolution of approximately 3 µs long discharge pulses without suffering from electric noise. Generally, it is important for the PROES technique that excited states de-excite
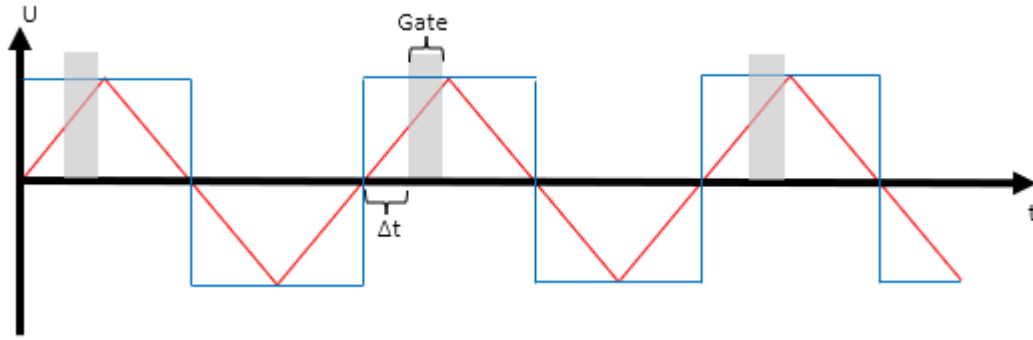
FIGURE 3.10:  Principle of PROES

through fluorescence within the periodic excitation cycle. The effective lifetime of excited states should be lower than the periodic time of excitation. This lifetime can be estimated with

$$\tau_{eff} = \frac{1}{\sum_k A_{i,k} + k_q n_{gas}}, \tag{3.5}$$

where $A_{ik}$ is the Einstein coefficient for spontaneous emission, $n_{gas}$ the gas density and $k_q$ the impact parameter for quenching.

To reduce electrical noise, a cooler is connected to the ICCD and provides cooling water with a temperature of $10\,°$C.

(ii) The second parameter for this PROES technique is the delay time $\Delta t$. If this parameter is set to be zero, the multi-channel plate opens immediately when the TTL-signal is released by the function generator. The TTL-signal has to be received with a delay by the multi-channel plate to scan the complete excitation-cycle. This delay is made by a so-called delay unit integrated in the ICCD-camera. By varying the delay time $\Delta t$, the emission can be scanned along the whole excitation cycle.

**Time-dependent discharge characteristic**

As described before, PROES allows to take time-resolved recordings of the discharge. However, it must be mentioned that the whole setup is complex. The time-dependent emission profile of the discharge is not displayed immediately and is therefore inconvenient to connect with the applied excitation. To avoid both points, a photomultiplier tube (PMT, Hamatsu) is used to detect time-resolved and spatially- and spectral-integrated emission of the MGA within the applied excitation. A collimator captures the emission that is afterwards transferred by a light fibre (Ocean Optics) with a diameter of $800\,\mu$m to the PMT. An optical filter (interference filter) can be inserted between light fibres output and PMT to investigate individual optical lines such as the $706\,$nm helium line. However, it has to be noted that no infinitely narrow line is passing through the interference filter but rather a line profile characterised by its

central wavelength and FWHM. The latter is in a range of about 8 nm for the used central wavelength of 706 nm.

**Species composition**

For the identification of the species involved in the discharge, the acquisition of an overview spectrum is a useful tool. The PGS-camera combination allows to detect an optical line with a high temporal and wavelength resolution but only a wavelength range of 8 nm can be taken, making a recording of an overview spectrum time-consuming. Therefore, the fibre output can be disconnected from the PGS and connected to an USB-spectrometer (Ocean optics) working with a spectral resolution of 0.25 nm per pixel in a spectral range between 200 and 1100 nm.

**Spatially- and phase-resolved imaging**

All three already mentioned optical diagnostics detect the emission spatially integrated. To get also spatially-resolved information of individual cavities along the two dimensional cavity-structure, a second ICCD camera (Andor iStar DH334T-18U-73) with $1024 \times 256$ pixels is installed in front of the flow-operating MGA as illustrated in figure 3.7. This camera is also synchronised in the same way as the attached ICCD-camera on the PGS. Additionally, an objective is connected to increase the spatial resolution to about 2 μm per pixel. As for PMT measurements, the same optical filter can be inserted between MGA and objective to get also spectrally-resolved information. Since the MGA is mounted on a manually driven stage and the collimator-fibre combination on a computer driven one, each cavity structure is optical available for this ICCD-camera. Therefore, it is possible to alternate between the camera and collimator-fibre combination based measurements taken under almost same conditions.

## 3.5   Optical diagnostics inside the vacuum chamber

Both MGA configurations can be investigated in dependency on pressure under a defined gas atmosphere in the vacuum chamber. For this, all already named optical diagnostic tools can be applied as illustrated in figure 3.11.

The optical access for the ICCD-camera for spatially-resolved two dimensional emission along the cavity structure is ensured by quartz windows. They have a diameter of 14 cm and are attached through flanges to the vacuum chamber. The camera is positioned at a distance of about 40 cm from the window.

A second manually driven stage with an attached collimator-fibre combination is placed inside the vacuum chamber consisting of a vacuum resistant feed-trough to lead the light-fibre out of the chamber. The output can be connected to the USB-spectrometer and to the PGS. A second feed-through guarantees the electrical HV supply for the MGA or reactor.
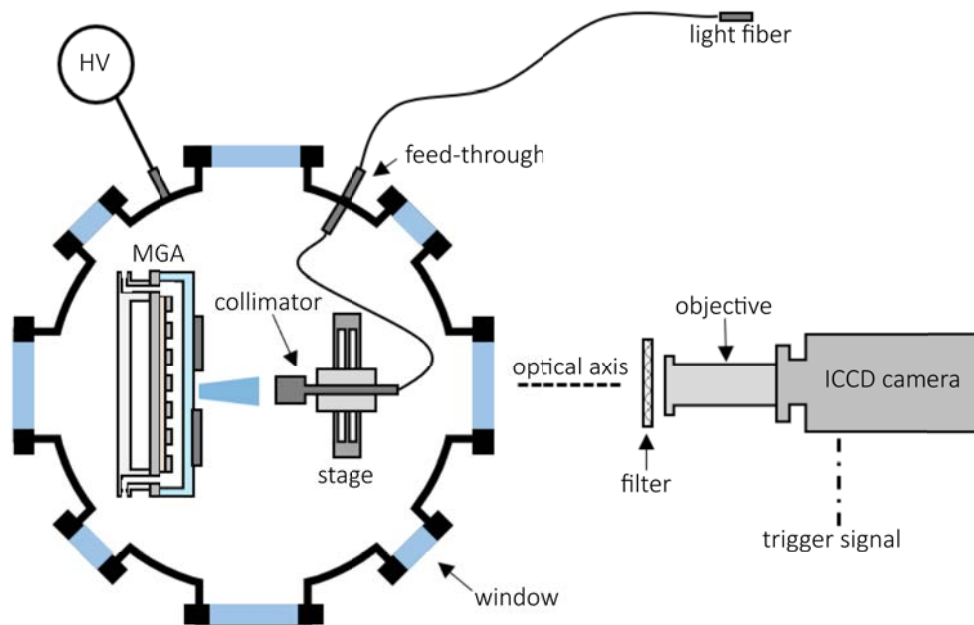
Figure 3.11: Sketch of the diagnostic system applied on the MGA
inside the vacuum chamber.

# Chapter 4

# Influence of cavity shape and surface properties on plasma arrays

Silicon-based devices with inverted pyramidal cavities showed two fundamental characteristics in the past, as described in subsection 2.2.1: (i) The discharge within the cavities shows a ring- or dot-like structure depending on the polarity of the applied voltage. (ii) The arrangement of hundreds of cavities shows an interaction of the cavities in form of an ionisation wave moving along the cavity surface. This behaviour is explained through a simulation by secondary electrons produced by ions and photons.

Here, a metal-grid array device has been developed containing cylindrical shaped cavities and a bare nickel-electrode. Internal properties as the applied electric field configuration and the secondary electron emission coefficient are different to the pyramidal shaped cavities. Therefore, it is assumed that the characteristics of the discharge within the cavities also behave differently. The following key-questions (KQ) will be discussed in this chapter focusing on these differences:

> **KQ** 1.1*: Do the cavity shape and the non-dielectrically covered nickel-electrode have an influence on global discharge properties such as pulsing, asymmetric discharge characteristic and ionisation wave propagation?*

> **KQ** 1.2*: Can further insights be gained into the wave mechanism with respect to already assumed processes such as photo-ionisation?*

Parts of these results have already been published in Sebastian Dzikowski *et al. 2020 Plasma Sources Sci. Technol. 29 035028* numbered here as [73].

## 4.1    Long-term stability

In the past, the SBA showed short lifetimes of few minutes making long-term spectro-scopic investigations nearly impossible. In contrast, the MGA introduced in this thesis reaches higher lifetimes of about 400 operation hours [73]. For optical investigations, however, not only a long operating time is an advantage, but also temporal stability should be achieved. The MGA was operated over a time of 240 min and recorded with respect to its emission structure in regular time steps by using the PMT under almost identical operation conditions to investigate its stability over time. Figure 4.1a) shows two exemplary PMT-signals of 150 μm cavities after 0 min (red solid line) and 240 min (red dashed line) operation time in dependency on the applied voltage excitation (black solid line) with an amplitude of 360 V and a frequency of 10 Hz. The MGA is operated in helium with a pressure of 600 mbar.
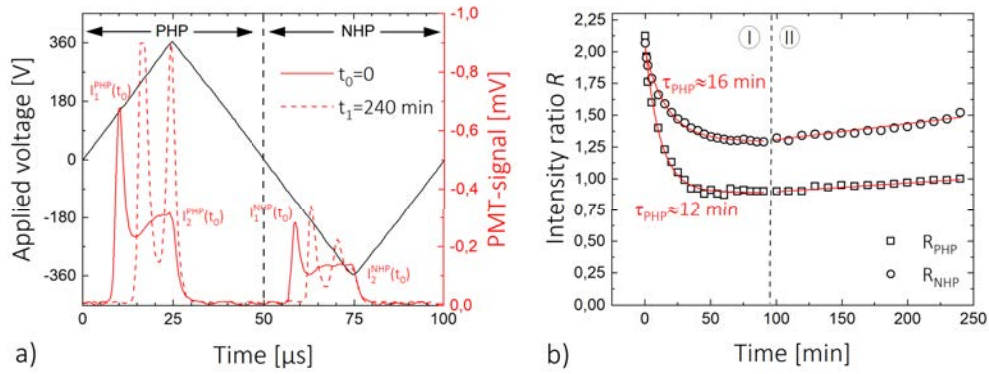


FIGURE 4.1: a) PMT-signal of 150 μm cavities after 0 min (red solid line) and 240 min (red dashed line) operation time depending on applied voltage excitation (black) with an amplitude of 360 V and a frequency of 10 kHz. The pressure is set to 600 mbar in helium. b) Ratio of peak intensities within PHP (squares) and NHP (circles) depending on the operation time. The operation conditions are equal to a).

Two changes in the shape and position of the detected PMT-signals can be recognised in both half-phases: (i) One emission peak occurs shortly after initial ignition at $t_0=0$ followed by a broader and smaller emission peak. In this series of measurements, a well-defined double peak structure forms during longer operating times for $t_1=240$ min (red dashed line 4.1a)). (ii) Additionally, the ignition voltage of the first emission peak within the double-peak-structure shifts to higher values compared to the structure detected at $t_0=0$ min.

In order to obtain process-specific time constants to identify any processes, all PMT-signals detected over time are analysed in relation to the peak intensity ratio $R(t_i)$ defined by

$$R(t) = \frac{I_1(t_i)}{I_2(t_i)} \propto \frac{n_1(t_i)}{n_2(t_i)} \tag{4.1}$$

since this shows a sufficient sensitivity and contains automatically information of both emission peaks. In the physical context, the amount of the excited species can be estimated from the respective peaks like in equation 2.5. The calculated ratio is shown as a function of the operation time in figure 4.1b) for PHP (squares) and NHP (circles) and can be divided into two parts:

I) The ratio of both phases drops rapidly and continues to approach a limit in the time range between $0\,\text{min}$ and about $100\,\text{min}$. To obtain a decay time $\tau$, the ratio $R(t_i)$ is fitted within the named time range with the following fit-function

$$R(t) = A \exp\left(-\frac{t}{\tau}\right) + R_\infty, \tag{4.2}$$

where $t$ is the operation time or the time of recording of the PMT-signal, $R_\infty$ the temporal final value and $A$ a coefficient for the starting condition. The fit is shown in figure 4.1b) (red solid line) and shows a good agreement with the measured ratio. Furthermore, it provides almost identical decay times of about $16\,\text{min}$ for NHP and $12\,\text{min}$ for PHP that can be associated to a thermal process of the MGA since typical plasma processes proceed at faster time scales (nano- to microseconds).

During operation, a part of the coupled power goes into an increasing gas temperature that heats up all assembled layers and promotes several plasma processes. Especially with regard to DBDs, an increasing temperature could influence the strong interaction between charged particles and dielectric surfaces at which particle desorption is enhanced at higher temperatures. The frequency $\nu_e^T$ of the thermodesorption of electrons is given by

$$\nu_e^T = \nu_0 \exp\left(-\frac{E_{ads}}{k_b T_w}\right) \tag{4.3}$$

and depends on the wall temperature $T_w$, the electron binding energy on dielectric surface $E_{ads}$ and frequency of oscillations for an electron near an adsorption site $\nu_0$. Impurities such as nitrogen deposited before operation on the dielectric surface can be removed during this thermal process. This can explain the higher decay time in the negative half-phase.

Furthermore, the recombination of electrons and ions on dielectric surfaces is also influenced by the wall temperature. Their recombination coefficient is given by

$$\alpha_{rw} = d_r \sqrt{\frac{\pi k T_w}{m_e}} \exp\left(-\frac{E_{diff}}{k_b T_w}\right) \tag{4.4}$$

and is a function of recombination radius $d_r$, the electron mass $m_e$ and the potential barrier between adsorption sites $E_{diff}$. The interaction of charged particles on dielectric surfaces was studied in detail in a theoretical work by Golubovskii et al. [19, 20]. The authors report that an increase of the recombination coefficient leads to a weaker shielding of electrical charges on dielectric surfaces and consequently to a pulsed current structure. This agrees well with the pulsed emission structure described here. The changing electron desorption and recombination on dielectric surfaces can also lead to a changing gap voltage manipulating the ignition voltage of the first occurring discharge pulse.

An additional technical aspect is based on the Ohmic heating during the operation time. This leads to a better attachment of the nickel-grid on the dielectric resulting in a better defined cavity confinement. Therefore, parasitic discharges located beneath the nickel-grid disappear and possible species losses out of the cavity volume are suppressed.

II) A slowly increasing linear trend of the ratio is observable in the time range between 100 min and 240 min. While it was observed that the temperature of the device has reached its equilibrium temperature after approximately 25 min, comparable to [91], a temperature effect can be neglected. Instead, it is possible that nitrogen and oxygen can enter the vacuum chamber from the outside when it is not completely tight. During the operation time of 240 min, the pressure has increased by 2 mbar to 602 mbar resulting in a contribution from impurities of about 0.3 %. A thermal process can be ruled out because the temperature of the array increased from 19 °C to 55 °C over the operation time of 240 min. This cannot explain the observed pressure increase based on the ideal gas law. Finally, the impurities reduce the ionisation energy from about 24 eV (He) to about 15.5 eV ($N_2$) and a discharge pulse can ignite and be sustained here easily. The role of impurities is discussed in more detail in 4.5.

## 4.2   UI-characteristic

The voltage-current (UI) characteristics are studied to obtain a first comparison between the MGA and the SBA. However, the information content of these measurements is limited, as several individual cavities are analysed simultaneously. Nevertheless, these integrated values provide first comparable information about time-resolved discharge structure and discharge mode without greater diagnostic or technical effort.

For this purpose, the MGA is excited with the same triangular voltage waveform as the SBA in the previous work. The frequency is set to 10 kHz and the helium pressure is kept constant at 500 mbar. Exemplary results from a previous work [92] are also depicted here to better clarify all differences and similarities between both devices.

Figure 4.2 shows the UI-characteristic (voltage black line, current red line) and the corresponding PMT-signal (blue line) of the emission for both devices at two different voltage amplitudes. The upper row shows the characteristic of the MGA containing $36 \times 36$ 150 µm cavities at a voltage amplitude of a) 330 V and b) 400 V. The lower row represents the characteristic of the SBA at c) 350 V and d) 390 V. The SBA consists of $50 \times 50$ cavities with a base length of 100 µm and an inter-cavity distance of 100 µm.
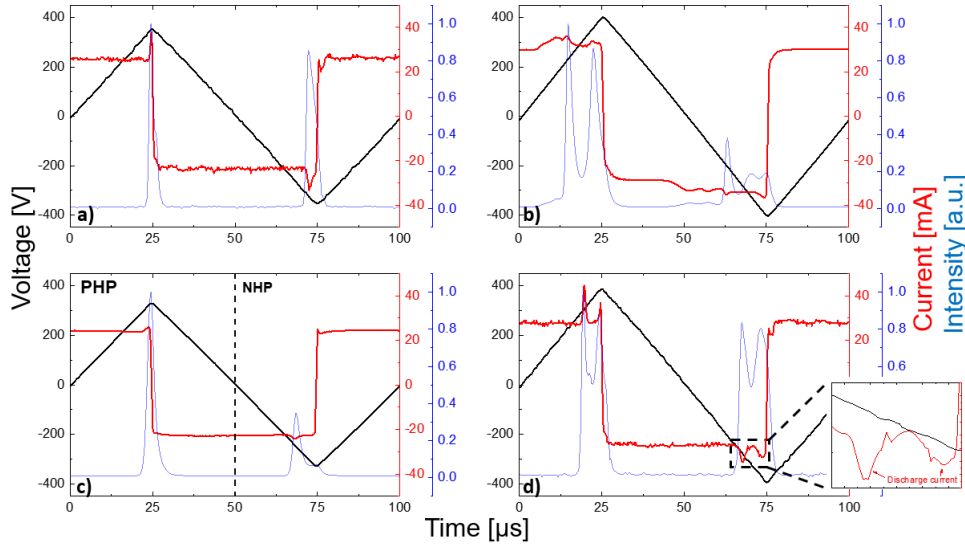


FIGURE 4.2: Current (red line) and emission (blue line) profile depending on the triangular voltage excitation (black line) for MGA (upper row) and SBA (lower row) [73]. The MGA contains $36 \times 36$ cavities having a diameter of 150 µm. The SBA consists of $50 \times 50$ cavities that have a base length of 100 µm. Both devices are operated with a frequency of 10 kHz in a defined helium atmosphere at a pressure of 500 mbar. The voltage amplitude increases from column to column.

Since both devices have a capacitor-like structure (electrode, dielectric, electrode) and can, therefore, be described through a capacitance $C$, an applied triangular voltage signal $U$ should provide a square shaped displacement current waveform $I$ based on $Q = CU \rightarrow \dot{Q} = I = C\dot{U}$.

When the required ignition voltage is reached within the increasing voltage excitation, an additional discharge current can be noted in form of a small peak during the PHP as well as during the NHP. As these discharge currents of approx. 5 mA are difficult to recognise on the full scale compared to the large displacement current of approx. 25 mA, an enlarged profile (dashed black box) is shown in 4.2d).

Emission peaks are detected at the same time when the discharge current occurs. A further increase of the voltage amplitude leads to more emission pulses. In the left-hand column of figure 4.2, there is only one emission peak in each half-cycle, while two peaks can be recognised in the right-hand column after a slight increase in voltage. This coherence is also illustrated in figure 4.3 presenting the number of discharge pulses depending on the applied voltage amplitude under almost identical operation

conditions. However, the amount of impurities is difficult to control and can also have an influence on this behaviour. In these measurements up to 5 pulses per half phase could be detected although both devices differ in geometry, material structure and setup. Both devices show a good agreement during both half-cycles and the discharge behaviour can, therefore, be described in the same way.

The interaction between the gap voltage generated by surface and volume charges and the voltage applied to the electrodes is a possible explanation for this agreement. The charges produced during the first discharge pulse and deposited on dielectrics, shield the applied voltage. Thefore, the discharge within the cavity cannot be sustained anymore. The applied voltage has to be increased to reach the necessary ignition voltage within the gap again which automatically occurs during the triangular voltage excitation. This procedure takes place from discharge pulse to discharge pulse until the reverse point of the applied voltage (voltage amplitude) is reached. After this, no more voltage is available to overcome the shielding and pulsing is terminated at each half-phase. By increasing the voltage amplitude, more voltage and a shorter time interval are available after ignition (first pulse) due to the time derivative of the voltage ($dU/dt$) resulting in several discharge pulses.

Since both devices show this pulsing despite their different setup, ions are expected to play also a major role in the discharge dynamics in addition to electrons. In case of the SBA, both electrodes are dielectrically covered. By assuming that the discharge dynamics is mostly driven by electrons due to their higher mobility, they are able to reach the dielectric and to provide shielding at each half-phase.

In the case of the MGA, this assumption might not be sufficient. Since the nickel electrode is not dielectrically covered, electrons disappear there and shielding cannot be established. This results in the assumption that the shielding process is dominated by surface charges of ions moving to the dielectric at the bottom of the cavity during the PHP.

The fact that charged particles in the SBA cannot disappear from the cavity via the dielectric surface can also explain the significantly higher emission background that occurs between the emission peaks. This emission background is much less pronounced in the case of the MGA. Therefore, the shielding by the ions must be lower in the MGA.

### 4.2.1  Discharge mode

Due to the knowledge of the UI-characteristic and geometric structure of both devices, the discharge mode can be estimated. As already described in section 2.1 a DBD can operate in an APGD or APTD mode that varies in current density. The MGA shows a discharge current of about $8\,\mathrm{mA}$ at a voltage of $400\,\mathrm{V}$. With the assumption that the whole current flows over all $36^2{=}1296$ cavities, a discharge current of about $36\,\mathrm{mA\,cm^{-2}}$ and a power density of about $3\,\mathrm{kW\,cm^{-3}}$ are achieved.

In case of the SBA a discharge current of about 18 mA flows over the base area of $50^2$=2500 cavities at the same voltage. This results in a current density of about $70\,\mathrm{mA\,cm^{-2}}$ and a power density of $24\,\mathrm{kW\,cm^{-3}}$. In comparison to the MGA, the current density is higher by a factor of two. The power density shows an eight times higher value.

Nevertheless, both current densities are in the same order of magnitude and can be attributed with respect to table 2.1 to the APGD mode. Finally, it can be summed up that both discharge sources show the similar temporal UI and emission characteristic and can be assigned to the same discharge mode. The differences in design and structure do not have an impact on that.
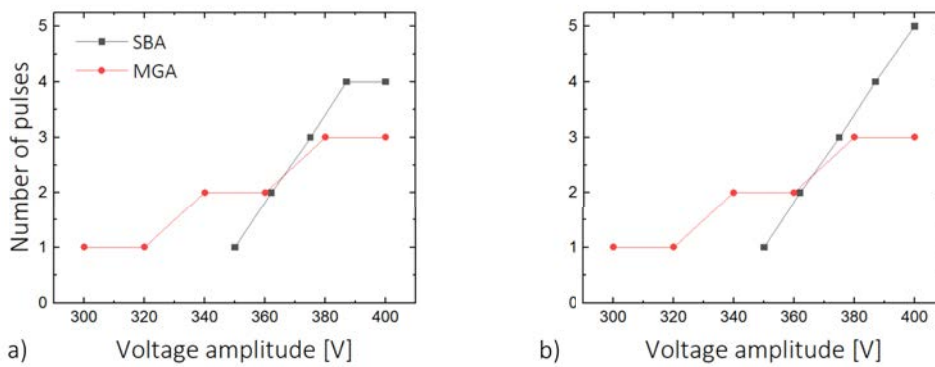


FIGURE 4.3: Number of occurring discharge pulses in MGA and SBA as a function of the voltage amplitude during a) PHP and b) NHP. Both devices are operated at 10 kHz and 600 mbar in helium. The MGA consists of 150 µm cavities while the cavities incorporated in the SBA have a base length of 100 µm.

## 4.3 Spatial discharge formation

### 4.3.1 Radial discharge structure

An asymmetric discharge characteristic was observed for silicon-based configurations based on the electron movement during the respective half-phase (see subsection 2.2.3.1). In case of the MGA, electrons can get lost on the bare nickel-electrode and therefore a less pronounced asymmetric effect is expected. This is analysed by a head-on inspection of the MGA by using spectral-integrated phase resolved imaging (PRI) shown in figure 4.4 according to the setup described in figure 3.11.

The first row of figure 4.4 shows these recordings in a head-on perspective (surface normal of MGA is parallel to optical axis) during PHP and NHP. The MGA consists of 150 µm cavities and is operated with a voltage of 300 V at a frequency of 10 kHz. The emission was integrated over a full discharge pulse as illustrated in figure 4.2.

In the MGA it is also observed that both polarities lead to a different radial discharge structure within the cavities. In PHP 4.4a) a broad circular emission structure appears.

In some cavities donut-shaped structures are formed. This means that less intensity comes from the cavity center whereas enhanced emission occurs close to the cavity edge. In contrast to this, the discharge is concentrated clearly in the cavity center during the NHP shown in 4.4b).

Since the asymmetric effect is obvious for all array configurations, the surface properties and the shape of the cavity do not seem to play a significant role. Instead, the applied electric field distribution and its strength within the cavities seem to be a dominant factor. This is investigated further in the next sub-section. In principle, an inverted pyramidal or cylindrical shaped cavity is incorporated in a parallel-plate capacitor-like structure where the internal electric field distribution has components oriented in cavity height direction. Additionally, the cavities are not enclosed but surrounded with the nickel-electrode on the top so that the electric field distribution might also contain a radial component. By applying voltages of about 400 V over distances of 40 µm, the strong resulting electric fields accelerate electrons along this radial and vertical field direction and lead to a Townsend avalanche. Depending on the respective phase, the discharge is finally located either inside the cavity centre or outside at the cavity edge.

### 4.3.2   Discharge expansion out of cavities

Up to now, only a phase-resolved radial discharge structure was investigated within the cavities. However, it is assumed relating to the asymmetric discharge characteristic explained in 2.2.3.1 that the discharge also changes its distribution in cavity height from half-phase to half-phase. One approach to investigate this is given by phase-resolved imaging in a grazing perspective. From this view, the optical axis is orthogonal to the surface normal of the array. However, in case of silicon-based devices such investigations are difficult since the cavity-structure is surrounded by glue for electrical connection. This prevents a direct optical access from the side and allows only a focused view under a small angle.

A solution is provided by the MGA. Since this device needs only a simple three-layer structure, the flexible nickel-grid can be placed on a dielectric anodised and concavely formed electrode illustrated schematically in figure 4.5a). In this case, the dielectric consists of aluminium oxide ($Al_2O_3$, epsilon$_r \approx 9$) with a thickness of about 30 µm. The concave formed electrode is made of aluminium and is electrically grounded. Its curvature radius is about 50 mm. Due to this configuration, only a single cavity row on top of the electrode can be focussed and stray light from adjacent cavities is mostly suppressed.

The middle row of figure 4.4 shows this recordings of 150 µm cavities after an integration time of 200 ns during PHP (c)) and NHP (d)). The MGA is operated under equal operation conditions as in the head-on perspective. By comparing both half-phases with each other, it is obvious that a clear emission structure (framed by white line)
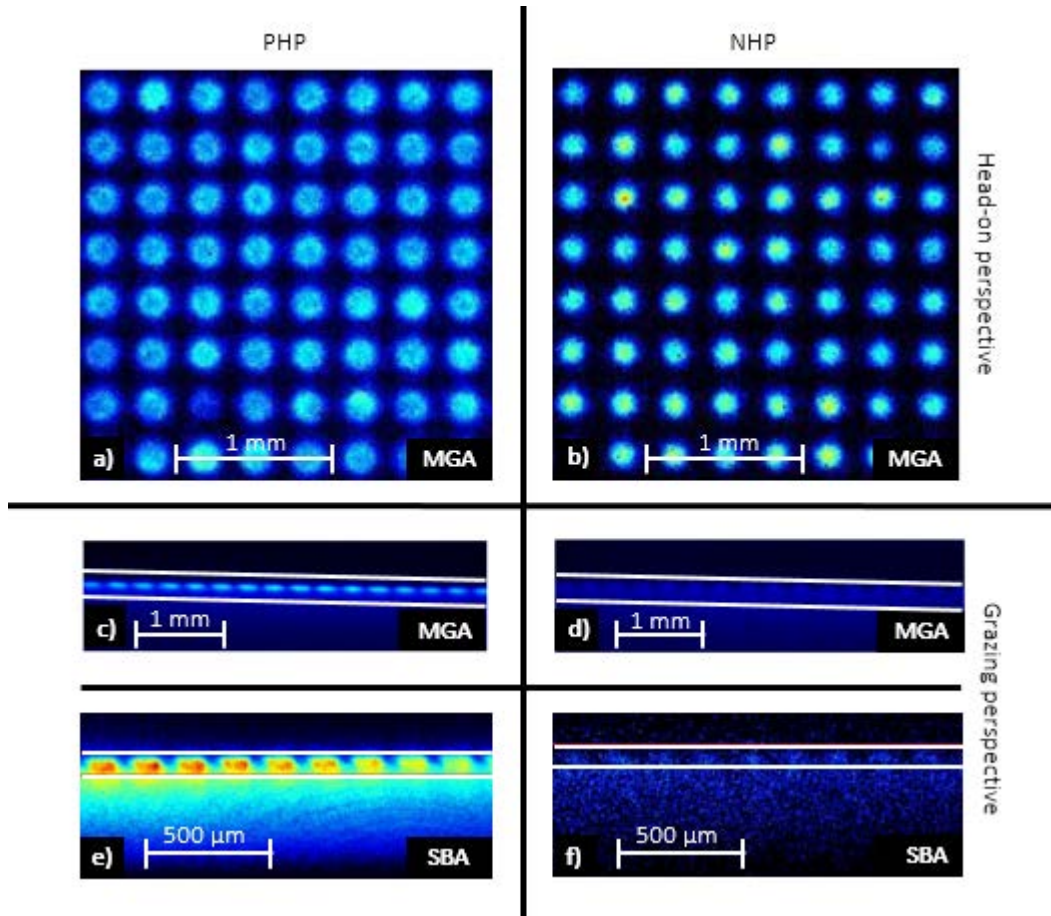
FIGURE 4.4: Spectral integrated phase resolved images for the PHP and NHP of MGA and SBA at maximum intensity [73]. The columns indicate the respective half period, the rows the perspective of the recording. The MGA is shown in the head-on perspective in image a) and b) and in the grazing perspective c) and d) operating at an amplitude of 300 V at 10 kHz. The SBA is shown in the grazing perspective in image e) and f). The white lines frame the cavity row. High emission intensity is displayed by bright and red colours, low intensity by dark and blue colours.

occurs only in the positive half-phase (c)), while this mostly disappears during the negative one (d)). The same effect is visible under a small angle for SBA containing inverted pyramidal cavities illustrated in the bottom row (e) and f)).

In connection to phase-resolved recordings in the head-on observation, this measurement supports the simple model of electron movement and serves additionally as explanation for the asymmetric discharge characteristic. This means that the vertical electric field component within the cavity is high enough to accelerate electrons out of the cavities for creating the discharge. In the negative half phase, these electrons are accelerated into the cavities by the vertical electric field component.

### 4.3.3   Influence of pressure

Investigations in the head-on perspective on cylindrical shaped and silicon-based arrays have shown that the radial discharge distribution changes its form with increasing pressure [17]. It was found out that the increased intensity at the cavity edge moves further to the powered electrode by about 35 µm during PHP when the pressure is increased from 500 mbar to 700 mbar.

By investigating the discharge from the side in the grazing perspective, its expansion width can be estimated in figure 4.4c). Here, it is defined by the distance between the metal-electrode surface and the point where the maximum intensity has dropped to its 1/e value. The investigation is always performed at time of maximum intensity corresponding the maximum PMT-signal shown in figure 4.2 to get a high single-to-noise ratio. With exception of the pressure, all other operating conditions are kept constant. The presented values are obtained by averaging the expansion width of a single cavity row over different rows that are brought into focus by turning the array.

Figure 4.5 shows the discharge expansion as a function of the pressure during PHP. It is shown that the expansion drops from about 90 µm to 55 µm when the pressure is increased by a factor of three.
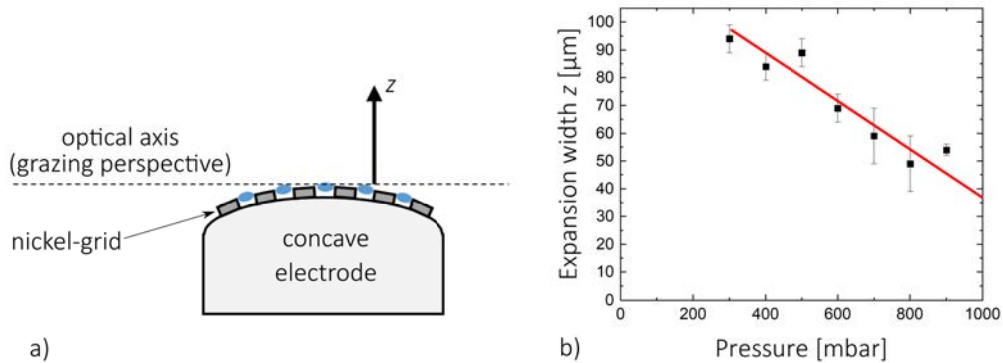


FIGURE 4.5: a) Schematic sketch of the concave-formed MGA for measuring the expansion width of the discharge along the cavity height $z$. In this kind of setup, the surface normal of a cavity row is orthogonal to the optical axis (grazing perspective). b) Expansion width of the discharge as a function of the pressure measured in the configuration as explained in a) on basis of recordings as showed in 4.4c). The MGA consists of 150 µm cavities and is applied with a voltage amplitude of 300 V at 10 kHz [73].

One explanation for this expansion is that the mean free path of electrons decreases with more collisions in a higher pressure regime. Therefore, electrons can only absorb the required energy for excitation and ionisation in higher electric field regions. These higher electric field regions are located close to the cavity edge and become stronger in direction to the dielectric surface. Finally, the discharge expansion must decrease with increasing pressures to be further maintained.

## 4.4 Ionisation-wave propagation

With regard to the asymmetric discharge characteristic, the phase dependent discharge structure in radial and vertical direction of only a single cavity was investigated. Based on section 2.2.3.2, not only the discharge of a single cavity is of importance for understanding the microplasma array but also the interaction between cavities. In previous works, the cavities of silicon-based devices did not show a simultaneous ignition but a collective behaviour in form of an ionisation wave propagating along the cavity surface. This ionisation wave travels during each individual discharge pulse as shown in figure 4.2c) and d). These individual pulses are also observed in the MGA as shown in 4.2a) and b) although the surface properties are different. Hence ionisation wave investigations were performed. In this way, the two array devices can be compared and the extent to which the surface properties are responsible for the mechanism of the ionisation waves can be investigated.

Figure 4.6 shows phase-resolved images of the discharge in the MGA in the head-on view during a single discharge pulse in the PHP. In these recording, bright colours stand for high intensities. The MGA consists of 150 μm cavities and is applied with a voltage amplitude of 400 V at a frequency of 10 kHz. The time resolution is set to 200 ns. The timestamps correspond to the delayed trigger signal for the ICCD-camera of the respective discharge pulse.

Not all cavities ignite at the same time, as observed with the SBA. At the beginning of the pulse (t= 0 ns) only cavities located at bottom left ignite. Afterwards, the ignition moves to the opposite corner (top right) where the discharge occurs at the end of the pulse (t= 1600 ns). In the meantime (t= 600-800 ns) almost all cavities are ignited which corresponds to the time of maximum intensity of the respective pulse. The same wave propagation is also visible during a pulse of the NHP (not shown here).

In order to better understand and compare the dynamics of the ionisation wave in both devices, the corresponding wave velocities can be considered. The knowledge of the geometry and dimension of the cavity arrangement and the possibility to record the wave propagation temporally-resolved allow to estimate the corresponding propagation velocities by assuming a steady motion. For this estimation, the time difference between the maximum intensity of two distant cavities is taken. An average of ten measurements has been made to oobtain a statistical error.

Figure 4.7 demonstrates the wave velocities as a function of the pressure recorded in 150 μm cavities during PHP (black) and NHP (red). The voltage amplitude is set to 400 V at a frequency of 10 kHz. Three facts are observed: (i) The velocities are in a range of $1.5 \, \mathrm{km \, s^{-1}}$. They are therefore in accordance with measurements [18] and simulations [22] made in SBA with inverted pyramidal cavities where velocities up to $10 \, \mathrm{km \, s^{-1}}$ were observed. (ii) The wave velocities increase from $0.8 \, \mathrm{km \, s^{-1}}$ to $2 \, \mathrm{km \, s^{-1}}$ while the pressure rises by 300 mbar. (iii) Within the error bars, no difference between
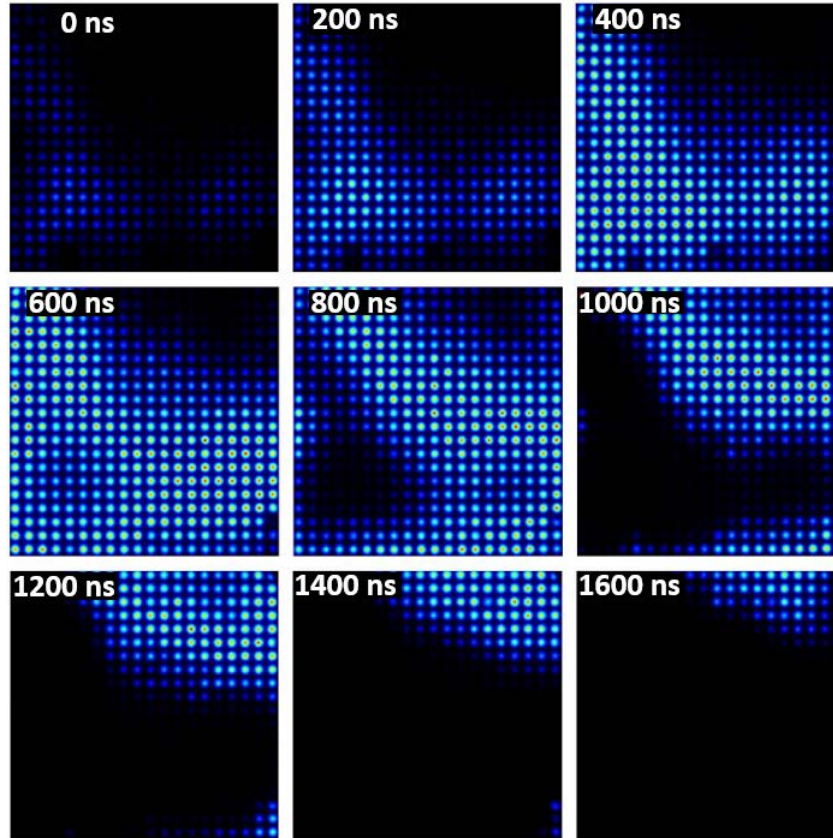
FIGURE 4.6: Phase-resolved and wavelength-integrated images of the propagating ionisation-wave recorded in the discharge pulse during PHP in the head-on observation [73]. The time resolution is set to 200 ns. The MGA consisting of 150 μm is applied with a voltage of 400 V and a frequency of 10 kHz. The time stamp in each image refers to the delayed trigger signal for the ICCD-camera. The time stamp at 0 ns corresponds to the ignition of a single pulse.

both half-phases can be noted. The reason why these error bars increase with higher pressure is that the start and end points of the propagating ionisation wave are not precisely defined. In a higher pressure regime, larger cavity areas ignite at the same time making it difficult to define a clear distance between two cavities.

Up to now, the mechanism for the ionisation wave propagation in micro-structured array devices is not completely understood. However, previous simulations and models can be compared to the results from this thesis. This is done in the following:

I) In the simulation made by Wollny et al. and explained in 2.2.3.2, photo-ionisation was identified as the dominant mechanism for wave propagation during NHP. However, this has to be considered with caution with regard to the phase-resolved images in the grazing view shown in 4.4d). As described before, the discharge occurs inside the cavities in this half-phase so that photons cannot reach adjacent cavities. This is supported by the pressure dependence of the discharge expansion, intensity and propagation velocities.
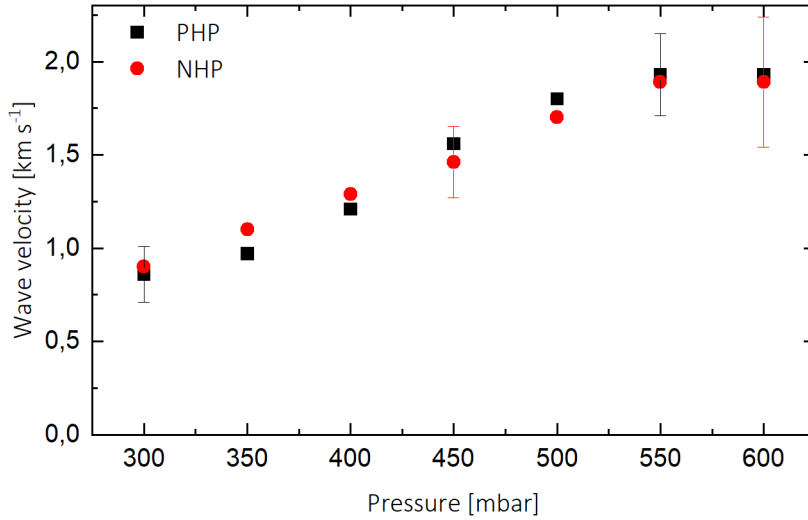
FIGURE 4.7: Wave velocities as a function of pressure recorded in 150 µm cavities during PHP (black) and NHP (red). The voltage amplitude is set to be 400 V at a frequency of 10 kHz [73]. For the determination of the velocities, a steady motion is assumed on the phase-resolved images as illustrated in 4.6.

It is not observed that the discharge expansion increases with higher pressure which makes it more difficult for the photons to reach neighbouring cavities. Further, produced photons are trapped in the cavity and only a limited interaction with adjacent cavities is possible.

Furthermore, it is shown in figure 4.8 that the intensity drops with increasing pressure. This measurement is done on 150 µm cavities with an applied voltage of 380 V and a frequency of 10 kHz. The production of photons decreases due to more collisions resulting in quenching as a dominant de-excitation process. Consequently, less photons are generated and photo-ionisation becomes inefficient although collisions increase between helium atoms and photons for photo-ionisation with higher pressure.

II) The production of secondary electrons by ions was considered as a second mechanism for the ionisation wave. In fact, this process can appear during NHP where electrons move to the bottom of the cavity and ions are accelerated out of the cavity. However, the electrons move to the opposite directions during PHP. This would also mean that the transport of electrons into neighbouring cavities creates starting electrons for ignition during PHP. This process should approximately occurs on the same time scale as for the ion induced electrons during NHP considering the observed similar propagation velocities. By assuming a drift dominated transport of electrons and ions in the cavities due to the high electric field $E$, the corresponding drift velocities $v_{d,i}$ of species $i$ can be estimated with
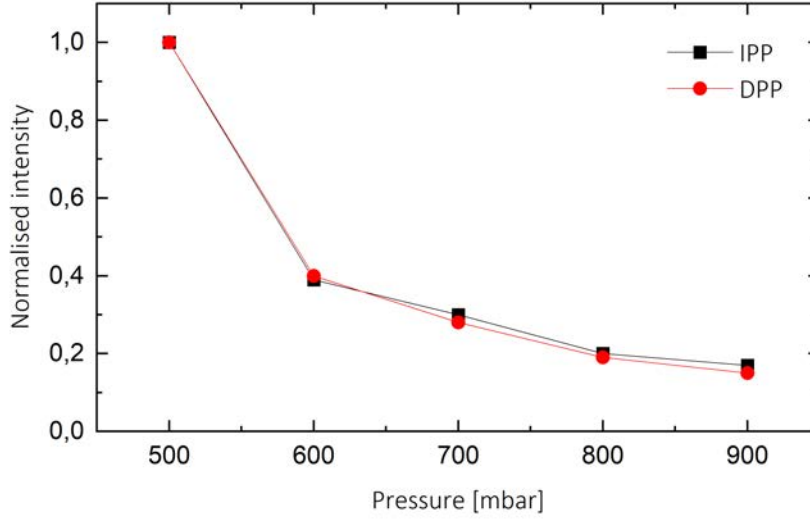
FIGURE 4.8: Normalised intensity as a function of the pressure recorded
from 150 μm cavities. The voltage is set to be 380 V at 10 kHz.

$$v_{d,i} = \mu E \tag{4.5}$$

where $\mu_i$ stands for the mobility of the respective species. This can be calculated
by using the Einstein-relation connecting the mobility and the diffusion $D_i$ with
each other by

$$\mu_i = \frac{e}{k_B T_g} D_i \tag{4.6}$$

and depends additionally on the gas temperature $T_g$. The diffusion constant is
given by

$$D = \frac{k_B T_g}{m_i \nu_m} \tag{4.7}$$

and is a function of the mass $m_i$ and the mean collisional frequency $\nu_m$. The
latter has a dependency on the gas density $n_g$, the total momentum transfer
cross-section $\sigma_t$ and the mean velocity of the respective specie $\overline{v}$ illustrated in
equation 4.8. The total momentum transfer cross-section $\sigma_t$ between electrons
and helium neutrals can be estimated to $7 \times 10^{-20}\,\mathrm{m}^2$ for electron energies of
about 2 eV [83]. In case of collisions between helium ions and atoms with a
temperature of 300 K, the cross-section is approximately $10^{-18}\,\mathrm{m}^2$ [84]. The gas
density can be substituted by using the ideal gas law to $n_g = p(k_B T_g)^{-1}$ where
$p$ stands for the pressure set to $10^5\,\mathrm{Pa}$.

$$\nu_m = n_g \sigma_t \overline{v} \tag{4.8}$$

Here, it is assumed that the particles follow a Maxwell velocity distribution whose mean velocity is calculated with

$$\overline{v} = \sqrt{\frac{8 k_B T_i}{\pi m_i}} \tag{4.9}$$

and depends on the temperatures of the respective species $T_i$. By substituting, the diffusion can be estimated finally through

$$D_i = \frac{(k_B T_g)^2 \sqrt{\pi}}{p \sigma_t \sqrt{8 k_B T_i m_i}} \tag{4.10}$$

resulting in $D_e = 2.8 \times 10^{-3} \, \mathrm{m^2 \, s^{-1}}$ for electrons and $D_{He} = 2.0 \times 10^{-5} \, \mathrm{m^2 \, s^{-1}}$ for helium atoms. The mobility is given by

$$\mu_i = \frac{e k_B T_g \sqrt{\pi}}{p \sigma_t \sqrt{8 k_B T_i m_i}} \tag{4.11}$$

and provides a value of $\mu_e = 0.11 \, \mathrm{cm^2 \, s^{-1} \, V^{-1}}$ for electrons and $\mu_{He} = 7.74 \times 10^{-4} \, \mathrm{cm^2 \, s^{-1} \, V^{-1}}$ for ions. By assuming that both species interact with the equal electric field, the drift velocity of electrons is higher by a factor of 140. Thus, it is rather improbable that an electron or ion transport is responsible for almost equal ionisation wave velocities in the respective half-phases.

III) An additional point questioning ion induced secondary electrons as the main process for ionisation wave propagation is considering the emission coefficient of the material and therefore the surface properties. For the inverted pyramidal cavities of the SBA the surface consists of $Si_3N_4$. This material has a secondary electron coefficient of 0.15 [22]. In contrast to this, the nickel-electrode of the MGA is not dielectrically covered and its secondary electron coefficient $\gamma_{see}$ can be estimated with the following equation

$$\gamma_{see} = 0.032(0.78 \epsilon_{ion} - 2 \epsilon_{wf}) \tag{4.12}$$

that depends on the ionisation energy $\epsilon_{ion}$ of species colliding on the nickel surface and on the work function of the material [93]. In this case, the nickel electrode has a work function of 5.15 eV and is bomberdeed by helium with an ionisation energy of 24.587 eV leading to a secondary electron emission coefficient of 0.284. Therefore, the probability to generate secondary electrons through ions is 90 % higher for the MGA than for the SBA which would promote the

ionisation wave propagation. However, this does not match with the propagation velocity that is ten times higher in SBA.

In conclusion, secondary electrons originating either from photons or ions are unlikely to be the source of the ionisation wave propagation. The simulated mechanism by Wollny et al. do not match with the asymmetric discharge characteristics and pressure dependent investigations. In order to get a species-based process that is approximately identical in its time scale for both half-phases, electrically neutral species can play a role. Since these species do not interact with the internal electric field, they are decoupled from the asymmetric discharge effect, which leads to unequal processes, as discussed before. The contribution of neutral species is investigated in the next section.

## 4.5   Uniform operation

All array devices show a pulsed discharge current and pulsed emission behaviour when excited by a triangular voltage as shown in figure 4.2a) and b). Each pulse has a duration of 2 µs and is associated with the ionisation wave travelling along the cavity surface. However, it has also been observed in the MGA under special conditions that current and emission structures are significantly broadened over time, which is described below.

Figure 4.9 shows exemplary the PMT-signal of 200 µm cavities from the gas-flow operated MGA. The helium gas flow is set to 2 slm at atmospheric pressure and the nickel-grid is applied with a voltage of 700 V at 15 kHz. The spatially-integrated emission signal has a smooth shape in both half-phases. Few microseconds before the applied voltage reaches its zero-crossing (change of polarity), a strong increasing peak indicating ignition occurs followed by a continuously rising intensity for 15 µs until the reversal of the voltage slope (voltage amplitude) is reached. The intensity in the NHP is around 20 % higher.

Since the discharge ignites already a few microseconds before the applied voltage reaches its zero-crossing, the definitions of PHP and NHP are no longer valid. Therefore, a different definition based on the potential is used for the rest of this thesis: the increasing potential phase (IPP, $dU/dt > 0$) and the decreasing potential phase (DPP, $dU/dt < 0$) as indicated through the black arrows in figure 4.9. An alternative formulation is based on the sign of the current.

The corresponding current signal is not illustrated because: (i) Since all four cavity structures are incorporated in the same nickel-foil, the obtained current-signal provides only information integrated over all four sub-arrays which makes it impossible to extract information about an individual cavity-structure. (ii) The following measurements are performed with the amplifier which is able to gain voltages up to 800 V to increase the power range. However, as can be seen in figure 4.9, this amplifier does not provide an
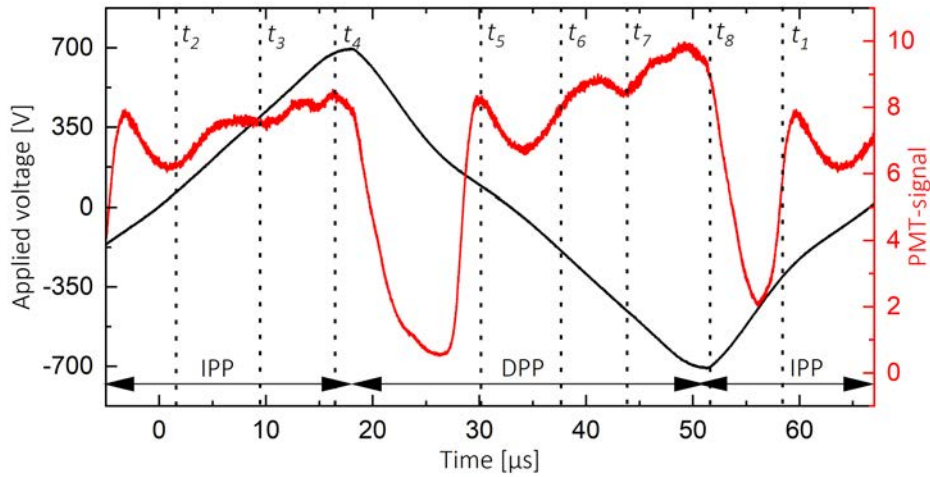
FIGURE 4.9: PMT-signal (full red line) of 200 µm cavities of the flow-operated MGA depending on the applied voltage waveform excitation (full black line) having an amplitude of 700 V at 15 kHz. The gas flow is set to be 2 slm at atmospheric pressure. The indicated time stamps are the following: $t_1$=58 µs, $t_2$=2 µs, $t_3$=9.5 µs, $t_4$=16 µs, $t_5$=30 µs, $t_6$=37.5 µs, $t_7$=44.5 µs and $t_8$=52 µs

ideal triangular excitation waveform due to its limited frequency response (100 kHz). With respect to $\dot{Q} = I = C\dot{U}$, the displacement current reflects these deviations and a clear separation between discharge current of an individual cavity-structure and displacement current is very challenging.

The current signal is further discussed in connection to a power estimation in chapter 6, where the flow-operated MGA is considered as a single device for gas reformation and a deviation from sub-array to sub-array is not required.

### 4.5.1 Quasi-simultaneous ignition

As stated above, the PMT-signal shows a clearly different appearance of emission structure in the MGA compared to previous measurements. Therefore, the spatial and temporal dynamics of this discharge mode along the cavity surface are of particular interest. Figure 4.10 illustrates wavelength-integrated and phase-resolved images of the discharge of the MGA in head-on view during IPP (left column) and DPP (right column) at certain times (pointed vertical lines) as indicated in figure 4.9. The time resolution is 200 ns and the operation conditions have not changed compared to figure 4.9.

It can be observed that, although the discharge again shows its asymmetry between IPP and DPP, there is no wave-shaped ignition characteristic, but a spatially homogeneous and quasi-simultaneous ignition of all cavities as illustrated in figure 4.10. This can explain the temporally broadened and spatially-integrated emission structure.

Additionally, all cavities show a continuous extinction and re-ignition during increasing voltage excitation which is similar to the occurrence of the ionisation wave. But here, it seems to be that this process occurs independently in each individual cavity and not through a wave-like interaction.

The different behaviour could also originate from a change of amplifier in the experimental setup. The occurrence of the ionisation wave was observed at the single cavity-structured MGA operated in the chamber by using the amplifier (FM Electronic DCU 600-40 HF) amplifying up to 400 V). In contrast, the quasi-simultaneous mode is detected in the flow-operated MGA that is powered by the amplifier (Trek PZD700A M/S) amplifying up to 800 V). However, the electrical supply cannot explain this behaviour since the quasi-simultaneous operation is also observed at voltages below 400 V using the weaker amplifier (not shown here).

Therefore, it can be concluded that the gas composition in and around the cavities has a significant influence on the interaction of the cavities with each other. In case of the flow-operated MGA, the whole device is permanently flushed with fresh pure helium which leads to only a small amount of impurities. The electrons within the MGA have to reach the effective ionisation energy of about 24.5 eV to trigger a first ionisation for ignition in surrounding cavities. In contrast to this, the amount of impurities in the chamber is higher due to the more complex gas supply and attached windows, flanges and valves. In case of nitrogen, this would result in a significantly decreased ionisation energy of about 15 eV and in consequence to higher ionisation rates.

A dominant process in plasmas operated in high pressures and helium to ionise impurities such as nitrogen corresponds to the Penning mechanism [64]. In this process, metastable species are involved and provide the necessary ionisation energy. This reaction is expressed by

$$N_2 + He^* \rightarrow N_2^+ + e^- + He \tag{4.13}$$

and can be a fundamental process for the ionisation wave propagation.

Since neutral metastable helium compounds are not able to interact with the applied electric field as long-lived energy carriers, they do not contribute to the asymmetric discharge dynamics.

However, such species can be transported from cavity to cavity through diffusion. This transport is much slower than the time scales compared to the observed wave velocities. To get a rough estimation over space $x$ and time $t$, Ficks second diffusion law is solved in only one dimension described by

$$\frac{\partial n(x,t)}{\partial t} = D \frac{\partial^2 n(x,t)}{\partial x^2}. \tag{4.14}$$

It depends on the diffusion constant $D$ and the space- and time-dependent particle density $n(x,t)$. A solution of this partially defined differential equation is given by

$$n(x,t) = \frac{n_0}{\pi Dt} \exp\left(\frac{-x^2}{4Dt}\right), \tag{4.15}$$

where $n_0$ is an integration constant. This relation allows to calculate the density depending on time and space in one direction. For the estimation here, the diffusion length $L_D$ is

$$L_D^2 = 4Dt. \tag{4.16}$$

Regarding the distance $L_D$ between two neighbouring cavities of typically $150\,\mu m$ and the diffusion constant $D$ for helium atoms is about $2.0 \times 10^{-5}\,m^2\,s^{-1}$ as already obtained by equation 4.10, the necessary passing time is t= $280\,\mu s$. This is compared to the transfer time derived from the wave velocity of $0.3\,\mu s$ and is therefore too slow to describe the behaviour.

A point supporting the photo-ionisation process is that nitrogen contains a spectrum in the visible/ ultra-violet range and is therefore a provider of high-energetic photons. In case of the pure helium discharge, the amount of such emission produced by e.g. $He_2$-excimers is almost not detectable that could also explain the absence of the ionisation wave. However, this process is questionable since the discharge changes its location from half-phase to half-phase and a radiation of photons into adjacent cavities is unlikely during the decreasing potential phase.

In this work, an attempt was made to reproduce the dependence of the wave phenomena on the amount of nitrogen, but typical amounts below $0.1\,\%$ cannot be controlled with the available technical equipment. Furthermore, the vacuum chamber was equipped with new seals and windows so that impurities are suppressed. Consequently, the MGA only shows uniform operation of all cavities up to now which is advantageous for the following chapters. However, the question of which mechanism is responsible for the ionisation wave propagation remains open and needs more research.

The next chapter is dealing with spatially- and cavity-integrated electric field strengths where a strong discharge dynamic and gradient in space and time would be disadvantageous for the interpretation. In case of a uniform operation, the discharge seems to be almost located inside the cavities leading to a better geometrically description of it.

### Summary

Although metal-grid- and silicon-based arrays differ in their cavity shape and material composition, these properties do not seem to have any influence on global discharge characteristics. The pulsing, the asymmetric discharge characteristic as well as the

ionisation wave propagation phenomena occur in both types of plasma arrays. While for the pulsing, the alternating shielding and reignition are the dominant processes, the vertical applied electric field must be responsible for the electron movement with regard to the asymmetric discharge characteristic in the respective half-phases. It is not possible to conclusively clarify which process is responsible for the propagating ionisation wave phenomena. However, the role of impurities such as nitrogen can be an important player since these particles can be ionised by metastable helium atoms via the Penning mechanism.
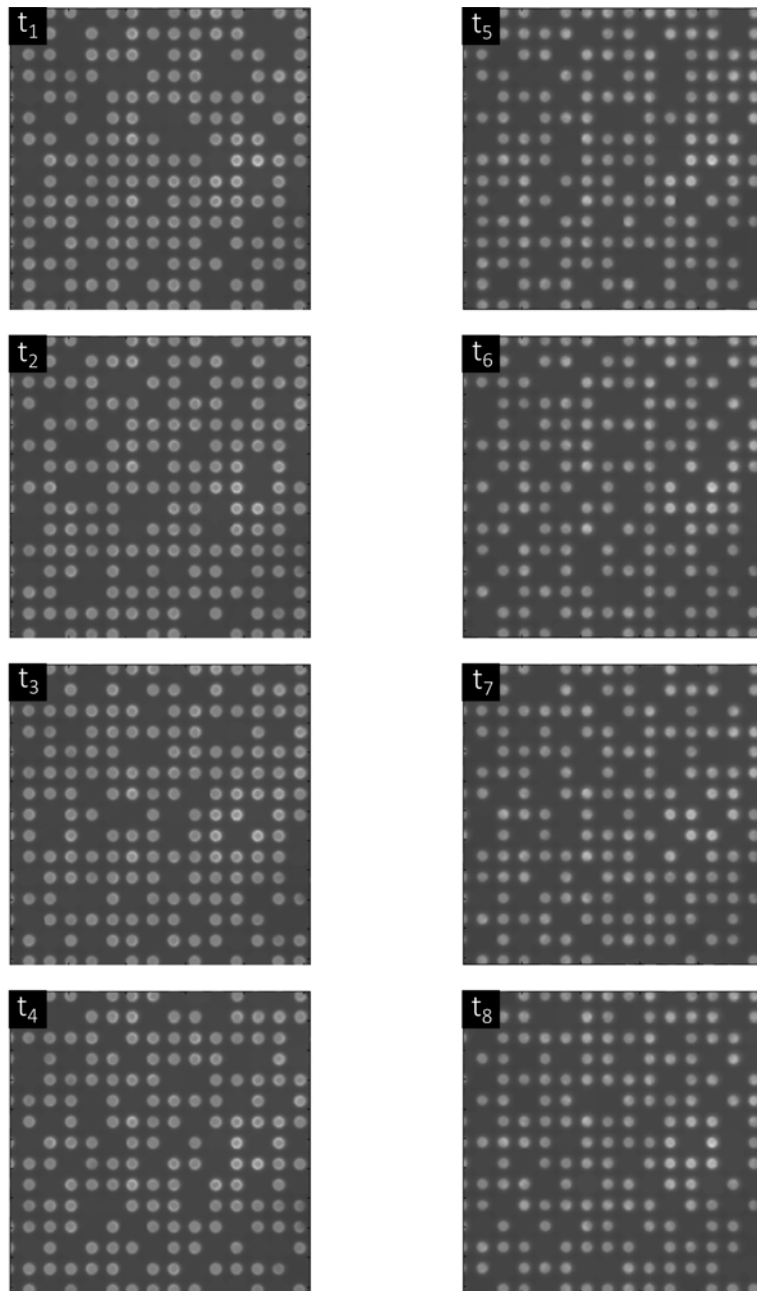
FIGURE 4.10: Time-resolved and wavelength-integrated images of the discharge in 200 µm cavities of the flow-operated MGA during IPP (left column) and DPP (right column). The images are recorded in the head-on observation under certain times as indicated in figure 4.9 (black pointed vertical lines) with a time-resolution of 200 ns. The MGA is applied with a voltage amplitude of 600 V at a frequency of 15 kHz. Bright colors corresponds high intensities. The indicated time stamps are the following: $t_1$=58 µs, $t_2$=2 µs, $t_3$=9.5 µs, $t_4$=16 µs, $t_5$=30 µs, $t_6$=37.5 µs, $t_7$=44.5 µs and $t_8$=52 µs

# Chapter 5

# Electric field strengths within a micro cavity plasma array

As already mentioned in the introduction, the electric field is a key parameter for plasma physics [37, 38]. It influences e.g. the energy and particle flux on surfaces and is, therefore, a setscrew for many possible applications [19, 38]. The electric field is of special importance for a DBD where a pore is integrated in the dielectric layer [36]. The strong electric field inside the pore leads to a significant increase in particle densities and temperatures which is advantageous for plasma catalysis [36]. Since this pore-like discharge shows a geometric commonality to the circular shaped cavities of an array, this makes the micro cavity plasma array interesting for plasma catalysis.

In addition, strong electric fields seem to be mainly responsible for the asymmetric discharge characteristic in microplasma arrays as mentioned in the chapter before. The strong electric field accelerates electrons and ions along the cavity height in different directions depending on the respective half-phase. With focus on this, the following key-questions (KQ) are addressed in this chapter:

> **KQ** 2.1*: How large are these electric field strengths and through which parameters they can be controlled?*

> **KQ** 2.2*: Can a distinction in electric field strength be notified between both half-phases? If so, how can these electric field strengths be connected to the asymmetric discharge characteristic?*

Parts of these results have already been published in Dzikowski *et al. 2022 Plasma Sources Sci. Technol. 29 035028* [94].

## 5.1 Splitting and shifting effect

In this chapter, the electric field strengths are only estimated by exploiting the Stark shifting and splitting effect. This technique can be used since the expected electric field strengths of the MGA are strong enough to lead to a significant Stark shifting and splitting (electric field strength of about $70 \, \text{kV} \, \text{cm}^{-1}$ for an applied voltage of

400 V divided by dielectric thickness of 60 μm). A spectral resolution of about 1 nm can be achieved for the PGS according to figure 2.13.

It is useful to compare the discharge of the MGA with another discharge source that is operated under similar conditions (e.g. pressure and gas) and characterised by lower electric field strengths to identify the Stark shifting and splitting effect. Here, the comparison is made between the MGA and the COST reference jet [8] that can replace the MGA in the diagnostic setup. This device consists of two plane parallel electrodes separated from each other by a distance of 1 mm and tightened by glass plates around. Since the applied voltage of about 300 V drops mainly within the Debye sheath, a region without an electric field is expected in the core. However, this is not the usual case since the COST reference jet shows an ohmic mode at atmospheric pressure.

Figure 5.1 illustrates the recorded spectra of both devices with an integration time of 10 min over the complete excitation cycle. This long integration time is chosen due to the low intensity. The MGA (red solid line) is operated with a voltage amplitude of 600 V at a frequency of 15 kHz. The COST jet (black solid line) is operated with radio frequency (RF, 13.56 MHz) excitation at a dissipated power of 1 W. Its spectrum is recorded without collimator by putting the light fibre at a distance of 1.5 mm to the discharge. In both cases the helium flow is at 1 slm.

While in the COST jet only a single narrow line occurs at 492.19 nm (marked by a dashed black line), the spectrum of the MGA shows a different behaviour. Two broadened peaks are detected that are separated from each other by a distance of 0.24 nm. The left peak corresponds to all forbidden transitions while the right peak contains all allowed transitions.

It is also striking that the right peak appears to be strongly broadened. A possible reason is that further optical lines overlap with the helium transitions. In the spectrum of the COST jet, the first negative emission band system from ionised nitrogen ($\text{B}^2\Sigma_\text{u}^+$ $\rightarrow \text{X}^2\Sigma_\text{g}^+$) is visible in the wavelength range between 492.4 nm and 494 nm where the allowed helium transitions occur.

However, nitrogen can not play a significant role in this wavelength range in the MGA because more probable transitions around 495.79 nm (not shown here) of this nitrogen emission band do not occur [95]. Moreover, further dominant optical lines from helium or typical impurities such as oxygen or water are not visible in this wavelength range. Consequently, the broadened emission structure in the MGA can be assigned only to the allowed shifted helium transitions.

Due to the fact that the Stark effect is not observable in the COST jet, this plasma device is used in the following as an absolute wavelength reference for the electric field measurements. After each measurement, the absolute wavelength scale of the PGS is calibrated with the COST jet.
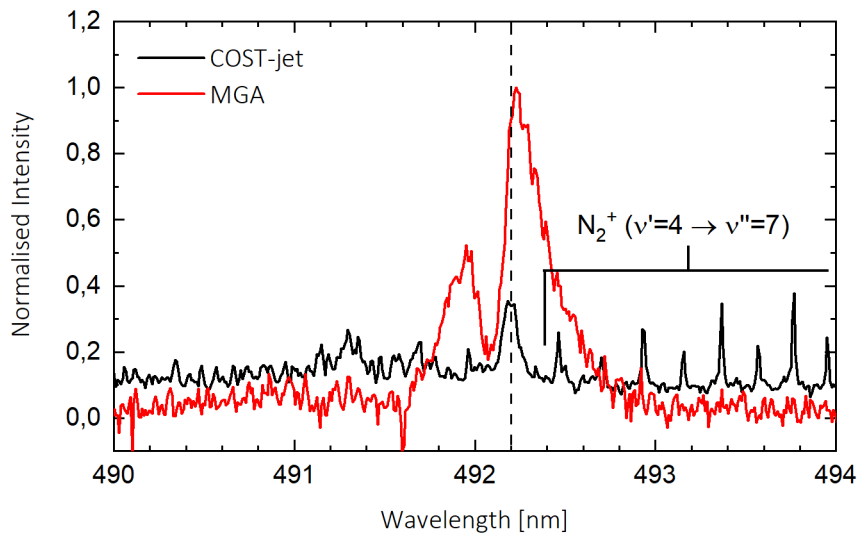
FIGURE 5.1: Recorded spectrum of the MGA (red) having $200\,\mu m$ cavities and COST reference jet (black). The MGA is operated with a voltage amplitude of $600\,V$ at a frequency of $15\,kHz$. The COST jet is operated with a power of about of $1\,W$. The integration time is set to $10\,min$ and the helium flow at $1\,slm$ in both cases.

## 5.2 Polarisation

As explained before in the fundamentals 2.3.3, the polarisation of radiation, its orientation to the electric field and the dependency on the magnetic quantum number are connected with each other. Kuraica and other authors took advantage of this to suppress the $\sigma$-polarised components [38, 48–52]. This results in less overlapping spectra and an easier subsequent analysis for determination of electric field strengths. On the other hand a polariser is responsible for a weaker intensity that is challenging for the faint helium transitions.

In the following, the role of the polariser on the spectrum of $200\,\mu m$ cavities will be investigated. For this purpose, a $0.8\,mm$ thin polarisation foil is inserted in the optical path between the light fibre and cavity structure. This polarisation foil has a transmission of only $42\,\%$. However, this had to be used since all other available polariser are too large to be integrated into the optical path. Its relative azimuthal angle to the cavity structure is varied afterwards. The MGA is operated at a voltage amplitude of $600\,V$ at a frequency of $15\,kHz$. The helium flow is set to $2\,slm$. The required integration time during IPP is set to $20\,min$. Figure 5.2 shows the normalised spectrum depending on the polariser settings. It is obvious that its integration (dotted line) as well as its relative orientation of $90\,°$ (dashed line) have no impact on the shape of the emission structure compared to a spectrum recorded without polariser (solid line). Only the intensity drops by $78\,\%$ (not shown here). This is also observed for all cavity diameters and during the DPP.
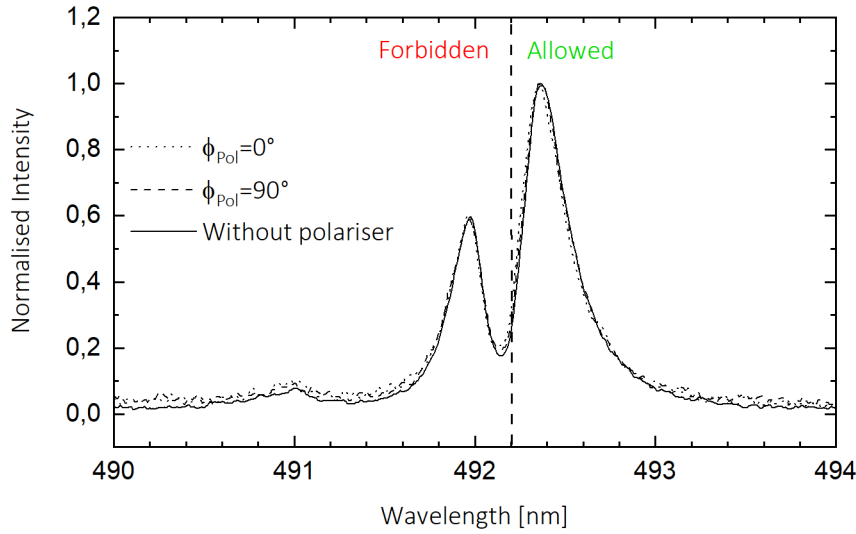
FIGURE 5.2: Recorded and normalised spectrum of the shifted and split 492.19 nm line depending on the polariser setting. This spectrum is recorded from 200 μm cavities during the IPP with an integration time of 20 min. The MCPA is operated at a voltage amplitude of 600 V at a frequency of 15 kHz. The helium flow is set to 2 slm. The polariser settings are i) without polariser (solid line), ii) with polariser (dotted line) and iii) its relative orientation of 90 ° to i) (dashed line).

This behaviour can be understood from the symmetric shape of the cavities and the dominant applied electric field inside. Figure 5.3 shows two cases that differ in the orientation of this electric field (black arrows). The left column describes the case that the applied electric field is perpendicular to the surface normal of the dielectric surface. Therefore, the electric field has only radial components resulting in only π-polarised radiation (red arrows) in the head-on observation.

By placing a polariser into the optical path, π-polarised components with the same orientation as the polariser can pass. Due to the rotational symmetry of the cavities, a rotation of the polariser has no impact.

The right column illustrates the situation if the applied electric field vector is parallel to the surface normal of the cavity. Thus, only circular polarised emission ($\sigma$, blue circles) leaves the cavities towards the head-on observation and π-polarised light is emitted in direction to the cavity walls. Since $\sigma$-polarised light can be regarded as a superposition of two 90 ° phase-shifted π-polarised components (blue arrows), these components can pass the polariser. As in the opposite case, rotation of the polariser has also no impact.

Since the applied electric field distribution within cavities is an overlap of radial and z-components and π- and $\sigma$-polarised emission differ in their wavelengths as the allowed [2-1]- and [1-1]-transition, no polarisation and no wavelength can be filtered out. In this way, all possible transitions have to be considered for determination of the
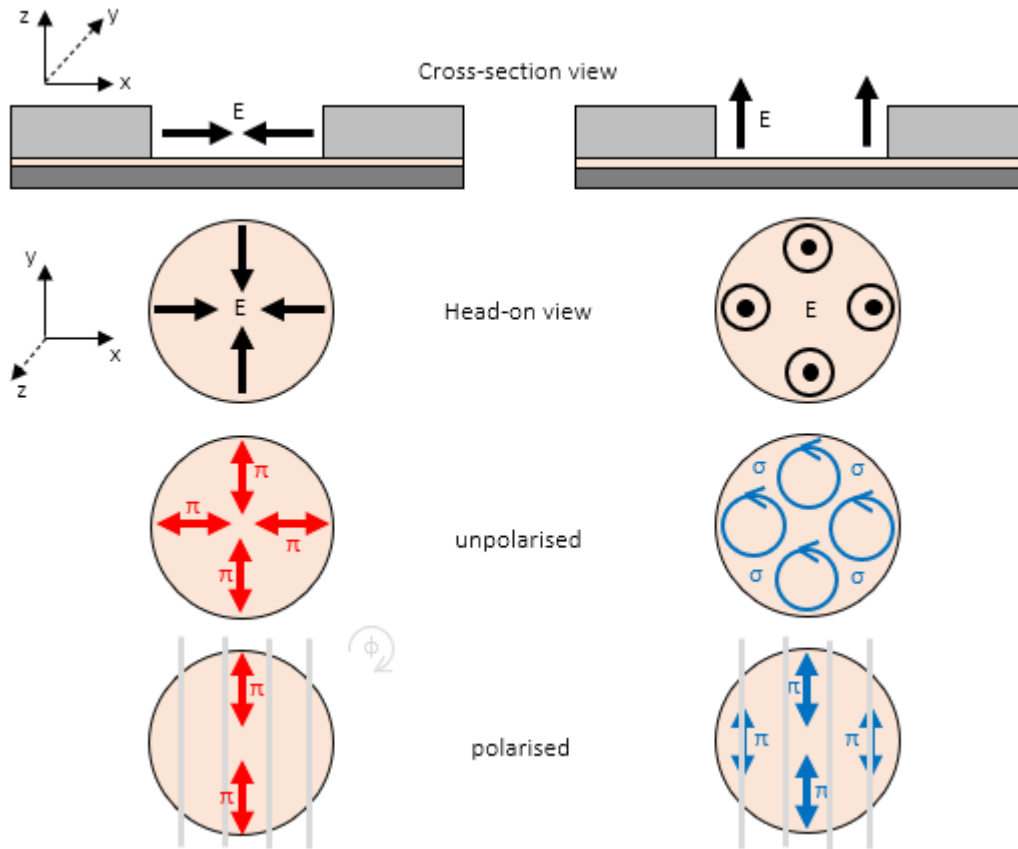
FIGURE 5.3: Schematic sketch of the polarised emission out of the cavities in two different orientation of the dominant electric field. The orientation is equal as in figure 3.2 and 3.3.

electric field. This is done by fitting a theoretical spectrum to the observed spectrum to separate all overlapping transitions. This is described in the following section.

## 5.3 Fitting procedure

The task of a fitting procedure is to separate all transitions in the emission structure to obtain displacements between them. These displacements can afterwards be transferred into electric field strengths by using the so-called allowed-forbidden method (see section 2.3.3). In comparison to previous works, the following fitting procedure has to consider the five allowed and forbidden transitions since the polariser does not suppress $\sigma$-polarised components.

This fitting procedure is based on the fact that an optical line can be described mathematically as a function of the wavelength $\lambda$. Generally, two descriptions are suitable as a simplification: a Gaussian $\mathcal{G}$ and a Lorentzian $\mathcal{L}$ function described in equation 5.1 and 5.2. Both descriptions depend on the intensity $A$, the central wavelength position $\lambda_0$ and the linewidth $\sigma$. This linewidth is connected to the full width of half maximum (FWHM) $\Delta\lambda$ as shown in equation 5.3.

$$\mathcal{G}(\lambda) = A \cdot \exp\left(-\ln(2)\left(\frac{\lambda - \lambda_0}{\sigma}\right)^2\right) \tag{5.1}$$

$$\mathcal{L}(\lambda) = \frac{A}{1 + \left(\frac{\lambda - \lambda_0}{\sigma}\right)^2} \tag{5.2}$$

$$\Delta\lambda = 2\sigma \tag{5.3}$$

Which of the two functions is applicable depends on the dominant broadening mechanisms. Since the resonance broadening described by a Lorentzian ($\Delta\lambda_{\mathcal{L}} = \Delta\lambda_{\mathrm{Res}} = 9.811 \times 10^{-2}$ nm) in equation 2.12 and the instrumental broadening combined with a Gaussian ($\Delta\lambda_{\mathcal{G}} = \Delta\lambda_{\mathrm{Instr}} = 1.562 \times 10^{-2}$ nm) in figure 3.9 show line broadening on a similar scale, both functions have to be combined. This can be done by a convolution of both functions resulting in a so-called Voigt profile $\mathcal{V}$. This convolution is described by equation 5.4 where $\tau$ is the displacement to the central wavelength position.

$$\mathcal{V}(\lambda) = (\mathcal{G} * \mathcal{L})(\lambda) = \int \mathcal{G}(\tau)\mathcal{L}(\lambda - \tau)d\tau \tag{5.4}$$

$$\Delta\lambda_{\mathcal{V}} = \sqrt{\Delta\lambda_{\mathcal{G}}^2 + \Delta\lambda_{\mathcal{L}}^2} = \sqrt{\Delta\lambda_{Instr}^2 + \Delta\lambda_{Res}^2} = 0.099\,\mathrm{nm} \tag{5.5}$$

However, this fitting approach is challenging due to its integral description and not practical for modelling. A mathematically simpler description is given by a so-called Pseudo-Voigt profile $\tilde{\mathcal{V}}$

$$\tilde{\mathcal{V}}(\lambda) = \alpha \cdot \mathcal{G}(\lambda, \lambda_0, A, \sigma) + (1 - \alpha) \cdot \mathcal{L}(\lambda, \lambda_0, A, \sigma) \tag{5.6}$$

that is only a linear combination of a Gaussian and a Lorentzian function. The contribution of both is expressed by $\alpha$ with $0 \leq \alpha \leq 1$. Since it is a mathematical approximation, the corresponding FWHM $\Delta\lambda_{\tilde{\mathcal{V}}}$ may not be calculated with equation 5.5 [96, 97]. Instead, a computer-modeled formula can be used given by

$$\Delta\lambda_{\tilde{\mathcal{V}}} = \left(\sum_{i=0}^{5} c_i \cdot \Delta\lambda_{\mathcal{G}}^{5-i} \cdot \Delta\lambda_{\mathcal{L}}^{i}\right)^{\frac{1}{5}} = 0.098\,\mathrm{nm} \tag{5.7}$$

The corresponding coefficients $c_i$ are listed in the following table

Since the deviation of the FWHM between the Voigt profile and the Pseudo-Voigt profile is about 1 %, this mathematical approximation is valid. As a result, equation

| $c_0$ | $c_1$ | $c_2$ | $c_3$ | $c_4$ | $c_5$ |
|---|---|---|---|---|---|
| 1 | 2.692 69 | 2.428 43 | 4.471 63 | 0.078 42 | 1 |

TABLE 5.1: Coefficients for equation 5.7 [96].

5.6 can describe an optical line. But to describe the complete emission structure, two aspects must be added: (i) The fit function has to consider all five allowed (indexed as A) and all five forbidden transitions (indexed as F). (ii) Discharges can take place in areas above or inside cavities where no or only small electric fields occur or the applied electric field is completely shielded. This results in a non-shifted and non-split 492.19 nm "field-free" contribution (indexed as ff) that must also be considered in the fitting procedure. In summary, the fit function has the following form

$$
\mathcal{F}(\lambda) = \sum_{i=1}^{5} \mathcal{V}_{Ai}(\alpha_{Ai}, A_{Ai}, \lambda, \lambda_{Ai}, \sigma_{Ai}) + \sum_{i=1}^{5} \mathcal{V}_{Fi}(\alpha_{Fi}, A_{Fi}, \lambda, \lambda_{Fi}, \sigma_{Fi})
$$
$$
+ \mathcal{V}_{ff}(\alpha_{ff}, A_{ff}, \lambda, 429.19 \,\text{nm}, \sigma_{ff})
$$
(5.8)

However, this fit function has in total 43 degrees of freedom leading to implausible solutions. To reduce the degrees of freedom, the following physical assumptions are made:

I) The first assumption is based on the three approximated line groups as illustrated in figure 2.13 in section 2.3.3. Since several transitions shift almost identically with the electric field strength, these can be combined to a single optical line. The first combined line contains all forbidden transitions with

$$
\{[0-0]_F^\pi, [0-1]_F^\sigma, [1-1]_F^\pi, [1-0]_F^\sigma, [2-1]_F^\sigma\} \rightarrow \lambda_{F,0,1,2} = \lambda_1
$$

The second combined line represenst the mean value of the following allowed transitions

$$
\{[0-0]_A^\pi, [0-1]_A^\sigma, [1-1]_A^\pi, [1-0]_A^\sigma\} \rightarrow \lambda_{A,0,1} = \lambda_2
$$

Its displacement (mean value) with respect to that of the first combined line is given by $\Delta\lambda_1 = \lambda_{A,0,1} - \lambda_{F,0,1,2}$. The third line is the following transition

$$
\{[2-1]_A^\sigma\} \rightarrow \lambda_{A,2} = \lambda_3
$$

The displacement to the first combined line is calculated with $\Delta\lambda_2 = \lambda_{A,2} - \lambda_{F,0,1,2}$.

II) It is assumed that all combined line shifts are caused by an unique electric field. This avoids that the combined lines and their relative displacements to each other shift differently. The correlation is given by equation 2.26.

III) Since all combined lines only shift by a few tenths of nanometer with respect to the field-free transition, the resonance broadening mechanism described in equation 2.12 does not change significantly. This means that all forbidden and allowed transitions can be described with identical linewidth $\sigma_i = \sigma$ and with a contribution between Lorentzian and Gaussian $\alpha_i = \alpha$.

By using these assumptions the final fit function $\mathcal{F}_{fin}$ contains only 8 instead of 43 degrees of freedom and is given by equation 5.9 where indices stand for the respective combined line or field-free component.

$$
\begin{aligned}
\mathcal{F}_{fin}(\lambda) = \mathcal{V}_1(\alpha, A_1, \lambda, \lambda_1, \sigma) + \mathcal{V}_2(\alpha, A_2, \lambda, \lambda_2, \sigma) + \\
\mathcal{V}_3(\alpha, A_3, \lambda, f(\lambda_1, \lambda_2), \sigma) + \mathcal{V}_{ff}(\alpha, A_{ff}, \lambda, 492.19\,\mathrm{nm}, \sigma)
\end{aligned}
\tag{5.9}
$$

This fit function provides the knowledge of $\lambda_1$ and lambda$_2$ which is necessary for the displacement $\Delta\lambda$ and finally for the electric field calculation as in equation 2.27. In this thesis, all illustrated electric field strengths are obtained by this fitting procedure.

An alternative fit function leading to almost equal electric field strengths ($\pm 3\,\mathrm{kV\,cm^{-1}}$) is given by equation 5.10. In this case the position of second and third combined lines depend on the central wavelength position of the first combined line. A disadvantage is that this procedure does not consider information of allowed transitions.

$$
\begin{aligned}
\mathcal{F}_{fin2}(\lambda) = \mathcal{V}_1(\alpha, A_1, \lambda, \lambda_1, \sigma) + \mathcal{V}_2(\alpha, A_2, \lambda, f(\lambda_1), \sigma) + \\
\mathcal{V}_3(\alpha, A_3, \lambda, f(\lambda_1), \sigma) + \mathcal{V}_{ff}(\alpha, A_{ff}, \lambda, 492.19\,\mathrm{nm}, \sigma)
\end{aligned}
\tag{5.10}
$$

In summary, physical assumptions and simplifications are made to establish a useful fitting procedure. Based on it, it is necessary to discuss how sensitive its performance and resulting electric field strengths are. This is done in the following subsection.

**Error analysis**

The top part of figure 5.4 shows an exemplary fitted spectrum of a discharge in 200 µm cavities and its composition of the three combined lines. The emission is accumulated over the whole DPP with an integration time of 10 min. The MGA is operated with a voltage of 600 V at a frequency of 15 kHz.

Despite the many used assumptions and simplifications, the measured spectrum is generally well reproduced by the fitting procedure. However, some differences up to

10 % and 5 % occur at the dip between forbidden and allowed components and at the flanks of the double peak structure. This is illustrated in the bottom part of figure 5.4.

Moreover, a second positive result is that the obtained electric field in this illustrated example is $27.18\,\mathrm{kV\,cm^{-1}}$ and therefore in the expected range. This value is well comparable with theoretical investigations on the SBA with inverted pyramidal cavities [98] and pore structures in DBD [36].

A further observation in this fitting example is that the ff-component is not detectable due to its weak intensity. This observation is also made for all other measurements in this thesis where the ff-component is either not detectable or has only a low intensity of about 2 % of the highest intensity peak. However, a correlation with the set operation parameters could not be found. Based on that, the fitting procedure can also be executed without the ff-component. A significant deviation of electric field strengths described in equation 5.9 is not noticeable and is in the range of about 5 %.

Although the fitting procedure reproduces the measured spectrum well and the obtained electric field strengths are in a reasonable range, the small differences and the missing ff-component in the fit and the quality of the electric field strengths have to be discussed under the following three aspects:

(i) The collimator captures the emission of all cavities. In case of the 200 µm cavities, the emission is integrated over 676 cavities and is not perfectly homogeneous over the whole array. Although the MGA shows a rather homogeneous and simultaneous ignition of all cavities and no wave-like discharge structure, it is still improbable that all cavities show the same electric field strength in spatial average. Therefore, the fitting procedure has the challenging task to fit the emission coming from different electric field regimes (cavities) only with a single electric field. This is not possible and the fit does not reproduce the complete measured spectrum and yields a cavity-averaged electric field strength.

(ii) Even more importantly, the spatial integration is achieved not only over a large number of cavities, but over the entire volume of each cavity. It is already known from the simulation for the SBA that strong gradients in the electric field occur due to the cavity geometry [98]. The same can be expected for the MGA. Although the electric field had not been simulated yet, a first estimation can be obtained from the analysis of a special discharge channel [80].

This channel consists of two nickel electrodes that formed a gap width of about 120 µm and are attached to the carrier. The gap width can also be varied. Figure 5.5a) shows this setup. The special feature of this channel is that its cross-section can be compared with the cross-section of a single cavity of the MGA along the cavity center in experiments and simulations. In this comparison, the gap width corresponds to the cavity diameter.

Figure 5.5b) illustrates exemplary the two-dimensional applied electric field distribution along the cross-section of the channel with a gap width of $200\,\mu m$ calculated by COMSOL Multiphysics 5.5. The applied voltage is set to $600\,V$. The left and right axis represent the nickel electrode edge while the x-axis stands for the dielectric edge. In the following, it is assumed that this cross-section also corresponds to the cross-section of a single cavity.

It is obvious in figure 5.5b) that the electric field strengths vary depending on the location along the cross-section. While the electric field strength is about $10\,kV\,cm^{-1}$ at the cavity opening on top, it increases in direction to the boundary edge between dielectric and nickel electrode. At this boundary edge, electric field strengths up to $200\,kV\,cm^{-1}$ are calculated.

Since the detection setup is not capable of resolving this inhomogeneous electric field distribution, the fitting procedure must again deal with emissions originating from different regimes of strong electric field strengths. This finally leads to a deviation between the fitted and measured spectrum.

A further observation from figure 5.5b) is that the applied electric field strengths higher than $15\,kV\,cm^{-1}$ exist everywhere along the cavity cross-section. It can be assumed that this is valid for the whole cavity volume due to the rotational symmetry. This can explain why the ff-component is almost not visible in the fit since no field-free region is present. The only regime where the ff-component can come from is either above the cavity volume (outside the cavity) or in areas where the applied electric field is shielded by charge carriers. This point is discussed later in this thesis.

(iii) The third point that can be responsible for the deviation between measured and fitted spectrum is the combination of the applied triangular voltage waveform excitation and the half-phase integrated detection. Based on it, the emission is averaged over a time where the applied voltage and therefore the applied electric field within the cavities changes.

However, it is possible to measure the electric field strengths time-resolved while the cavity- and spatial-integration is kept unchanged due to technical aspects and low emission intensity. This time dependence is discussed in the following section where two different time resolutions are presented.

**Summary**

The electric field strengths are high enough in the cavity volume to detect the Stark shift. Since the polariser cannot suppress $\sigma$-polarised components, the fitting procedure had to be modified in comparison to previous works dealing with this technique. Despite many physical simplifications and assumption, the fitting procedure provides reasonable and comparable electric field strengths to geometrically similar devices.
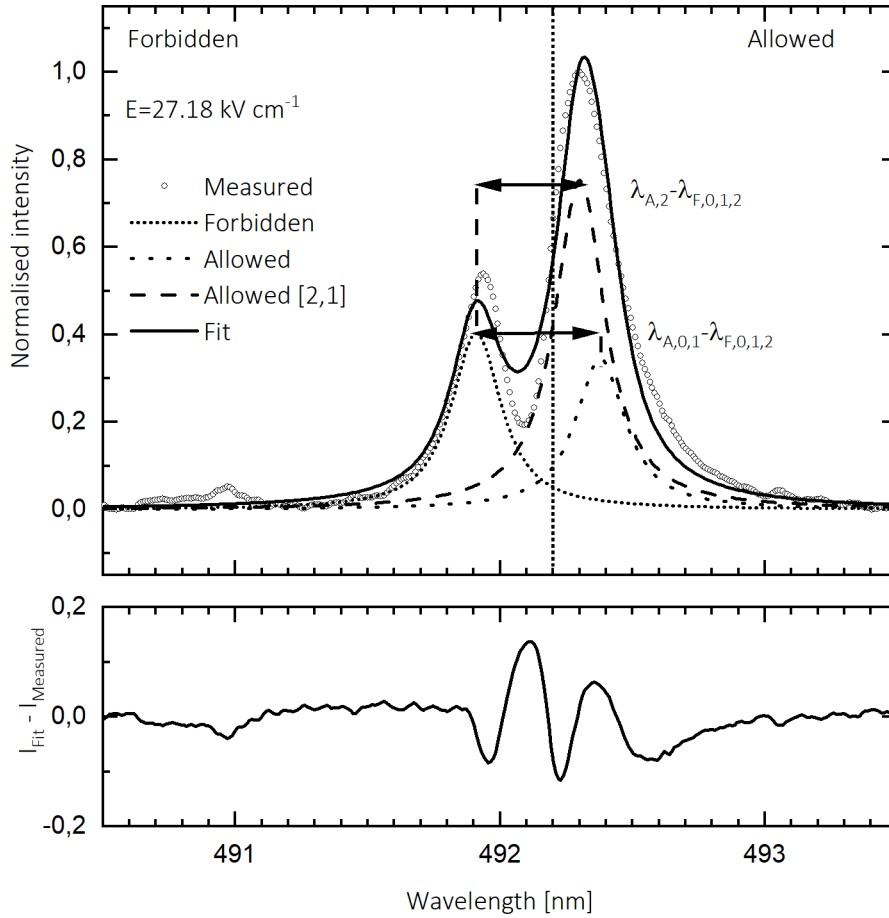
FIGURE 5.4: Example of a fit (solid line) on a measured spectrum (circles) detected on the 200 μm cavities during the DPP [94]. The nickel-grid was operated with a voltage of 600 V at a frequency of 15 kHz. The fit consists of the allowed (pointed and dashed line) and forbidden (short pointed) transitions divided in their $\pi, \sigma$- and $\sigma$- components.

## 5.4 Time-resolved measurements

In addition, temporal effects can also significantly influence the fitting procedure next to the spatial arguments due to the triangular waveform excitation. An increasing voltage over time leads to a higher applied electric field in the cavities and thus to overlapping electric fields within a half-phase (IPP or DPP).

However, the time-resolution for such time-resolved measurements is limited by the relative intensity of the used lines. As mentioned before, the 492.19 nm and 492.06 nm lines show a low intensity in general. Therefore, the time-resolved measurements are done with 200 μm cavities showing the highest intensity of all cavity structures. The reactor is operated with a voltage amplitude of 700 V at a frequency of 15 kHz close to its maximum power (800 V, 15 kHz) in order to reach intense emission without
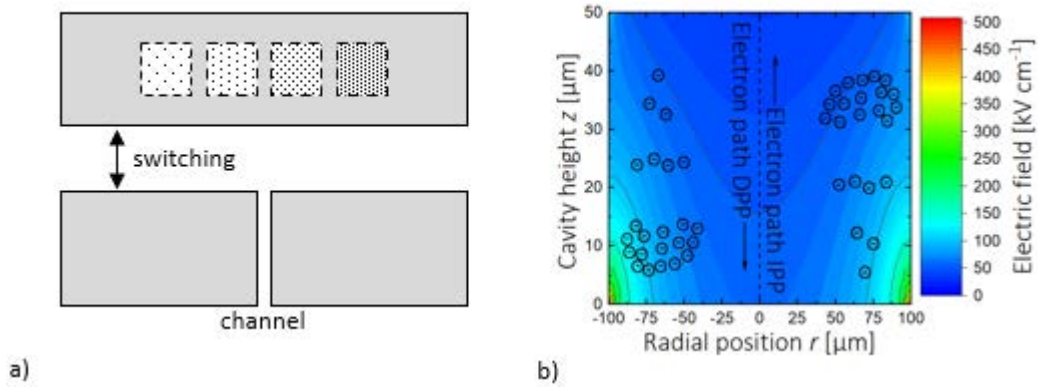
FIGURE 5.5: a) Sketch of the nickel electrode containing four different cavity structures and of two rectangular nickel electrodes forming a micro-channel [80]. Both electrode configurations can be switched and applied in the reactor system. b) Colour coded map (high values in red, low values in blue) of the applied electric field distribution within a cavity (channel) having a diameter of 200 μm in cross-section view. The applied voltage is at 600 V. This distribution is calculated with COMSOL Multiphysics 5.5. The left and right y-axis represent the nickel electrode edge. The x-axis stands for the dielectric.

thermally overloading the reactor. Since the cycle duration and emission structures are 30 μs long as shown in figure 4.9, time-resolutions of 1 μs and 500 ns are chosen to get time-resolved electric field strengths.

### 5.4.1 Time-resolution of 1 μs

Figure 5.6 gives the temporal trend of electric field strengths (blue squares) over the complete excitation cycle (black line) with a time-resolution of 1 μs. The corresponding normalised PMT signal (red line) is also illustrated to compare the electric fields with the discharge operation.

Several pieces of information can be derived from this figure: (i) The electric field strengths differ significantly between IPP and DPP. While the IPP shows values of about $25\,\mathrm{kV\,cm^{-1}}$, around $30\,\%$ higher strengths are detected in DPP. In this phase the electric fields are between $30\,\mathrm{kV\,cm^{-1}}$ and $35\,\mathrm{kV\,cm^{-1}}$. This observation is also visible in all following electric field measurements. In general, the temporal changes during the complete excitation are about $5\,\mathrm{kV\,cm^{-1}}$ and negligible in comparison to spatial deviations within a cavity as shown in figure 5.5b). (ii) The electric field trends of IPP and DPP seem to differ. In DPP, a slow decay is detectable while the trend is rather constant in IPP. (iii) No drop in electric field strengths is visible during the first discharge pulse as one would expect a shielding due to generated charged particles. This concerns the ranges between $55\,\mu s$ and $60\,\mu s$ in IPP and $26\,\mu s$ and $32\,\mu s$ in DPP where a strong increase of the PMT-signal can be observed.

These observations can be understood in a simple picture based on the structure of the

MGA, its asymmetric discharge characteristic as already explained in 4.3 and time-dependent generated charge distribution effects. Furthermore, it has to be considered that the detected emission is spatially-integrated. The excitation is primarily caused in first approximation through electron impact excitation.

The temporally rather constant electric field strengths during both phases are in good agreement with the operation principle of a DBD. This kind of discharge gets extinguished when the charged particle density on the dielectric becomes too large. However, the discharge can be reignited if the required voltage for ignition within the cavity is reached again by the increasing voltage excitation (applied electric field) or by electric fields generated through charged particles in volume or on surfaces [19]. These ions have a great impact on the discharge which is shown in figure 5.6 where the discharge already ignites before zero-crossing of the applied voltage is reached. Due to the permanent resetting of the gap voltage (electric field) in all single cavities, a certain average electric field can be established that gets additionally smoothed by the superposition of contributions from all cavities.

Secondly, the structure of the MGA and its bipolar voltage excitation cause asymmetric discharge characteristics leading to a different direction of movement of electrons and different electric fields.

As a reminder, in this asymmetry, electrons are accelerated towards the dielectric surface into the cavity during DPP. There, they can excite helium atoms mostly in a higher electric field region. In contrast to this, electrons get accelerated during IPP towards the cavity opening where rather low electric field strengths occur. This is illustrated in figure 5.5c) where the applied electric field distribution is depicted. The strongest electric fields appear at the edge between dielectric and nickel electrode. The electric field decreases in direction to the cavity opening. Finally, electrons cannot disappear from the dielectric surface after finishing their movement during DPP since they cannot flow away to the nickel-grid. As a result, an electron surface charge distribution is produced over time that might increase during the time-dependent excitation and causes a shielding of the applied electric field. Due to that, the measured electric field strengths must decrease in this phase.

During IPP, the electrons move in direction to the bare nickel electrode and disappear there. An electron surface charge density cannot built up. However, produced ions can move to the dielectric and cause the same effect as the electrons during DPP but their mobility is smaller than of the electrons. This was already explained in detail in section 4.4.

The fact that the electric field does not drop during ignition is discussed in the following subsection dealing with the measurements with a time-resolution of $500\,\mathrm{ns}$.
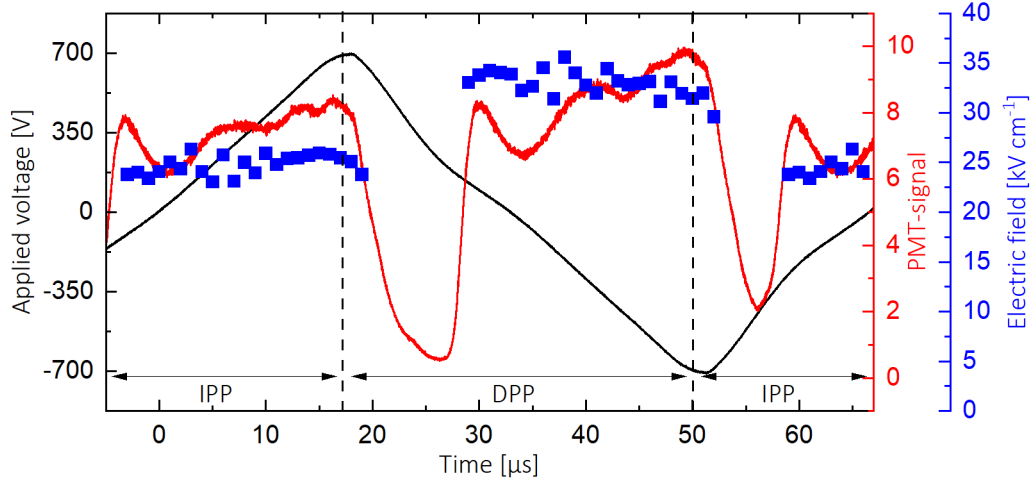
FIGURE 5.6: Time-resolved electric field strengths (blue squares) and PMT signal (red line) depending on applied excitation (black line) having a voltage amplitude of 700 V and a frequency of 15 kHz [94]. This measurement is executed on 200 µm cavities with a time-resolution of 1 µs and an integration time of 5 min.

### 5.4.2 Reproducibility and time-resolution of 500 ns

This interval is additionally investigated with a higher time resolution of 500 ns illustrated in figure 5.7 to confirm the constant electric field strengths during the ignition phase. Recordings in an interval in which the PMT signal (red line and axis) is less than 50 % of the maximum intensity cannot be analysed due to a poor signal-to-noise ratio. In general, higher time-resolutions are responsible for larger uncertainties in electric field strengths. Moreover, it must be taken into account that errors can also occur during this cavity- and location-integrated measurement method. Therefore, the measurements are performed three times at identical operation conditions with a time-resolution of 500 ns to discuss the errors and reproducibility. The cavity diameter, the applied voltage and frequency are kept constant with respect to the measurement with 1 µs time-resolution. However, the integration time is doubled to 10 min to get a sufficiently good signal-to-noise ratio while improving the time resolution.

The electric field strengths (blue squares, blue axis) are in a good agreement with the values of the 1 µs time-resolution. During the IPP shown in 5.7a), it can be seen within the error bars that the electric field first increases up to a value of about $27 \, \text{kV cm}^{-1}$ and then begins to drop just before the maximum PMT-signal is reached.

However, the DPP illustrated in 5.7b) does not show this effect although the shielding process should be more probable due to the higher electron mobility in this phase. Hence, it is assumed that a high surface charge density is present in each case which strongly influences the applied electric field.

The reproducibility of the electric field strength can be discussed based on different measurement series, which are shown exemplary in figure 5.7a). Here the electric field strength is shown for three different measurements and its average of all measurements. Despite the high temporal resolution of 500 ns and some assumptions in the fitting procedure, the relative error between the single measurements is around 15 %. As expected, the relative error decreases in average to about 9 % in case of half-phase resolved measurement due to a better signal-to-noise ratio.

These time-resolved measurements show that the electric field strengths do not change strongly with time. For this reason, the following measurements are executed in a half-phase resolution. This allows measurements without thermally stressing the MGA for a longer time period due to long integration times. Hence, further investigations on the distinction of the electric field between IPP and DPP and the producing volume and surface charge density can be made. An additional point is that parameter variations can be executed in a more practicable way. This makes it easier to investigate the effects already mentioned and to find the responsible adjusting screws for controlling the electric field.
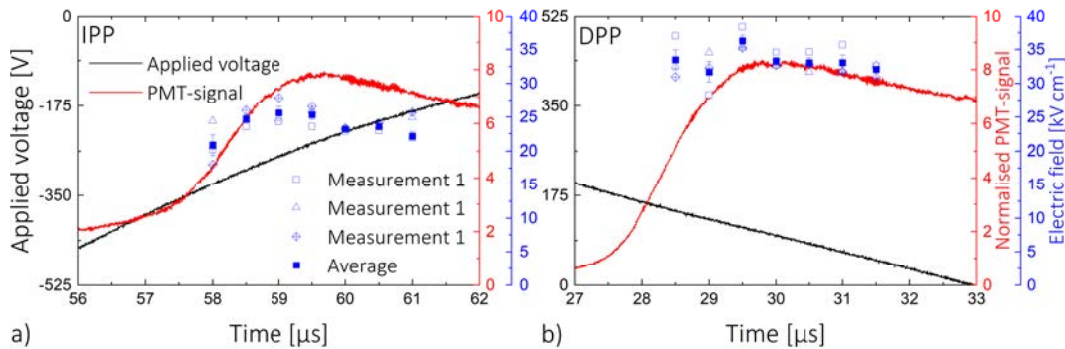


FIGURE 5.7: Time-resolved electric field strengths (full blue squares, blue axis) and PMT signal (red line, red axis) depending on applied voltage excitation (black line) with a voltage amplitude of 700 V and a frequency of 15 kHz during a) IPP and b) DPP. This measurement is executed on 200 µm cavities with a time-resolution of 500 ns and an integration time of 5 min.

## 5.5 Parameter variation

### 5.5.1 Cavity diameter

In general, a MGA is characterised by its cavity diameter or cavity dimension. This geometry has a great impact in the operation characteristics in a MGA which was already investigated in an experiment dealing with four different silicon-based sub-arrays in a $2 \times 2$ pattern [14].

Figure 5.8 shows the dependence of the electric field strengths on the cavity diameter between 100 µm and 200 µm for IPP (black symbols with dotted line) and DPP (red

symbols with dotted line). The metal-grid array is operated with an applied voltage of 600 V at a frequency of 15 kHz. The integration time is 25 min.
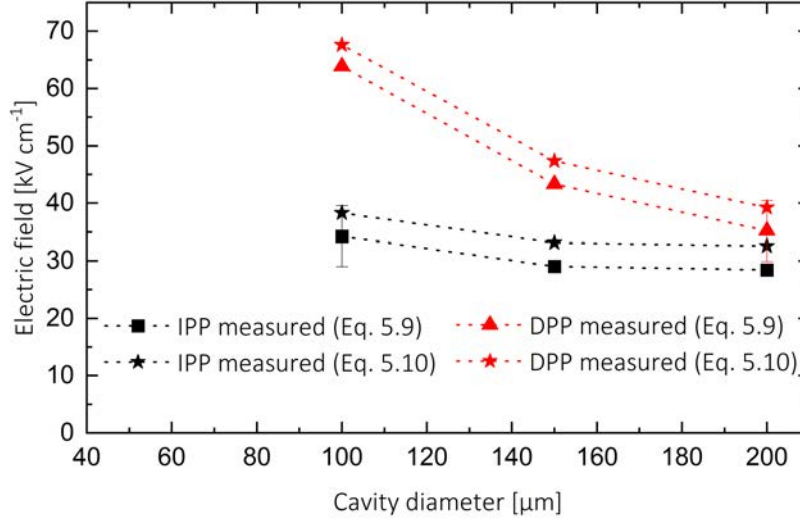


FIGURE 5.8: Measured electric field strengths depending on the cavity diameter during IPP (black) and DPP (red) [94]. The voltage amplitude is set to 600 V and the frequency is kept constant at 15 kHz. To illustrate differences obtained through the fitting procedure, the measured electric fields of equation 5.9 and 5.10 are presented.

The field strengths for the 50 μm cavities are not evaluated since the corresponding spectra could not be analysed. This is can be explained by the observation that not all 50 μm cavities are igniting as already explained in subsection 3.2.2. In conclusion, the poor signal-to-noise ration does not allow to deploy the Pseudo-Voigt fit procedure.

As described in 5.3, two possible fitting procedures are available for determining the electric field strengths: i) the allowed-forbidden method (equation 5.9) and ii) the method where just the shifting of the forbidden transitions is taken into account (equation 5.10). The result of both fitting procedures is shown in figure 5.8 to get an estimation how large the influence of the fitting procedure on the electric field strength is. As expected, both fitting procedures lead to the same trend. However, they differ in their absolute values of about $4 \, \text{kV} \, \text{cm}^{-1}$ which is assumed as a fitting error $\Delta E_{fit}$. The statistical error $\Delta E_{stat}$ is determined by 3 measurements to $3 \, \text{kV} \, \text{cm}^{-1}$. The total error $\Delta E_{tot}$ of the allowed-forbidden method is estimated with

$$\Delta E_{tot} = \sqrt{\Delta E_{fit}^2 + \Delta E_{stat}^2} = 5.3 \, \text{kV} \, \text{cm}^{-1} \tag{5.11}$$

and drawn as an error bar for some points.

Concerning the electric fields, it is obvious that it increases with smaller cavity diameter in both phases as previously expected. This agrees with the simulation

dealing with an engraved pore in a DBD [36]. During DPP (red triangles dotted line), a decrease from about $65\,\text{kV}\,\text{cm}^{-1}$ to $35\,\text{kV}\,\text{cm}^{-1}$ with larger cavities takes place. A weaker effect is noticeable during IPP (black squares dotted line) where the electric field decreases from about $35\,\text{kV}\,\text{cm}^{-1}$ to $30\,\text{kV}\,\text{cm}^{-1}$. As a result, both field strengths seem to approach each other with larger cavity dimensions. These values are in a good agreement to the values measured in the time-resolved investigations.

As for the different electric fields between IPP and DPP, the asymmetric discharge structure and electric field distribution within the cavity can also explain the stronger cavity diameter dependence during the DPP. In this phase, the electric field rises by about $85\,\%$ while an increase of only $20\,\%$ takes place during IPP by halving the cavity diameter. A decrease in cavity diameter leads to an overlap of the high electric field regions at the boundary edge between dielectric and nickel electrode as already shown in figure 5.5b). As a result electrons move into a higher electric field region and excite helium atoms there. Since the applied electric field inhomogeneity does not occur at the cavity opening, the IPP is less influenced by a diameter scaling.

### 5.5.2 Pressure

Plasma enhanced catalysis is just reasonable if the discharge is operated at atmospheric pressure as vacuum and pump technology is too expensive on an industrial scale. However, it is useful to investigate the pressure dependence in detail because it has an impact on the global discharge characteristic. It is known from previous measurements that the radial emission profile within the cavities also changes with pressure [17] and could thus changes the effective interaction region between discharge and catalytic surface.

To investigate the electric field dependence on pressure, the single MGA containing cavities with a diameter of $150\,\mu\text{m}$ is operated in the vacuum chamber as described in figure 3.11 in section 3.5. The pressure is varied from $400\,\text{mbar}$ to $900\,\text{mbar}$. The voltage amplitude is set to $600\,\text{V}$ at a frequency of $15\,\text{Hz}$. The integration time is $10\,\text{min}$.

As can be seen in figure 5.9 the measured electric field strength increases with rising pressure in both half-phases. While in IPP (black squares, dotted line) the electric field rises from $17\,\text{kV}\,\text{cm}^{-1}$ to $30\,\text{kV}\,\text{cm}^{-1}$, in DPP (red triangles, dotted line) the electric fields increases from $32\,\text{kV}\,\text{cm}^{-1}$ to $65\,\text{kV}\,\text{cm}^{-1}$.

A parameter that strongly depends on the pressure and may explain the increasing trend of electric field strengths is the mean free path. This parameter decreases with higher pressure and electrons are not been likely to gain the required energy for ionisation and excitation of helium atoms. As a consequence, the discharge is more concentrated along the boundary edge between nickel-grid and dielectric surface where high electric field strengths are located and from where the emission is mostly detected.

This matches with observations made in SBA where the discharge moves and contracts to the cavity edge (high electric field regime) when the pressure is increasing [17].

All in all, a larger interaction area between the discharge and the catalytic surface might be rather realised in the low pressure regime. This is also supported by the fact that more ionised species are produced in this regime which are finally the interacting particle.
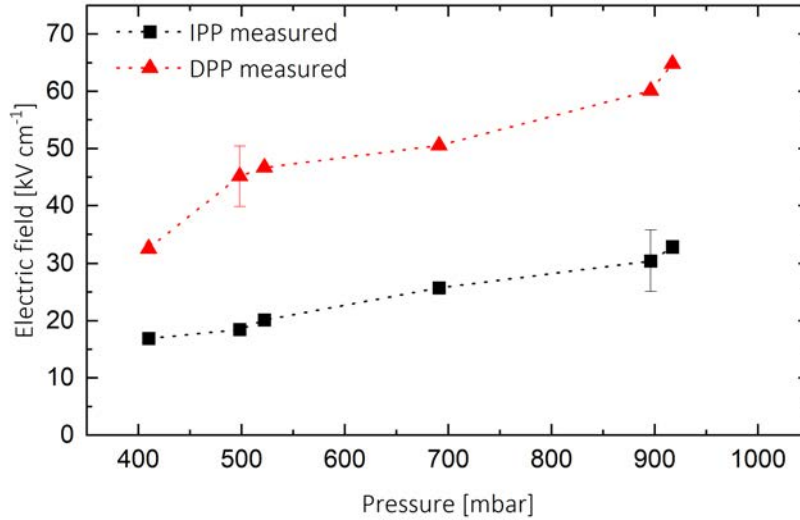


FIGURE 5.9: Measured electric field strengths depending on the pressure for IPP (black squares, dotted line) and DPP (red triangles, dotted line) [94]. The single MGA with 150 μm cavities is operated in the vacuum chamber as described in 3.5. The voltage amplitude is set to 600 V at a frequency of 15 Hz. The integration time is 10 min.

### 5.5.3 Voltage variation

A parameter that has a direct influence on the magnitude of the applied electric field distribution and is very practical to vary by the function generator is the applied voltage. Zhang et al. investigated theoretically its influence on the DBD configuration having an engraved pore in one of the dielectrics [36]. They observed that the electric field inside the pore increases with higher applied voltages.

Here, the electric field is measured depending on the applied voltage between 400 V and 800 V shown in figure 5.10 to support the theoretical results. The frequency is kept constant at 15 kHz. The integration time is set to 15 min.

Figure 5.10a) shows that a doubling of the amplitude does not cause a huge change of the electric field strengths for the 200 μm cavities. During DPP (red triangles, red dotted line) the electric field drops from about $39\,\mathrm{kV\,cm^{-1}}$ to $32\,\mathrm{kV\,cm^{-1}}$ while it stays rather constant at $28\,\mathrm{kV\,cm^{-1}}$ during IPP (black squares, black dotted line).

While for these 200 μm cavities the change is rather small, the same variation executed for 100 μm cavities shows a larger difference between IPP and DPP. This is depicted in figure 5.10b). In this case the electric field strengths show clearly a decreasing trend for both half-phases. In IPP the electric field has a value of $35\,\mathrm{kV\,cm^{-1}}$ at $400\,\mathrm{V}$ and drops by $15\,\%$ within the voltage increase. A similar decrease is noticeable during DPP where the electric field drops from $70\,\mathrm{kV\,cm^{-1}}$ to $60\,\mathrm{kV\,cm^{-1}}$.

This measurement supports the good reproducibility that is reached between the parameter variations. By taking the measured field strengths at $600\,\mathrm{V}$ of the 100 μm and 200 μm cavities into account, these are in good agreement with values obtained in the cavity diameter variation under an applied voltage of $600\,\mathrm{V}$ shown in figure 5.8.
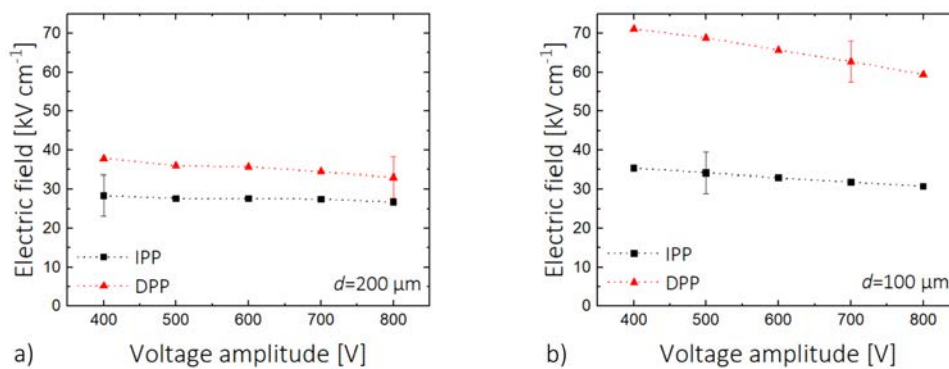


FIGURE 5.10: Measured electric field strengths depending on the applied voltage amplitude for a) 200 μm and b) 100 μm cavities during IPP (black squares, black dotted line) and DPP (red triangles, red dotted line) [94]. The frequency is kept constant at $15\,\mathrm{kHz}$. The integration time is $15\,\mathrm{min}$.

These measured trends are in a good agreement with the physical picture based on a built up charge distribution as discussed for the time-resolved measurement before in 5.4.1. A higher voltage increases the power coupled into the discharge and yields higher ionisation rates (higher electron and ion densities). This is confirmed by figure 5.11a) showing the normalised integrated intensity of 200 μm cavities which is measured at identical operation parameters as the electric field measurements. It is obvious that a higher applied voltage leads to an increasing intensity generated by a higher amount of excited particles in both half-phases. Therefore, it can also be assumed in the approximation that the number of ionisation events also rises resulting in a more effective shielding.

This shielding effect of the applied electric field through produced charges can be explained by considering the ignition voltage as a function of the applied voltage illustrated in figure 5.11b).

It is observable during the increasing potential phase that an applied voltage amplitude of $500\,\mathrm{V}$ needs to be set to reach the ignition voltage of $100\,\mathrm{V}$ while the ignition voltage is about $-300\,\mathrm{V}$ at an applied voltage amplitude of $800\,\mathrm{V}$. This means that the ignition
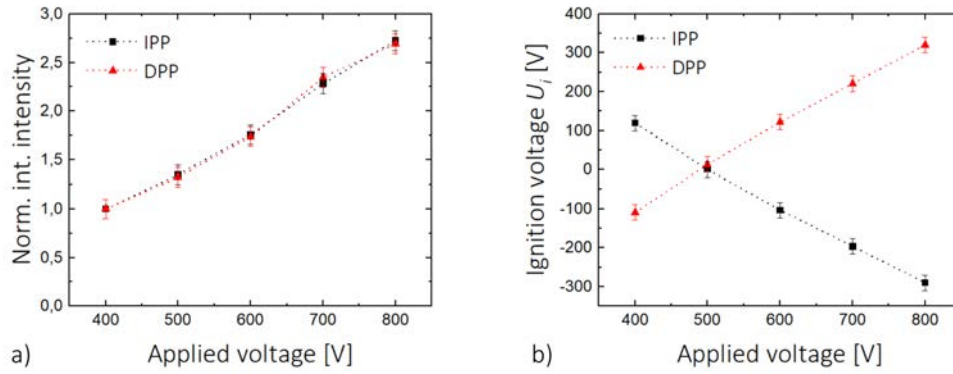
FIGURE 5.11: Normalised integrated intensity (a) and ignition voltage (b) of 200 μm cavities depending on the applied voltage amplitude for IPP (black squares, black dotted line) and DPP (red triangles, red dotted line). The frequency is kept constant at 15 kHz. The error bars are determined by statistical deviations of 3 measurements.

timing shifts from the time span after the zero-crossing point to the time span before. The zero-crossing point describes the moment in time, where the applied voltage waveform excitation transits the value of 0 V. In case of the IPP, the polarity of the applied voltage changes from minus to plus. The identical effect also takes place with the opposed algebraic sign of the ignition voltage during the decreasing potential phase. The polarity of the ignition voltage changes from plus to minus.

This effect of the ignition timing transition is based on the interaction between the electric field applied to the electrodes and an electric field generated by residual charges. A discharge can only ignite before zero-crossing if the required ignition voltage is supported by surface or volume charges that remain after the discharge in the previous half-cycle. Since the nickel electrode is not covered by a dielectric, charged particles disappear there while they remain on the dielectric surface. In reverse, this means that these generated surface or volume charges counteract the applied electric field in the half-phase before and the effective electric field within the cavity is shielded.

Due to the fact that the charged particle density rises with increasing voltage amplitudes, the drift current onto the dielectric also increases. This drift current is given by

$$j_{i(e)}^{d} = n_{i(e)} v_{i(e)}^{d} \tag{5.12}$$

and depends on the respective electron and ion density $n_{i(e)}$ and its drift velocities $v_{i(e)}^{d}$.

In conclusion, the applied electric field strength generates a high number of electrons and ions and both are able to shield the applied electric field in the respective half-phase.

### 5.5.4 Excitation

As explained in 3.3, the MGA is typically operated with a triangular voltage waveform excitation. However, it is known from other measurements that an operation with a square voltage waveform excitation leads to higher intensities and a more peak-structured emission (not shown here).

Thus, the phase-resolved electric field strength of the 200 µm is investigated depending on the applied excitation form. This is illustrated in figure 5.12. The voltage amplitude of all excitations is set to 600 V at a frequency of 15 kHz. The integration time is 15 min.

No significant changes between all excitation forms take place in general. However, a small deviation of about $2\,\text{kV}\,\text{cm}^{-1}$ during IPP (see figure 5.12a)) and DPP (see figure 5.12b)) is noticeable between similar sinusoidal and triangular excitation and square excitation.

This effect can be explained by considering the average voltage $U_{avr}$ during one quarter of the excitation where the discharge mainly occurs in the respective half-phase. It is calculated with

$$U_{avr} = \frac{4}{T} \int\limits_0^{T/4} U(t)dt \tag{5.13}$$

and depends on the applied voltage waveform $U(t)$ and the cycle duration $T$. These averaged voltages are also shown in figure 5.12 and can be well compared with the electric fields measured in the voltage amplitude variation on 200 µm cavities as illustrated in figure 5.10a). In both measurements, a doubling of the voltage amplitude or average voltage causes slowly decreasing electric field strengths. Moreover, this effect is stronger during the DPP in both measurements.

The reason for the drop in the electric field is again assumed to be the shielding caused by more and more generated electric charges.

In conclusion, the excitation waveform is also a parameter to adjust the internal electric field inside the cavities. For plasma catalysis, the triangular voltage waveform excitation can be the best adjustment since the largest amount of charged particles is produced leading to the best shielded internal electric field.

### 5.5.5 Frequency variation

The last parameter varied in this thesis is the frequency of the periodic excitation. As mentioned above the decrease of the electric field in dependency on the applied voltage is explained by electric shielding caused by surface charges that are deposited on the dielectric. To control the number of these residual charges surviving from
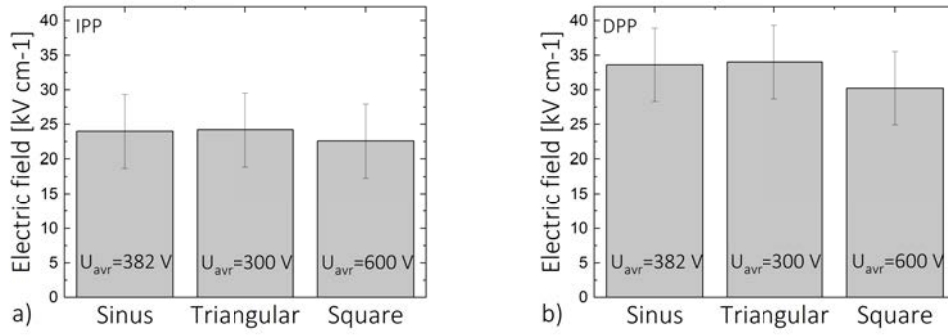
FIGURE 5.12: Measured electric field strengths depending on applied voltage excitation during a) IPP and b) DPP. The frequency is kept constant at 15 kHz. The applied voltage amplitude is set to 600 V. The electric field is measured on the 200 μm cavities. The integration time is 15 min.

discharge pulse to discharge pulse, the frequency is varied as it controls the time duration between this charge deposition.

Therefore, the electric field is analysed depending on the frequency range between 5 kHz and 25 kHz on the 200 μm cavities. Frequencies out of this range cannot be examined due to the amplifier's limitations. The corresponding voltage amplitude is set to 600 V. The integration time is kept constant with 15 min.

As can be seen in figure 5.13 an increasing frequency results in decreasing electric field strengths. During the IPP (black squares, black dotted line) the field drops from $32\,\mathrm{kV\,cm^{-1}}$ to $27\,\mathrm{kV\,cm^{-1}}$ while it decreases from $38\,\mathrm{kV\,cm^{-1}}$ to $32\,\mathrm{kV\,cm^{-1}}$ in the opposite phase.

In a simple approach, an increasing frequency is also responsible for a higher coupled power into the discharge causing an increasing electron and ion density. These charges shield the applied electric field as it was seen before for the voltage variation. It can be further explained by an accumulation of surface and volume residual charges from the previous half-phase and can therefore promote the initial discharge conditions for the subsequent discharge. This can be done in two different ways.

(i) The initial conditions of the IPP are affected by the end of the DPP where electrons are accelerated to the dielectric and cannot disappear there. In this time, ions drift to the nickel electrode and get lost. The number of electrons on the dielectric leads to an increase of the gap voltage within the cavity that leads to the same shielding effect as in the voltage variation (higher electric field → higher ionisation rate → higher charge density → higher shielding). Additionally, these electrons serve as initial electrons for a multiplication event during ignition similar to a Townsend avalanche which leads to an even higher electron density that shields the occurring electric field.

(ii) The beginning of the DPP is influenced by the IPP before where electrons drift to the nickel electrode and ions can be captured on the dielectric. Since these ions cannot be multiplied in a Townsend-like avalanche due to their low mobility, they serve only as an amplification of the internal electric field. This would also lead to the same effect as was seen before for the voltage variation (higher electric field → higher ionisation rate → higher charge density → higher shielding).
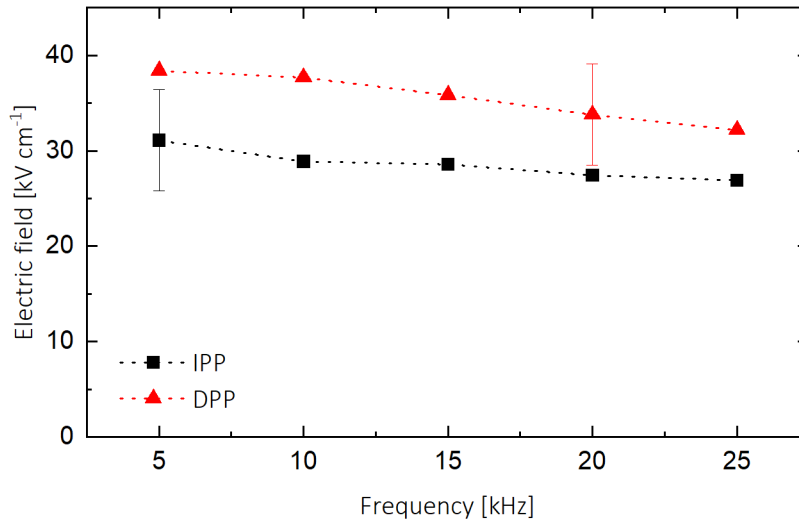


FIGURE 5.13:   Measured electric field as a function of the applied frequency during IPP (black squares) and DPP (red triangles) [94]. The cavities have a diameter of $200\,\mu m$ and the voltage amplitude is set to $600\,V$.

**Summary**

The electric field was determined depending on all variables and their different variation possibilities. Especially, the bipolarity of excitation and the cavity dimensions show a strong impact on the field strengths. All of these variations show good reproducibility and agreed well with each other regardless of the time resolution used for the measurements. In addition to the applied electric field distribution within the cavity, generated charge distributions seem to possess an influence on the electric field.

## 5.6   Modelling of electric field strengths

As shown before the electric field can be controlled by numerous operation parameters. This raises the question which processes take place in the cavities and how these are responsible for the measured electric fields. A complete theoretical model to explain these processes, taking into account the temporal and spatial dependencies in this geometric structure, would be very complex and could only be realised at great expense.
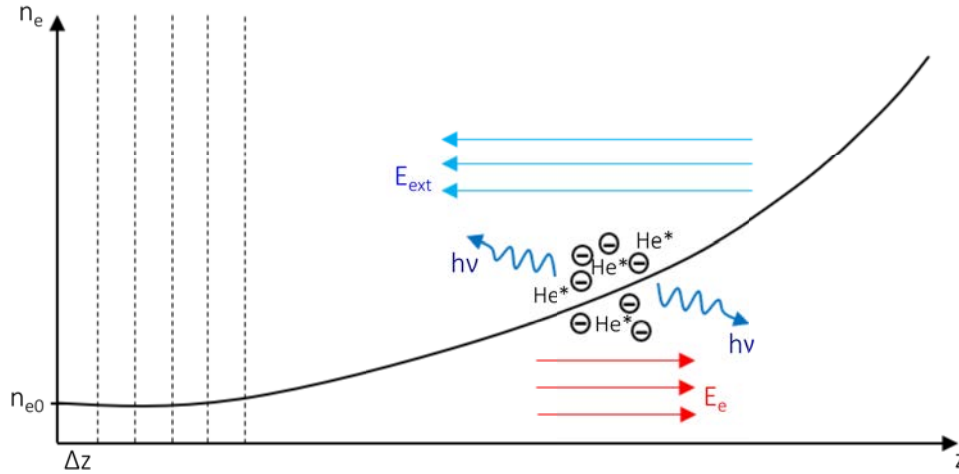
FIGURE 5.14:  Idea of the modell

Nevertheless, some insights into possible processes can also be obtained through a simplified model by using very rough assumptions. This simplified model should take up the following two basic points:

a) As postulated before or in previous works, the asymmetric discharge characteristic is caused by an electron avalanche which moves either to the cavity opening during the IPP or to the dielectric during the DPP. Based on that, this model contains a Townsend mechanism which leads to an increase of the electron density $n_e$ along the cavity height $z$ in the respective half-phase. This is sketched as an example for the IPP in figure 5.14.

b) This second point considers that the Stark effect technique applied in this thesis to determine the electric field strengths is emission based. The measured electric field values correspond to the shielded electric fields that the excited helium particles $n_{exc}$ experience at time of de-excitation by spontaneous emission. For that reason, the excited particle density is also required. Thee shielded electric fields are composed of the applied external electric field $E_{ext}$, local electric fields $E_{e,i}$ produced by electrons and ions in the volume and an electric field $E_{sur}$ generated by surface charges. Since both densities and some electric field contributions influence each other, this model has to be calculated self-consistently from $z_i$ to $z_{i+1}$.

The following assumptions are made to implement both points:

I) Since the external electric field distribution within the cavity is not homogeneous, the emission and consequently the excited particle density have to be considered as spatially averaged.

II) It is simplified that the electron avalanche moves only in z-direction and has therefore no radial components.

III) Point I) leads to the challenges of modelling excited particle densities $n_{exc}$. It is essential to know which mechanism generates excited species and which processes are responsible for their de-excitation. In this model it is assumed that only electrons are responsible for excitation.

IV) As shown in time-resolved measurements (section 5.4), the temporal effects are small. Thus, this model is set up time independent. In order to take into account the bipolarity and thus the asymmetric discharge characteristic, both half-phases are considered separately to understand the difference between electric field strengths in IPP and DPP.

V) It is assumed that a high density of residual charges is available at the beginning of the discharge. Therefore, a typical DBD electron density is set as initial electron density $n_{e,0}(r)$. Here, a value of $10^{12}\,\mathrm{cm}^{-3}$ is chosen. It is assumed as a further simplification that the initial electron density is constant along the cavity radius which leads to $n_{e,0}(r) = n_{e,0}$.

VI) Furthermore, electron losses by drifts and recombination are not considered in this model as a further simplification.

VII) The ion density can be neglected since the ions have a lower mobility than the electrons. Therefore, the local electric field is dominated by $E_{e,i} \approx E_e$

VIII) At least, no surface charges are existing and therefore is $E_{sur} = 0$

All in all, this simplified basic model has the task to combine the production of electrons of sufficient energy to excite helium particles and their subsequent spontaneous emission in presence of the applied external electric field distribution within the cavity.

**External electric field distribution**

The fundament of this simple model is the applied electric field distribution on which all further calculations are based. This is obtained as an approximation from the micro channel device explained before. Figure 5.15a) shows a false color map of the simulated electric field distribution within a cavity (channel) having a diameter (gap) of $200\,\mu m$. The applied voltage is set to $600\,V$. Bright colours (red) represent high electric field strengths while dark colours (blue) stand for low electric fields. At this point three further simplifications are made: (i) The electron movement is based on the simple picture of the asymmetric discharge characteristic. This means that the electrons move from the dielectric (z= 0) to the cavity opening (z= $50\,\mu m$) in the IPP and the opposite direction during the DPP. This leads to the simplification that only the internal cavity volume is taken into account and not the volume above. (ii) It is assumed that the electrons do not have a radial movement component in direction to the nickel electrode although the applied electric field has components in this direction. For simpler calculations these components are neglected and the electrons only move in $z$-direction (dielectric surface normal). (iii) As explained before
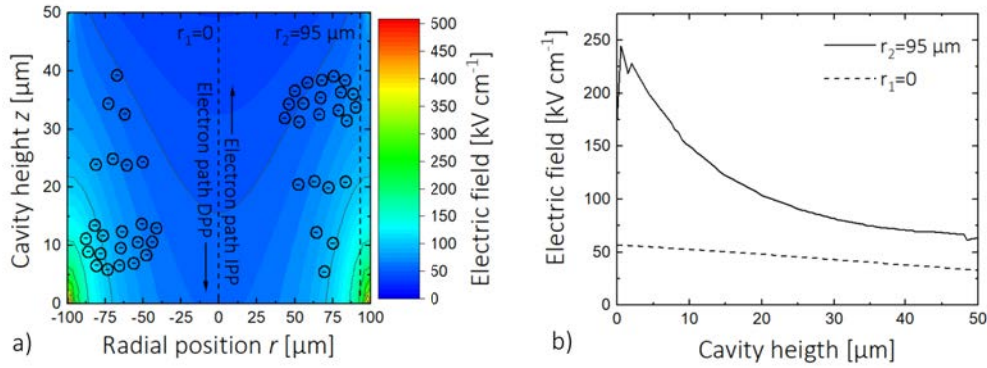
FIGURE 5.15: a) Coloured map of the electric field distribution within cavity (channel) with a diameter (gap) of $200\,\mu m$ [94]. The applied voltage is at $600\,V$. Bright colours represent high electric field strengths, dark colours stand for low electric field strengths. b) Electric field profiles obtained from a) along cavity centre ($r_1=0\,\mu m$, dashed line) and at close to the cavity edge ($r_2=95\,\mu m$, solid line). The indicated electrons represent the electron avalanche in the half-phase.

this model is time-independent given the small temporal deviations in the measured electric field during the applied excitation cycle. Based on this, the nickel electrode is applied with a constant voltage all time corresponding to a square voltage waveform excitation.

As assumed in (i) and (ii), the electrons pass an electric field profile $E(z,r)$ in $z$-direction at each radial position $r$. This is summarised in figure 5.15b) showing the shape of the electric field profile at the position $r_1=0\,\mu m$ and $r_2=95\,\mu m$. It is noticeable that these profiles have a strong dependence on the radial position. While at the cavity centre ($r_1=0\,\mu m$) the electric field decreases almost linearly along the cavity height from about $50\,kV\,cm^{-1}$ to $25\,kV\,cm^{-1}$, the decreasing trend is much stronger at the cavity edge ($r_2=95\,\mu m$). At this position the electric field decreases exponentially from about $250\,kV\,cm^{-1}$ to $75\,kV\,cm^{-1}$.

The measurements are executed spatially-integrated. This means that emission from every radial position is included for determining the electric field strengths. With regard to the model, this should not only take into account the electric field profiles at the two radial positions $r_1$ and $r_2$, but also incorporates all radial positions along the cavity. However, to keep the numerical calculation time to a reasonable level, the electric field profile is considered with a resolution of $0.5\,\mu m$ resulting in 401 positions in case of $200\,\mu m$ cavities.

This resolution remains fixed for the calculation of the following electron energy, electron density and excited helium density.
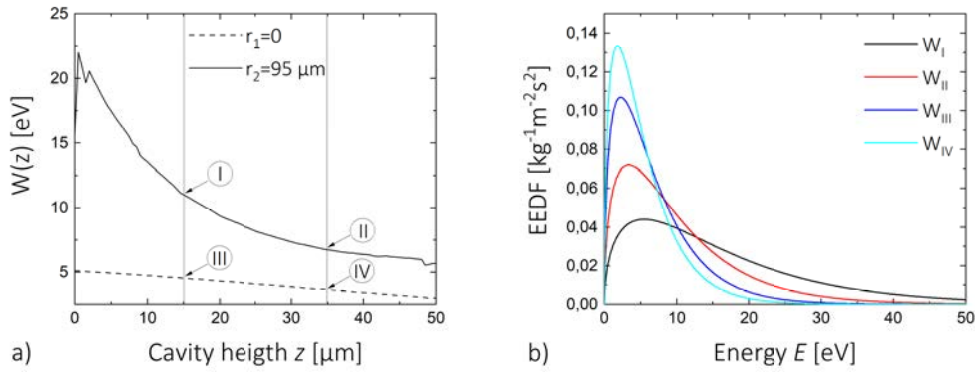
FIGURE 5.16: a) Electron energy depending on the cavity (channel) height with a diameter (gap) of $200\,\mu m$ along cavity centre ($r_1$=0R=0, dashed line) and at close to the cavity edge ($r_2$=0.95R=95 µm, solid line). The applied voltage is at $600\,V$. b) Normalised electron energy distribution function (EEDF) depending on four different positions (I, II, III and IV) within the cavity (channel) as illustrated in a).

## Electron energy

With respect to the electric field profiles $E(z,r)$, the electron energy $W_e(z,r)$ is calculated by assuming that the electrons reach their energy within their mean free path $\lambda_{mean}$ in presence of the electric field. This is described with the following equation

$$W_e(z,r) = E_{shield}(z,r)e\lambda_{mean} = (E_{ext}(z,r) - E_e(z,r))e\lambda_{mean} \qquad (5.14)$$

The corresponding mean free path is calculated with

$$\lambda_{mean} = \frac{k_B T_g}{p\sigma_{cs}} \qquad (5.15)$$

and depends on the gas temperature $T_g$, the pressure $p$ and the total cross-section $\sigma_{cs}$ between electron and helium atoms. Here, it is estimated with $10^{15}\,cm^2$ [83].

Figure 5.16a) shows the calculated electron energies along the electron path for both radial position as defined before ($r_1$= 0 µm, $r_2$= 95 µm). The gas temperature and pressure are set to $300\,K$ and $10^5\,Pa$. Both profiles show the same behaviour as the electric field strengths as shown in figure 5.15b). Depending on the location, electron energies up to $20\,eV$ are reached for a radial position close to the cavity edge. Figure 5.16b) shows the normalised electron energy distribution function (EEDF) at four different positions (I, II, III and IV) as indicated in a). As expected, higher electric fields at the respective position lead to a broad EEDF resulting in a larger number of high energetic electrons.

**Electron density**

As already mentioned, it is assumed here that excited helium particles are only generated by electrons, which is why knowledge of their density is very important. In combination with the calculated electron energies, it is then known where a large number of electrons with the required excitation and ionisation energies occur within the entire cavity volume.

Here, the spatial electron density $n_e(z, r)$ is built up along $z$-direction in form of a Townsend avalanche that is originally calculated with

$$n_e(z, r) = n_{e,0} \exp(\alpha d) \tag{5.16}$$

and depends on the initial electron density $n_{e,0}(z, r)$, the volume ionisation coefficient $\alpha$ and the electron path $d$ between both electrodes.

However, this equation is only valid for a simple plane-to-plane electrode configuration that is not given for the cavity geometry where an inhomogeneous applied electric field distribution occurs. Due to this, two modifications are necessary: (i) the volume ionisation coefficient has to be changed from $\alpha$ to $\alpha(z, r)$ and cannot be considered as constant as in the plane-to-plane setup. Therefore, a distinct approach must be taken. Here, a heuristic description of the volume ionisation coefficient is chosen, described by

$$\alpha(z, r) = \lambda_{mean}^{-1} \exp\left(-\frac{E_{ion}}{W_e(z, r)}\right) \tag{5.17}$$

and depends on the ionisation energy $E_{ion}$ and the electron energy $W_e(z, r)$. In case of helium, the ionisation energy is about 23 eV. (ii) Additionally, the effective path in which the electrons can be multiplied must change from the electrode distance $d$ to $\Delta z$. Both aspects lead to

$$n_e(z + \Delta z, r) = n_e(z, r) \exp(\alpha(z, r)\Delta z) \tag{5.18}$$

describing the electron multiplication after a small path $\Delta z$ instead of the complete cavity height in presence of the occurring electric field at a fixed radial position. Based on this equation 5.18 the electron density is calculated in $z$-direction by the following procedure

$$n_e(z_0, r) = n_{e,0}(r)$$

$$n_e(z_1, r) = n_e(z_0, r) \cdot \exp\left\{\alpha(z_1, r)\Delta z\right\}$$

$$n_e(z_2, r) = n_e(z_1, r) \cdot \exp\left\{\alpha(z_2, r)\Delta z\right\} = n_e(z_0, r) \cdot \exp\left\{\alpha(z_1, r)\Delta z\right\} \cdot \exp\left\{\alpha(z_2, r)\Delta z\right\}$$

$$\vdots$$

$$n_e(z_N, r) = n_e(z_0, r) \cdot \exp\left\{\alpha(z_1, r)\Delta z\right\} \cdot \exp\left\{\alpha(z_1, r)\Delta z\right\} \cdots \exp\left\{\alpha(z_N, r)\Delta z\right\} \quad (5.19)$$

$$n_e(z_i, r) = n_{e,0}(r) \prod_{i=1}^{N} \exp\left\{\alpha(z_i, r)\Delta z\right\}$$

First, an initial electron density $n_{0,e}$ is postulated at beginning of the electron path $z_0$. In this model it is either the dielectric surface ($z= 0$) or the cavity opening ($z= 50\,\mu$m) depending on which half-phase is considered. In the IPP the electrons start from the dielectric (high electric field) while its path begins at cavity opening (low electric field) in the DPP.

For the next position $z_1$ with $z_1 = z_0 + \Delta z$ the corresponding electron density $n_e(z_1)$ is calculated with equation 5.18. However, the volume ionisation coefficient is calculated with equation 5.17 along the path $\Delta z$. This calculated electron density $n_e(z_1)$ serves afterwards as the initial electron density for $n_e(z_2)$ and this procedure is repeated successively.

Finally, this procedure is executed at each radial position along the complete cavity height of $50\,\mu$m with a path of $\Delta z = 0.5\,\mu$m resulting in N=101 steps.

Figure 5.17a) and b) show the calculated electron densities in form of a false color map (top row, red colors represent high densities and blue colors represent low densities) and the two exemplary profiles in $z$-direction (cavity height) at $r_1 = 0$ and $r_2 = 95\,\mu$m (bottom row) within the $200\,\mu$m cavity during IPP (left column) and DPP (right column). The applied voltage is set to $600\,$V. As mentioned before, it is assumed that a high density of residual charges is available at the beginning of the discharge. Here, the initial electron density $n_{e,0}(r)$ is equal to a typical DBD electron density with a value of $10^{12}\,$cm$^{-3}$. As a further simplification it is assumed that this initial electron density is constant along the cavity radius resulting in $n_{e,0}(r) = n_{e,0}$.

As can be seen in the false color maps (a), b)), the initial electrons are only multiplied to a significantly higher number close to the edge of the cavity. By taking the profiles in $z$-direction into account (c), d)), it is visible that the electron density increases by a factor of only 1.2 at the cavity centre while an increase factor of about 35 in IPP and 90 in DPP occurs close to the cavity edge. A further point is that the high density region expands along the entire cavity edge during the IPP. It is hence more extended in comparison to the structure during DPP. In this phase the maximum density is reached only at the boundary edge between dielectric and nickel electrode.

By considering the respective profiles one can notice a stationary density reached in direction to the cavity opening during IPP. This can be associated with the decreasing electron energy and hence missing energy for further ionisation. Since this energy rises continuously in direction to the dielectric in DPP, the electron density shows the same profile.
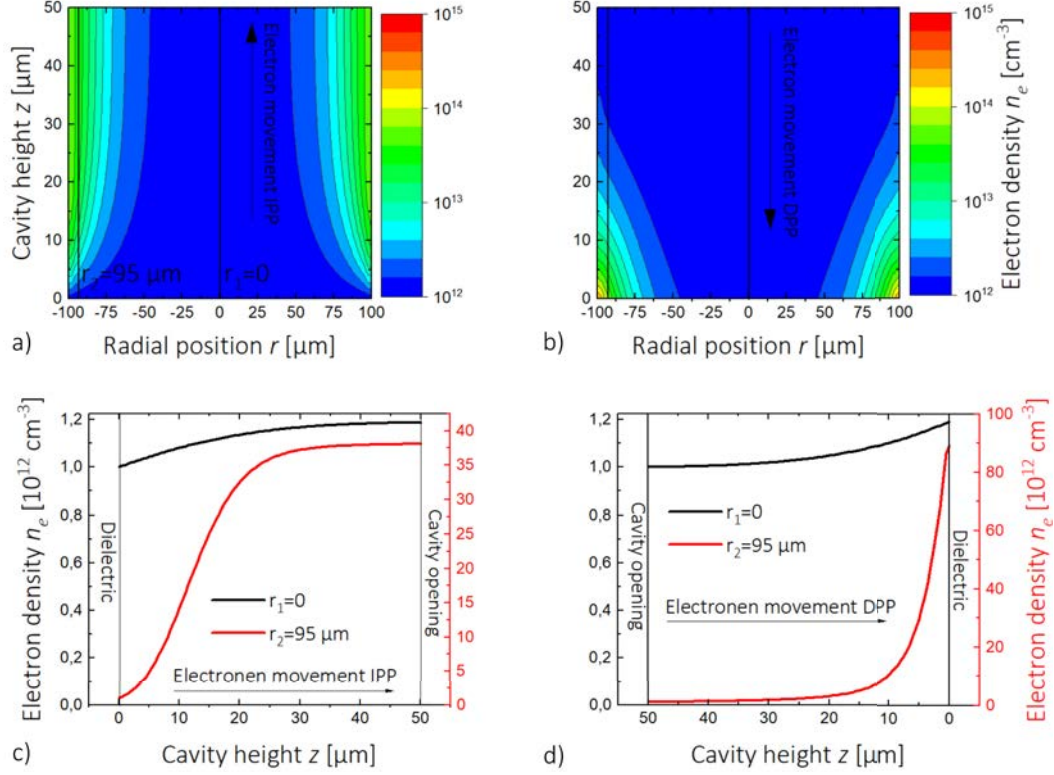


FIGURE 5.17: Calculated electron densities in form of a false color map (top row, red colors represent high densities and blue colors stand for low densities) during a) IPP and b) DPP and two exemplary profiles in $z$-direction (cavity height) at $r_1 = 0$ and $r_2 = 95\,\mu\text{m}$ (bottom row) within the $200\,\mu\text{m}$ cavity during c) IPP and d) DPP. The applied voltage is set to $600\,\text{V}$. The initial electron density is $10^{12}\,\text{cm}^{-3}$.

Due to the knowledge of the spatial distribution of the electron density, a shielding effect can be estimated by using the Poisson equation given by

$$\frac{dE_e(z,r)}{dz} = \frac{e}{\epsilon_0}(n_i(z,r) - n_e(z,r)) = -\frac{e}{\epsilon_0}n_e(z,r). \tag{5.20}$$

This additionally depends on the ion density $n_i$ which can be neglected since the ions have a lower mobility than the electrons. Therefore, the local electron density is important and the shielded electric field $E_{shield}(z,r)$ is calculated with

$$E_{shield}(z,r) = E_{ext}(z,r) - E_e(z,r) \tag{5.21}$$

and implemented in the movement process of electrons.

## Excited particle density

The Corona-model is used to calculate the excited helium particle density $n_{exc}(z, r)$. This means that the excited helium particles are just produced by electron impact excitation while de-excitation only takes place by spontaneous emission. The Corona-model is quantitatively given by the following time-dependent differential equation

$$\frac{dn_{exc}(z, r)}{dt} = n_e n_g X_{exc}(z, r) - A_{eff} n_{exc}(z, r) \tag{5.22}$$

and depends on the production term consisting of the gas density $n_g$ and excitation rate coefficient $X_{exc}(z, r)$. The destruction term contains the effective Einstein coefficient $A_{eff}$ for de-excitation. This coefficient has the following form

$$A_{eff} = A_{nat} + A_{que} \tag{5.23}$$

and is composed of the natural Einstein coefficient for spontaneous emission $A_{nat}$ and a contribution caused by quenching $A_{que}$. Since the discharge is only operated with helium, quenching is neglected in a first order and $A_{eff} \approx A_{nat}$ can be assumed. Here, it is $A_{eff} = 1.9863 \times 10^7 \, s^{-1}$ for the allowed 492.19 nm transition [76].

Due to the fact that the discharge dynamics and the time-resolution of the electric field measurements are in the microsecond range and consequently by a factor of 100 slower than the lifetime of the excited helium particles, only a stationary density $n_{exc,sta}(z, r)$ is considered. This is given by

$$\frac{dn_{exc}(z, r)}{dt} = 0 \Rightarrow \quad n_{exc,sta}(z, r) = \frac{n_e n_g X_{exc}(z, r)}{A_{nat}} = \frac{p n_e X_{exc}(z, r)}{k_B T_g A_{nat}} \tag{5.24}$$

where the gas density $n_g$ is substituted by the ideal gas law $p = n_g k_B T_g$. The excitation rate coefficient $X_{exc}(z, r)$ is expressed by

$$X_{exc}(z, r) = \int_{E_{exc}}^{\infty} \sigma_{exc}(E) \sqrt{\frac{2E}{m_e}} f(E) dE \tag{5.25}$$

and depends on the excitation energy $E_{exc}$ and the energy-dependent cross-section $\sigma_{exc}$ for electron impact excitation. This is estimated by equation 2.7 for the 492.19 nm transition as already mentioned in sub-section 2.3.1. Additionally, an electron energy distribution function is required. Here, the Maxwellian distribution is used that depends on the electron temperature. Since the electron temperature is unknown for the discharge of the MGA, an estimation is used. Here, the hard assumption is

made that the electron temperature corresponds to the energy $W_e(z,r)$ absorbed by
the electrons on their mean free path through the applied electric field as explained
in equation 5.14. This assumption results in the following form of the Maxwell
distribution function

$$f(E,z,r) = \frac{2}{(W_e(z,r))^{3/2}} \sqrt{\frac{E}{\pi}} \exp\left\{\frac{-E}{W_e(z,r)}\right\} \tag{5.26}$$

that fulfils the normalisation requirement

$$\int_0^\infty \mathrm{f}(E)\mathrm{d}E = 1 \tag{5.27}$$

This approach is exemplary illustrated for fixed positions in figure 5.15b). Finally, this
Maxwell distribution is set up for all $401 \times 101$ ($r \times z$) positions and the stationary
excited helium particle density can be calculated.

Figure 5.18 shows a false color map of the excited particle density distribution (top
row, bright colors (red) represent high densities, dark colors (blue) represent small
densities) during a) IPP and b) DPP and the same two profiles along $z$-direction at
$r_1 = 0$ and $r_2 = 95\,\mu$m (bottom row) for c) IPP and d) DPP based on the electron
density contribution illustrated before.

It is obvious that the strongest excited helium particle density also occurs at the
cavity edge as the electron density. IPP and DPP differ in that the hotspot from
which the density decreases is shifted in height. During IPP the maximum is at about
$12\,\mu$m whereas it is at the dielectric during DPP. This is also visible by taking the
profiles along $z$-direction (5.18c) and d), red line) into account. Furthermore, the
cavity centre seems to be unchanged between IPP and DPP that can also be seen by
considering the respective profile along $z$-direction (5.18c) and d), black line).

**Cavity integration and complete overview**

The calculations shown before provide a distribution of the electric field $E(z,r)$, the
shielded electric field $E_{shield}(z,r)$, and the excited particle density $n_{exc}(z,r)$, the
electron density $n_e(z,r)$ depending on the cavity radius $r$ and cavity height $z$.

A weighting with the cavity radius $r$ is required to get an averaged profile that only
depends on the cavity height $z$ and is comparable with the spatially integrated electric
field measurements. This weighting considers the fact that a larger proportion of
emission in the spatially integrated measurement comes from areas of the cavity with
a larger radius. The transformation of the respective calculated distribution $Y(z,r)$
into the respective profile $Y(z)$ along only the cavity height is made with the following
equation
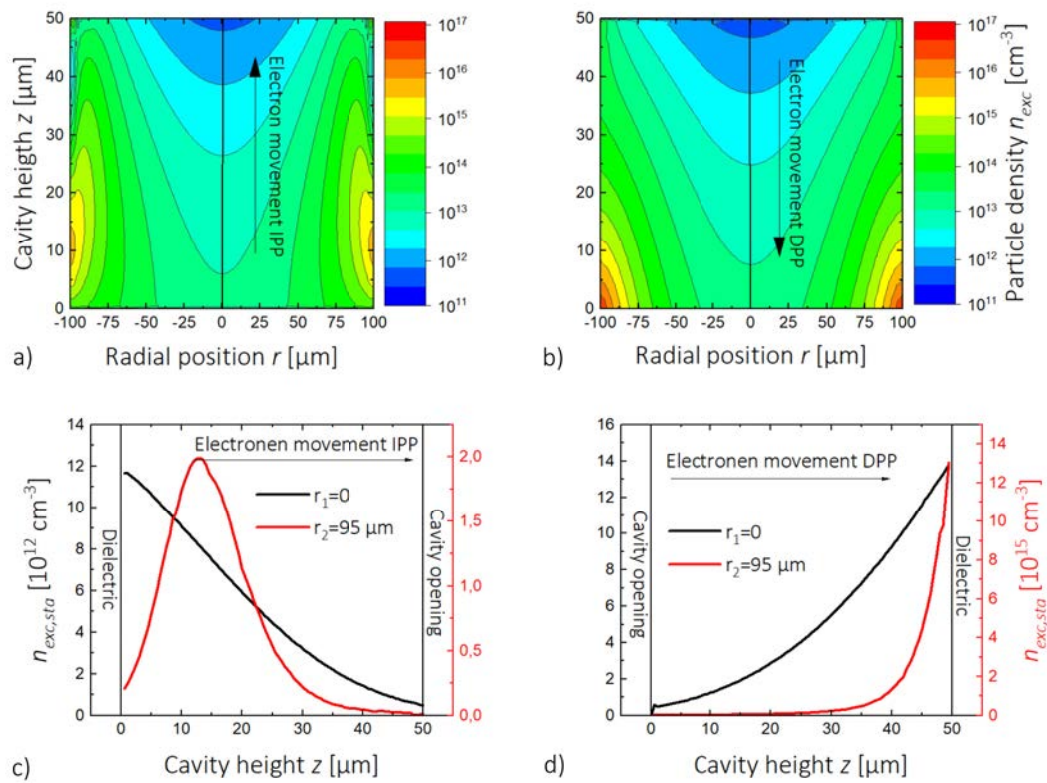
FIGURE 5.18: Calculated excited helium particle densities in form of a coloured map (top row, bright colours represent high densities) during a) IPP and b) DPP and two exemplary profiles in $z$-direction (cavity height) at $r_1 = 0$ and $r_2 = 95\,\mu\text{m}$ (bottom row) within the $200\,\mu\text{m}$ cavity during c) IPP and d) DPP. The applied voltage is set to $600\,\text{V}$. The initial electron density is $10^{12}\,\text{cm}^{-3}$.

$$Y(z) = \frac{\sum_{i=1}^{401} Y(z, r_i) \cdot r_i}{\sum_{i=1}^{401} r_i}.$$ (5.28)

Based on the basic model, figure 5.19 represents the integrated and weighted applied electric field (solid line, left axis), shielded electric field (dashed line, left axis), normalised electron density (dotted line, right axis) and normalised excited helium particle density (dotted pointed dashed line, right axis) in $z$-direction for a) IPP and b) DPP. The applied voltage is 600 V. The initial electron density is $10^{12}\,\mathrm{cm}^{-3}$.
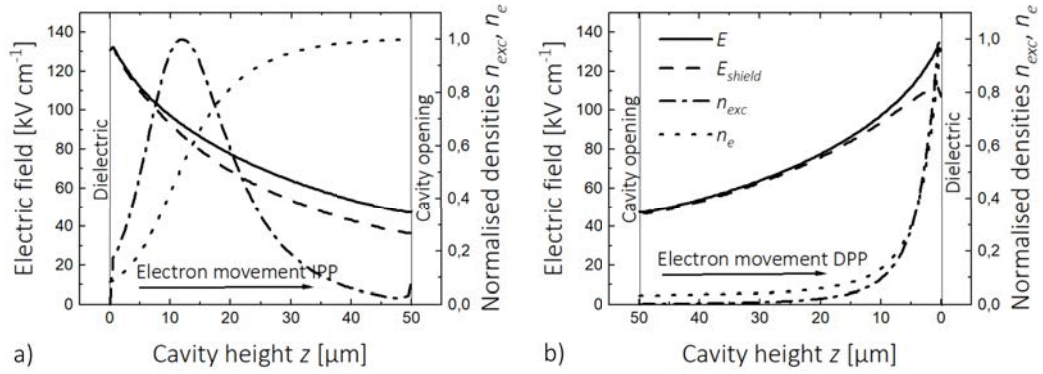


FIGURE 5.19: Integrated and weighted profile of electric field (full line, left axis), shielded electric field (dashed line, left axis), electron density (pointed line, right axis) and excited helium particle density (pointed dashed line, right axis) in $z$-direction for a) IPP and b) DPP [94]. The nickel electrode is applied with 600 V. The initial electron density is $10^{12}\,\mathrm{cm}^{-3}$.

Now the dynamics can be explained as follows: At the beginning of the IPP, the initial electrons start their movement in a high electric field regime and therefore have the required energy for ionisation and excitation. As a first result, the electron density increases by multiplication in form of an electron avalanche and shielding becomes more effective. The density of the excited helium particles rises due to electron impact excitation. Since the electrons move further in a lower electric field regime also resulting in a lower electron energy, ionisation and excitation processes begin to reduce slowly. For the electron density, this means that a plateau is reached and the shielding does not become stronger. As mentioned before, electron losses by drifts and recombination are not considered in this model. The density of the excited helium particles initially reaches a maximum at z= 12 µm and thereafter the de-excitation process by spontaneous emission is more effective than electron impact excitation. All in all, the excited helium particle density reaches its peak at z= 15 µm cavity height. Since the emissivity depends linearly on the excited particle density described in equation 2.5, the largest contribution of the measured electric field comes from the maximum value of the excited helium particle density profile.

In case of the DPP the involved processes show a simpler behaviour. Since the electrons start at a low applied electric field regime, ionisation as well as excitation do

not occur due to insufficient electron energy. Following the electron path in a high electric field regime, electrons can adsorb more and more energy leading to a strong increase of electron and excited helium particle density which reach their maximum densities at the dielectric surface at z= 0. Due to the rising electron density, shielding gets more dominant and leads to an electric field reduction of about 20 % at the end of the electron path in this phase.

From this, three general important conclusions can be drawn:

I) By comparing the electric field and helium density profiles of both phases with each other, it can be explained why higher electric field strengths are measured in IPP then in DPP. While the maximum excited helium particle density is reached close to the dielectric in a high electric field regime during DPP, the maximum of excited species is generated 12 μm away from dielectric surface in a rather lower field regime during IPP.

II) Due to the strong increase in the electron density during the DPP, the model shows that shielding gets more effective and the electric field finally drops. This supports the explanation that a charge density is built up during the excitation in DPP leading to a slowly decreasing trend of the electric field strengths in the time-resolved measurements as shown in figure 5.6.

III) This effect can only be shown in this model for initial electron densities higher than $10^{12}\,cm^{-3}$ that correspond to typical DBD electron densities. Since typical initial electron densities are in a significantly lower range, this may also indicate that a large amount of residual charges in the form of surface charges contribute to the electron avalanche.

## 5.7 Evaluation and comparison of modelled and measured electric field

As mentioned before, this model can explain the difference between electric field strengths during IPP and DPP. In the following, it is discussed how this basic model reflects the individual parameter variations described before in section 5.5.

The line-of sight-character of the experiments (head-on observation) has to be taken into account, to compare the measured values with the electric field strengths obtained by the model. Since the emission of excited particles takes place at all points along the cavity height $z$, the calculated electric field strengths $E_{cal}$ are obtained by averaging the shielded electric field $E_{shield}$ with weighting the excited helium particle density $n_{exc}$ which is described by

$$E_{cal} = \frac{\sum_{i=1}^{101} E_{shield}(z_i) \cdot n_{exc}(z_i)}{\sum_{i=1}^{101} n_{exc}(z_i)}. \tag{5.29}$$

## 5.7.1   Cavity diameter

The basic model does not directly consider the cavity diameter. However, a change of the cavity dimension leads to another applied electric field distribution within the cavity that is fundamental for this model. Therefore, the applied electric field distribution is calculated for each cavity diameter by COMSOL and afterwards implemented in this model.

Figure 5.20 shows calculated electric field strengths depending on the cavity diameter for IPP (black dashed line) and DPP (red dotted dashed line). Despite all the simplifications and assumptions that the model contains, it reproduces the measured electric field trends for both phases quite well. Regarding the absolute values, these are higher by a factor of about 2.2 (subsequently corrected by this factor for better comparison). This may be attributed to the simplification that all accelerated electrons only have a movement in $z$-direction (cavity height).
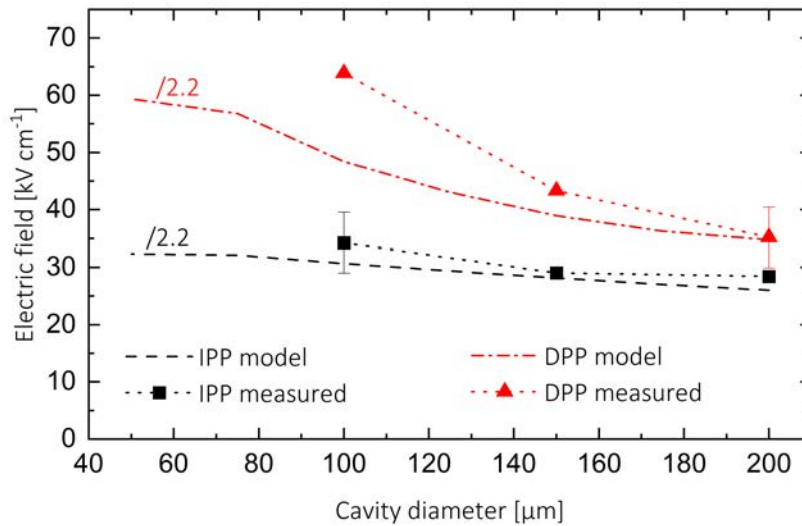


FIGURE 5.20: Measured (dashed line with symbols) and modelled (dashed line) electric field strengths depending on the cavity diameter during IPP (black) and DPP (red) [94]. The voltage amplitude is 600 V and the frequency is kept constant at 15 kHz.

The simplification of the model results in an overestimation of the electron paths located closely to the nickel electrode. In these areas close to the cavity edge, the applied electric field distribution also has radial components that push the electrons towards the nickel electrode during the IPP and towards the centre of the cavity during the DPP. Therefore, electrons do not move only in $z$-direction but also in $r$-direction around the boundary edge between dielectric surface and nickel electrode. Instead, the electrons move straight forward in z-direction in a high electric field region in the model. This allows a fast multiplication and the generation of many excited particles.

Electrons starting for example at $r_1 = 95\,\mu m$ at the dielectric (IPP, z= 0) should

disappear quickly at the uncovered and positively charged nickel electrode. Therefore, their path is in comparison to the simplification of the model shortened and very high electron and excited helium particle densities cannot generate. This also means that strong electric field contributions do not get detected.

During the DPP, the electrons are deflected into the centre of the cavity, which is characterised by lower electric fields. Thus, a high electron and excited particle density cannot built up close to the edge as already shown in figure 5.18.

These radial electric field components are stronger for smaller cavity diameters. This leads to an increasing deviation between calculated and measured electric field strengths for smaller cavities.

This finding can be supported by the radial emission profile of the cavities detected with the head-on perspective. These profiles are illustrated in figure 5.21 depending on the cavity diameter. For a better comparison, the profiles are normalised with regard to their intensity and cavity radius. The MGA is applied with a voltage of 600 V at 15 kHz. The strong 706 nm helium transition is observed with the ICCD-camera since the 492.19 nm transition is not as intense. This emission line is characterised by an excitation energy of 23.1 eV [76] that is almost identical to the excitation energy of the 492.19 nm line. Therefore, the same energetic electrons are observed in the first order. The spectral resolution is given by the cavity diameter divided by 1024 detector pixels of the ICCD-camera.

During the IPP a kind of spatial modulation of the measured radial emission profile for 200 µm and 150 µm cavities is observed. This represents a double-peak structure in which the maximum values are located close to the cavity edge. Cavities of 100 µm do not show this effect.

Additionally, it is observed that the relative proportion of the discharge expansion along the cavity diameter increases with higher cavity diameters. This is expressed by the FWHM in the normalised radial position view. Since the radial electric field components get more dominant and the available path for movement is smaller with smaller cavities, electrons cannot be multiplied to a higher quantity to excite helium atoms. Therefore, no stronger emission appears close to the cavity edge and the modulation disappears and the FWHM decreases.

In contrast to the profile during IPP, a rather bell-shaped structure is formed in the opposite phase where the FWHM is decreasing with decreasing cavity diameter resulting in a more Gaussian-shaped profile. In this phase, the movement of electrons in the opposite direction takes place. This leads to a movement towards the centre of the cavity and no modulation can be detected.
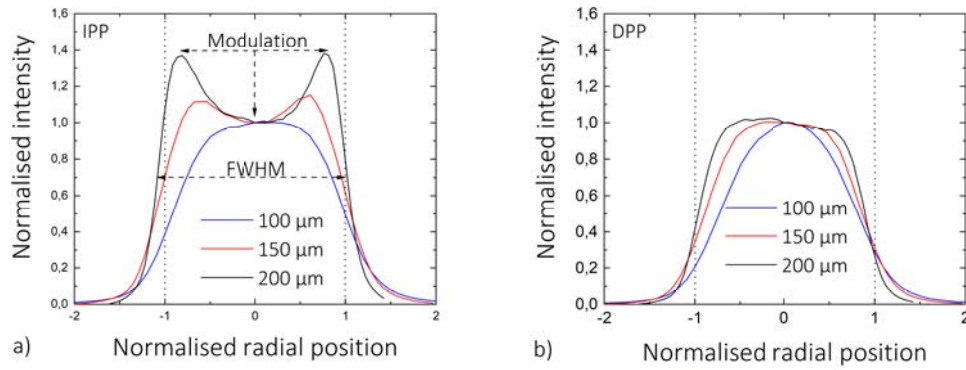
FIGURE 5.21: Radial 706 nm emission profile within 200 μm, 150 μm and 100 μm cavities during a) IPP and b) DPP [94]. The MGA is applied to a voltage of 600 V. The frequency is set to 15 kHz. For a better comparison the intensity axis is normalised on the intensity value at the radial position $r=0$. Additionally, the radial axis is normalised on the respective cavity radius.

### 5.7.2   Pressure

The pressure inside the MGA is directly connected to the mean free path and gas density and subsequently influencing the basic model. Therefore, electric field strengths are calculated depending on the pressure which are shown in figure 5.22 additionally to the observed values for IPP (black dashed line) and DPP (red dotted dashed line).

Calculated electric field strengths are obtained depending on the pressure and shown additionally to the observed values for IPP (black dashed line) and DPP (red pointed dashed line) in figure 5.22.

It can be seen that the model reproduces the observed electric field strengths with varying the diameter. However, the absolute values are again too high by a factor of 2.2.

The first reason why the electric field rises with higher pressure can be understood through the shift of the maximum excited particle density to the higher electric field region illustrated in figure 5.19a). This shift to the higher electric field region matches well with the observation made for silicon-based arrays. It was observed for these arrays that the modulation compared to figure 5.21a) shifts to the cavity edge and thus into higher electric field regions [17].

A second reason is the volume ionisation coefficient $\alpha$, which is strongly dependent on the pressure. This is reduced overall by the collision probability term as shown in the following

$$\alpha(z,r) = \lambda_{mean}^{-1} \underbrace{\exp\left(-\frac{E_{ion}}{W_e(z,r)}\right)}_{collision\ probability}. \qquad (5.30)$$
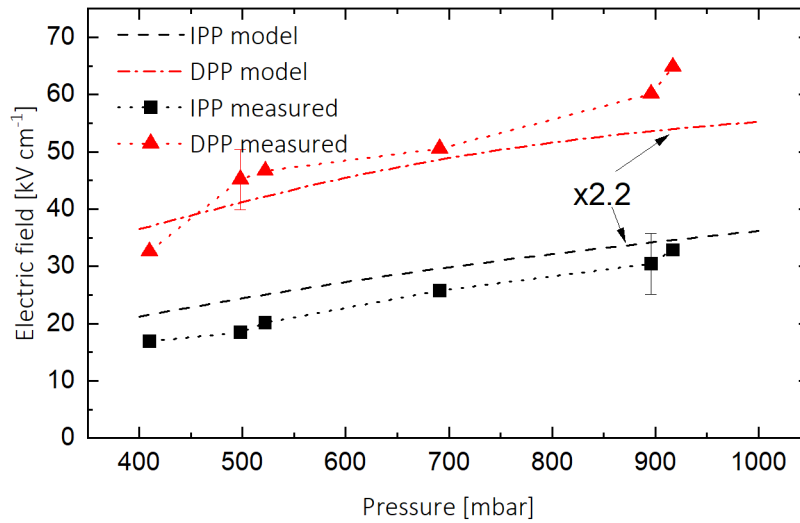
FIGURE 5.22: Measured and calculated electric field strengths depending on the pressure for IPP (black squares, dotted line) and DPP (red triangles, dotted line) [94]. The single MGA with 150 μm cavities is operated in the vacuum chamber as described in 3.5. The voltage amplitude is set to 600 V at a frequency of 15 Hz. The integration time is 10 min.

While the reciprocal of the free mean path increases with higher pressure, the decreasing collisional probability is here the dominant factor and leads to less ionisations. Therefore, less electrons are produced for a better shielding and the electric field strengths must increase in both phases.

### 5.7.3 Voltage

The applied voltage amplitude plays an important role in the basic model and is influenced by the electric field distribution obtained from COMSOL. This model provides an opposite trend of the electric field strengths depending on the applied voltage amplitude as shown in figure 5.10. Here, a higher applied voltage amplitude leads to increasing electric field strengths.

The reason for the uncompensated growth of the applied electric field in the model is the result of a small shielding effect.

The first point is that the model does neither consider the changing starting conditions of the electron avalanche nor the increasing initial electron density for rising applied voltages. This initial electron density is always set to be $10^{12}\,cm^{-3}$. Therefore, the electron density that is necessary for shielding the rising applied electric field cannot be reached. However, a higher applied voltage amplitude is responsible for a higher emission intensity as well as a shift of the ignition voltage along the excitation cycle as interpreted through figure 5.11. Both facts are indicators for a rising initial electron density when the applied voltage amplitude increases.

The second point is that no built-up surface charges are implemented in the model since these follow a dynamic process such as electron and ion drift and plasma surface interactions. However, this might have a huge impact on the electric field strengths.

In DPP, electrons start their path at the cavity opening and collide with helium atoms within their mean free path. Since the mean free path is only a statistical value, a large amount of electrons can reach the dielectric faster due to less collisions. Since more and more electrons are produced along their path to the dielectric through multiplication, the electron accumulation on the dielectric becomes larger. As a result, a surface charge density is built up which counteracts the applied electric field. This results in a drop of the electric field strengths.

During the IPP, this electric field drop must be induced by an ion drift to the dielectric. Electrons move towards the uncovered nickel electrode where they disappear and a surface charge density cannot built up. Since the ion drift is proportional to the electric field, the accumulation onto the dielectric has to increase with rising applied voltage amplitudes and also provides a decrease of the electric field.

Although this model does not consider the dynamic and production of surfaces charges on the dielectric, a first idea of the influence on the electric field strengths can be even obtained.

Figure 5.23 illustrates calculated electric field strengths depending on a surface charge density during both half-phases. This is shown for the $200\,\mu m$ cavities where the simplification of only vertically moving electrons in $z$-direction is valid. In contrast to calculations done on the cavity diameter and pressure variation, it is assumed now that surface charges are already on the dielectric before the electron avalanche begins. In IPP (black line) ions cover the dielectric while in DPP (red line) the dielectric is occupied by electrons.

From this figure it is clear that surface charge densities below $10^{10}\,cm^{-2}$ do not cause significant changes in the electric field. However, an increase into a range between $10^{10}\,cm^{-2}$ and $10^{11}\,cm^{-2}$ that is typical for DBDs [19] (grey marked) leads to a drop of the calculated fields in the range of the observed electric field strengths. During DPP a drop from about $100\,kV\,cm^{-1}$ to $70\,kV\,cm^{-1}$ is observed while it falls from $80\,kV\,cm^{-1}$ to $60\,kV\,cm^{-1}$ at IPP. Since the surface charge density has to rise with increasing applied voltages, this may explain the stronger electric field drop in the voltage variation and in the time-resolved measurement during DPP.

### 5.7.4   Frequency

While the voltage is a dominant parameter for the production of surface charges, the frequency may be responsible for their survival on the dielectric. In the basic model this dependency is taken into account by the initial electron density. If no frequency-dependent particle loss processes occur, it can be assumed that at higher frequencies
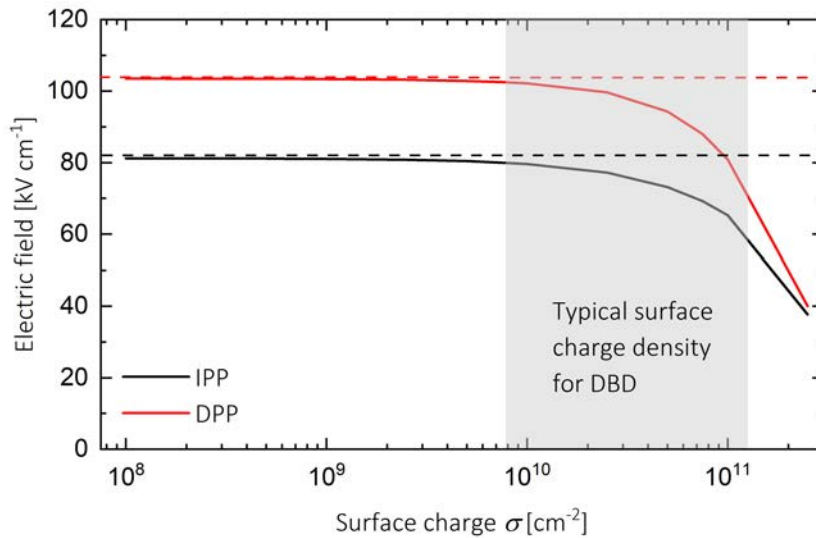
FIGURE 5.23: Calculated electric field strengths depending on the surface charge density $\sigma$ for both phases. The initial electron density is set to $10^{12}\,\mathrm{cm}^{-3}$. The nickel grid is applied with a voltage of $600\,\mathrm{V}$. During IPP (black line) the surface is set with ions, while electrons cover the dielectric during DPP (red line). The grey marked area represents typical surface charge densities of DBDs [19].

more electrons are available for the subsequent half-phase, as fewer particle losses occur in the meantime. This assumption can only be valid for IPP since electrons can be deposited on the dielectric in the half-phase before (DPP). In contrast, the nickel-grid is bare and allows electrons to disappear during IPP. Therefore, less electrons are available for the electron avalanche during DPP. The initial electron density must not be identical for both half-phases in the basic model.

Further, produced residual charges may influence temporarily the beginning of the subsequent half-phase. For example, ions move towards the dielectric during the IPP and remain there. After this half-phase is completed and a negative voltage is applied to the nickel electrode, these deposited ions amplify the internal electric field, resulting in greater electron multiplication and shielding. As a consequence, the electric field has to drop. The same effect can also occur in reverse: After DPP, the dielectric surface is covered with electrons that enhance the electric field for the electron avalanche in the subsequent IPP.

## Summary

A simple stationary model was developed to better understand the physical process within the cavities. This corona-model considers the internal applied electric field, the electron and excited particle density. The main result is that the discharge is generated by a Townsend-mechanism where the electron avalanche is creating mainly in direction of the horizontal electric field direction during the respective half-phase

(asymmetric discharge characteristic). Especially, the trends of the pressure and cavity diameter variation can be described well with exception of the absolute values. In case of the cavity dimension, the high electric field regions close to the edge come together and increase the electric field strength. A higher pressure leads to a lower collisional probability and therefore to a smaller number of electrons for shielding. However, the trends according to the applied voltage amplitude and frequency cannot be confirmed by the model due to the assumption of a constant dependence of the electric surface charge density on voltage and frequency.

# Chapter 6

# Potential for catalytic operation and surface interaction

Low-temperature plasma sources are an important part of solutions for environmental applications [23, 24] as described in the introduction. For example, dielectric barrier discharges (DBD) were already successfully used for exhaust gas purification to remove CO [25], NOx [26], $SO_2$ [27] or volatile organic compounds (VOCs) [28]. In particular, microplasmas were investigated to be useful for conversion of such exhaust gases due to their low-temperature nature and chemical reactivity [29].

It should be noted, however, that this type of plasma-chemical conversion suffers from low energy efficiencies and poor selectivity. The combination of such non-thermal plasma sources with a heterogeneous catalyst is a very promising way to avoid these negative characteristics. The idea of this combination is to bring the respective strength of the individual components into play to evoke synergistic effects, higher conversion efficiencies and a generally better performance than the catalyst and plasma source would achieve separately [31, 35].

A simulation motivating the potential of microplasma arrays for plasma enhanced catalysis is based on the influence of the catalyst on the discharge performance. Zhang et al. have found that a few hundred micrometer pore in the dielectric (catalytic) material causes strong electric fields. These electric field strengths positively influence plasma enhanced catalysis by increasing particle densities and temperatures.

The metal-grid array (MGA) introduced in this thesis offers the advantage that a dielectric material can be included in the discharge volume and removed after plasma operation for surface investigations.

Since the investigations in this thesis have provided good insights into the electric fields of arrays, it is now possible to attempt a look at plasma catalysis in pore-like structures. It should be noted that the experimental and diagnostic setup is not capable of investigating the plasma catalytic effect on the micrometer scale. However, a first insight can be gained from the global properties. Based on this, the following key question can be answered:

*KQ* 2.1*: Does the catalyst implemented in the MGA have an effect on the global discharge characteristics, gas conversion and selectivity?*

These investigations were carried out in collaboration with project A7 of the CRC1316 located at the Chair of Technical Chemistry from the Ruhr-University Bochum.

## 6.1   Catalyst application

As mentioned above, the metal-grid allows to be combined with a catalytic material. In this thesis, manganese dioxide ($\alpha$-$MnO_2$) is used. There are several reasons for using this material: (i) Compared to noble metallic catalysts, it is readily available and economical for experimental purposes [99]. (ii) Moreover, manganese dioxide is compared to other catalytic materials like e.g. lead (Pb) or chromium (Cr) less toxic and hence easier to handle. (iii) Finally, it shows the highest activity for the oxidation of alkanes such as n-butane ($C_4H_{10}$) [100].

The catalyst is applied to the dielectric of the MGA by using a spray-coating procedure that was established in the project A7 of the CRC1316 [99]. The starting materials for this catalyst are $KMnO_4$ and $Mn(NO_3)_2$, which are synthesized rapidly under alkaline conditions into $MnO_2$ in a micro-mixer. The suspension is then quenched by spray drying to avoid large particle sizes. After synthesis, the resulting particles are washed off to reduce the potassium content. This suspension is sprayed along the dielectric with a spray gun mounted on a xy-driven robotic arm. Since the dielectric is put on a $450\,°C$ heated thermal plate and the suspension is applied stepwise with a volume of about $30\,\mu L$, the water vaporises immediately leaving a $\alpha$-$MnO_2$ phase deposited on the dielectric.

By varying the step width and pump volume, the load and the surface coverage of the coating can be controlled. Generally, loads up to $3\,mg\,cm^{-2}$ are possible. A disadvantage is that the catalyst cannot be applied as a homogeneous coating on the dielectric. Instead, agglomerations of the catalytic material are observed whose thickness of about $10\,\mu m$ does not change, but its surface coverage on the dielectric increases with increasing load [99]. Further experiments may show that a catalyst load of $3\,mg\,cm^{-2}$ is necessary to achieve a complete coverage of the dielectric surface.

Figure 6.1 shows a laser scanning microscope (LSM) image of the assembled reactor where the catalyst is applied with a load of a) $0.1\,mg\,cm^{-2}$ and b) $0.25\,mg\,cm^{-2}$ on the dielectric. The cavity has a diameter of $200\,\mu m$. It can be seen that there is no homogeneous coverage of the catalyst on the dielectric. Instead, an inhomogeneous aggregation is formed with a maximum height of $14.23(355)\,\mu m$ in a) and $15.73(412)\,\mu m$ in b). Increasing the load by a factor of 2.5 leads only to a slight increase in surface coverage.

Up to now, there is no better method of applying the catalyst on the dielectric. For this reason, the low surface coverage is accepted for the first measurements and loads between $0.1\,\mathrm{mg\,cm^{-2}}$ and $0.25\,\mathrm{mg\,cm^{-2}}$ are used.

Finally, it should be noted that the catalyst is not strongly bound to the dielectric surface so that the $50\,\mathrm{\mu m}$ cavities become clogged during during assembly and do not ignite. As a consequence, these cavities could not be tested. However, this problem does not occur for the 200, 150 and $100\,\mathrm{\mu m}$ cavities.
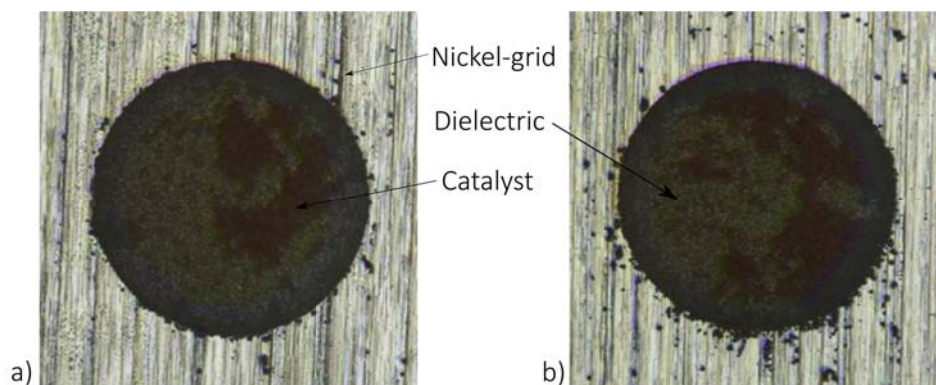


FIGURE 6.1: LSM picture of a single cavity with a diameter of $200\,\mathrm{\mu m}$ where $\alpha$-$\mathrm{MnO_2}$ is deposited with a load of a) $0.1\,\mathrm{mg\,cm^{-2}}$ and b) $0.25\,\mathrm{mg\,cm^{-2}}$. These images were taken before initial operation.

## 6.2 Influence of catalyst on operation in pure helium

As mentioned above, the catalyst is not strongly bound to the dielectric and consequently leads to pollution within the device. Electrical and optical investigations are executed to check the comparability of the global performance of the coated and uncoated device and the influence of the catalyst on the discharge.

### 6.2.1 Experimental setup

For these purposes, two arrays are used. Both devices consist of the identical grids with cavity structures of 200, 150, 100, and $50\,\mathrm{\mu m}$ in diameter but differ in the loading of the catalyst on the dielectric. While the first array uses no catalyst at all, a load of $0.25\,\mathrm{mg\,cm^{-2}}$ is applied in the second device.

Both arrays are connected in series in their gas supply and parallel in their electrical supply as demonstrated in figure 6.2a) and 6.2b). Both figures are already described in 3.2 and 3.3 and serve here as reminder.

This arrangement offers the following advantages in terms of gas supply: (i) Both devices operate with the same gas composition and impurities. Possible differences in their discharge performance cannot be reflected on this factor. Both devices are operated in helium only with no admixtures to avoid possible conversion processes through the catalyst. (ii) Removing or installing the catalyst in the same device after

each measurement is avoided. This means that sensitive components such as the grid or the dielectric are not mechanically affected and no additional impurities are introduced into the reactor housing.

Regarding the electric supply, the advantage is that both devices work with the identical electrical excitation and each parameter adjustment is very practical. Especially, the phase is not changed which makes phase-resolved measurements easy to compare.
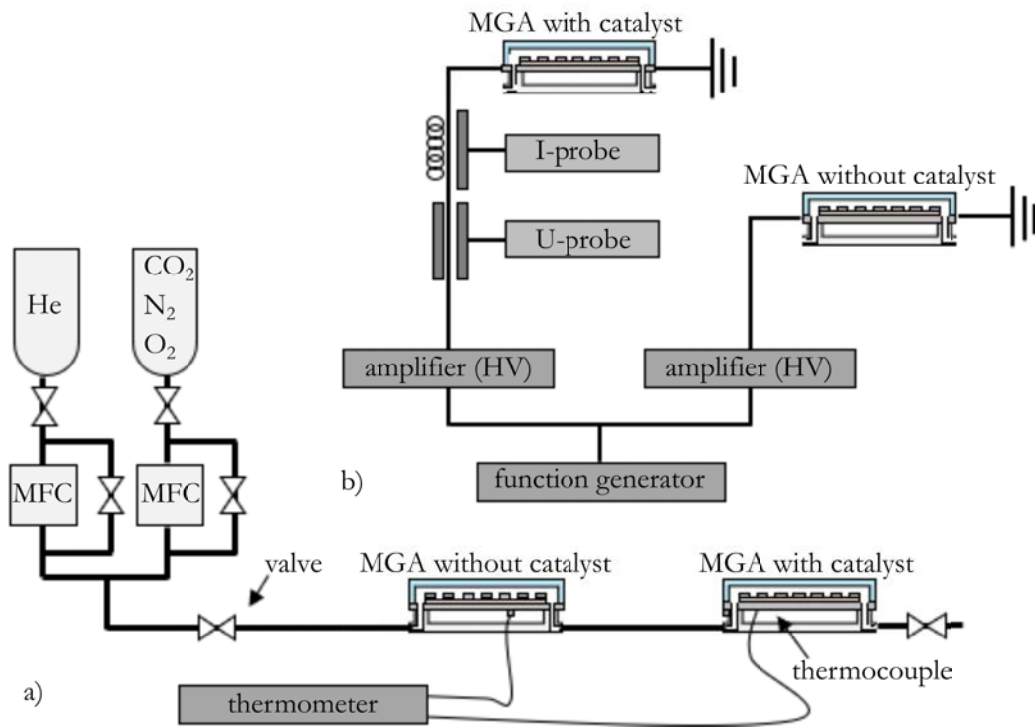


FIGURE 6.2: Sketch of the gas supply a) and electrical supply b) of the two-device system. This figure serves as a reminder. A detailed description is given in section 3.2 and 3.3.

Figure 6.3 shows a sketch of the used experimental setup. This figure also serves as a reminder and is described in detail in 3.4.

## 6.2.2   Electrical investigations

Electrical investigations could provide information to identify distinctions between the covered and uncovered device without huge technical effort. However, these signals are integrated over all four cavity-structures and therefore difficult to evaluate.

Figure 6.4 illustrates the current profile (red) in dependence on the applied voltage excitation (black) characterized by an amplitude of $600\,\text{V}$ and a frequency of $15\,\text{kHz}$ for both devices. For the device where manganese dioxide is integrated, a surface coverage of $0.25\,\text{mg}\,\text{cm}^{-2}$ is applied to the dielectric. The graph shows no significant changes between both devices. Only a small phase shift is visible in the current profile.
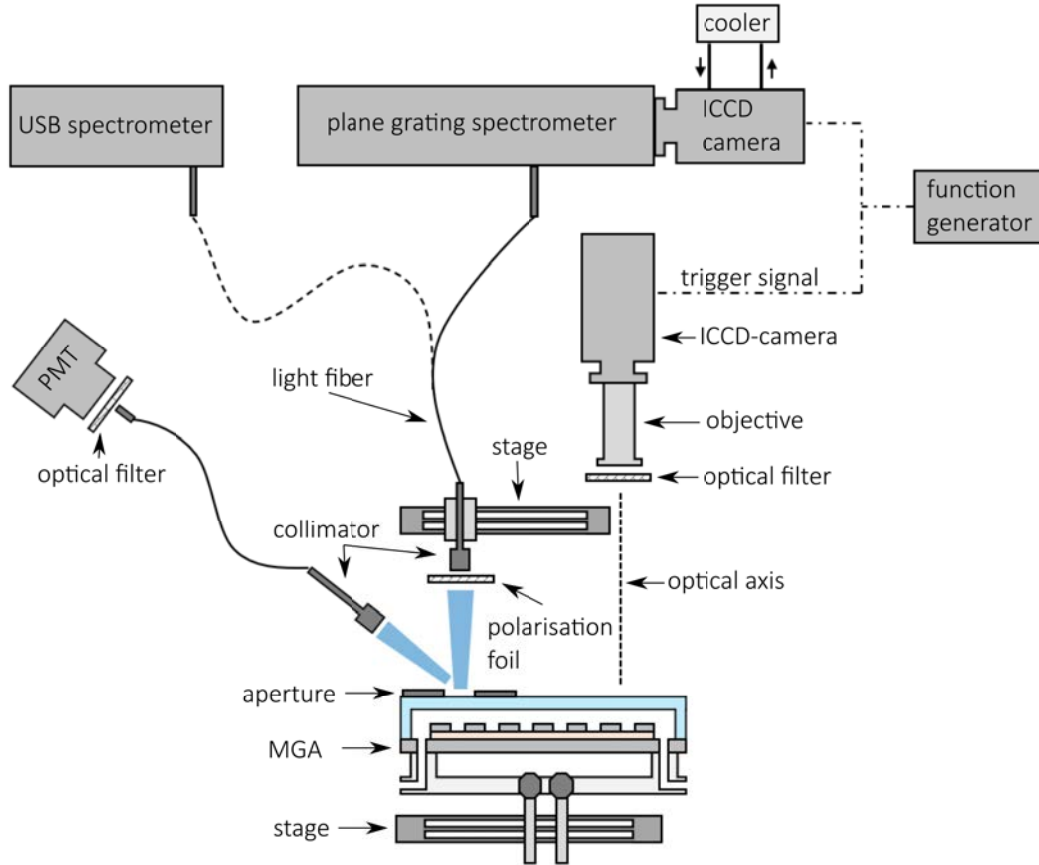
FIGURE 6.3: Sketch of the optical diagnostic system applied on the
flow-operated MGA.

To consider the voltage and current in all operating cavities, the average power $\overline{P}$
during the complete excitation is calculated by using the following equation

$$\overline{P} = \frac{1}{T} \int\limits_0^T U(t) \cdot I(t,\phi) dt \tag{6.1}$$

where $U(t)$ and $I(t,\phi)$ stand for the time $t$ dependent voltage and current profile, $\phi$
represents the phase shift between both and $T$ is the cycle duration of the applied
excitation. Figure 6.5 shows the averaged power over an excitation cycle as a function
of the applied voltage amplitude. In order to estimate the accuracy, the mean value
and the error bars of 6 measurements are illustrated. The power estimation is done
for a device without integrated catalyst (black squares), for a device with a catalyst
load of $0.1\,\mathrm{mg\,cm^{-2}}$ (red dots) and for a device with a catalyst load of $0.25\,\mathrm{mg\,cm^{-2}}$
(blue triangles). The helium gas flow is kept constant at $2\,\mathrm{slm}$. The frequency is set
to $15\,\mathrm{kHz}$.

As expected, the increased applied voltage amplitude generally leads to an increased
average power. In case of the device without catalyst, an average power of about
$8\,\mathrm{W}$ is reached at a voltage of $600\,\mathrm{V}$. In the range between $400\,\mathrm{V}$ and $600\,\mathrm{V}$, the
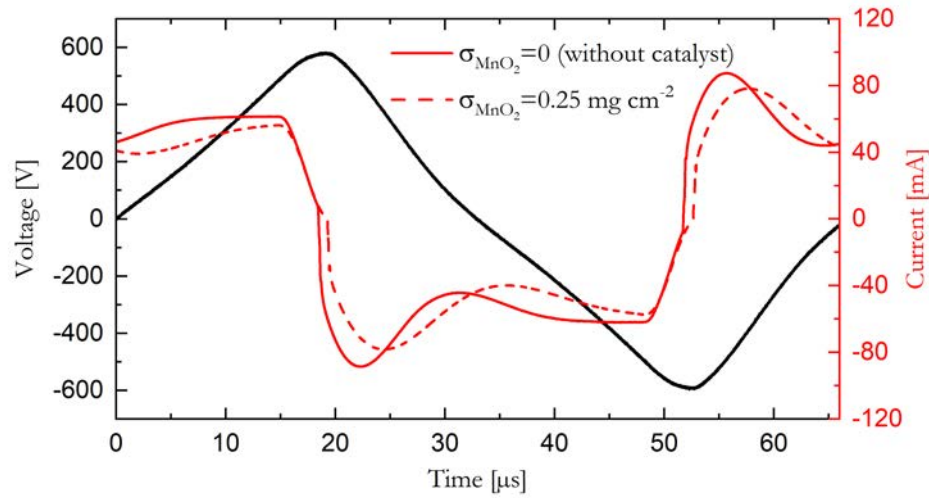
FIGURE 6.4: Current profile integrated over all four cavity-structures of the MGA without catalyst (red solid line) and with catalyst (red dashed line) depending on the applied voltage excitation (black) having an amplitude 600 V and a frequency of 15 kHz. The dielectric of catalytic operated MGA is covered with a $MnO_2$-load of $0.25\,\mathrm{mg\,cm^{-2}}$. The helium gas flow is set to be 2 slm.

non-catalytic operating device has the highest average power while an increasing load of the catalyst results in lower values. This trend is not detected for higher voltage amplitudes. The reason for this might be the poor bonding of the catalyst on the dielectric surface. As mentioned before, this poor bonding leads to clogged cavities during assembly. A higher load is expected to increase the probability of clogging resulting in fewer ignited cavities and finally in lower currents and average power.

A problem of this power estimation is that the power does not only increase through higher currents in all operating cavities but also through more and more ignited cavities when the applied voltage amplitude rises. It must be taken into account that not all cavities of the structure ignite as soon as the ignition condition is reached. This may be due to the fact that the components such as the grid and dielectric do not have a homogeneous thickness. Further, they are mechanically modified during assembly or contamination changes the effective distance between the high-voltage driven nickel-grid and the electrically grounded magnet. Especially, the last point might have a huge impact for devices where the catalytic material is applied to the dielectric. This can explain the unclear trend between all three devices for applied voltages higher than 600 V.

The fact that the 50 µm large cavities only partially ignite in the uncovered device and not at all in the covered device does not play a significant role in the average power estimation. The cavity area as well as the cavity volume of all 50 µm large cavities correspond only to about 10 % of the entire area and volume of all cavities. By assuming an identical current density in all four cavity structures, the current
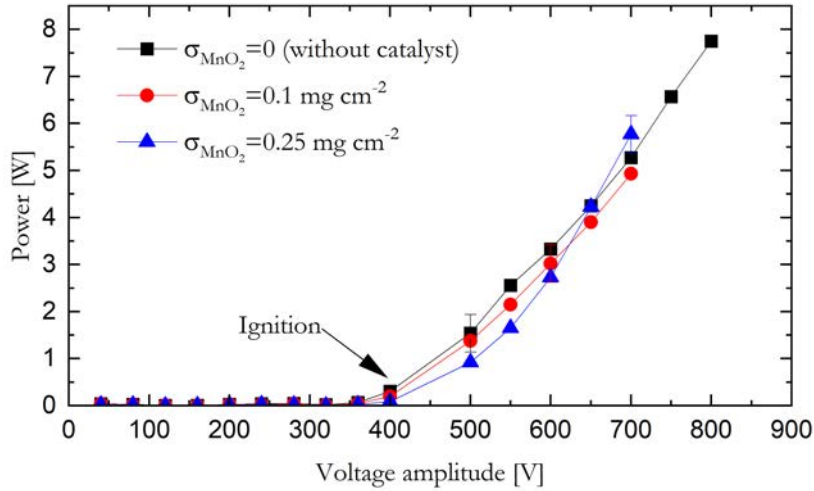
FIGURE 6.5: Power integrated over all four cavity structures as a function of the voltage amplitude for a MGA without catalyst (black) and a catalytic driven device containing a $MnO_2$-coverage of $0.1\,mg\,cm^{-2}$ (red) and $0.25\,mg\,cm^{-2}$ (blue). The frequency is set to be $15\,kHz$ and the helium gas flow is $2\,slm$.

contribution of the $50\,\mu m$ should not be of significant relevance.

All in all, it has to be considered that the error bars of the respective curves (devices) overlap. It can be concluded that the catalyst has no significant influence on the power of the array.

### 6.2.3   Optical investigations

Electrical investigation provide only insights integrated over all four cavity-structures as the discharge current from all individual cavity-structures flows at the same time and cannot be separated from each other. Optical investigations are able to give information of an individual cavity-structure by adjusting the light fibre on it.

#### 6.2.3.1   Time-dependent emission characteristic

The PMT is used for investigating the changes in the temporal discharge performance between the covered and uncovered device. Figure 6.6 shows the corresponding normalised signals (red) depending on the applied voltage excitation (black) for an uncovered (left column) and covered MGA (right column). The surface coverage of the covered device is $0.25\,mg\,cm^{-2}$. The respective row stands for the cavity diameter decreasing from $200\,\mu m$ (top) to $100\,\mu m$ (down). Both devices are operated with a $2\,slm$ helium gas flow and with a voltage amplitude at $600\,V$ at $15\,kHz$.

All cavity structures of the covered and uncovered device still show a temporally broadened emission structure that can be also associated with the quasi simultaneous ignition of all cavities as explained already in 4.5.1. The corresponding PRI-recording

looks identical to the pictures illustrated in figure 4.10 and are hence not illustrated here again.
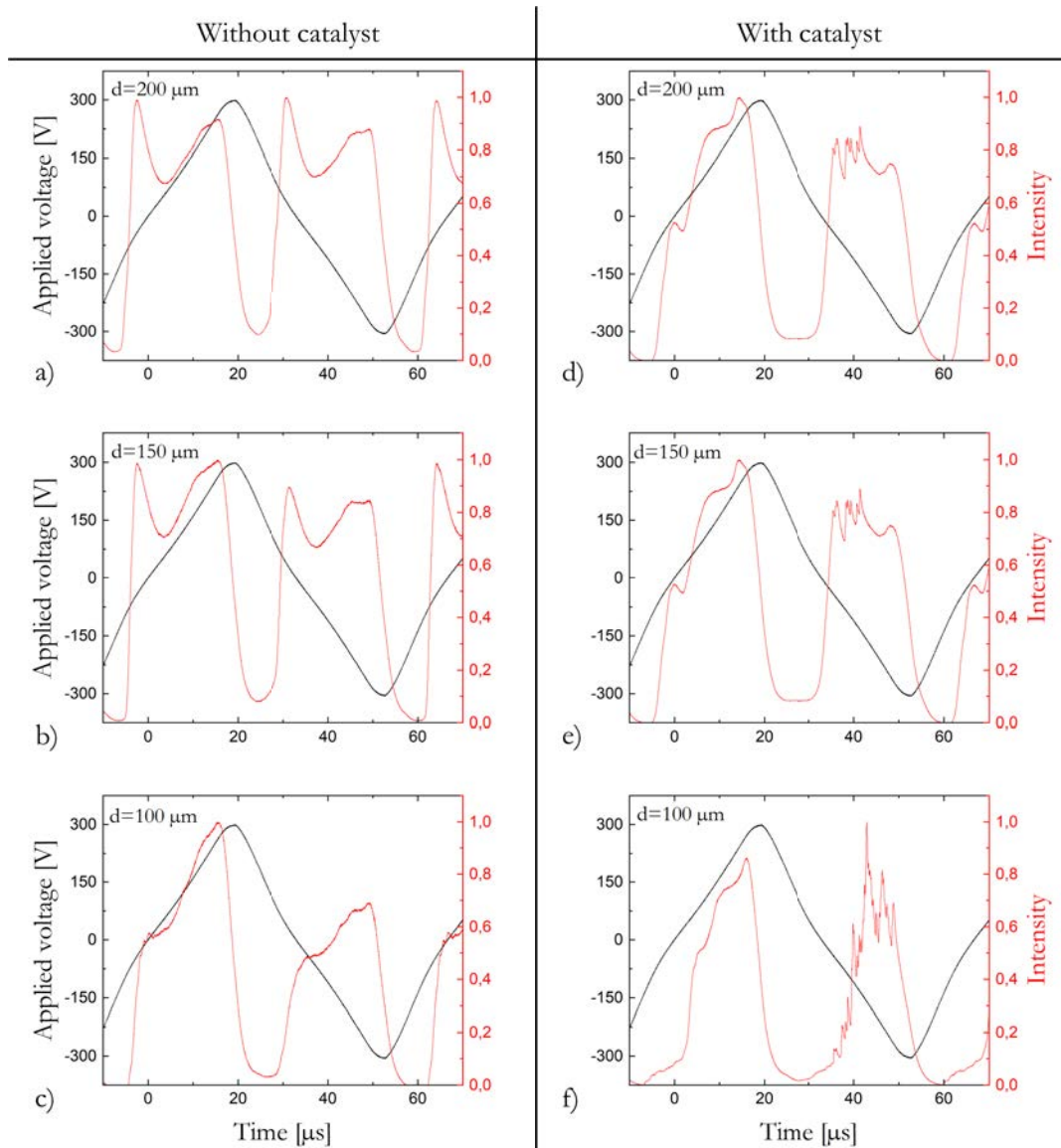


FIGURE 6.6: normalised signals (red) depending on the applied excitation voltage (black) for a uncovered (left column) and covered MGA (right column). The surface coverage of the covered device is $0.25\,\text{mg}\,\text{cm}^{-2}$. The respective row stands for the cavity diameter decreasing from $200\,\mu\text{m}$ (top) to $100\,\mu\text{m}$ (down). Both devices are supplied with a $2\,\text{slm}$ helium gas flow and with a voltage amplitude at $600\,\text{V}$ at $15\,\text{kHz}$.

Additionally, some differences between both devices are visible: (i) During the decreasing potential phase, short emission peaks interfere with the broad emission structure in the covered device. The number as well as the amplitude of these peaks increase clearly in the $100\,\mu\text{m}$ large cavities. (ii) Moreover, the discharge in the uncovered device occurs about $5\,\mu\text{s}$ earlier than in the covered device in this phase. (iii) During the rising potential phase, the first discharge pulse which can be observed especially in the $200\,\mu\text{m}$ and $150\,\mu\text{m}$ cavities of the uncovered device, disappears almost completely.

The first observation (i) fits well to the idea of the asymmetric discharge characteristic. During the DPP, the discharge takes place deeper inside the cavities and is therefore located closer to the catalyst. Due to the irregularities of the catalyst on the dielectric surface, the local electric field increases and leads to multiple spikes. It is expected that the 100 µm large cavities are stronger influenced by the irregularities and the generally higher electric field strengths.

Regarding the second and third observation (ii, iii), it must be taken into account that the first strong discharge pulse already starts before the zero-crossing of the applied voltage which is caused through surface charges. As mentioned in 5.4, these surface charges are deposited on the dielectric surface and cause an earlier ignition while the applied voltage becomes continuously smaller before the zero-crossing point is reached. Due to the inhomogeneous coverage of the catalyst on the dielectric, the nickel-grid is not placed ideally on it and no well defined cavity confinement is realised. Thus, surface charges can disappear easier which firstly leaves less charges for ignition and secondly leads to an ignition which only depends on the increasing applied voltage after the zero-crossing point. Consequently, no first discharge pulse can arise within the cavity structures where the catalyst is integrated.

### 6.2.3.2 Wavelength resolved investigation

The PMT recordings showed that an interaction between the catalyst and the discharge takes place. To verify this, wavelength resolved investigations are made to observe catalytic material which can leave the surface and enter the discharge. There it gets excited and radiates specific optical wavelengths.

Figure 6.7 shows an overview spectrum of the discharge in 200 µm cavities of the uncovered (black) and covered (red) device. The operation conditions are equal to figure 6.6. It is obvious that the device containing catalytic material shows still clear emission of the ionised nitrogen band ($B^2\Sigma_u^+ \rightarrow X^2\Sigma_g^+$) and stronger emission of atomic oxygen in addition to the helium lines after an operation of about 3 h. Since this device is placed first in this serially connected two device system, oxygen and nitrogen cannot enter the discharge from the general gas supply or through the coupler between both devices.

As described at the beginning of this chapter, the catalyst is applied on the dielectric by using a spray-coating procedure. In this procedure, a catalyst-water emulsion is sprayed on the dielectric that is afterwards heated up in ambient air to let the water vaporise. During this step, nitrogen and oxygen will deposit on the catalyst surface and also under the nickel-grid.

This deposited nitrogen can also be a reason for the occurring multiple discharge peaks observed in catalytic driven cavity structures during the DPP. In this phase, nitrogen might enter the discharge and promote additional Penning-ionisation.

A further source of oxygen could be the catalyst itself which consists of oxygen (O) and manganese (Mn). However, strong optical lines of Mn are not observed between 300 nm and 900 nm making this source rather unlikely.

Even a longer array operation of about one day during the conversion measurements demonstrated in the next section could not completely flush out the nitrogen. Finally, it can be assumed that the impurities are well trapped between the catalytic material and /or under the nickel-grid.
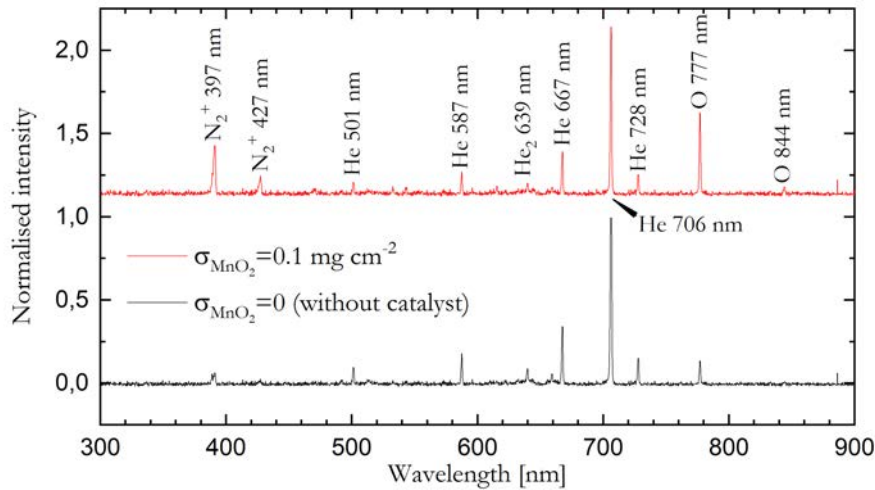


FIGURE 6.7: Recorded overview spectrum of the discharge within 200 μm cavities of non-catalytic operated MGA (black) and catalytic operated MGA (red). Both devices are supplied with a voltage of 600 V and a frequency of 15 kHz. The gas flow is set to 2 slm. The dielectric of the catalytic operated MGA is covered with a $MnO_2$-load of 0.1 mg cm$^{-2}$. This spectrum is an integration of 5 recordings where each recording has an exposure time of 500 ms.

**Summary**

In conclusion, it can be summed up that the catalyst sprayed on the dielectric has no significant influence on the discharge in the cavities. The covered device still shows the quasi-simultaneous ignition of all cavities and the phase-dependent discharge asymmetry. Moreover, the voltage-current characteristics and power estimation show no difference between covered and uncovered device. Small differences arise in the temporal characteristics and in the species composition of the discharge.

## 6.3   Gas conversion

The measurements demonstrated before showed the impact of the catalyst on the discharge within the cavities and therefore serve as fundamental understanding of this kind of discharge since the impact of the catalyst and its handling in combination with the array were unknown. The influence of the catalyst on the gas conversion with the

micro-array discharges is presented in the following. These important measurements are done in cooperation with the chair of Technical Chemistry within the CRC1316.

### 6.3.1 Experimental setup

Figure 6.8 illustrates the setup for investigating the global plasma-catalyst interaction. The project A7 of the CRC1316 has also successfully used this setup for investigating the plasma-catalyst interaction in an almost similar device where a surface dielectric barrier discharge is enclosed in a housing [99]. A schematic of this reactor is added in the appendix B.1. Here, the two different flow-operated micro-cavity plasma arrays are individually integrated in place of the reactor in this setup.

Since the project A7 could obtain first promising results with regard to gas conversion in catalytic and non-catalytic operation, almost the same selection of parameters such as gas mixtures and catalysts is chosen [99]. This has the advantage that suitable starting points for these parameters are already available and do not have to be found. Furthermore, both devices can be compared in terms of their gas conversion.
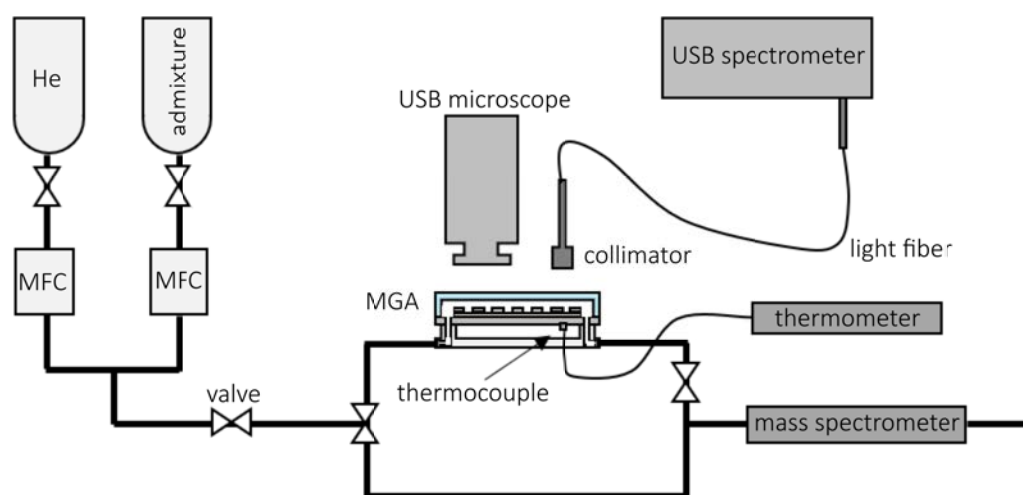


FIGURE 6.8: Schematic of the setup for investigating gas conversion of the MGA.

The inlet of the integrated MGA is connected via a $2\,\text{m}$ long stainless steel pipe with an outer diameter of $6\,\text{mm}$ to the gas supply where gas admixtures such as carbon monoxide (CO), carbon dioxide ($CO_2$), methane ($CH_4$) and n-butane ($C_4H_{10}$) can be added to a helium gas flow. The flow of the respective gas is controlled through an individual mass flow controller (Bronkhorst F-201CV). These gas mixtures flow through the MCPA and through a $2.5\,\text{m}$ long stainless steel pipe towards a quadrupole mass spectrometer (QMS, IPI GAM 400) which detects the gas composition over time. This makes it possible after an absolute calibration to detect the absolute quantities in which added gas mixtures have dissociated and subsequently been converted into other molecules. The detailed setup of this mass spectrometer is described in 6.3.1.1.

Several valves are integrated between the gas pipes to keep the MCPA out of operation for a longer period of time in a pure nitrogen environment. This reduces the amount of impurities from air that settles in the cavities and also shortens the time it takes to flush these impurities out of the cavities. Moreover, the valves provide the option of bypassing the gas flow around the array. This bypassing has two advantages: (i) This allows the investigation whether the catalyst integrated in the MCPA has an influence on the gas conversion without ignited discharge. For the reaction $2H_2 + O_2 \rightarrow 2H_2O$ where hydrogen ($H_2$) and oxygen ($O_2$) of water ($H_2O$), a platinum catalyst is already active at room temperature and becomes more operative for higher temperatures generated through the discharge [101]. (ii) Moreover, the bypassing facilitates the absolute calibration of the QMS by eliminating the need to purge the entire volume of the integrated device with calibration gas.

### 6.3.1.1   Quadropole mass spectrometer

The operation of the QMS can be divided into three principal parts: First, incoming products are ionised. This is done by an electron gun which provides electron impact ionisation. The ions produced are then accelerated into an analyser by applying a voltage.

The selection of the species is done by a quadrupole MS characterised by four cross-arranged rod electrodes. A sketch of it and its electrical connection is presented in figure 6.9. The electrodes facing each other always have the same electrical potential. Between these electrodes, a pass potential $u(t)$ is applied. This consists of a DC-part $U$ and a high frequent AC-part $V \cdot cos(\omega t)$ described by the amplitude $V$ and frequency $w$. The resulting electric field forces the ions on a sinusoidal trajectory inside. The distance of the ions to the electrodes is determined only by the mass-to-charge ratio. Consequently, species which do not have the right mass-to-charge ratio, collide with the electrodes and disappear. By varying the frequency and voltage amplitude, the mass to charge ratio of the respective specie can be set. In the case that several species are expected, all respective mass-to-charge ratios are accommodated one after the other in a so-called cycle in the settings. After passing the analyser, the ions are collected by a detector. This is a secondary electron multiplier that works like a PMT, in which ions collide with a so-called conversion dynode and generate secondary electrons. These are accelerated to a series of subsequent dynodes.

Although the QMS is very sensitive and has response times in the nanosecond range, it has to be stated that these investigations provide only cavity-structure integrated information. This means that the gas conversion of the individual cavity structure cannot be investigated with this device. The setup is depicted as a sketch in figure 6.8.

Principally, the catalyst implemented in the MGA can also work and cause gas conversion and reformation without a running discharge. To record a reference mass
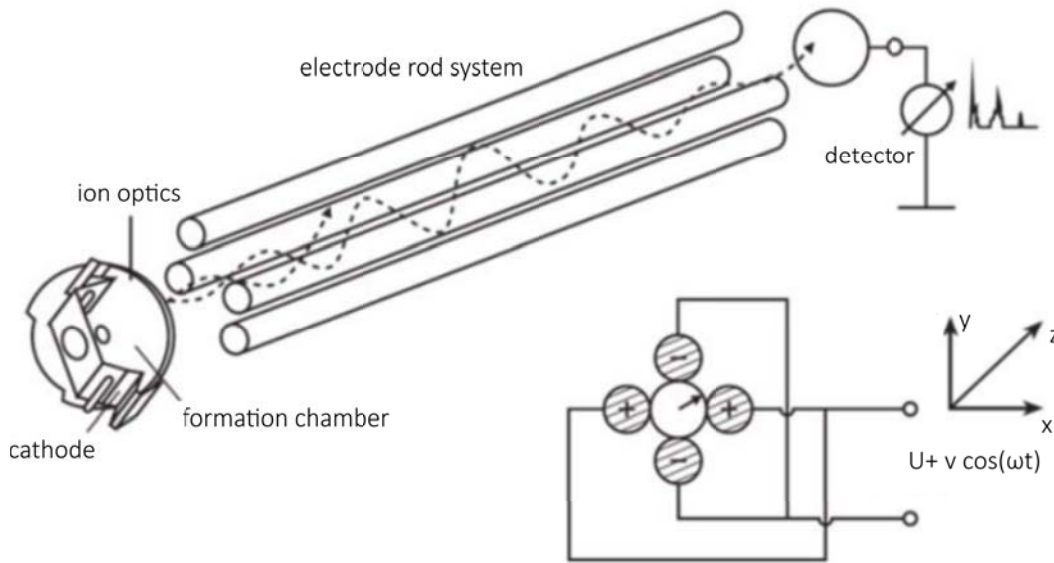
FIGURE 6.9: Schematic sketch of the QMS modified from [102].

spectrum as a kind of background without plasma or catalytic effects, the gas flow to the reactor can be shut off via valves and diverted to the mass spectrometer via a bypass.

Furthermore, it has to be stated that the QMS is absolutely calibrated for this purpose. This means that the obtained mass spectrum provide absolute concentrations of individual species and no ion current values.

### 6.3.1.2 Optical methods for species composition and cavity insights

For monitoring which species are involved in the discharge during catalytic or non-catalytic operation, optical emission spectroscopy (OES) is a useful tool. A collimator, which looks into the cavities from above, is connected via an optical fibre to a USB spectrometer, which is characterised by a spectral resolution of 0.25 nm per pixel in a spectral range between 200 and 1100 nm. This spectral range provides a good overview of the spectrum without much effort.

Since this is the first time that the MCPA has been operated with the mentioned gas admixtures, it is not known how the cavities will react or be affected by produced chemical deposits. For example, it is known from project A7 that coking can take place. Therefore, a simple USB-microscope (AmScope) with a resolution of 512×512 pixels is installed also in a head-on perspective from above to get a fast insight into the cavities.

## 6.4   Coking and surface cleaning

Up to now, the MGA has never been operated with such admixtures as named above and therefore no operation reactions are known. However, coking was observed in similar surface DBDs by adding the same gases [personal communication, Dr. Christian Oberste-Beulmann]. During plasma operation, these admixtures are dissociated and produce carbon particles that subsequently deposit in the complete discharge volume. This can lead to the following problems:

(i) As mentioned before, the QMS is connected to the gas outlet of the respective plasma source only trough a 3 cm long capillary with an inner diameter of about 100 µm that can be easily clogged by high concentrations of carbon particles. This could possibly lead to the destruction of the QMS. This has to be prevented by choosing proper operation conditions of the respective plasma source. (ii) The clogging can also be expected in the cavities of the MGA where the carbon particles might be mainly produced by the discharge inside the cavities. Since this clogging process takes place in a time range of only few minutes until the cavities do not operate anymore, the time is too short to get several usable QMS-recordings (accumulations). Therefore, the following investigations are performed by using the nickel-grid with only 200 µm large cavities (shown as $d$ in figure 3.2). The probability of clogging should be clearly smaller for this cavity size.

Figure 6.11 shows photographs of 200 µm large cavities for various conditions taken with an USB-microscope. In all photographs, the helium gas flow is set to 2 slm.

   a) This image is taken before the first operation and serves as a reference picture to determine changes on the dielectric and nickel-grid after operation with the named admixtures.

   b) This photograph shows the discharge in the cavities shortly before an admixture is added. The applied voltage amplitude is set to 600 V at a frequency of 15 kHz. Before adding any admixtures, the device is flushed permanently with helium until no traces of admixtures are visible in the optical and mass-spectroscopic overview spectra.

   c) Here, the cavity structure is depicted after an operation time of about 20 min with a $CO_2$ admixture of 8 sccm. Compared to a), it is clearly noticeable that the dielectric surface is coked.

   d) This image shows that the coking effect occurs significantly stronger by using a $CH_4$-admixture of 25 sccm. After an operation time of about 4 min, the dielectric surface and nickel-grid were completely coked.

   e) This image shows the cavity structure after a 4 min long discharge operation where oxygen admixture of 10 sccm is added to the helium flow. Previously, the

nickel-grid and the dielectric were completely coked as described in d). It is obvious that the dielectric surface is clean again comparable to figure a).

Figures c) and d) clearly show that the discharge dissociates $CO_2$ and $CH_4$, which leads to the deposition of carbon on the dielectric surface and the nickel-grid. As also observed in project A7, the coking is significantly stronger when $CH_4$ is added instead of $CO_2$. For this reason, $CH_4$ is not used again to avoid any damages on the QMS.

The conversion from $CO_2$ into carbon and $O_2$ is also detected in a QMS-spectrum showing the ion current as a function of the mass number. Figure 6.10 shows a spectrum when the discharge is on (red) and off (black).

The signal of $CO_2$ (mass number $A_{CO_2} = 44\,u$) clearly decreases when the discharge is operating. Simultaneously, the $O_2$-signal ($A_{O_2} = 32\,u$) increases. Here, it has to be noted that the QMS was not absolutely calibrated and all used pipes were quite dirty at this measurement due to a long time of non-use. Therefore, the signal of hydrogen ($A_{H_2} = 2\,u$) and water ($A_{HO_2} = 18\,u$) is relative high. Nevertheless, the conversion of $CO_2$ could be estimated at only $2\,\%$.

By taking figure e) into account, it becomes clear that the deposited carbon on the dielectric and nickel-grid is removed by operating a helium discharge with oxygen. The oxygen reacts with the carbon back to $CO_2$ or CO.

These measurements make two important points clear: (i) Gas conversion takes place in the array. The QMS is able to detect even small conversion rates. This is promising for investigating the impact of the catalyst on the conversion rates. (ii) While $CO_2$ and CO show relatively low conversion rates in range of about $2\,\%$ even at high powers, $C_4H_{10}$ could be converted up to $30\,\%$ at room temperature at similar device [99]. Moreover, the used $\alpha$-$MnO_2$ catalyst is well known for a high activity for the oxidation of $C_4H_{10}$ [100]. However, $C_4H_{10}$ is also prone to strong coking, which can now be prevented by using additional oxygen in the discharge.
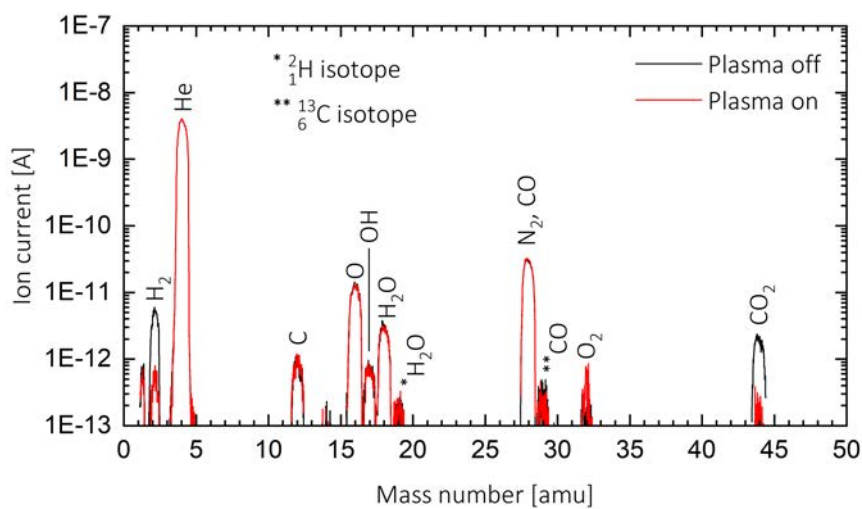
FIGURE 6.10: Overview QMS spectrum of a powered (black) and non-powered (red) flow-operated MGA. In both cases, the gas flow consists of 2 slm helium and 6 sccm $CO_2$. During operation, the MGA is applied with a voltage of 600 V at a frequency of 15 kHz. This spectrum is not absolutely calibrated.
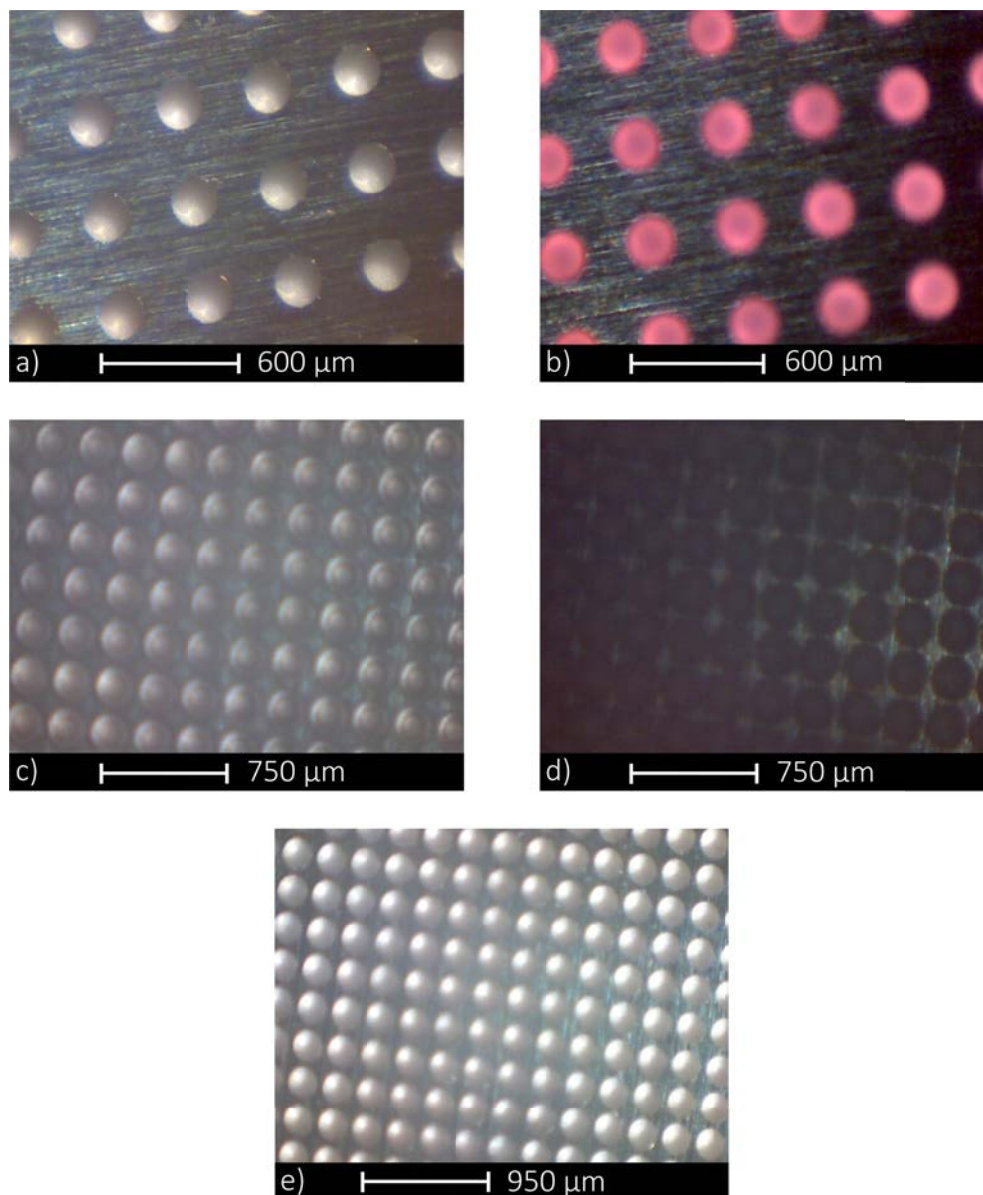
FIGURE 6.11: Insight into 200 μm large cavities of the flow-operated MGA recorded with an USB-microscope under different moments. a) Cavities separated from each other through 200 μm before the first operation. b) Cavities in operation with a pure helium flow at 2 slm and an electrical excitation of 600 V and 15 kHz. c) Cavities separated from each other through 50 μm after operation with an admixture of 8 sccm $CO_2$ and d) 25 sccm $CH_4$. e) Cavities after operation with a $O_2$ admixture of about 10 sccm.

## 6.5  Conversion and selectivity

Based on the presented results above, an admixture of 0.5 sccm $C_4H_{10}$ is added to the 2 slm helium flow for the following conversion tests. 10 sccm $O_2$ is additionally admixtured to avoid coking. In order to demonstrate an initial parameter dependence of the conversion, a voltage variation is selected, as this parameter is directly related

to the previously analysed electric field strengths and also to the power input. The frequency is set at 15 kHz.

For the voltage variation, two points have to be considered: (i) Due to the 4.5 m long gas pipes (2 m before and 2.5 m after the discharge source) and many couplers, many impurities such as water, oxygen and nitrogen are already present in the system after a short off-time. These impurities must be taken into account in the measured QMS-spectra, as they or their atomic fragments can also occur as conversion products. Additionally, $N_2$ has the same mass number as CO that is also expected as a conversion product. Based on this, the CO concentration would be overestimated under dirty conditions. To remove these impurities, long flushing times are necessary. This prevents a transient behaviour of the signal of the respective mass number when only one mass spectrum per voltage adjustment is recorded.

(ii) Furthermore, some signals require much more time until they are stable after changing the voltage. This would also result in disturbed values if only one mass spectrum per voltage is recorded.

To address both points, the QMS offers the opportunity to record the concentration of a few selected species instead of the time-consuming measurement of a whole mass spectrum ranging from 0 to 50 u. On this basis, only the species that showed the highest sensitivity in previous measurements are scanned, which shortens the overall recording and operating time. The corresponding time resolution is 1 s. Moreover, this allows to detect the selected species concentrations over a long operation time in which the voltage is varied after reaching an almost stable specie concentration. Here, the concentration of CO, $CO_2$, $O_2$ and $C_4H_{10}$ are selected. Additionally, He is selected to identify variations in the gas supply.

On this basis, the time measurement process is carried out in the following three sections :

I) During the first 95 min, the system is flushed to remove most of the impurities out of the system. The discharge is switched off during this time.

II) After the first 95 min, the discharge is operated at 500 V. The voltage is not changed for the next 30 min to estimate the temporal behaviour of the specie concentration. This process is repeated in 50 V steps up to 700 V.

III) In the last 20 min, the discharge is switched off again in order to compare the amount of impurities with the first 95 min. This and the first time range are used to estimate a background fit, which is calculated in the next subsection.

To investigate the influence of the catalyst on the conversion and selectivity, this QMS measurement process is done on the covered and uncovered device under equal gas composition and operation conditions. The used loads are $0.1 \, \mathrm{mg \, cm^{-2}}$ and $0.25 \, \mathrm{mg \, cm^{-2}}$.

The UI-characteristic at each voltage adjustment is additionally recorded to estimate the power as described in 6.2.2 for a better comparison between both devices.

Figure 6.12 shows the concentration of the selected species depending on the operation time in which the MGA is turned on (section I, $t \approx 0 - 95\,\text{min}$), operated under various voltage amplitudes ranging from 0 to $700\,\text{V}$ (section II, $t \approx 96 - 270\,\text{min}$) and finally turned off (section III, $t \approx 271 - 315\,\text{min}$). The date for helium are not shown because no variations were be observed.

It can be observed that the discharge leads to the destruction of $C_4H_{10}$ and $O_2$ and the production of CO and $CO_2$ after successively increasing the applied voltage, which is illustrated by the dashed vertical lines. It can also be seen that the concentration of the respective species recorded shortly before ignition of the discharge is not reached again when the discharge is switched off. This means that impurities were not flushed completely out of the gas system and an equilibrium concentration was still not reached. This fact needs to be considered for the calculation of the correct conversion and selectivity rates by using a background fit shown in the following.
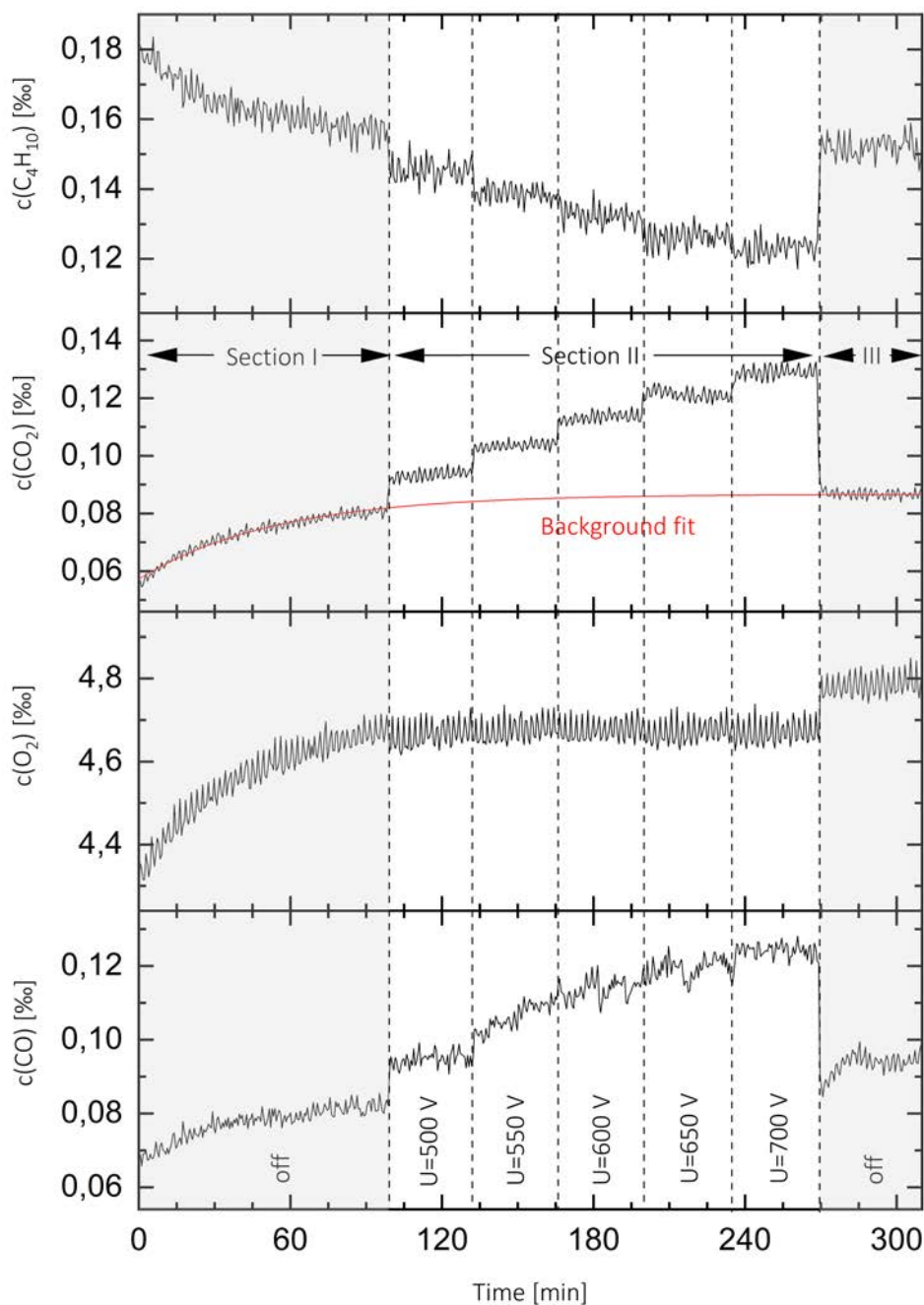
FIGURE 6.12: CO-, $CO_2$-, $O_2$- and $C_4H_{10}$-concentration as a function of time in which the applied voltage is changed. The MGA is operated with a helium gas flow of 2 slm and 0.5 sccm $C_4H_{10}$- and 10 sccm $O_2$-admixture. The nickel-grid is applied with a frequency at a 15 kHz and the dielectric is not covered with a catalyst. The background fit (red) is exemplary shown for the $CO_2$-signal.

### 6.5.1 Background fit

To estimate the temporal background concentration $c_{bg,species}$ for the respective specie, a time-depending exponential fit function is used determined by the recorded concentration when the discharge is turned off (0-97 min and 270-307 min in figure 6.12). This fit function has the following form

$$c_{bg,species}(t) = A \exp\left(-\frac{t}{\tau_{species}}\right) + c_0 \tag{6.2}$$

and depends on the time $t$, the fit constant $A$, the decay constant $\tau_{species}$ and initial concentration $c_0$. Its course is also exemplary demonstrated for the $CO_2$-concentration (red solid line) in figure 6.12. The concentration during the time without discharge is estimated well by the fit function and the decay constant of about 53 min is in an expected range and clearly higher than the residence time ($\tau_{residence} = (V_{pipe} + V_{MGA})\phi^{-1} \approx (32 \, cm^3 + 3 \, cm^3)(2000 \, cm^3 \, min^{-1})^{-1} \approx 1 \, s$) so that the background can be described by an exponential behaviour. The further parameters are shown in the appendix B.2.

### 6.5.2 Conversion rates

In general, the conversion rate $X$ is defined by the following equation

$$X_{C_8H_{10}}(t) = 1 - \frac{c_{after}}{c_{before}}, \tag{6.3}$$

depending on the species concentration before the reaction $c_{before}$ and on the concentration that is still present after the reaction $c_{after}$. Since the concentration signals are noisy, the average concentrations during the time when the voltage amplitude $U$ is kept constant is taken into account. The conversion rate $X_{C_4H_{10}}(U)$ is finally calculated with

$$X_{C_4H_{10}}(U) = 1 - \frac{\bar{c}_{C_4H_{10}}(U)}{\bar{c}_{bg,C_4H_{10}}(U)} \tag{6.4}$$

where $\bar{c}_{bg,C_4H_{10}}(U)$ stands for the estimated averaged concentration without discharge operation and $\bar{c}_{C_4H_{10}}(U)$ for the measured averaged concentration at plasma operation at respective adjusted voltage amplitude.

Figure 6.13 shows the conversion rate of the device without applied catalyst (black squares), with a catalytic load of $0.1 \, mg \, cm^{-2}$ (red circles) and $0.25 \, mg \, cm^{-2}$ (blue triangles) which is averaged over five measurements depending on the power. The error bars represent the absolute statistical error which is calculated to about $1\%$. The power estimation is described in 6.2.2. The frequency is kept constant at $15 \, kHz$. The $2 \, slm$ helium gas flow is admixtured with $0.5 \, sccm \, C_4H_{10}$ and $10 \, sccm \, O_2$.

(i) An increase in power by a factor of five initially leads to an increase in the conversion rate from around 7 % to 25 %. (ii) It appears that the conversion rates are higher for the non-catalytic device, but within the statistical error bars there is no significant difference in conversion rates between all devices. The catalyst introduced should therefore have no influence on the conversion. (iii) It is also visible that the power is not identical in all devices although all devices were operated with the same voltage variation.

Thus, the conversion must be driven only by the discharge which dissociates $C_4H_{10}$ and $O_2$ and allows more reactions to $CO_2$ and CO. This could also be observed in the similar surface DBD. A rising applied voltage leads to a higher applied electric field which must be shielded by a higher number of charged particles. These charged particles serve as reaction partners for the dissociation process.

By taking this into account, it matches with the results obtained by Zhang et al. where a rising applied voltage promotes plasma-catalysis in a pore-like discharge volume [36]. Indeed, as shown in figure 5.10, the electric field decreases by about 7 % between 400 V and 800 V for the IPP and by 18 % for the DPP for 200 µm cavities. However, these decreasing trends are caused by a high number of charged particles which shield the applied electric field. Moreover, these charged particles increase the coupled power and serve as reactants for the dissociation process and are available for the plasma-catalyst interaction.

One factor that distorts this measurement is the fact that not all cavities in the catalytic driven devices are in operation. As mentioned above, the catalyst is responsible for clogging cavities where no discharge can be ignited, and hence no conversion can take place and less power is available. This leads to lower conversion rates. To solve this problem, it would be necessary to count all cavities in operation using an ICCD camera during head-on observation and then normalize the output to the number of cavities in operation.
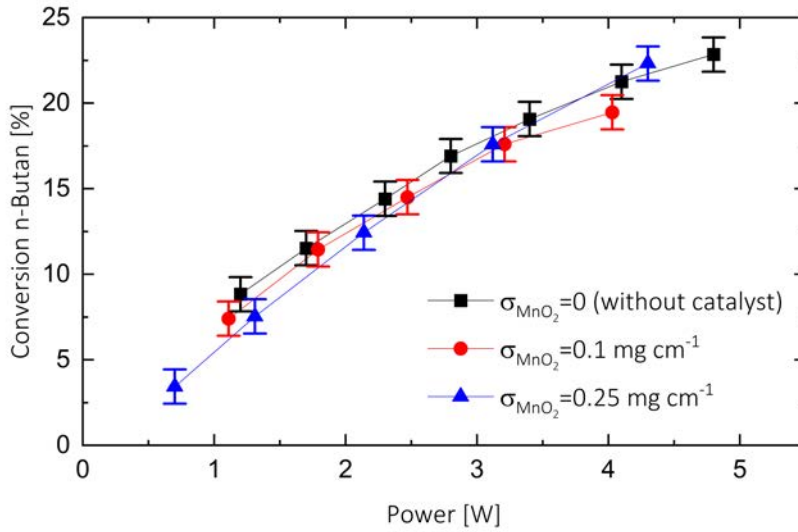
FIGURE 6.13: $C_4H_{10}$-conversion as a function of the power of MGA without catalyst (black squares), with catalyst load of $0.1\,\mathrm{mg\,cm^{-2}}$ (red circles) and catalyst load of $0.25\,\mathrm{mg\,cm^{-2}}$ (blue triangles). The frequency is kept constant at $15\,\mathrm{kHz}$. The $2\,\mathrm{slm}$ helium gas flow is admixed with $0.5\,\mathrm{sccm}$ $C_4H_{10}$ and $10\,\mathrm{sccm}$ $O_2$.

### 6.5.3 Selectivity

The catalyst does not have an impact on the conversion of $C_4H_{10}$ as shown before. However, the catalyst can influence the subsequent oxidation of CO to $CO_2$ which are both conversion products of $C_4H_{10}$. This was also observed in the similar surface DBD and it is expected since the used $\alpha$-$MnO_2$ catalyst is developed for this purpose. The so-called selectivity $S_{CO_2}(U)$ gives an estimation of the produced $CO_2$ in relation to the conversion of $C_4H_{10}$. This selectivity depends on the profit $P_{CO_2}(U)$ and is calculated with

$$S_{CO_2}(U) = \frac{P_{CO_2}(U)}{X_{C_4H_{10}}(U)} = \frac{\bar{c}_{CO_2}(U) - \bar{c}_{bg,CO_2}(U)}{X_{C_4H_{10}}(U)}. \tag{6.5}$$

Figure 6.14 illustrates the $CO_2$-selectivity averaged over five measurements depending on the power of the device without catalyst (black squares), with a catalytic load of $0.1\,\mathrm{mg\,cm^{-2}}$ (red circles) and $0.25\,\mathrm{mg\,cm^{-2}}$ (blue triangles). The error bars represent the absolute statistical error which is calculated to about $2.5\,\%$. The operation conditions are equal as in figure 6.13. In case of the uncovered device, the $CO_2$-selectivity rises from $35\,\%$ to $40\,\%$ with increasing power and reaches a plateau. For a catalytic load of $0.1\,\mathrm{mg\,cm^{-2}}$, the $CO_2$-selectivity rises from approx. $25\,\%$ to $30\,\%$. When the catalytic load is increased to $0.25\,\mathrm{mg\,cm^{-2}}$, the $CO_2$-selectivity increases from approx. $30\,\%$ to $35\,\%$.

The result that the catalytic driven devices provide a lower $CO_2$-selectivity is unexpected. The catalyst should increase the $CO_2$-selectivity compared to the general characteristics of the catalyst and measurements done in the surface DBD. The following three reasons can be responsible for this lower $CO_2$-selectivity: (i) The main reason is the low temperature which insufficient for the thermal activation of the $\alpha$-MnO$_2$ catalyst. Figure 6.15 shows the magnet temperature measured during the gas conversion process as a function of power of the device without applied catalyst (black squares), with a catalytic load of $0.1\,\mathrm{mg\,cm^{-2}}$ (red circles) and $0.25\,\mathrm{mg\,cm^{-2}}$ (blue triangles). The magnet temperature is averaged over five measurements. The statistical error corresponds to about $2\,\mathrm{K}$. The operation conditions are unchanged. The temperature is in a range between $300\,\mathrm{K}$ and $350\,\mathrm{K}$. It can be assumed that the temperature at the catalytic surface is higher. However, the catalyst is only separated by the $40\,\mathrm{\mu m}$ thick dielectric. The temperature near the catalyst might therefore be in the same order of magnitude as the magnet temperature and is too low for promoting thermic catalysis of CO to $CO_2$.
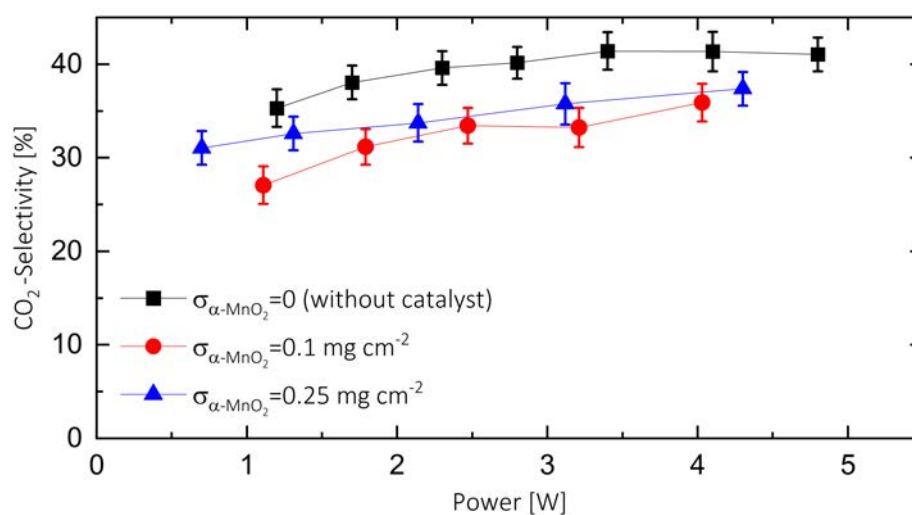


FIGURE 6.14: $CO_2$-selectivity depending on the power of MGA without introduced catalyst (black squares), with catalyst load of $0.1\,\mathrm{mg\,cm^{-2}}$ (red circles) and catalyst load of $0.25\,\mathrm{mg\,cm^{-2}}$ (blue triangles). The frequency is kept constant at $15\,\mathrm{kHz}$. The $2\,\mathrm{slm}$ helium gas flow is added with $0.5\,\mathrm{sccm}$ $C_4H_{10}$ and $10\,\mathrm{sccm}$ $O_2$.

Temperatures between $393\,\mathrm{K}$ and $413\,\mathrm{K}$ are required to detect a significant increase of the $CO_2$-selectivity in the similar surface DBD [99]. These high temperatures cannot be reached in the MGA since the magnet would be destroyed and demagnetised.

(ii) A second possible explanation is the coverage of the catalyst on the dielectric. As discussed in section 6.1, no homogeneous coverage of the catalyst on the dielectric is realised by the spray-coating procedure. Instead, an inhomogeneous aggregation is created with a height of approx. $15\,\mathrm{\mu m}$. The colliding electrons and ions on the not
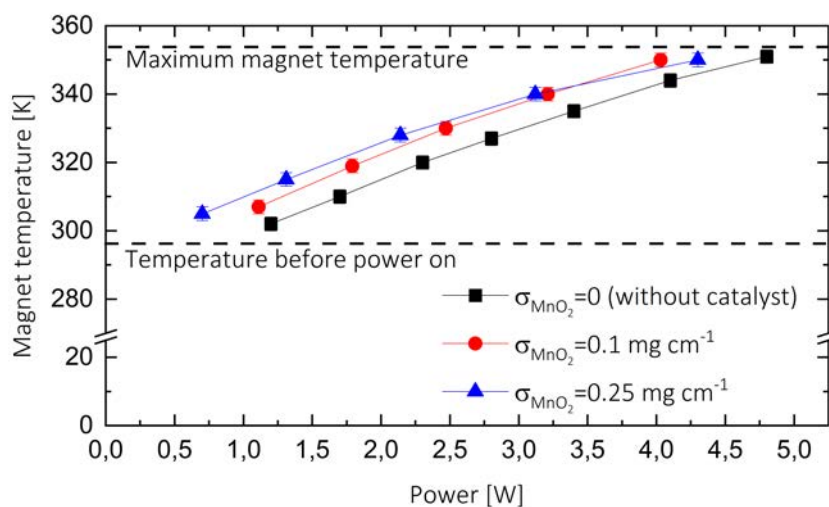
FIGURE 6.15: Magnet temperature depending on the power. The MGA is applied with a frequency of 15 kHz. The helium gas flow is set to be 2 slm and admixtured with 10 sccm $O_2$ and 0.5 sccm $C_4H_{10}$.

fully covered dielectric surface in the respective half phase cannot interact with the catalyst and the transformation of CO to $CO_2$ is therefore prevented.

(iii) The third possibility is that the nickel-grid is not ideally positioned on the catalytic dielectric film due to this agglomeration. This results in parasitic discharges occurring between covered dielectric and nickel-grid. A part of the power is not coupled during gas reformation and the $CO_2$-selectivity is therefore smaller.

**Summary**

In conclusion, the integrated $\alpha$-$MnO_2$ catalyst has a negative influence on the conversion and selectivity. The $C_4H_{10}$-conversion decreases if a catalyst is introduced and is only driven by the discharge. This is very much in line with the similar surface DBD. The $CO_2$-selectivity is also reduced in catalytic conditions. The main reason is that the temperature for the thermal activation of the $\alpha$-$MnO_2$ catalyst is not reached.

## 6.6 Surface investigations after discharge operation

The previous sections showed that gas conversion occurs in the micro cavity plasma array. The most dominant and visible example is the coking process on the nickel-grid and dielectric. By using the QMS, further products such as CO, $CO_2$ and $O_2$ could be identified.

However, the QMS cannot detect chemical species which deposit completely on the nickel-grid or dielectric during the discharge. It is possible that pyrolysis occurs in the MCPA which is a thermal-chemical transformation process. In this process, organic substances e.g. $C_4H_{10}$ react under high temperatures and mostly oxygen exclusion

avoiding combustion. As a result, not all species can be fully oxidised and undesirable by-products are formed. In addition, the QMS cannot determine how the previously integrated catalyst and the dielectric have survived plasma operation.

Therefore, it is necessary to extract the components such as the nickel-grid and dielectric from the MCPA after operation for subsequent surface investigations to examine these effects. This is possible in the MCPA due to the magnetic mounting of its components. These components can be extracted individually after plasma operation for surface investigations.

### 6.6.1 Laser scanning microscope

Laser scanning microscope (LSM) images are used as a first direct method to detect any changes or depositions on the dielectric or nickel-grid. Figure 6.16 shows images of both components which were exposed to the plasma treatment before. Figure 6.16a) shows the dielectric after an operation time of about 360 h in pure helium. The cavities have a diameter of 200 µm and separated from each other with an edge-to-edge distance by 100 µm. It is visible that each single cavity produces a deposit in form of black circle. Its diameter corresponds to the diameter of the cavity.
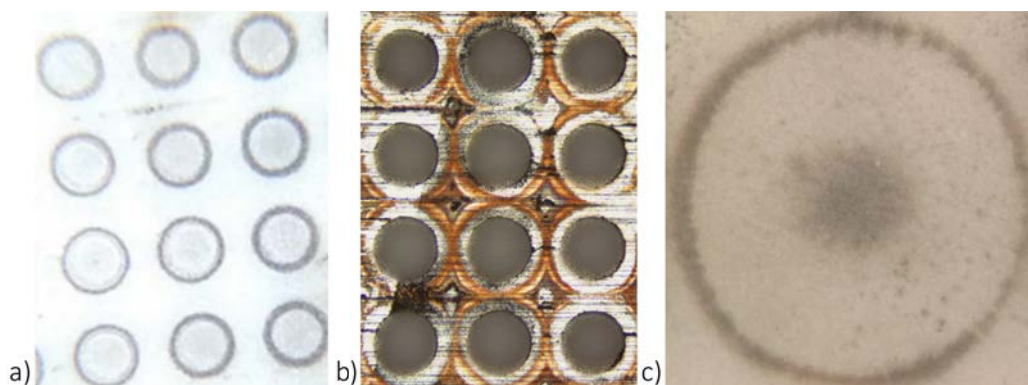


FIGURE 6.16: Photographs of several components after plasma-operation. a) Dielectric after an operation time of about 360 h in pure helium. The cavities have a diameter of 200 µm and separated from each other with an edge-to-edge distance of 100 µm. b) Nickel-grid after catalytic operation with 0.5 sccm admixtured $C_4H_{10}$. The cavities have a diameter of 200 µm and are separated by 100 µm. c) An enlarged image of a dielectric used under the same conditions as in b).

Figure 6.16b) reveals the nickel-grid after an operation with the integrated catalyst and 0.5 sccm admixtured $C_4H_{10}$. In this case, a brown coloured structure is deposited around the cavities on the nickel-surface. This can be an indicator for a chemical process outside the cavity volume. Furthermore, a kind of burned structure can be observed on the cavity at bottom left.

An enlarged image of the deposit on the dielectric is illustrated in figure c). The geometric dimensions are the same as in b). As in a), a large dark ring is visible with

the difference that that there is an additional spot in the middle. This might be a hint that a chemical process occurs during IPP as well as during DPP.

Based on these LSM-images, the question arises which chemical species are involved. In general, there are two different methods for analysing this. In a chemical approach, an attempt is made to remove the deposit by solvents and then to investigate it by further elaborate chemical procedures. However, it is not ensured that all deposited chemical species survive this solution or react with that. Not only species from the surface become solved but potentially material from the carrier (dielectric). In this thesis, x-ray photoelectron spectroscopy (XPS) is chosen as an analytical method which is a surface sensitive diagnostic tool. A positive feature of this device is that the structure deposited on the samples is not destroyed during the analysis. Its concept and obtained results are described in the following.

### 6.6.2 XPS-measurements

#### 6.6.2.1 Concept

XPS is a diagnostic tool to identify the chemical composition of the surfaces and is based on the photoelectric effect describing the escape of electrons out of a solid material through electromagnetic radiation. In a first step, the bound electron is excited, then transported through the solid to the surface, where it is finally released. The main part of XPS is the exposure of a sample with X-ray radiation with the energy $h\nu$ which triggers electrons to get out. Their kinetic energy $E_{kin}$ can be used to determine also their binding energy $E_B$ by using the following equation

$$E_{kin} = h\nu - E_R - E_B - \phi_p \tag{6.6}$$

and depends additionally on recoil energy $E_R$ and work function $\phi_p$. The former stands for the energy which an electron owns after a photon was emitted and is in a range between 0.1 eV and 0.01 eV. This is clearly too low compared to the uncertainties of the other variables and therefore negligible. The latter corresponds to the energy required to leave the solid material. In case that the work function of the material is known, the binding energy of the electron can be calculated. Since each atom has its own distribution of energy states and the value of the binding energy depends on the chemical environment of the atom, the chemical composition of the sample can be determined quantitatively.

However, the work function is unknown because its simultaneous measurement with the binding energy is not possible. To solve this problem, the sample is brought into electrical contact with the XPS. As a result, the Fermi-levels of the sample and the spectrometer equalize and $\phi_p$ corresponds the work function of the spectrometer.

The schematic sketch of the used XPS (PHI5000) is illustrated in figure 6.17. An electron beam generated in an electron gun impacts on an aluminium anode. These electrons have an energy of about 15 keV. This excites the electrons in the outer atomic shell and relaxes them, emitting X-rays. Afterwards, the radiation passes through a monochromator whereby only a photon energy of about 1486.6 eV is generated and focused as an 100 µm large spot on the sample. The released photoelectrons pass then a semi-spherical analyser where a certain voltage is applied to allow only electrons of a specific energy to pass the analyser. Two electron sources (guns) are installed in the XPS setup. The first source serves as a neutraliser for analysing non-conductive samples and provides low-energetic electrons to compensate positively charged space zones in the sample produced by electron escapes. The second source can be used for the Auger-electron spectroscopy (AES). The ion source (gun) is used to shoot high-energetic ions on the sample to i) remove impurities or material of the sample or to ii) execute deepth-resolved XPS-measurements. As a detector a multichannel detector is used which consists of two parallel plates with 16 connecting channels which serve as an electron multiplier. By applying a voltage of about 2 kV on the plates, incident electrons get accelerated from the first to the second plate where they generate secondary electrons. The resulting current is proportional to the number of incident electrons in the respective channel.
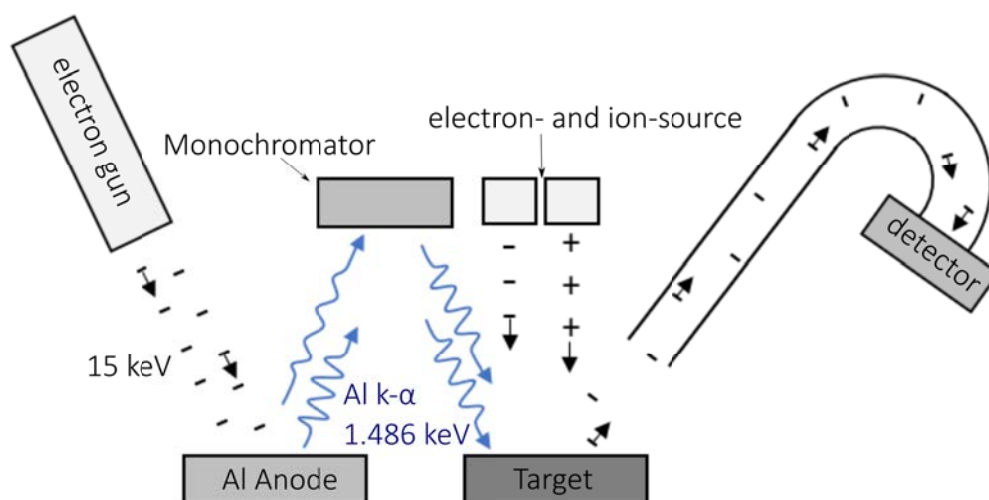


FIGURE 6.17: Schematic of the XPS measurement.

#### 6.6.2.2 Dielectric used in a pure helium discharge

Figure 6.18 demonstrates a XPS-spectrum obtained from an unused (black line) and used (red line) dielectric as illustrated in figure 6.16a). By comparing both spectra with each other, it is obvious that changes occur in a range between 0 eV and 200 eV and between 600 eV and 900 eV. These occurring peaks correspond to nickel, cobalt and iron which are main and minor elements of the nickel-grid. This may be explained

through a sputter process whereby nickel gets into the discharge and is finally deposited on the dielectric layer. Since the internal electric field has its maximum value along the boundary edge between the nickel grid and the dielectric and the distance between the two is smallest there, the nickel is mainly deposited around the edge and a ring-shaped structure is formed.
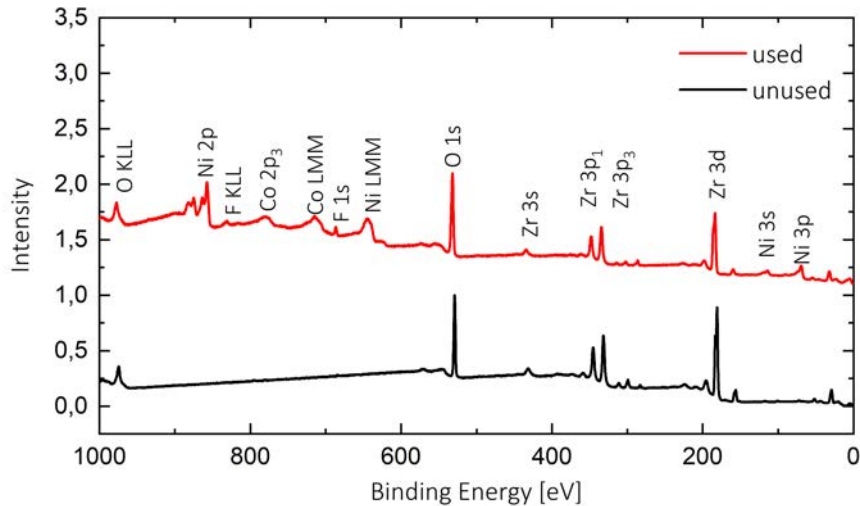


FIGURE 6.18: Measured XPS-spectrum of the dielectric as shown in figure 6.16a) of the MGA after an operation time of about 6 months in pure helium.

### 6.6.2.3 Dielectric after catalytic operation

Figure 6.19 shows the XPS-spectrum of the dielectric after catalytic operation with $C_4H_{10}$ and $O_2$ as shown in figure 6.16c) at several positions. A reference spectrum of the coated dielectric was done before catalytic operation (black solid line) to detect differences. Moreover, a spectrum was recorded after catalytic operation at the following positions:

II) Underneath the nickel-grid between two cavity structures (black dashed line).

III) In the center of the cavity structure (red solid line).

IV) At the edge of the cavity structure (red dashed line).

V) At the edge of the cavity structure in ambiance of the brown structure as recorded in 6.16b) (blue solid line).

At first, it is obvious that the spectra recorded at location II) is very similar to the reference spectrum. This was expected, as no discharge ignites underneath the nickel-grid and therefore no reactions should occur.

By comparing these two spectra with the recordings taken on the location III) and IV), differences can be observed. The peaks which corresponds to the binding of

carbon of magnesium carbide ($Mg_2C_2$, $Mg_2C_3$). Both are components of the dielectric and are used as hardeners. These bonds on the surface must have been destroyed during the discharge. Thermal decomposition can be ruled out because this requires temperatures above $750\,K$. Another difference is that an additional peak occurs, which can be assigned to the C binding of C-H or adventitous carbon. Since the discharge was operated with $C_4H_{10}$ that can create many species with C-H binding, and the sample was also in contact with the atmosphere during removal out of the MGA, both possibilities can be appropriate.

Similar effects can be observed at V). The peaks of the carbon binding of $Mg_2C_2$ are not visible. A small peak can only be detected for the carbon binding of $Mg_2C_3$. In addition, a peak can be observed which can be assigned to the C binding of C-O. The exact species could not be determined here. However, as $C_4H_{10}$ and $O_2$ were used for the discharge, many possibilities are existing.

This experiment shows that the dielectric is changed by the discharge and that further species are formed and deposited on the dielectric, although the conditions were not ideal for XPS measurements. Parameters such as gas admixtures were changed. In addition, the dielectric was removed and prepared for the XPS measurements without protection from the atmosphere. Some damages, especially on the catalytic layer, may also have occurred when removing the nickel-foil and dielectric.
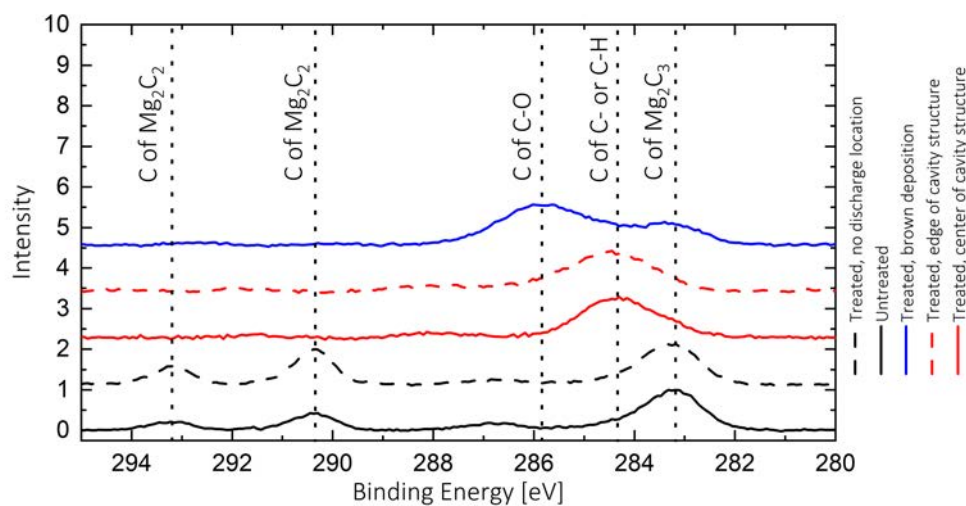


FIGURE 6.19: Measured XPS-spectrum of an untreated (red) and a used dielectric (brown) as shown in figure 6.16c) at several positions (brown- discharge location, magenta- no discharge location) after a catalytic operation with $C_4H_{10}$.

**Summary**

All in all, it can be summarised that the concept of MGA allows to investigate all individual components after plasma operation. Moreover, LSM images as well as XPS

recordings show effects on the dielectric and nickel-grid through the discharge as e.g. species deposition and structure changing of the dielectric. On the other hand, it has to be said that these measurements, especially the XPS-measurements are not performed under ideal conditions so that there is still much need for optimisation. It is possible that the catalyst coating is damaged during disassembling the MCPA. Moreover, all used components are not transported to the respective diagnostic tool in a clean gas atmosphere but only in ambient air which disturbs XPS-measurements.

# Chapter 7

# Conclusion

In this thesis, a modular- and layer-structured metal-grid array (MGA) was developed to examine the influence of cavity shape and material composition on the discharge performance of microplasma-arrays in general but also electric field strengths and plasma-enhanced catalysis in micro-structured cavities. Due to its durability and possibility of being equipped with a catalyst, it serves as an attractive device for plasma-enhanced catalysis and a good alternative for silicon-based devices.

The first part of chapter 4 dealt with the question to which extent a bare electrode and cylindrical cavity shape influence the known properties as pulsing, asymmetric discharge characteristic and ionisation wave propagation and how comparable silicon-based and metal grid arrays are. It can be stated as an overall result that both factors do not play a significant role for these discharge properties and that MGA and silicon-based arrays (SBA) are identical in their discharge performance. Using UI- and photomultiplier tube (PMT)-characteristics, it was found that pulsing occurs although electrical charge carriers can disappear on the nickel-grid and thus cannot contribute to a shielding process. For further interpretations this means that the simple picture where ions remain left during an electron avalanche is not right. Instead, it has to be considered that also ions are able to reach the dielectric due to high electric fields. Moreover, the discharge pulse of both configurations can be assigned to the atmospheric pressure glow discharge despite the differences in their structure.

Since the MGA configuration owns a flexibility in its components, phase-resolved imaging (PRI) could be applied in a grazing-perspective to focus on only one cavity line of a concave-formed nickel-grid. By using this setup, the picture of the asymmetric discharge characteristic posted in previous works could be confirmed: accelerating electrons create a discharge up to $50\,\mu m$ out of the cavities when the nickel-grid is biased positively and inside the cavities in the other phase. At the same time, the discharge is located close to the cavity edge during the IPP and centrally located during the DPP. Since the shape of the cavities does not seem to be responsible, the electrons could be accelerated by the strong electric field, which is mainly generated by the plane-parallel aligned electrodes. All in all, this asymmetry is still interesting for investigating IPC and PCC in a single device.

The investigation of the ionisation wave propagation obtained very interesting findings. In the case of the MGA, these show velocities of up to $0.5\,\mathrm{km\,s^{-1}}$ independent of the applied half-phase, which is also in good agreement with measured and simulated velocities in silicon-based devices. However, the photoionisation and ion-induced mechanisms assumed in the simulations cannot explain the wave propagation in both phases due to the discharge asymmetry along the cavity height from half-phase to half-phase and the different surface properties. Since the ionisation wave-propagation disappears in an operation under clean conditions, the future attention must be focussed on gas composition in and around the cavities rather than on geometric aspects. Nitrogen as a known impurity is able to decrease the ionisation energy and is at the same time an important factor for Penning ionisation through metastables or vibrationally excited species. In addition, it has to be mentioned that both species are independent on the asymmetric discharge characteristic due to their electrical neutrality.

High-resolution optical emission spectroscopy was used to detect the Stark effect. By using reasonable assumptions and theoretically calculated correlations by Foster, the measured displacements could be converted into spatial-integrated and time-resolved electric field strengths. These are in the range of about $30\,\mathrm{kV\,cm^{-1}}$ and show a good agreement with simulated electric field strengths of similar devices. In all measurements, regardless of the used temporal resolution, it was possible to measure stronger electric fields occur during the DPP. This might be correlated with the fact that in this phase, the discharge takes place closer to the dielectric where the highest applied electric field are existing. On average, the electric field strengths of the DPP are approximately $15\,\%$ larger than in the other phase. In addition, time-resolved measurements with a resolution of $1\,\mu\mathrm{s}$ showed that the electric field strengths decrease very slowly over time with the DPP, while they remain constant with the IPP. This is explained by a slight build-up of surface charges density on the dielectric, which counteracts the applied electric field.

In half-phase resolved measurements, the electric field strength could be determined as a function of many typical operation parameter. The strongest dependence is on the cavity diameter. In this case, the electric field decreased from $70\,\mathrm{kV\,cm^{-1}}$ to $30\,\mathrm{kV\,cm^{-1}}$ when the cavity diameter is halved from $200\,\mu\mathrm{m}$ to $100\,\mu\mathrm{m}$ during the decreasing potential phase. This trend was clearly lower in the other phase. This was connected to the fact that the applied electric field within the cavities is not homogeneously distributed. The highest electric field is located at the boundary edge between the dielectric surface and the nickel-grid where the discharge occurs during DPP and is therefore more sensitive to changing cavity diameters. Also, a strong dependency could be observed for the pressure at which the metal-grid array operates. IPP as well as DPP showed in this case the same trend that the electric field strength rises with higher pressures. This was explained by a decreasing ionisation probability whereby shielding becomes less effective. Both, the amplitude and frequency of the

applied voltage, have no significant influence on the electric field. In case of the former, the electric field remains constant in 200 μm cavities and slowly decreases in 100 μm cavities, although the applied electric field is doubled.

To better understand the physical excitation process, a simple stationary Townsend model was set up. This model supports the observed asymmetric discharge characteristic and the assumption that electrons accelerate along the cavity height and are responsible for excitation and ionisation. Based on that, it was also possible to explain the distinction in electric field strengths between the increasing and decreasing potential phase. With the exception of the absolute values, the trends for the cavity and pressure variation can be reproduced.

Since the MGA is modular, it was possible to introduce a catalytic material into the discharge volume that does not influence the general discharge performance. However, it must be mentioned that the catalyst has no influence on the conversion rates, so that synergetic effects could not be determined. Instead, only the discharge has converted n-butane into oxygen, carbon, carbon monoxide and carbon dioxide. For further measurements, it is necessary to heat the device to ensure that the catalyst becomes thermally active. By investigating the dielectric surface during and after operation, it could be observed that an interaction between discharge and surface takes place. The dielectric showed ring shaped traces which could be identified by XPS measurements to nickel, cobalt and iron. All in all, the modular MGA exhibit advantages over other devices since it can be disassembled into its components for detailed surface investigations.

# Chapter 8

# Outlook

In order to answer open aspects and questions of this work in the future, a brief outlook is given here.

In case of the ionisation wave propagation, it is absolutely necessary to investigate the cavity-structure under controlled nitrogen admixtures in the $0.1\,\%$ range since this species shows a possible correlation to the ionisation wave appearance. If it is possible to control the appearance of the wave, a relative simple experiment could be done to identify whether it is a photon- or charged particle-based process. The idea is sketched in figure 8.1a). In the usual $1\,cm^2$ large cavity structure, a cross-formed area without any cavities can be used to place various materials inside. In case of quartz-glass, photons could still reach adjacent cavities to trigger a first ionisation while the path of charged particles is prevented. By placing a dielectric and non-transparent material, both kind of species might not arrive surrounding cavities as shown in b). Since the ionisation wave can travel in random directions along the cavity structure, the cavity-free cross-shaped area would allow to place these material in propagation direction.

A further challenge that has to be approached is dealing with electrical investigations. One problem is the slow time behaviour of the amplifier, which produces non-ideal waveform excitations and thus blurred displacement currents. Due to this, a distinction to the discharge current is clearly restricted. To solve this problem, an electrical filter could be connected between the MGA and the amplifier to smooth this signal. Another point to obtain a better discharge- to displacement-current ratio might be reached by more incorporated cavities in the nickel-foil. This would yield a better separation of both current forms and information such as power capacitances could be received through Lissajous-figures. Last but not least, the plastic carrier needs to be modified to allow an individual operation of all four sub-arrays under equal gas conditions.

With respect to the plasma-enhanced catalysis, no synergetic effect could be determined. The main challenge is the limited and uncontrollable temperature of the metal-grid array during operation. Especially, the integrated magnet and used glue to tight
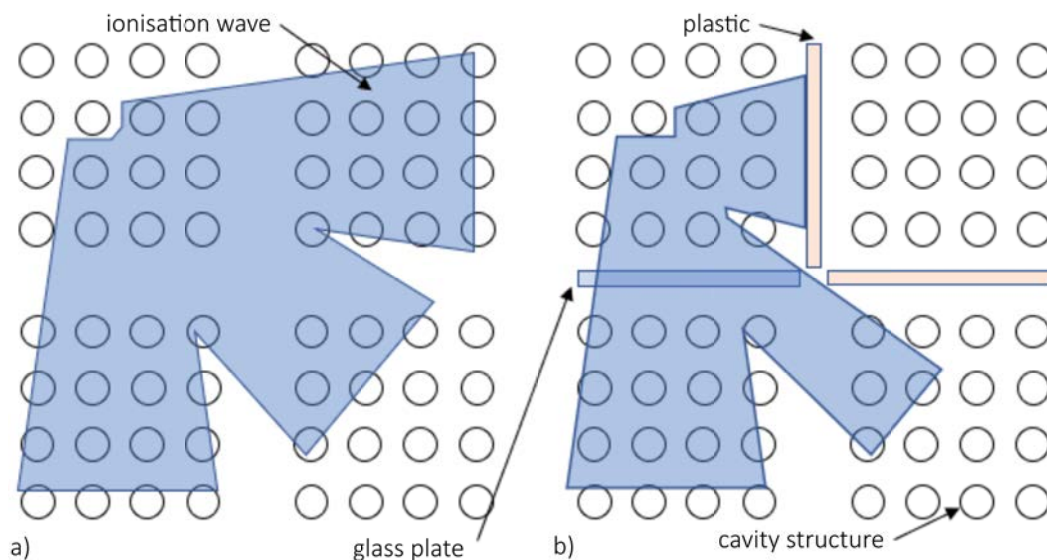
FIGURE 8.1: Experiment for investigation ionisation wave propagation
a) without materials between cavities and b) with different materials

the flow-operated MGA must be exchanged with materials that are able to resist temperatures of about $180\,°C$. To control the temperature typical plasma parameter variations, some kind of heating-system is required. A promising idea could be to place the bottom side of the magnet on a metal block heated either electrically or through a temperature controlled flow of hot oil. This could already allow thermal catalysis of CO to $CO_2$ that can then afterwards be optimised through plasma-specific processes.

A further optimisation must consider the actually used catalyst and its coverage on the dielectric. It would be better to use a dielectric material that can be covered with the catalyst without subsequent agglomeration. A second opportunity could be a mechanical or chemical treatment before coverage. In project A3 of the CRC1316, glass carrier were sandblasted before the catalyst is applied on it. In the case of the metal-grid array, a homogeneous surface would lead to a better defined cavity volume at the bottom and fewer gaps are formed between the electrode and dielectric in which parasitic discharges occur.

Further work is required on the electric fields. Although the Stark effect procedure provides reasonable values and trends, still the measurements were performed spatially integrated and a lot of assumptions went into the fitting procedure. The next step towards validation could be to examine almost identical structures with more spatially and temporally sensitive diagnostic instruments. A concrete way might be to use a channel-like structure in place of the cavities where laser radiation can pass through. Based on it, Electric-Field-Induced Second-Harmonic Generation (EFISHG) can be applied. However, with respect to the Stark effect procedure, only a view from the side into the discharge volume allows the identification and separation of $\pi$- and $\sigma$-polarised components. Another possibility would be to map the discharge volume

via the plane grating spectrometer directly on the camera and thus obtain a kind of two-dimensional electric field map.

The channel-like structure might not only be interesting for the electric field measurements but also for plasma catalysis aspects. Laser-based methods such as Two-Photon Absorption Laser-Induced Fluorescence (TALIF) or Laser-Induced Fluorescence (LIF) could be applied to investigate spatial-resolved respective densities in catalytic operation. Especially, close to the dielectric or alternatively catalytic surface, recombination process could be examined with that.

In the course of this work, surface charges have become increasingly important for the interpretation of discharge performance in micro cavity plasma arrays. However, its quantitative value is still unknown. An attractive tool to measure might be the so-called laser charge ablation. After a discharge pulse is finished, a laser spot is radiated on the dielectric to detach these residual charges. The creating current can than be measured with a probe and calculated into surface charge densities.

In conclusion, it can be said that there are still open questions in the field of micro cavity plasma arrays that can be addressed in the future, e.g. with the proposed focal points.

# Appendix A

# Fundamentals

## A.1  Coefficients for helium cross-sections

| $i$ | 1 | 2 | 3 | 4 | 5 |
|---|---|---|---|---|---|
| $A_i$ | $5.420 \times 10^{-3}$ | $1.1980 \times 10^{-2}$ | $-3.173 \times 10^{-2}$ | $1.606 \times 10^{-2}$ | $1.060 \times 10^{-1}$ |

TABLE A.1: Fitting coefficients of excitation cross-section from ground state to Helium $4^1D$-state by using equations 2.7 and 2.8 [75].

## A.2  Derivation of the Stark effect in helium by using perturbation theory

The following derivation of the Stark effect in helium by using perturbation theory is taken completely from [48] and is not the work of my own.

To be able to calculate the electric field from the spectra that will be measured, it is necessary to know the energy levels of helium in an external electric field. Therefore, the time-independent Schrödinger equation needs to be solved

$$H\Psi = E\Psi. \tag{A.1}$$

For the hydrogen atom, with hamiltonian

$$H_H = -\frac{\hbar^2}{2m}\nabla^2 - \frac{e^2}{4\pi\epsilon_0}\frac{1}{r}, \tag{A.2}$$

exact solutions to the Schrödinger equation can be found by using spherical coordinates and separation of variables

$$\Psi(r, \theta, \phi) = R(r)Y(\theta, \phi). \tag{A.3}$$

Elaborated calculations can be found in the literature [103–106] and here, only the results will be given. The radial wave function is given by

$$R_{nl}(r) = \sqrt{\left(\frac{2}{na_0}\right)^3 \frac{(n-l-1)!}{2n[(n+l)!]^3}} \exp\left\{-\frac{r}{na_0}\right\} \left(\frac{2r}{na_0}\right)^l \left[L_{n-l-1}^{2l+1}\left(\frac{2r}{na_0}\right)\right], \quad \text{(A.4)}$$

where $a_0$ is the Bohr radius and $L_{q-p}^p(x)$ is an associated Laguerre polynomial, given by

$$L_{q-p}^p(x) = (-1)^p \left(\frac{d}{dx}\right)^p L_q(x) \quad \text{(A.5)}$$

and $L_q$ is the qth Laguerre polynomial

$$L_q(x) = \exp(x)\left(\frac{d}{dx}\right)^q (\exp(-x)x^q). \quad \text{(A.6)}$$

The angular wave function is given by

$$Y_l^m(\theta, \phi) = \epsilon\sqrt{\frac{2l+1(l-|m|)!}{4\pi(l+|m|)!}} P_l^m(cos(\theta))\exp(im\phi) \quad \text{(A.7)}$$

in which $\epsilon = (-1)^m$ for m $\geq$ 0 and $\epsilon = 1$ for m $\leq$ 0. $P_l^m$ is the associated Legendre function, defined by

$$P_l^m = \left(1-x^2\right)^{\frac{|m|}{2}} \left(\frac{d}{dx}\right)^{|m|} P_l(x) \quad \text{(A.8)}$$

and $P_l(x)$ is the lth Legendre polynomial, defined by the Rodrigues formula

$$P_l(x) = \frac{1}{2^l l!}\left(\frac{d}{dx}\right)^l (x^2-1)^l. \quad \text{(A.9)}$$

The total wave function is then found by substituting equations A.4 and A.7 back into equation A.3.

For the helium atom, however, these exact solutions do not exist, but it will be shown that the solutions for the hydrogen atom can also be used for the helium atom. The hamiltonian of the helium atom is given by

$$H_{He} = -\frac{\hbar^2}{2m}\nabla_1^2 - \frac{e^2}{2\pi\epsilon_0}\frac{1}{r_1} - \frac{\hbar^2}{2m}\nabla_2^2 - \frac{e^2}{2\pi\epsilon_0}\frac{1}{r_2} + \frac{e^2}{2\pi\epsilon_0}\frac{1}{r_{12}} \quad \text{(A.10)}$$

where $r_1$ and $r_2$ give the distance from the nucleus to electrons 1 and 2, and $r_{12}$ gives the mutual distance between the two electrons. The first two terms correspond to one electron of the atom, the second two terms to the other electron, and the last term to the interaction between the two electrons. One electron occupies the ground state and the other electron occupies an excited state. When the excited level is a low-lying level, the wave functions of the two electrons overlap and thus they can influence one another. Here, the two electrons are considered to be far enough apart to not influence one another. The validation of this approximation is found by looking at the Coulomb force

$$F_e = \frac{e^2}{4\pi\epsilon_0} \frac{1}{r_{12}},\tag{A.11}$$

where the distance between the two electrons, $r_{12}$, will be linked to the radius of the electron orbital, given by

$$a_n = \frac{a_0 n^2}{Z},\tag{A.12}$$

in which $a_0$ is the Bohr radius. For the case when both electrons are in the ground state (n=1), the maximum distance between the two electrons is twice the radius of the first electron orbital:

$$r_{12} = 2a_1 = a_0.$$

In the case considered here, one electron is in the first electron orbital and one electron in the fourth electron orbital (n=4). The minimum distance between these two electrons is

$$r_{12} = a_4 - a_1 = \frac{15a_0}{2}.$$

Thus, the distance between the electrons in this case is at least a factor 15/2 larger than the distance between two electrons in the ground state. Regarding equation A.11, this yields a Coulomb force of at least $(15/2)^2$ times smaller, validating the approximation that wave functions of the two electrons in our case are not overlapping.

Another argument is found by looking at the exchange integral $J_{ex}$, which is a measure for the frequency with which the two electrons exchange their quantum states [105], given by

$$J_{ex} = \frac{4Z^3(Z-1)^{2n+1}n^2}{[Z(n+1)-1]^{2n+3}} \frac{2n+3}{2n-1}\tag{A.13}$$

After time interval $\pi/2J_{ex}$, the two electrons have interchanged their respective roles, and after time interval $\pi/J_{ex}$, they are back in their original orbits. Here, time is measured in the atomic unit $1/4\pi R_y$, where Ry is the Rydberg frequency. The period of exchange $\tau$ (in cgs units) is then given by

$$\tau = \frac{\pi}{J_{ex}}\frac{1}{4\pi R_y} = \frac{1}{4J_{ex}R_y} = \frac{0.75 \times 10^{-16}\,\text{s}}{J_{ex}}. \tag{A.14}$$

The transitions of the helium atom used in this study take place at n=4 and helium has Z=2, yielding $J_{ex} = 2.56 \times 10^{-8}$ and $\tau = 17.56\,\text{s}$. The residence time of the helium atoms in the plasma jet in this study is much smaller, in the order of µs to ns, thus the exchange period of the electrons is long enough to have no overlap in their wave functions.

Therefore, the interaction term in the hamiltonian can be neglected and what is left is the hamiltonian of the hydrogen atom with an extra charge.

Placing the atom in an externally applied electric field leads to a perturbation of the hamiltonian, because of the interaction between the electron of the atom and the electric field, given by

$$H^{1'} = eFz, \tag{A.15}$$

where the applied field $F = |\tilde{E}|$ is directed along the positive z-axis. To account for the extra charge in the nucleus of the helium atom, compared to the hydrogen atom, an extra entry is added to the perturbed hamiltonian, which corresponds to the difference in energy between the hydrogen and helium terms with the same $n$, as a function of $l$

$$H^{1''} = hc\nu_l, \tag{A.16}$$

in which $\nu_l$ is the difference (in $\text{cm}^{-1}$) between the helium and the corresponding hydrogen terms. The total perturbation to the hamiltonian (equation A.2) is then

$$H^1 = H^{1'} + H^{1''} = eFz + hc\nu_l. \tag{A.17}$$

To solve the Schrödinger equation with this addition, perturbation theory needs to be applied. Since the solution of the unperturbed Schrödinger equation leads to degenerate energy levels, the non-degenerate perturbation theory is not valid and thus degenerate perturbation theory has to be applied.

When the energy $E_n^0$ is $g_n$-fold degenerate,there are $g_n$ wave functions with the same energy $E_n^0$. The unperturbed Schrödinger equation

$$H^0 \Psi_n^0 = E_n^0 \Psi_n^0 \tag{A.18}$$

then changes into

$$H^0 \Psi_{ni}^0 = E_n^0 \Psi_{ni}^0, i = 1, 2, ..., g_n, \tag{A.19}$$

where $H^0$ is given by equation A.2. The degenerate wave functions can be written as a linear combination

$$\psi_n^0 = \sum_{i=1}^{g_n} c_{ni} \psi_{ni}^0, \tag{A.20}$$

which is too an eigenfunction of the unperturbed hamiltonian, with the same eigenvalue

$$H^0 \psi_n^0 = \sum_{i=1}^{g_n} c_{ni} H^0 \psi_{ni}^0 = E_n^0 \sum_{i=1}^{g_n} c_{ni} \psi_{ni}^0 = E_n^0 \Psi_n^0 \tag{A.21}$$

Still, the Schrödinger equation (equation A.1) needs to be solved, which changes into

$$(H^0 + H^1)\psi_{ni} = E_{ni}\psi_{ni}, i = 1, 2, ..., g_n. \tag{A.22}$$

Because $H^1$ is a small perturbation, the eigenvalues and eigenfunctions can be written as expansion series

$$E_{ni} = E_n^0 + E_{ni}^1 + E_{ni}^2 + ..., i = 1, 2, ..., g_n. \tag{A.23}$$

$$\psi_{ni} = \psi_n^0 + \psi_{ni}^1 + \psi_{ni}^2 + ..., i = 1, 2, ..., g_n. \tag{A.24}$$

where $E_n^0$ is the same for all values of i. Substituting these expressions into equation A.22 gives, up to first order,

$$H^0 \psi_{ni}^0 = E_n^0 \psi_{ni}^0 \tag{A.25}$$

$$H^0 \psi_{ni}^1 + H^1 \psi_{ni}^0 = E_n^0 \psi_{ni}^1 + E_n^1 \psi_{ni}^0 \tag{A.26}$$

where equation A.25 is just the unperturbed Schrödinger equation (equation A.18). The first order correction will now be calculated, and analogously higher order corrections can be calculated. Taking the inner product of $\psi_{\text{ni}}^0$ with equation A.26 gives

$$\langle\psi_{ni}^0|H^0\psi_{ni}^1\rangle + \langle\psi_{ni}^0|H^1\psi_{ni}^0\rangle = E_n^0\langle\psi_{ni}^0|\psi_{ni}^1\rangle + E_{ni}^1\langle\psi_{ni}^0|\psi_{ni}^0\rangle \tag{A.27}$$

The hermitian property of $H^0$ makes the first term on the left and right hand side cancel against one another, leaving

$$\langle\psi_{ni}^0|H^1\psi_{ni}^0\rangle = E_{ni}^1\langle\psi_{ni}^0|\psi_{ni}^0\rangle \tag{A.28}$$

Substituting equation A.20 and using the orthonormality $\delta_{\text{kn}} = \langle\psi_{\text{ki}}^0|\psi_{\text{ni}}^0\rangle$ yields

$$\sum_{j=1}^{g_n} c_{nj}\langle\psi_{ni}^0|H^1|\psi_{nj}^0\rangle = E_{ni}^1\sum_{j=1}^{g_n} c_{nj}\langle\psi_{ni}^0|\psi_{nj}^0\rangle = E_{ni}^1 c_{ni} \tag{A.29}$$

or

$$\sum_{j=1}^{g_n} c_{nj}\left(H_{ni,nj}^1 - E_{ni}^1\delta_{ij}\right) = 0, \tag{A.30}$$

where $H_{\text{ni,nj}}^1 = \langle\psi_{\text{ni}}^0|H^1|\psi_{\text{nj}}^0\rangle$. For equation A.30, a trivial solution is $c_{\text{nj}} = 0$ for all $j$. A non-trivial solution only exists if the determinant with elements $\left(H_{\text{ni,nj}}^1 - E^1\delta_{\text{ij}}\right)$ vanishes, which yields the secular equation

$$|H_{ni,nj}^1 - E_{ni}^1\delta_{ij}| = 0. \tag{A.31}$$

Satisfied, it will give $g_n$ roots: $E_{\text{n1}}^1, E_{\text{n2}}^1, ..., E_{\text{ng}_n}^1$, yielding the first-order corrections to the degenerate eigenvalues

$$E_{ni} = E_n^0 + E_{ni}^1, i = 1, 2, ..., g_n. \tag{A.32}$$

Because of the perturbation, the degeneracy is removed as it vanishes. Instead, the degenerate level $E_n$ is split into sublevels with energies given in equation A.32 and the appropriate wave functions $\psi_{ni}$.

Returning to the case of the helium atom in an external electric field, the energy levels $E_n$ (principal quantum number $n$) split into $m$ (magnetic quantum number) sub-levels, in which the individual terms are arranged to index $l$ (angular momentum quantum number). Since only linearly polarized light is taken into account, $\Delta m = 0$

and thus m $=$ m′. The secular equation (equation A.31), which needs to be solved, becomes then

$$|H^1_{nlm,nl'm} - E^1\delta ll'| = 0, |m| \le l \le (n-1), \tag{A.33}$$

where the matrix elements $H^1_{nlm,nl'm}$ are given by the inner product of equation A.17 with the unperturbed eigenfunctions $\psi_{nlm}(r,\theta,\phi)$. Then, equation A.33 gives

$$\begin{vmatrix} H_{ll} & H_{l,l+1} & ... & H_{l,n-1} \\ H_{l,l+1} & H_{l+1,l+1} - E^1 & ... & H_{l+1,n-1} \\ ... & ... & ... & ... \\ H_{n-1,l} & H_{n-1,l+1} & ... & H_{n-1,n-1} - E^1 \end{vmatrix} = 0. \tag{A.34}$$

The quantum numbers $n$ and $m$ are still inside equation A.34, but since they are constant for every element in the matrix, they are not written for simplicity. The matrix elements $H_{ll'}$ are given by

$$H_{ll'} = eF \int \psi_{nlm}(\vec{r})z\psi^*_{nl'm}(\vec{r})d\vec{r} + hc\nu_l \int \psi_{nlm}(\vec{r})\psi^*_{nl'm}(\vec{r})d\vec{r}. \tag{A.35}$$

The second integral yields hc$\nu_l\delta_{ll'}$, while using spherical coordinates ($z = \text{rcos}(\theta)$) and equation A.3, the first integral becomes

$$eF \int\limits_0^\infty R_{nl}rR_{nl'}r^2dr \int\limits_0^{4\pi} Y_{lm}cos(\theta)Y^*_{l'm}d\Omega.$$

The radial wave function is given by equation A.4, yielding A.7 [103, 105]

$$\int\limits_0^\infty R_{nl-1}rR_{nl}r^2dr = \int\limits_0^\infty R_{nl}rR_{nl-1}r^2dr = \frac{3}{2}a_0n\sqrt{n^2-l^2} \tag{A.36}$$

and the angular wave function is given by equation A.7, yielding [103, 105]

$$\int\limits_0^{4\pi} Y_{l-1m}cos(\theta)Y^*_{lm}d\Omega = \int\limits_0^{4\pi} Y_{lm}cos(\theta)Y^*_{l-1m}d\Omega = \sqrt{\frac{l^2-m^2}{(2l+1)(2l-1)}} \tag{A.37}$$

Thus, the first term of equation A.35 is given by

$$H_{l-1,l} = H_{l,l-1} = \frac{3}{2}eFa_0n\sqrt{n^2-l^2}\sqrt{\frac{l^2-m^2}{(4l^2-1)}}, \tag{A.38}$$

which are off-diagonal elements, while the second term is given by

$$H_{l,l'} = hc\nu_l \delta_{l,l'}, \tag{A.39}$$

which are diagonal elements. Dividing all elements by $-1$ and setting

$$f(n,m,l) = f_{nml} = \frac{(n^2 - l^2)(l^2 - m^2)}{4l^2 - 1} \tag{A.40}$$

and

$$\kappa = \frac{3ea_0}{2hc} \approx 6.40 \times 10^{-5}\,\text{cm}^{-1}, \tag{A.41}$$

gives the secular equation for the helium atom

$$\begin{bmatrix} \nu_l + E^1 & -n\kappa F\sqrt{f_{nml+1}} & 0 & ... \\ -n\kappa F\sqrt{f_{nml+1}} & \nu_{l+1} + E^1 & -n\kappa F\sqrt{f_{nml+2}} & ... \\ 0 & -n\kappa F\sqrt{f_{nml+2}} & \nu_{l+2} + E^1 & ... \\ ... & ... & ... & ... \end{bmatrix} = 0. \tag{A.42}$$

The displacements of the energy levels are measured from the diffuse (D) line, therefore, $x = E^1 + \nu_1$, which is the displacement of the helium line in $\text{cm}^{-1}$, measured from the D-line and $\lambda_l = \nu_2 - \nu l$ are substituted into the previous matrix to yield the final secular equation

$$\begin{vmatrix} x + \lambda_l & -n\kappa F\sqrt{f_{nml+1}} & 0 & ... \\ -n\kappa F\sqrt{f_{nml+1}} & x + \lambda_{l+1} & -n\kappa F\sqrt{f_{nml+2}} & ... \\ 0 & -n\kappa F\sqrt{f_{nml+2}} & x + \lambda_{l+2} & ... \\ ... & ... & ... & ... \end{vmatrix} = 0. \tag{A.43}$$

In this study, two helium lines are considered. The secular equation will be solved for both lines, yielding expressions for the wavelength shift as a function of the electric field.

The allowed transition at the $492.2\,\text{nm}$ helium line is $1s4d^1D \rightarrow 1s2p^1P^0$ and the forbidden transition is $1s4f^1F^0 \rightarrow 1s2p^1P^0$. Therefore, we have the line groups $4(S, P, D, F) \rightarrow 2P$, or $n = 4(l = 0, 1, 2, 3) \rightarrow n = 2(l = 1)$, at S=0. For $m = 1$, and $|m| \leq l \leq (n-1) \leftrightarrow 1 \leq l \leq 3$ and the matrix in equation A.43 is a $3 \times 3$ matrix, thus the equation we need to solve is

$$\begin{vmatrix} x + \lambda_l & -n\kappa F \sqrt{f_{4,1,2}} & 0 \\ -n\kappa F \sqrt{f_{4,1,2}} & x & -n\kappa F \sqrt{f_{4,1,3}} \\ 0 & -n\kappa F \sqrt{f_{4,1,3}} & x + \lambda_3 \end{vmatrix} = 0.$$

From the date in A.2 and A.3, $\lambda_1$ and $\lambda_3$ have been calculated to give $\lambda_1 = 46.3\,\mathrm{cm}^{-1}$ and $\lambda_3 = 46.3\,\mathrm{cm}^{-1}$. Furthermore, we have

$$f(4,1,2) = \frac{12}{5}, f(4,1,3) = \frac{8}{5}$$

to get

$$\begin{vmatrix} x + \lambda_l & -4\kappa F \sqrt{\dfrac{12}{5}} & 0 \\ -4\kappa F \sqrt{\dfrac{12}{5}} & x & -4\kappa F \sqrt{\dfrac{8}{5}} \\ 0 & -4\kappa F \sqrt{\dfrac{8}{5}} & x + \lambda_3 \end{vmatrix} = 0.$$

Expanded, this gives the characteristic polynomial equation

$$x^3 + x^2(\lambda_1 + \lambda_3) + x\left[\lambda_1\lambda_3 - 4(4\kappa F)^2\right] - (4\kappa F)^2\left(\frac{8}{5}\lambda_1 + \frac{12}{5}\lambda_3\right) = 0, \qquad \text{(A.44)}$$

which has three solutions, for the energy levels $\mathrm{l} = 1, 2, 3 \leftrightarrow \mathrm{P, D, F}$.

For the $\mathrm{n} = 4$, $\mathrm{m} = 0$, $\mathrm{S} = 0$ level, $|\mathrm{m}| \leq \mathrm{l} \leq (\mathrm{n} - 1) \leftrightarrow 0 \leq \mathrm{l} \leq 3$ and the matrix in equation A.43 is a $4 \times 4$ matrix, thus the secular equation becomes

$$\begin{vmatrix} x + \lambda_0 & -4\kappa F \sqrt{5} & 0 & 0 \\ -4\kappa F \sqrt{5} & x + \lambda_1 & -4\kappa F \sqrt{\dfrac{16}{5}} & 0 \\ 0 & -4\kappa F \sqrt{\dfrac{16}{5}} & x & -4\kappa F \sqrt{\dfrac{9}{5}} \\ 0 & 0 & -4\kappa F \sqrt{\dfrac{9}{5}} & x + \lambda_3 \end{vmatrix} = 0.$$

where

$$f(4,0,1) = 5, f(4,0,2) = \frac{16}{5}, f(4,0,3) = \frac{9}{5}$$

have already been substituted and $\lambda_0 = -506.2\,\mathrm{cm}^{-1}$. The characteristic polynomial equation is

$$x^4 +$$

$$x^3(\lambda_0 + \lambda_1 + \lambda_3) +$$

$$x^2\left(\lambda_0\lambda_1 + \lambda_1\lambda_3 + \lambda_0\lambda_3 - 10(4\kappa F)^2\right) +$$

$$x\left[\lambda_0\lambda_1\lambda_3 - (4\kappa F)^2\left(5\lambda_0 + \frac{9}{5}\lambda_1 + \frac{41}{5}\lambda_3\right)\right] - (4\kappa F)^2\lambda_0\left(\frac{9}{5}\lambda_1 + \frac{16}{5}\lambda_3\right) +$$

$$9(4\kappa F)^4 = 0. \tag{A.45}$$

For the $n = 4$, $n = 2$, $S = 0$ level, $|m| \leq l \leq (n-1) \leftrightarrow 2 \leq l \leq 3$ and the matrix in equation A.43 is a $2 \times 2$ matrix, thus the secular equation becomes

$$\begin{vmatrix} x & -4\kappa F \\ -4\kappa F & x + \lambda_3 \end{vmatrix} = 0.$$

where

$$f(4, 2, 1) = 1$$

has already been substituted and the characteristic polynomial is

$$x^2 + \lambda_3 x - (4\kappa F)^2 = 0 \tag{A.46}$$

| S | n | L | J | Conf. | Term symbol | Energy [cm$^{-1}$] |
|---|---|---|---|-------|-------------|---------------------|
| 0 | 4 | 0 | 0 | 1s4s | $^1$S | 190 940.226 355 |
| 0 | 4 | 1 | 1 | 1s4p | $^1$P$^0$ | 191 492.711 909 |
| 0 | 4 | 2 | 2 | 1s4d | $^1$D | 191 446.455 740 5 |
| 0 | 4 | 3 | 3 | 1s4f | $^1$F$^0$ | 191 451.897 460 84 |
| 0 | 4 | 0 | 1 | 1s4s | $^3$S | 190 298.113 260 |
| 0 | 4 | 1 | 2 | 1s4p | $^3$P$^0$ | 191 217.040 967 |
| 0 | 4 | 2 | 3 | 1s4d | $^3$D | 191 444.480 929 2 |
| 0 | 4 | 3 | 4 | 1s4f | $^3$F$^0$ | 191 451.881 088 55 |

TABLE A.2: Energy levels of helium [107]

| S | n | L | J | Conf. | Term symbol | Energy [cm$^{-1}$] |
|---|---|---|---|---|---|---|
| -1/2 | 4 | 0 | 1/2 | 4s | $^2$S | 102 823.853 021 1 |
| -1/2 | 4 | 1 | 1/2 | 4p | $^2$P$^0$ | 102 823.848 582 5 |
| -1/2 | 4 | 2 | 3/2 | 4d | $^2$D | 102 823.894 250 |
| -1/2 | 4 | 3 | 5/2 | 4f | $^2$F$^0$ | 102 823.909 490 |
| 1/2 | 4 | 0 | 1/2 | 4s | $^2$S | 102 823.853 021 1 |
| 1/2 | 4 | 1 | 3/2 | 4p | $^2$P$^0$ | 102 823.894 317 5 |
| 1/2 | 4 | 2 | 5/2 | 4d | $^2$D | 102 823.909 487 1 |
| 1/2 | 4 | 3 | 7/2 | 4f | $^2$F$^0$ | 102 823.917 091 |

TABLE A.3: Energy levels of hydrogen [108]

# Appendix B

# Potential for catalytic operation and surface interaction

## B.1   Twin SDBD electrode configuration
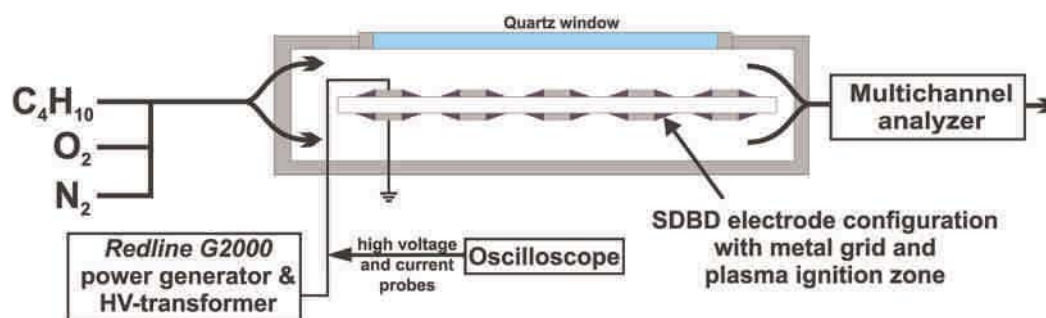


FIGURE B.1: Sketch of the twin SDBD electrode configuration [99].

## B.2   Coefficients for Background fit

| $A$ [‰] | $\tau_{species}$ [s] | $c_0$ [‰] |
|---|---|---|
| $-0.002\,94$ | $-3242.62$ | $0.008\,67$ |

TABLE B.1: Fitting coefficients of background fit

# Bibliography

[1]   Francis F. Chen. "Industrial applications of low–temperature plasma physics". In: *Physics of Plasmas* 2.6 (1995), pp. 2164–2175.

[2]   I. Adamovich et al. "The 2017 Plasma Roadmap: Low temperature plasma science and technology". In: *Journal of Physics D: Applied Physics* 50.32 (2017), p. 323001.

[3]   Seiji Samukawa et al. "The 2012 Plasma Roadmap". In: *Journal of Physics D: Applied Physics* 45.25 (2012), p. 253001.

[4]   Roxana Silvia Tipa and Gerrit M. W. Kroesen. "Plasma-Stimulated Wound Healing". In: *IEEE Transactions on Plasma Science* 39.11 (2011), pp. 2978–2979.

[5]   M. Moisan et al. "Low-temperature sterilization using gas plasmas: a review of the experiments and an analysis of the inactivation mechanisms". In: *International Journal of Pharmaceutics* 226.1-2 (2001), pp. 1–21.

[6]   M. Laroussi. "Sterilization of Contaminated Matter with an Atmospheric Pressure Plasma". In: *IEEE Transactions on Plasma Science* 24 (1996).

[7]   K. H. Becker, K. H. Schoenbach, and J. G. Eden. "Microplasmas and applications". In: *Journal of Physics D: Applied Physics* 39.3 (2006), R55–R70.

[8]   J. Golda et al. "Corrigendum: Concepts and characteristics of the 'COST Reference Microplasma Jet' (2016 J. Phys. D: Appl. Phys . 49 084003)". In: *Journal of Physics D: Applied Physics* 52.2 (2019), p. 029503.

[9]   N. Bibinov et al. "Spectroscopic characterization of an atmospheric pressure $\mu$-jet plasma source". In: *Journal of Physics D: Applied Physics* 44.34 (2011), p. 345204.

[10]  Patrick Preissing et al. "Three-dimensional density distributions of NO in the effluent of the COST reference microplasma jet operated in He/N 2 /O 2". In: *Plasma Sources Science and Technology* 29.12 (2020), p. 125001.

[11]  David Steuer et al. "2D spatially resolved O atom density profiles in an atmospheric pressure plasma jet: from the active plasma volume to the effluent". In: *Journal of Physics D: Applied Physics* 54.35 (2021), p. 355204.

[12]  S.-J. Park et al. "Silicon microdischarge devices having inverted pyramidal cathodes: Fabrication and performance of arrays". In: *Applied Physics Letters* 78.4 (2001), pp. 419–421.

[13] J. G. Eden and S-J Park. "Microcavity plasma devices and arrays: a new realm of plasma physics and photonic applications". In: *Plasma Physics and Controlled Fusion* 47.12B (2005), B83.

[14] M. K. Kulsreshath et al. "Width-dependent interaction of trench-like microdischarges arranged in sub-arrays on a single silicon-based chip". In: *Plasma Sources Science and Technology* 23.4 (2014), p. 045012.

[15] J. G. Eden and S.-J. Park. *Eden Park Illumination.* URL: https://edenpark.com/.

[16] H. Boettner et al. "Excitation dynamics of micro-structured atmospheric pressure plasma arrays". In: *Journal of Physics D: Applied Physics* 43.12 (2010), p. 124010.

[17] M. K. Kulsreshath et al. "Ignition dynamics of dry-etched vertical cavity single-hole microdischarge reactors in ac regime operating in noble gases". In: *Journal of Physics D: Applied Physics* 47.33 (2014), p. 335202.

[18] Paul M. Bryant et al. "Time-Resolved Imaging of a Silicon Micro-Cavity Discharge Array". In: *IEEE Transactions on Plasma Science* 36.4 (2008), pp. 1248–1249.

[19] Yu B. Golubovskii et al. "Influence of interaction between charged particles and dielectric surface over a homogeneous barrier discharge in nitrogen". In: *J. Phys. D: Appl. Phys.* 35 (2002), pp. 751–761.

[20] Yu B. Golubovskii et al. "Modelling of the homogeneous barrier discharge in helium at atmospheric pressure". In: *Journal of Physics D: Applied Physics* (2003), pp. 39–49.

[21] Alexander Wollny et al. "Ignition of a Microcavity Plasma Array". In: *IEEE Transactions on Plasma Science* 39.11 (2011), pp. 2684–2685.

[22] Alexander Wollny et al. "Ionization wave propagation on a micro cavity plasma array". In: *Applied Physics Letters* 99.14 (2011), p. 141504.

[23] K. Becker et al. "Environmental and biological applications of microplasmas". In: *Plasma Physics and Controlled Fusion* 47.12B (2005), B513–B523.

[24] J. Christopher Whitehead. "Plasma catalysis: A solution for environmental problems". In: *Pure and Applied Chemistry* 82.6 (2010), pp. 1329–1336.

[25] Rasoul Yarahmadi and Somayeh Soleimani-Alyar. "A Laboratory Study of Low-Temperature CO Removal from Mobile Exhaust Gas Using In-Plasma Catalysis". In: *Emission Control Science and Technology* 6.1 (2020), pp. 17–27.

[26] Peter A. Gorry, J. Christopher Whitehead, and Jinhui Wu. "Adaptive Control for NOx Removal in Non-Thermal Plasma Processing". In: *Plasma Processes and Polymers* 4.5 (2007), pp. 556–562.

[27] Rong Mingzhe et al. "Experimental Study of $SO_2$ Removal by Pulsed DBD Along with the Application of Magnetic Field". In: *Plasma Science and Technology* 9.6 (2007), pp. 717–720.

[28] Xinbo Zhu et al. "Catalyst screening for acetone removal in a single-stage plasma-catalysis system". In: *Catalysis Today* 256 (2015), pp. 108–114.

[29]   A. Koutsospyros et al. "Destruction of hydrocarbons in non-thermal, ambient-pressure, capillary discharge plasmas". In: *International Journal of Mass Spectrometry* 233.1-3 (2004), pp. 305–315.

[30]   Kevin Ollegott et al. "Fundamental Properties and Applications of Dielectric Barrier Discharges in Plasma–Catalytic Processes at Atmospheric Pressure". In: *Chemie Ingenieur Technik* 92.10 (2020), pp. 1542–1558.

[31]   J. Christopher Whitehead. "Plasma–catalysis: the known knowns, the known unknowns and the unknown unknowns". In: *Journal of Physics D: Applied Physics* 49.24 (2016), p. 243001.

[32]   E. C. Neyts and A. Bogaerts. "Understanding plasma catalysis through modelling and simulation—a review". In: *Journal of Physics D: Applied Physics* 47.22 (2014), p. 224010.

[33]   Ayman A. Abdelaziz, Tatsuo Ishijima, and Takafumi Seto. "Humidity effects on surface dielectric barrier discharge for gaseous naphthalene decomposition". In: *Physics of Plasmas* 25.4 (2018), p. 043512.

[34]   A. J. M. Pemen et al. "An SDBD Plasma-Catalytic System for On-Demand Air Purification". In: *IEEE Transactions on Plasma Science* 46.12 (2018), pp. 4078–4090.

[35]   Tarryn Blackbeard et al. "The Effect of Temperature on the Plasma-Catalytic Destruction of Propane and Propene: A Comparison with Thermal Catalysis". In: *Plasma Chemistry and Plasma Processing* 29.6 (2009), pp. 411–419.

[36]   Yu-Ru Zhang et al. "Can plasma be formed in catalyst pores? A modeling investigation". In: *Applied Catalysis B: Environmental* 185 (2016), pp. 56–67.

[37]   S. M. Starikovskaia et al. "On electric field measurements in surface dielectric barrier discharge". In: *Journal of Physics D: Applied Physics* 43.12 (2010), p. 124007.

[38]   N. Cvetanović et al. "Electric field measurement in gas discharges using stark shifts of He I lines and their forbidden counterparts". In: *Journal of Physics D: Applied Physics* 48.20 (2015), p. 205201.

[39]   K. V. Kozlov. "Spatio-temporally resolved spectroscopic diagnostics of the barrier discharge in air at atmospheric pressure". In: *J. Phys. D: Appl. Phys. 34 3164* (2001).

[40]   Daiki Tanaka et al. "Two-dimensional potential and charge distributions of positive surface streamer". In: *Journal of Physics D: Applied Physics* 42.7 (2009), p. 075204.

[41]   Valentin I. Gibalov and Gerhard J. Pietsch. "The development of dielectric barrier discharges in gas gaps and on surfaces". In: *J. Phys. D: Appl. Phys. 33 2618* (2000).

[42]   Farah Aljammal et al. "Pigtailed Electrooptic Sensor for Time- and Space-Resolved Dielectric Barrier Discharges Analysis". In: *IEEE Transactions on Instrumentation and Measurement* 70 (2021), pp. 1–9.

[43]   Keegan Orr et al. "Measurements of electric field in an atmospheric pressure helium plasma jet by the E-FISH method". In: *Plasma Sources Science and Technology* 29.3 (2020), p. 035019.

[44]   Benjamin M. Goldberg et al. "Electric field in an AC dielectric barrier discharge overlapped with a nanosecond pulse discharge". In: *Plasma Sources Science and Technology* 25.4 (2016), p. 045008.

[45]   Zaenab Abd Allah, J. Christopher Whitehead, and Philip Martin. "Remediation of dichloromethane (CH2Cl2) using non-thermal, atmospheric pressure plasma generated in a packed-bed reactor". In: *Environmental science & technology* 48.1 (2014), pp. 558–565.

[46]   Ronny Brandenburg. "Dielectric barrier discharges: progress on plasma sources and on the understanding of regimes and single filaments". In: *Plasma Sources Science and Technology* 26.5 (2017), p. 053001.

[47]   John S. Foster. "Application of quantum mechanics to the stark effect in helium". In: *Proceedings of the Royal Society of London A: Mathematical, Physical and Engineering Sciences* (1927).

[48]   Marlous Hofmans and Ana Sobota. "Influence of a target on the electric field profile in a kHz atmospheric pressure plasma jet with the full calculation of the Stark shifts". In: *Journal of Applied Physics* 125.4 (2019), p. 043303.

[49]   Goran B. Sretenović et al. "Spectroscopic measurement of electric field in atmospheric-pressure plasma jet operating in bullet mode". In: *Applied Physics Letters* 99.16 (2011), p. 161502.

[50]   Goran B. Sretenovic et al. "Spectroscopic Study of Low-Frequency Helium DBD Plasma Jet". In: *IEEE Transactions on Plasma Science* 40.11 (2012), pp. 2870–2878.

[51]   B. M. Obradović, S. S. Ivković, and M. M. Kuraica. "Spectroscopic measurement of electric field in dielectric barrier discharge in helium". In: *Applied Physics Letters* 92.19 (2008), p. 191501.

[52]   M. M. Kuraica and N. Konjević. "Electric field measurement in the cathode fall region of a glow discharge in helium". In: *Applied Physics Letters* 70.12 (1997), pp. 1521–1523.

[53]   R. Dussart et al. "Integrated micro-plasmas in silicon operating in helium". In: *The European Physical Journal D* 60.3 (2010), pp. 601–608.

[54]   Judith Golda et al. "Circular Emission and Destruction Patterns on a Silicon-Based Microdischarge Array". In: *IEEE Transactions on Plasma Science* 42.10 (2014), pp. 2646–2647.

[55]   Valentin Felix et al. "Origin of microplasma instabilities during DC operation of silicon based microhollow cathode devices". In: *Plasma Sources Science and Technology* 25.2 (2016), p. 025021.

[56]   W. Siemens. "Ueber die elektrostatische Induction und die Verzögerung des Stroms in Flaschendrähten". In: *Ann. Phys. (Berlin)* (1857), pp. 66–122.

[57]  F. Massines and G. Gouda. "A comparison of polypropylene-surface treatment by filamentary, homogeneous and glow discharges in helium at atmospheric pressure". In: *Journal of Physics D: Applied Physics* 31.3411 (1998).

[58]  B. Eliasson and U. Kogelschatz. "UV excimer radiation from dielectric-barrier discharges". In: *Appl. Phys.* B46 (1988), pp. 299–303.

[59]  Masafumi Jinno et al. "Luminance and efficacy improvement of low-pressure xenon pulsed fluorescent lamps by using an auxiliary external electrode". In: *Journal of Physics D: Applied Physics* 40.13 (2007), pp. 3889–3895.

[60]  U. Kogelschatz. "Dielectric-Barrier Discharges: Their History, Discharge Physics, and Industrial Applications". In: *Plasma Chem. Plasma Process.* (2003), pp. 1–46.

[61]  U. Kogelschatz. "Filamentary, patterned, and diffuse barrier discharges". In: *IEEE Transactions on Plasma Science* 30.4 (2002), pp. 1400–1408.

[62]  F. Massines et al. "Recent advances in the understanding of homogeneous dielectric barrier discharges". In: *The European Physical Journal Applied Physics* 47.2 (2009), p. 22805.

[63]  E. Marode. "The mechanism of spark breakdown in air at atmospheric pressure between a positive point and a plane. I. Experimental: Nature of the streamer track". In: *Journal of Applied Physics* 46.5 (1975), pp. 2005–2015.

[64]  I. Radu, R. Bartnikas, and M. R. Wertheimer. "Frequency and voltage dependence of glow and pseudoglow discharges in helium under atmospheric pressure". In: *IEEE Transactions on Plasma Science* 31.6 (2003), pp. 1363–1378.

[65]  R. Bartnikas. "Note on discharges in helium under a.c. conditions". In: *J. Phys. D: Appl. Phys. 1 659* (1968).

[66]  N. Naudé et al. "Electrical model and analysis of the transition from an atmospheric pressure Townsend discharge to a filamentary discharge". In: *Journal of Physics D: Applied Physics* 38.4 (2005), pp. 530–538.

[67]  F. Massines et al. "Physics and chemistry in a glow dielectric barrier discharge at atmospheric pressure: diagnostics and modelling". In: *Surface and Coatings Technology* 174-175 (2003), pp. 8–14.

[68]  Yu B. Golubovskii et al. "Influence of interaction between charged particles and dielectric surface over a homogeneous barrier discharge in nitrogen". In: *Journal of Physics D: Applied Physics* 35 (2002), pp. 751–761.

[69]  Françoise Massines et al. "Experimental and theoretical study of a glow discharge at atmospheric pressure controlled by dielectric barrier". In: *Journal of Applied Physics* 83.6 (1998), pp. 2950–2957.

[70]  R. Bartnikas and J. P. Novak. "Effect of overvoltage on the risetime and amplitude of PD pulses". In: *IEEE Transactions on Dielectrics and Electrical Insulation* 2.4 (1995), pp. 557–566.

[71]  R. Bartnikas. "Partial discharges. Their mechanism, detection and measurement". In: *IEEE Transactions on Dielectrics and Electrical Insulation* 9.5 (2002), pp. 763–808.

[72]   Phelps A. V. and Molnar J. P. "Lifetimes of Metastable States of Noble Gases". In: *Phys. Rev.* 89(6) (1953), pp. 1202–1208.

[73]   Sebastian Dzikowski et al. "Modular constructed metal-grid arrays - an alternative to silicon-based microplasma devices for catalytic applications". In: *Plasma Sources Science and Technology* 29.3 (2020), p. 035028.

[74]   U. Fantz. "Basics of plasma spectroscopy". In: *Plasma Sources Science and Technology* 15.4 (2006), S137–S147.

[75]   Yu. Ralchenko et al. "Electron-impact excitation and ionization cross sections for ground state and excited helium atoms". In: *Atomic Data and Nuclear Data Tables* 94.4 (2008), pp. 603–622.

[76]   National Institute of Standards and Technology. *Atomic Spectra Database Lines Form.* 2021. URL: https://physics.nist.gov/PhysRefData/ASD/lines_form.html.

[77]   Gordon Drake. "High Precision Calculations for Helium". In: *Springer Handbook of Atomic, Molecular, and Optical Physics.* New York, NY, USA: Springer, 2006.

[78]   B. M. Obradović and M. M. Kuraica. "On the use of relative line intensities of forbidden and allowed components of several HeI lines for electric field measurements". In: *Physics Letters A* 372.2 (2008), pp. 137–140.

[79]   John S. Foster. "Relative Intensities of Stark Components in Helium". In: *Proceedings of the Royal Society of London A: Mathematical, Physical and Engineering Sciences* (1928).

[80]   Simon Kreuznacht, Marc Böke, and Volker Schulz-von der Gathen. "Intra-cavity dynamics in a microplasma channel by side-on imaging". In: *Plasma Sources Science and Technology* 30.1 (2021), p. 015014.

[81]   Francis F. Chen. *Introduction to Plasma Physics and Controlled Fusion.* 2. ed., 5. printing. Plasma Physics. New York, NY, USA: Springer US, 2006.

[82]   S. Iseni et al. "On the validity of neutral gas temperature by emission spectroscopy in micro-discharges close to atmospheric pressure". In: *Plasma Sources Science and Technology* 28.6 (2019), p. 065003.

[83]   J. L. Pack et al. "Longitudinal electron diffusion coefficients in gases: Noble gases". In: *Journal of Applied Physics* 71.11 (1992), pp. 5363–5371.

[84]   A. Chicheportiche et al. "Comparative study of collision cross-sections and ion transport coefficients from several He interaction potentials". In: *J. Phys. B: At. Mol. Opt. Phys.* 46 (2014), p. 065201.

[85]   J. Held et al. "Velocity distribution of titanium neutrals in the target region of high power impulse magnetron sputtering discharges". In: *Plasma Sources Science and Technology* 27.10 (2018), p. 105012.

[86]   Stefan Spiekermeier et al. "Helium metastable density evolution in a self-pulsing APPJ". In: *Journal of Physics D: Applied Physics* 48.3 (2015), p. 035203.

[87]   Jacob B. Schmidt et al. "Comparison of femtosecond- and nanosecond-two-photon-absorption laser-induced fluorescence (TALIF) of atomic oxygen in

atmospheric-pressure plasmas". In: *Plasma Sources Science and Technology* 26.5 (2017), p. 055004.

[88] R. Ono and T. Oda. "OH radical measurement in a pulsed arc discharge plasma observed by a LIF method". In: *IEEE Transactions on Industry Applications* 37.3 (2001), pp. 709–714.

[89] Marc Leimkühler. "Generation of Metastables by kHz-driven Microplasma Array devices". Master-Thesis. Bochum, Germany: Ruhr-University Bochum, 2018.

[90] T. Gans, V. Schulz-von der Gathen, and H. F. Döbele. "Prospects of Phase Resolved Optical Emission Spectroscopy as a Powerful Diagnostic Tool for RF-Discharges". In: *Contributions to Plasma Physics* 44.56 (2004), pp. 523–528.

[91] Sebastian Dzikowski. "Invesigation of Microarray Plasmas with an adjacent dielectric". Master-Thesis. Bochum, Germany: Ruhr-University Bochum, 2016.

[92] Henrik Böttner. "Dynamics in micro-scaled atmospheric pressure plasma arrays". Dissertation. Bochum, Germany: Ruhr-University Bochum.

[93] R. A. Baragiola et al. "Ion-induced electron emission from clean metals". In: *Surface Science* 90 (1979), pp. 240–255.

[94] Sebastian Dzikowski et al. "Electric field strengths within a micro cavity plasma array measured by Stark shift and splitting of a Helium line pair". In: *Plasma Sources Science and Technology* 29.3 (2022), p. 035028.

[95] R. W. B. Pearse and A. G. Gaydon. *The identification of molecular spectra.* 3rd ed. London, United Kingdom: Chapman and Hall, 1963.

[96] T. Ida, M. Ando, and H. Toraya. "Extended pseudo-Voigt function for approximating the Voigt profile". In: *Journal of Applied Crystallography* 33.6 (2000), pp. 1311–1316.

[97] P. Thompson, D. E. Cox, and B. Hastings. "Rietveld Refinement of Debye-Scherrer Synchrotron X-ray data from $Al_2O_3$". In: *J. Appl. Cryst.* 1987.20 (1986), pp. 79–83.

[98] Mark J. Kushner. "Modeling of microdischarge devices: Pyramidal structures". In: *Journal of Applied Physics* 95.3 (2004), pp. 846–859.

[99] Niklas Peters et al. "Catalyst-enhanced plasma oxidation of n-butane over $\alpha - MnO_2$ in a temperature-controlled twin surface dielectric barrier discharge reactor". In: *Plasma Processes and Polymers* 18.4 (2021), p. 2000127.

[100] Yujie Xie et al. "Effect of the crystal plane figure on the catalytic performance of MnO 2 for the total oxidation of propane". In: *CrystEngComm* 17.15 (2015), pp. 3005–3014.

[101] Christian Oberste-Beulmann. "Plasma-Catalytic Removal of Oxygen Traces from Hydrogen-Rich Gas Mixtures". Dissertation. Bochum, Germany: Ruhr-University Bochum, 2023.

[102] Pfeiffer Vacuum. *Massenspektrometer Manual.* 2002.

[103] M. M. Kuraica. "Razvoj novih spektroskopskih metoda za dijagnostiku tinjavog pražnjenja". Dissertation. Belgrade, Serbia: University of Belgrade, 1998.

[104] D. J. Griffiths and E. G. Harris. *Introduction to Quantum Mechanics.* 2nd ed. Upper Saddle River, New Jersey, USA: Pearson Prentice Hall, 2005.

[105] H. A. Bethe and E. E. Salpeter. *Quantum Mechanics of One- and Two-Electron Atoms.* 1st ed. Berlin,Germany: Springer, 1957.

[106] D. D. Fitts. *Principles of Quantum Mechanics.* 1st ed. University of Cambridge, UK: Cambridge University Press, 1999.

[107] D. C. Morton, Q. Wu, and G. WF. Drake. "Energy levels for the stable isotopes of atomic helium(4He I and 3He I)". In: *Canadian Journal of Physics* (2006).

[108] A. E. Kramida. "A critical compilation of experimental data on spectral lines and energy levels of hydrogen, deuterium, and tritium". In: *Atomic Data and Nuclear Data Tables* 96 (2010), pp. 586–644.

# List of Figures

# List of Tables

# *Acknowledgements*

An dieser Stelle möchte ich allen Personen meinen herzlichen Dank aussprechen, die mich auf dem Weg bis hier hin begleitet haben und/ oder mich zum Gelingen dieser Arbeit unterstützt haben. Ich bedanke mich besonders bei

...**Dr. Volker Schulz-van der Gathen**, der mir seit dem Bachelor immer mit Rat und Tat bei allen wissenschaftlichen Vorhaben zur Seite stand und mit seiner öfters getätigten Aussage "Alles wird gut!" für Sicherheit und Optimismus gesorgt hat, besonders in Zeiten, die schwierig waren. Ich bin besonders dankbar für deine ganze wissenschaftliche Expertise und Lebenserfahrung, die immer mit uns in der Arbeitsgruppe geteilt wurden. Besonders bedanken möchte ich mich auch für das sehr genaue Korrekturlesen sämtlicher wissenschaftlicher Abhandlungen, die ich in meiner Zeit an der RUB verfasst habe. Alle Korrekturen steigerten die Qualität erheblich.

...**Prof. Dr. Achim von Keudell**, der mir nicht nur die Möglichkeit gab am Lehrstihl für Experimentalphysik II dieses Promotionsvorhaben zu realisieren, sondern auch immer für Fragen, Kommentare und Diskussionen zur Verfügung stand.

...**Dr. Marc Böke**, der mich bei der Einwertung sämtlicher Ergebnisse unterstützt und mir bei allesamt Veröffentlichungen und Vorträgen unter die Arme gegriffen hat.

...**Prof. Dr. Judith Golda**, die mich seit dem Bachelor stets motiviert, nach allen Vorträgen aufgebaut und bei allen wissenschaftlichen Diskussionen und Vorhaben mit ihrem Input unterstützt hat. Außerdem bedanke ich mich für die Übernahme des Zweitgutachtens.

...**Prof. Dr. Peter Awakowicz**, der bei allen Projekttreffen große Neugier am Array zeigte und für einen wertvollen wissenschaftlichen Austausch zur Verfügung stand.

...**Dr. Katharina Laake geb. Grosse**, die immer ein offenes Ohr für Privates hatte und meine gesamte Arbeit korrekturgelesen hat.

...**Dr. Patrick Preissing** für die vielen Unterhaltungen zu Themen von A bis Z im Flur und Büro, Mensa und Cafete, Labor und Müllraum, auf dem Campus und außerhalb des Campus.

...**Adrian Marczak** für die vielen scherzhaften Unterhaltungen über Privates, Technik, Geschichte und Politik. Außerhalb bedanke ich mich für die Hilfe bei allen IT-Problemen, die ich entweder an der RUB oder zu Hause hatte.

...**Sascha Thielmann-Monje**, der für eine angenehme und lustige Büroatmosphäre gesorgt und mich bei den XPS-Messungen unterstützt hat.

**Dr. Julian Held**, der mir stets bei der Neujustage des PGS zur Seite stand.

...**David Steuer**, der mich bei den Experimenten zur Plasma-Katalyse begleitet und mich mit vielen Lösungen und Ideen im Hinblick auf das Array unterstützt hat.

*I feel the weight of the world on my shoulder*
*As I'm gettin' older, y' all, people gets colder*
*Most of us only care about money makin'*
*Selfishness got us followin' the wrong direction*

*Wrong information always shown by the social media*
*Negative images is the main criteria*
*Infecting the young minds faster than bacteria*
*Kids wanna act like what they see in the cinema, yo'*

*Whatever happened to the values of humanity?*
*Whatever happened to the fairness and equality?*
*Instead of spreading love we're spreading animosity*
*Lack of understanding, leading us away from unity*

*That's the reason why sometimes I'm feelin' under*
*That's the reason why sometimes I'm feelin' down*
*There's no wonder why sometimes I'm feelin' under*
*Gotta keep my faith alive 'til love is found*

*Now ask yourself*

***Where is the love?***

# Lebenslauf

## Persönliche Daten

| | |
|---|---|
| Name | Sebastian Dzikowski |
| Geburtsdatum | 15.12.1990 |
| Geburtsort | Hattingen |

## Beruflicher Werdegang

| | |
|---|---|
| Seit 05/2022 | KPMG Wirtschaftsprüfungsgesellschaft, Düsseldorf |

## Promotionsvorhaben

| | |
|---|---|
| Seit 03/2017 | Promotionsvorhaben in der Physik, Lehrstuhl für Experimentalphysik II, Ruhr-Universität Bochum |
| 03/2017 – 12/2021 | Wissenschaftlicher Mitarbeiter, Lehrstuhl für Experimentalphysik II, Ruhr-Universität Bochum |

## Studium

| | |
|---|---|
| 10/2014 – 09/2016 | Studium der Physik (M. Sc.), Ruhr-Universität Bochum |
| 09/2011 – 10/2014 | Studium der Physik (B. Sc.), Ruhr-Universität Bochum |

## Schulausbildung

| | |
|---|---|
| 08/2008 – 07/2011 | Abitur (Allgemeine Hochschulreife) |
| 09/2002 – 06/2008 | Wilhelm-Kraft Gesamtschule, Sprockhövel |
| 08/1997 – 07/2002 | Gemeinschaftsgrundschule Sprockhövel, Sprockhövel |

Sprockhövel, 25.10.2024